Full-wave modeling of lower hybrid waves on Alcator C-Mod

by

Orso Meneghini

Submitted to the Department of Nuclear Science and Engineering
in partial fulfillment of the requirements for the degree of

Doctor of Philosophy in Applied Plasma Physics

at the

MASSACHUSETTS INSTITUTE OF TECHNOLOGY

February 2012

Author .....
Department of Nuclear Science and Engineering
November 22, 2011

Certified by .....
Ronald R. Parker
Professor, Department of Nuclear Science and Engineering
Thesis Supervisor

Certified by .....
Paul T. Bonoli
Senior Research Scientist, MIT Plasma Science and Fusion Center
Thesis Reader

Certified by .....
Syunichi Shiraiwa
Research Scientist, MIT Plasma Science and Fusion Center
Thesis Reader

Accepted by .....
Mujid S. Kazimi
TEPCO Professor of Nuclear Engineering
Chair, Department Committee on Graduate Students

Full-wave modeling of lower hybrid waves on Alcator C-Mod

by

Orso Meneghini

Submitted to the Department of Nuclear Science and Engineering
on November 22, 2011, in partial fulfillment of the
requirements for the degree of
Doctor of Philosophy in Applied Plasma Physics

Abstract

This thesis focuses on several aspects of the Lower Hybrid (LH) wave physics, the common theme being the development of full-wave simulation codes based on Finite Element Methods (FEM) used in support of experiments carried out on the Alcator C-Mod tokamak. In particular, two non-linear problems have been adressed: high power antenna-plasma coupling and current drive (CD). In both cases, direct solution of the wave equation allowed testing the validity of approximations which were historically done and consider full-wave effects and realistic geometries.

The first code, named POND, takes into account the interaction of high power LH waves and the plasma edge based on the non-linear ponderomotive force theory. Simulations found the effect of ponderomotive forces to be compatible with the density depletion which is measured in front of the antenna in presence of high power LH waves.

The second code, named LHEAF, solves the problem of LH wave propagation in a hot non-Maxwellian plasma. The electron Landau damping (ELD) effect was expressed as a convolution integral along the magnetic field lines and the resultant integro-differential Helmholtz equation was solved iteratively. A 3D Fokker-Planck code and a synthetic Hard X-Ray (HXR) diagnostic modules are used to calculate the self-consistent electron distribution function and evaluate the resulting CD and bremsstrahlung radiation.

LHEAF has been used to investigate the anomalous degradation of LHCD efficiency at high density. Results show that while a small fraction of the launched power can be absorbed in the SOL by collisions, it is a strong upshift in the $n_{\parallel}$ spectrum that makes the overall LHCD efficiency low by allowing the waves to Landau damp near the edge. Wavelet analysis of the full-wave fields identified spectral broadening to occur after the waves reflect and propagate in the SOL. This work explains why on Alcator C-Mod the eikonal approximation is valid only in the low to moderate density regime, and why parasitic phenomena introduced in previous work can reproduce phenomenologically well the experimental results.

Thesis Supervisor: Ronald R. Parker
Title: Professor, Department of Nuclear Science and Engineering

Thesis Reader: Paul T. Bonoli
Title: Senior Research Scientist, MIT Plasma Science and Fusion Center

Thesis Reader: Syunichi Shiraiwa
Title: Research Scientist, MIT Plasma Science and Fusion Center

Acknowledgments

I would like to start by thanking my advisor, Prof. Ron Parker, who was able to guide me with his numerous advices while still giving me the freedom to work in my own way. I am especially thankful to Ron for his constant support and allowing me to present my work in many conferences and laboratories around the world.

A special thank goes to Dr. Syunichi Shiraiwa. This thesis would not have been possible without Syunichi. He has been a fantastic mentor, a generous friend and to me he is like family. From Syunichi I have learned an incredible amount of physics, most of all just by sharing a small desk in the Alcator C-Mod control room. I will mostly miss our innumerable adventures and our daily discussions during lunch time.

Next I would like to acknowledge my thesis reader Dr. Paul Bonoli, for constantly providing feedback and encouraging my research. In this respect I often had the chance to appreciate Paul's integrity. Paul was always available for help and talking to him is always a pleasure.

More in general, I felt honored to work with the MIT-PSFC faculty, staff and students. They are very ingenious people who are real experts in their fields and I have learned something from each one of them. In my daily work I have enjoyed discussing of RF physics with Dr. Greg Wallace, Dr. John Wright, Dr. Andrea Schmidt, Ian Faust and Mike Garrett. I am also indebted to all those who keep Alcator C-Mod running and in particular I would like to give a special thank to Atma Kanojia, David Johnson, Pat MacGibbon and David Terry for taking care of the LH system. Working with them was a great deal of fun. It was also a pleasure working and receiving advice from Bill Beck and Rui Vieira, who are real masters in their disciplines. Of the fellow students Id like to single out Yuri Podpaly, Zac Hartwig and Clarice Aiello for being my comrade in arms during the qualifying exam.

Some sections of this thesis would have not been possible without the contributions of a few individuals. Among many other things, it was Syunichi who started working on plasma wave modeling using COMSOL, his are many ideas and scripts which at the base of the LHEAF code. He is the author of the 3DFP code VERD which is used in LHEAF and of the data visualization software iScope which to me has made data analysis somewhat fun to do. Dr. Brian LaBombard has offered much advice on how to implement the SOL model in the LHEAF code. It was Dr. Steve Wukitch who pushed me to design the microwave probe diagnostic and David Johnson helped me significantly with the most experimental aspects of the electronic and microwave design of this diagnostic. Cornwall Lau provided the SOL reflectometer data used in the POND code. Andrea Schmidt and Ian Faust have been maintaining the HXR camera diagnostic to which I refer so much throughout the thesis.

Finally, my deepest gratitude goes to my beautiful Luz who is a great travel companion, both literally and in life, and my parents and my sister for their love and their unconditional support.

Contents

List of Figures

List of Tables

Summary and main results of this thesis

For each chapter in this thesis the main results are summarized and the subsequent advances in the understanding of Lower Hybrid (LH) wave physics and RF simulations are highlighted.

Chapter 3 - Alcator C-Mod and the 4-way-splitter LH antenna

For this thesis, the RF design of a new LH four-way-splitter antenna [1] for Alcator C-Mod was carried out using the Microwave Studio software and the TOPLHA [2, 3] code, which is based on linear LH wave coupling theory. Similarly to a multijunction design [4], the poloidal-splitter antenna redistributes the power at the front of the launcher, resulting in a simple low loss feeding network. However, since the power splitting is done poloidally, the launched parallel wave spectrum can be changed with the same flexibility of conventional grill antennas [5]. In this respect the four-way-splitter design represents a breakthrough in that it overcomes the major limitation for multijunction antennas. For the same reason, the directivity of the antenna is not affected by the plasma load (see Fig. 3-8), another known issue of multijunction antennas.

The system was optimized for equal power splitting in the case of equal loads on each rows, at the expense of a higher reflection coefficient (Fig. 3-10). Particular attention was also given to the problem of equal power splitting and the tradeoff between wave field magnitude at the grill mouth and reflection coefficient was highlighted. With respect to the first generation antenna, the new system is successful at reducing the overall transmission losses and delivering more power to the plasma.

Chapter 4 - Microwave probe diagnostic

Poloidal variations of the edge density were predicted to affect the evenness of the poloidal power splitting, suggesting the necessity of forward and reflected power measurements at each row of the launcher (Fig. 3-11). For this reason, for this thesis, a new antenna diagnostic based on the microwave probe concept [6] has been designed and installed on the four-way-splitter launcher. This diagnostic is composed of a set of 32 microwave probes that non-perturbatively monitor the forward and reflected power in a carefully selected set of waveguides composing the grill.

With such diagnostic the four-way-splitter concept was benchmarked against the numerical simulation done at the design stage. In particular, the launched power spectrum reconstructed from the microwave probe diagnostic was confirmed to be clean and to reproduce well the commanded one. Study of the poloidal power redistribution confirmed the overall resiliency of the four-way-splitter performance on the plasma equilibrium, as shown in Fig. 4-23.

Additional components, including RF absorbers, adaptors and fixtures have also been designed, manufactured and used to calibrate the microwave probes and the four-way-splitter antenna itself. Multiple calibration schemes were used and cross-verified to each other. The development of an off-site calibration routine further confirmed the accuracy of the calibrations done prior to the beginning

of operations.

Chapter 5 - Lower hybrid wave coupling on Alcator C-Mod

High reflection coefficients ($> 15\%$) have been a long standing issue for Alcator C-Mod LH systems. For this thesis, high power coupling experiments ($> 1\ MW/m^2$) were performed on Alcator C-Mod to survey the dependency of coupling on density, launcher position and antenna phasing. As shown in Fig. 5-3, coupling was observed to degrade for higher launched $n_{\parallel}$, suggesting that the waves have to tunnel through a millimetric evanescent layer between the plasma and the launcher. A new model with a variable vacuum gap for increasing plasma densities was proposed to match the experimental measurements with calculation from the GRILL linear coupling code.

Subsequent edge density profile measurements by means of an X-mode SOL reflectometer [7, 8] were able for the first time to accurately measure the density profile in the presence of high power LHRF, as highlighted in Fig. 5-4. In general, a density depletion is observed within the first few *mm* away from the grill mouth, while farther inside of the plasma the density increases, possibly due to RF-induced ionization or convective cell formation. Two dimensional coupling simulations with the Finite Element Method (FEM) software COMSOL using the reflectometer density profiles (i.e. no free parameters) were found to reproduce within few percent the measured reflection coefficient. Good coupling was recovered for non-perturbative power level experiment (few Watts), thus confirming the role of high power LHRF waves on the edge plasma profiles.

Linear coupling theory for LH waves [5] has been shown to break down at high power densities. Coupling physics in the non-linear regime has been investigated with the non-linear fullwave FEM code POND, which was developed to self-consistently take into account the effect of ponderomotive forces [9, 10, 11]. The code has been verified against 1D calculations available from literature [9]. The main advantage of using a FEM scheme is the possibility of extending the numerical simulations to 2D or even 3D, thus allowing for the description of complicated geometries or non-uniformities in the plasma.

The simulation results plotted in Fig. 5.4.2 were found to be compatible with the density depletion measured in front of the launcher during high power operation thus providing an unprecedented strong validation of the ponderomotive theory. It was also found that retaining higher order modes at the waveguide openings and the standing wave pattern of overlapping resonance cones, further exacerbates the density depletion in front of the launcher and gave better agreement with the reflectometer measurements.

Chapter 6 - Integrated LHCD modeling with LHEAF

Ray-tracing coupled with a Fokker-Planck (FP) code has been a common method for modeling LHCD. Although this approach has been successful in predicting essential aspects of LHCD in many experiments, disagreements persist with some experimental observations and call into question the validity regime of the ray-tracing approach. To address these issues, for this thesis the fullwave FEM code LHEAF [12, 13] has been developed.

The LHEAF formulation is based on an innovative iterative scheme which allows the inclusion of hot plasma effects in a conventional 3D FEM code [12]. The integro-differential equation arising from the description of waves in a hot dispersive plasma, is split into two coupled equations which are solved iteratively. The main idea behind this approach is that the electron Landau damping term can be approximated by an effective local damping $\bar{\bar{\epsilon}}_{\mathrm{ELDeff}}$ whose value is found iteratively by successive refinements of an initial guess. According to this scheme, at the N^{th} step of the iteration loop, the electric field $E^{(\mathrm{N})}(z)$ is computed by solving the partial differential equation:

$$\nabla \times (\nabla \times \vec{E}^{(\mathrm{N})}(\vec{x})) + \frac{\omega^2}{c^2}\left(\bar{\bar{\epsilon}}_{\mathrm{cold}} + \bar{\bar{\epsilon}}^{(\mathrm{N})}_{\mathrm{LEDeff}}\right) \cdot \vec{E}^{(\mathrm{N})}(\vec{x}) = 0 \tag{1}$$

Subsequently, an updated value of $\bar{\bar{\epsilon}}^{(N+1)}_{ELDeff}$ is computed as a one dimensional convolution integral along the magnetic field lines:

$$\bar{\bar{\epsilon}}^{(N+1)}_{ELDeff} = \frac{-i}{E^{(N)}} \frac{\hat{z}\hat{z}}{\sqrt{2\pi}} \cdot \int dz' \epsilon_{ELD}(z - z') E_z^{(N)}(z') \tag{2}$$

and is substituted to find the electric field at the next step of the iteration. This procedure is repeated until the power deposition converges.

In its implementation LHEAF makes also use of periodic boundary conditions for the decomposition of the wave propagation into its toroidal modes [14]. The main advantage of using a FEM approach is that the edge and core plasma are treated simultaneously, thus bridging the historical disconnect between the edge coupling problem and core propagation/absorption problem. Furthermore, the LHEAF iterative formulation makes the numerical problem to scales more favorably to reactor scale plasma simulations than spectral and semi-spectral approaches.

LHEAF has been verified with ray-tracing and spectral fullwave codes for a simple Alcator C mockup geometry for a Maxwellian plasma [12, 13, 15], as shown in Figs. 6-10 and 6-11. The good scalability of the LHEAF code permitted the first ever fullwave simulations of LH wave propagation in ITER scale plasmas, which was found to be in good agreement with ray-tracing calculations [16]. This result is a further encouraging evidence that ray-tracing Fokker-Plank modeling can be reliably used for ITER and the next generation of tokamaks, where strong single-pass damping of the waves is expected due to higher electron temperatures.

Inclusion of a 1D Fokker-Planck module in the iteration loop accounts for the deformation of the distribution function on the wave damping [17]. A 3D bounce-averaged zero-banana-width relativistic Fokker-Planck module named VERD (VElocity and Radial Diffusion) is used to postprocess the wave fields of the last iteration and generate a 2D distribution function that is used to accurately evaluate the driven current [18]. The initial speculation that 2D velocity effects are not dominant for the calculation of the power absorption was subsequently verified when the VERD 3DFP was used at the last iteration of the LHEAF loop. Although a full iteration with the VERD solver has not been yet done, for the moment this result does not invalidate the use of a 1DFP code in the iteration loop and of a VERD code only for postprocessing the final result, thus minimizing the computation time while at the same time providing reliable current drive predictions. In addition to comparing the current profile, the development of a HXR camera synthetic diagnostic [19, 20] has allowed direct comparison of the simulations with the measurements of the HXR camera diagnostic installed on Alcator C-Mod [21].

In general, for Alcator C-Mod LHCD discharges in the "moderate" multi-pass absorption regime, LHEAF simulations result in a broader power deposition, current and HXR profiles than what is predicted by ray-tracing Fokker-Planck codes. Specifically, an in depth analysis of a nearly fully non-inductive discharge has been presented. The simulated current density profiles from LHEAF were found to agree better than ray-tracing with the profiles inferred from magnetic equilibrium reconstructions constrained by both kinetic and motional Stark effect pitch angle measurements (when available). The overall characteristics of the HXR profiles is well captured in the LHEAF simulation. Analysis of the wave $n_{\parallel}$ spectrum points to differences in the filling of the wave kinematic domain to be at the base of the discrepancy between fullwave and ray-tracing calculations [18]. Such differences have been attributed to fullwave effects such as diffraction and focusing.

Chapter 7 - Simulation of high density Alcator C-Mod discharges using LHEAF

The anomalous fall off in LHCD efficiency at high density which has been observed in several devices has motivated the LHCD community to consider additional phenomena besides the wave propagation to explain this result. The most prominent theories incude spectral broadening due to scattering from fluctuations [22], modification of the launched spectrum by parametric decay instability [23, 24], and absorption of RF energy in the SOL by electron-ion collisions [25].

For this thesis an advanced Pulse Height Analysis (PHA) analysis was developed to correct for pileup and baseline drift effects on the Alcator C-Mod HXR camera diagnostic. Initial studies [25, 26, 27] identified the presence of a break-in-slope in the HXR emission occurring around the line average density $\bar{n}_e = 10^{20}\ m^{-3}$. Thanks to this improved analysis, it was realized that such feature was an artifact induced by the existing PHA routine and that instead the HXR emission drops almost exponentially across all densities. The qualitative change in the behaviour of the HXR decline fundamentally redefines the nature of the LHCD density limit. Whatever the processes involved, they should not occur suddenly but must instead degrade the LHCD efficiency continuously across the whole density range which was probed in the experiments. Comparison of the HXR count rates are shown in Figs. C-5 and C-6.

As a next step, the full wave FEM code LHEAF was applied to the LHCD density limit problem, to investigate the role of fullwave effects and of the SOL in the loss of current drive efficiency. For this purpose, a realistic 2D SOL model that takes into account the effect of flux expansion and parallel heat transfer was included in LHEAF [28] , shown in Fig. 7-4.

A systematic study using three similar discharges at different densities has shown that the decrease in LHCD efficiency can be reproduced (Fig. 7-7) without invoking any additional loss processes other than electron Landau damping [29]. This result differs from previous ray-tracing Fokker-Planck studies, which require a significant fraction of the power to be lost in the SOL by collisional damping (more than 60% at high density) to obtain good agreement with the experiments [25]. Figure 7-5 shows the waves parallel electric field and power deposition profiles for the three density cases.

While the drop in HXR emissivity is independent of the amount of radial diffusion used in the simulations, some transport mechanism is needed for redistributing the fast electron population across the plasma and the synthetic HXR camera to better agree with the experimental measurements. The effect of radial diffusion has been studied parametrically and was found to have substantial impact on the shape of the HXR profiles. As the amount of diffusion is increased, the emission from the edge chords of the diagnostic show a significant drop, suggesting that also in the experiment fast electrons generated at plasma periphery might be transported outside of the LCFS where they are promptly lost.

Analysis of the quantities involved in the 3D Fokker-Planck calculation as a function of parallel velocity $v_\parallel$ and minor radius reveals that the wave spectrum is broad and that most of the LH power is absorbed at low $v_\parallel$ and near the edge (see Fig. 7-14). Differences between raytracing and fullwave results have been identified in this region of phase space, which is consistently found to be void of rays where instead significant wave power is observed. Absence of rays with a sufficiently slow phase velocity prevents the spectral gap to be bridged, causing ray-tracing simulations to deposit power more in the plasma core and enhancing the role of collisions. This is a remarkable result, (especially considering that in ray-tracing a broad $n_\parallel$ spectrum is launched) which points either to the SOL model and/or fullwave effects as being the cause of this difference.

The dynamics of the observed spectral upshift/broadening has been investigated by use of Continuous-Wavelet-Transforms to decompose the complicated fullwave field pattern into its spectral components parallel to the static magnetic field (see Fig. 7-18). From the CWT analysis it is inferred that the local wave spectrum strongly upshifts after reflection and propagation in the SOL. Near the plasma core, broad spectral features associated with wave diffraction at caustic surfaces are also observed, in agreement with beam-tracing simulations [30]. Also, wave field patterns typical of the fast-wave propagation have also been identified [31], a sign that some power is mode-converted from slow-wave to fast-wave.

LHEAF simulations provide a new interpretation of the density limit based on an efficient upshift of the $n_\parallel$ spectrum. While a small fraction of the launched power can be absorbed in the SOL by collisions, the main feature leading to a precipitous drop in efficiency is related to a strong $n_\parallel$ upshift which allows the LH waves to Landau damp near the edge at relatively low temperature and with low LHCD efficiency (see Fig. 7-22). The resulting physical picture is rather different from the one developed previously using ray-tracing codes which instead pointed to a strong collisional damping

in the SOL as the reason why current drive is lost. Although the LHEAF result does not exclude in itself the role of parasitic losses in the SOL, it is an important finding that the experimental trends can be reproduced to a large degree without invoking effects which are affected by large experimental uncertainties.

Chapter 1

Background of plasma waves physics

The first two chapters introduce the background theory which is necessary for describing the physics relevant to Lower Hybrid Current Drive (LHCD). The derivations in the following sections are a personal re-adaptation of the work published in Ref. [32, 33, 34, 35, 36, 37] and from the lecture notes of the Plasma Waves course which is taught by Prof. Porkolab at MIT.

1.1 Plasma waves in a cold uniform plasma

The Helmholtz equation for electromagnetic waves is derived by combining Faraday and Ampere laws of Maxwell's Equations

$$\nabla \times \vec{E} = -\frac{\partial \vec{B}}{\partial t} \tag{1.1a}$$

$$\nabla \times \vec{B} = \mu_0 \vec{J} + \frac{1}{c^2}\frac{\partial \vec{E}}{\partial t} \tag{1.1b}$$

which leads to

$$\nabla \times \nabla \times \vec{E} = -\frac{1}{c^2}\frac{\partial^2 \vec{E}}{\partial t^2} - \frac{\partial}{\partial t}(\mu_0 \vec{J}) \tag{1.2}$$

In this expression, the plasma contributes to the wave propagation through the current $\vec{J}$, which is induced by the charged particles as they move with the waves:

$$\vec{J} = \sum_s \vec{J}_s = \sum_s n_s q_s \vec{v}_s \tag{1.3}$$

where n_s is the number density of particles of species s with charge q_s. The quantity q_s is taken to be algebraic, not absolute, so that the electron charge $q_e = -e$ while ion charges are $q_i = Z_i e$.

1.1.1 Uniform plasma approximation

Assuming that the plasma is homogeneous (uniform) in space and the wave fields are harmonic, allows to Fourier analyze the wave equation both in space and time. This is an important step that allows to convert integro-differential equations in $\vec{k}$ and ω into algebraic equations. Taking the first order quantities of the wave fields to have the form of $\exp\left(i(\vec{k}\cdot\vec{x} - \omega t)\right)$ results in the

transformation $\nabla \leftrightarrow i\vec{k}$ and $\frac{\partial}{\partial t} \leftrightarrow -i\omega$ [1].

Each Fourier component of Eq. 1.6 can thus be expressed as

$$\vec{k} \times \vec{k} \times \vec{E} + i\omega\mu_0 \vec{J} + \frac{\omega^2}{c^2}\vec{E} = 0 \tag{1.4}$$

Now, using Ohm's Law to relate the current J to the wave field E in terms of the conductivity tensor $\bar{\bar{\sigma}}$:

$$\vec{J} = \bar{\bar{\sigma}} \cdot \vec{E} \tag{1.5}$$

one obtains:

$$\vec{k} \times \vec{k} \times \vec{E} + i\omega\mu_0 \bar{\bar{\sigma}} \cdot \vec{E} + \frac{\omega^2}{c^2}\vec{E} = 0 \tag{1.6}$$

Substituting the definition of index of refraction $\vec{n} = \frac{c\vec{k}}{\omega}$ into results in

$$\vec{n} \times \vec{n} \times \vec{E} + \bar{\bar{\epsilon}} \cdot \vec{E} = 0 \tag{1.7}$$

where the dielectric tensor $\bar{\bar{\epsilon}}$ is written in terms of the conductivity and susceptibility tensors $\bar{\bar{\sigma}}$ and χ as:

$$\bar{\bar{\epsilon}} = \bar{\bar{I}} + \sum_s \bar{\bar{\chi}}_s = \bar{\bar{I}} + \frac{ic^2\mu_0}{\omega}\bar{\bar{\sigma}} \tag{1.8}$$

which simplifies Eq. 1.7 to

$$(\vec{n}\vec{n} - n^2\bar{\bar{I}}) \cdot \vec{E} + \bar{\bar{\epsilon}} \cdot \vec{E} = 0 \tag{1.9}$$

and can be written in a compact form as

$$\hat{D} \cdot \vec{E} = 0 \tag{1.10}$$

where $\hat{D}$ is the a linear operator, named the *wave operator.*

This equation has the form of three coupled, linear, homogeneous algebraic equations for the three unknowns E_x, E_y, E_z. As there are no source terms in Eq. 1.10, the non-trivial roots ($\vec{E} \neq 0$) describe the natural modes of oscillation (eigenmodes) of the system and can be found by imposing the determinant of the 3×3 tensor $\hat{D}$ to be zero. This condition gives the *dispersion relation*, that is a scalar relation that determines ω as a function of $\vec{k}$ (for example, in the special case of wave propagation in vacuum this relationship is given by $\omega = kc$). The resulting eigenvalue problem in a cartesian coordinate system takes the general form:

$$\det(\hat{D}) = \begin{vmatrix} n_y^2 + n_z^2 - \epsilon_{xx} & -n_x n_y - \epsilon_{xy} & -n_x n_z - \epsilon_{xz} \\ -n_x n_y - \epsilon_{yx} & n_x^2 + n_z^2 - \epsilon_{yy} & -n_y n_z - \epsilon_{yz} \\ -n_x n_z - \epsilon_{zx} & -n_y n_z - \epsilon_{zy} & n_x^2 + n_y^2 - \epsilon_{zz} \end{vmatrix} = 0 \tag{1.11}$$

Up to this point we have made no approximations and the wave equations are exact for harmonic waves in a uniform medium. Worth stressing is that the description of the plasma effects on the wave propagation is contained in $\bar{\bar{\epsilon}}$, and as such depend on which model is introduced to determine $\bar{\bar{\sigma}}$. The most simple model for $\bar{\bar{\sigma}}$ assumes that the plasma is cold (i.e. $T_s = 0$). Other models allow finite temperature effects for some (e.g. electrons) or all of the species present in the plasma. Allowing for finite temperature introduces a number of interesting effects ranging from corrections to the wave propagation, the appearance of new propagation modes, mode-conversion effects and collisionless damping. The study of hot plasmas requires the use of kinetic theory and will be deferred to the later part of this chapter.

[1] The choice of this sign convention is such that the wave propagation for positive ω takes place in the $\vec{k}$ direction.

1.1.2 Cold plasma approximation

The derivation of the conductivity tensor $\bar{\bar{\sigma}}$ requires finding a relationship between the wave electric field $\vec{E}$ and the particle velocities $\vec{v}$. The derivation for a cold magnetized plasma begins with the linearized momentum conservation equation for a charged particle of species s in the presence of a magnetic field

$$m_s \frac{\partial \vec{v}_s}{\partial t} + m_s \vec{v}_s \cdot \nabla \vec{v}_s = q_s(\vec{E} + \vec{v}_s \times \vec{B}) \tag{1.12}$$

Expanding the dependent variables in the usual series for perturbation theory, we now assume that $\vec{B}$ is static and uniform in space in zeroth-order, and that $\vec{v}_s$, $\vec{J}$ and $\vec{E}$ are all zero in zeroth-order. To zeroth-order, Eq. 1.12 is therefore trivially satisfied, while to the first order, after Fourier analysis,

$$-i\omega m_s \vec{v}_{s1} = q_s(\vec{E}_1 + \vec{v}_{s1} \times \vec{B}_0) \tag{1.13}$$

Since all the charged species contribute to the plasma current, their contributions should be added together (i.e. the conductivity tensor is additive in its components). Solving the previous force balance equation leads for each of the species (for the sake of simplifying the notation, the subscript s has been dropped):

$$\begin{aligned} v_{1x} &= \frac{iq}{m\omega}(E_{1x} + v_{1y}B_0) \\ v_{1y} &= \frac{iq}{m\omega}(E_{1y} - v_{1x}B_0) \\ v_{1z} &= \frac{iq}{m\omega}E_{1z} \end{aligned} \tag{1.14}$$

where we assumed that $\vec{B_0} = B_0\hat{z}$.

Solving this system of equations, and defining $\omega_p = \sqrt{\frac{nq^2}{\epsilon_0 m}}$ and $\Omega = \frac{qB}{m}$ as the *plasma frequency* and the *cyclotron frequency* of each plasma species, results in:

$$\begin{aligned} v_{1x} &= \frac{1}{1-\Omega^2/\omega^2}\left(\frac{iq}{m\omega}E_{1x} - \frac{q^2B_0}{m^2\omega^2}E_{1y}\right) \\ v_{1y} &= \frac{1}{1-\Omega^2/\omega^2}\left(\frac{iq}{m\omega}E_{1y} + \frac{q^2B_0}{m^2\omega^2}E_{1x}\right) \\ v_{1z} &= \frac{iq}{m\omega}E_{1z} \end{aligned} \tag{1.15}$$

From Eq. 1.15 we can form the matrix $\bar{\bar{\sigma}}$ by using the relation that $\vec{J} = \sum nq\vec{v}$

$$\bar{\bar{\sigma}} = \sum \frac{q^2 n}{m} \begin{pmatrix} \frac{i\omega}{\omega^2-\Omega^2} & \frac{-\Omega}{\omega^2-\Omega^2} & 0 \\ \frac{\Omega}{\omega^2-\Omega^2} & \frac{i\omega}{\omega^2-\Omega^2} & 0 \\ 0 & 0 & \frac{i}{\omega} \end{pmatrix} \tag{1.16}$$

where the sum is performed over all species.

Using the familiar notation of Stix [32], we can now express the elements $\bar{\bar{\epsilon}}$ using Eq. 1.8. The resulting dielectric tensor is the *cold plasma dielectric tensor* $\bar{\bar{\epsilon}}_{\text{cold}}$, which is *anisotropic* and *Hermitian* (i.e. loss-less):

$$\bar{\bar{\epsilon}} = \begin{pmatrix} S & -iD & 0 \\ iD & S & 0 \\ 0 & 0 & P \end{pmatrix} \equiv \bar{\bar{\epsilon}}_{\text{cold}} \tag{1.17}$$

where

$$P = 1 - \sum \frac{\omega_p^2}{\omega^2} \tag{1.18}$$

$$S = 1 - \sum \frac{\omega_p^2}{\omega^2 - \Omega^2} \tag{1.19}$$

$$D = \sum \frac{\Omega \omega_p^2}{\omega(\omega^2 - \Omega^2)} \tag{1.20}$$

By substituting Eq. 1.17 into Eq. 1.11 one gets

$$\vec{n} \times \vec{n} \times \vec{E} + \bar{\bar{\epsilon}}_{cold} \cdot \vec{E} = 0 \tag{1.21}$$

and the resulting dispersion relation becomes noticeably simpler:

$$\begin{vmatrix} S - n_{||}^2 & -iD & n_\perp n_{||} \\ iD & S - n_{||}^2 - n_\perp^2 & 0 \\ n_{||} n_\perp & 0 & P - n_\perp^2 \end{vmatrix} = 0 \tag{1.22}$$

where the subscript $_{||}$ and $_\perp$ have been used to denote the vector components which are respectively parallel and perpendicular to the static background magnetic field, or in mathematical terms

$$\hat{n}_{||} = n_z = \frac{\vec{n}(\vec{n} \cdot \vec{B})}{|\vec{B}|^2} \tag{1.23}$$

$$\hat{n}_\perp = -\frac{\vec{B} \times (\vec{B} \times \vec{n})}{|\vec{B}|^2} \tag{1.24}$$

Worth pointing out now is that $\bar{\bar{\epsilon}}_{\text{cold}}$ has no $\vec{n}$ dependence, meaning that its properties are *local*. Consequently the wave equation, which was expressed in the spectral domain in Eq. 1.7 takes the form of a Partial Differential Equation (PDE) when cast into real space:

$$\nabla \times \nabla \times \vec{E} - \frac{\omega^2}{c^2} \bar{\bar{\epsilon}}_{cold} \cdot \vec{E} = 0 \tag{1.25}$$

In view of the fact that the dielectric tensor is additive in its components, not only each species contributes separately, but also the contributions from different portions of the distribution function can be identified and tracked. This property allows cold and hot plasma effects to be treated individually and subsequently combined.

1.1.3 Zoology of plasma wave principal solutions

When solving the dispersion relation there will be in general multiple roots, each corresponding to an independent wave (i.e. mode) with different propagation characteristics. This is quickly seen by considering a 2D slab structure, such that the background magnetic field is in the $\hat{z}$ direction and there is no variation in the $\hat{y}$ direction. Under this approximation then $n_y = 0$. For a given plasma (density n_e, magnetic field B), wave source (frequency ω) and antenna launching structure (enforcing an $n_z = n_{||}$ at the plasma edge (x=0)) two solutions for $n_x = n_\perp$ can be found. [2]

[2]The 2D slab structure introduced in this section will be often used throughout this thesis. For toroidal devices, the x, y and z coordinates can be thought to correspond to the (minor) radial, poloidal and toroidal directions respectively. In this geometry, any antenna structure will be assumed to be at the edge ($x = 0$).

Assuming $n_{||}$ to be known and solving Eq. 1.22 for $n_\perp$, leads to a bi-quadratic equation for $n_\perp^2$

$$0 = C_4 n_\perp^4 + C_2 n_\perp^2 + C_0 \tag{1.26}$$

where

$$C_4 = S \tag{1.27a}$$

$$C_2 = (n_{||}^2 - S)(P + S) + D^2 \tag{1.27b}$$

$$C_0 = P((n_{||}^2 - S)^2 - D^2) \tag{1.27c}$$

Equation 1.26 can be solved for $n_\perp^2$ using the quadratic solution

$$n_\perp^2 = \frac{-C_2 \pm \sqrt{C_2^2 - 4C_4C_0}}{2C_4} \tag{1.28}$$

The first main categorization of cold plasma waves is done based on the *phase velocity*, that is defined as $\vec{v}_{\rm ph} = \frac{\omega}{|\vec{k}|}\hat{k}$ and is the speed of a constant phase point on a wave[3]. For the case in which both roots of Eq. 1.28 are real and positive, the (+) root is the *slow-wave*, while the (-) root is the *fast-wave*, in view of their different perpendicular phase velocity.

A different way of expressing the solution of the cold plasma dispersion relation is in terms of the angle $\theta = \arctan\frac{n_\perp}{n_{||}}$ that the wave-vector $\vec{n}$ forms with the underlying static magnetic field $\vec{B} = \hat{z}B$. By substituting the definitions $n_{||} = n\cos\theta$ and $n_\perp = n\sin\theta$ in Eq. 1.7 one obtains the bi-quadratic equation for n^2 as a function of θ:

$$0 = An^4 - Bn^2 + C \tag{1.29}$$

where

$$A = S\sin^2\theta + P\cos^2\theta \tag{1.30a}$$

$$B = (S^2 - D^2)\sin^2\theta + PS(1 + \cos^2\theta) \tag{1.30b}$$

$$C = P(S^2 - D^2) \tag{1.30c}$$

or alternatively in terms of the angle θ, as:

$$\tan^2(\theta) = \frac{-P(n^2 - (S + D))(n^2 - (S - D))}{(Sn^2 - (S^2 - D^2))(n^2 - P)} \tag{1.31}$$

From Eq. 1.31 one can easily identify the dispersion relation for the cases of *parallel propagation* ($\theta = 0$):

$$\begin{aligned} &P = 0 \text{ , electrostatic plasma oscillations} \\ &n^2 = S + D \text{ , electromagnetic wave with right-handed polarization} \\ &n^2 = S - D \text{ , electromagnetic wave with left-handed polarization} \end{aligned} \tag{1.32}$$

and *perpendicular propagation* ($\theta = \pi/2$):

$$\begin{aligned} &n^2 = P \text{ , ordinary wave} \\ &n^2 = \frac{S^2 - D^2}{S} \text{ , extraordinary wave} \end{aligned} \tag{1.33}$$

In addition to the *slow-wave*, *fast-wave* nomenclature, plasma waves are also classified depending

[3]By contrast the *group velocity*, that is defined as $\vec{v}_{\rm g} = \frac{d\omega}{d\vec{k}}$ and is the speed at which the wave power (and information) travels.

on the direction of propagation $\vec{n}$ with respect to the oscillating wave electric field $\vec{E}_1$, as *longitudinal* ($\vec{n} \parallel \vec{E}_1$) or *transverse* ($\vec{n} \perp \vec{E}_1$). Transverse parallel waves are further classified with respect to the direction of the circular polarization of the electric field with respect to the static magnetic field $\vec{B}$ as *right-handed* or *left-handed.* Similarly, perpendicular electromagnetic waves are classified depending on the polarization of the oscillating wave electric field $\vec{E}_1$ with respect to the static magnetic field $\vec{B}$ as *ordinary (O-mode)* ($\vec{E}_1 \parallel \vec{B}$) or *extraordinary (X-mode)* ($\vec{E}_1 \perp \vec{B}$) waves. The O-mode is *transverse*, whereas the X-mode is partly *transverse* and partly *longitudinal.* Finally, waves in plasmas can be classified as *electromagnetic* or *electrostatic* according to the presence or absence of a significant oscillating magnetic field $\vec{B}_1$.

1.1.4 Electrostatic waves

Electrostatic waves do not exist in vacuum, but can exist in a plasma. For these waves the magnetic field component is negligible $\vec{B}_1 \sim 0$, therefore by applying Faraday's law of induction to plane waves one finds $\nabla \times \vec{E}_1 \sim 0$ and $\vec{E} = -\nabla\phi = -i\vec{k}\phi$. From this follows that $\vec{E} \parallel \vec{n}$ (or equivalently $\vec{E} \propto \vec{n}$), implying that an electrostatic wave must be purely longitudinal.

The electrostatic dispersion relation can be obtained by dotting the wave equation Eq. 1.7 with $\vec{n}$. This operation results in

$$\vec{E} \cdot \bar{\bar{\epsilon}} \cdot \vec{E} = 0 \tag{1.34}$$

Following the definition of electrostatic waves $\vec{E} \propto \vec{n}$, the dispersion relation for this type of waves takes the form

$$\vec{n} \cdot \bar{\bar{\epsilon}} \cdot \vec{n} = 0 \tag{1.35}$$

By using vector identities we can write Eq. 1.7 as

$$(\vec{n} \cdot \vec{E})\vec{n} - n^2\vec{E} + \bar{\bar{\epsilon}} \cdot \vec{E} = 0 \tag{1.36}$$

and then by splitting $\vec{E}$ into $\vec{E} = \vec{E}_\parallel + \vec{E}_\perp$ with respect to $\vec{n}$

$$(\vec{n} \cdot \vec{E}_\parallel) \cdot \vec{n} - n^2(\vec{E}_\parallel + \vec{E}_\perp) + \bar{\bar{\epsilon}} \cdot (\vec{E}_\parallel + \vec{E}_\perp) = 0 \tag{1.37}$$

Since the first two terms cancel, and by assumption $|E_\perp| \ll |E_\parallel|$, one can deduce

$$\vec{E}_\perp \approx \frac{\bar{\bar{\epsilon}} \cdot \vec{E}}{n^2} \tag{1.38}$$

Since an electrostatic wave needs to have $E_\perp \ll E_\parallel$, a sufficient condition for applying the electrostatic approximation is that $n^2 \gg \epsilon_{mn}$ for all m and n.

Now, if we restrict ourselves to the same 2D slab geometry as of Sec. 1.1.3 (such that $\vec{n} = \vec{n}_x + \vec{n}_z = \vec{n}_\perp + \vec{n}_\parallel$), then Eq. 1.35 reduces to

$$Sn_\perp^2 + Pn_\parallel^2 = 0 \tag{1.39}$$

which can be recast to

$$S\sin^2\theta + P\cos^2\theta = 0 \tag{1.40}$$

or

$$\tan^2(\theta) = -\frac{P}{S} \tag{1.41}$$

Equations 1.39, 1.40 and 1.41 are all different forms of the electrostatic dispersion relation.

Substituting, for $\theta = \pi/2$

$$1 - \frac{\omega_{pe}^2}{\omega^2 - \Omega_e^2} - \frac{\omega_{pi}^2}{\omega^2 - \Omega_i^2} = 0 \tag{1.42}$$

this predicts the *upper* and *lower hybrid* resonances (i.e. $n^2 \to \infty$)

$$\omega^2 \approx \omega_{uh}^2 = \omega_{pe}^2 + \Omega_e^2 \tag{1.43}$$

$$\omega^2 \approx \omega_{LH}^2 = \Omega_i^2 + \omega_{pi}^2/(1 + \omega_{pe}^2/\Omega_e^2) \tag{1.44}$$

In the center of a Tokamak, Ω_e and ω_{pe} are typically of the same order, in which case $\omega_{LH} > \Omega_i$ and $\omega_{LH} < \Omega_e$. From Eq. 1.38 one sees that the LH wave becomes electrostatic as $\omega \to \omega_{LH}$

1.1.5 Cutoff, resonances and caustics

For certain plasma parameters the index of refraction $n = ck/\omega$ can go to either zero (*cutoff*) or infinity (*resonance*). The general condition for cutoffs and resonances is given by Eq. 1.29 as

$$C = P(S^2 - D^2) = 0 \ , \text{ cutoffs} \tag{1.45}$$

$$A = S\sin^2\theta + P\cos^2\theta = 0 \to \tan^2\theta = -P/S \ , \text{ resonances} \tag{1.46}$$

At a cutoff occurs the wavelength and the phase velocity tend to infinity and the transition is made from a region of possible propagation to a region of evanescence. Cutoffs are well described by the cold plasma approximations. At a cutoff the wave is reflected, though this is not necessarily true when a single component of $\vec{n}$ goes to zero, which is a less stringent condition. Note that the cutoff points are independent of the direction of propagation of the wave relative to the magnetic field.

At a resonance the wavelength and the phase velocity drop to zero and it is reasonable to anticipate that the wave would dissipate before it could travel a finite distance if any dissipation is present into the system. In practice, at a resonance the wave can be reflected, transmitted, absorbed, and/or converted into a companion mode. It is this combination of possibilities to which *mode-conversion* theory is addressed. This theory is nontrivial in its mathematical sophistication, but it incorporates a substantial amount of physics and is involved in virtually every type of plasma wave energy absorption except Landau damping and collisional damping.

Finally, a *caustic* surface is defined as the location where only a component of the wave vector $\vec{k}$ goes to zero (as opposed to $k = 0$) [38] . At a caustic the waves become tangential to these sufaces and tend to focus in their vicinity (a focal point is in fact a special case of two caustic surfaces which coalesce into a single point which lies on the wave path itself).

1.1.6 Collisional wave damping

In the limit of low collision frequencies, collisions may be treated as a perturbation, thus giving rise to a supplementary term in the cold dispersion relation [39, 40]. Coulomb collisions between two plasma species (say electrons e colliding with an ions species i of charge Z_i) with collisional frequency ν_{ei}, are introduced into the cold plasma formalism by adding the momentum-loss term $-m_e\nu_{ei}\vec{v}_e$ to the right-hand side of the electron momentum equation 1.12. This modification results in an *anti-Hermitian* (i.e. loss) correction to the cold plasma dielectric tensor ϵ_{cold}. Worth pointing out is that collisional damping can be accounted for by simply replacing the electron mass m_e, whenever it occurs, by an effective complex electron mass

$$m_e \to m_e(1 - i\nu_{ei}/\omega) \tag{1.47}$$

The collision frequency ν_{ei} is a function of the electron velocity (i.e. their temperature, for a maxwellian plasma) and can be derived from a test particle picture [41] to be

$$\nu_{ei} \approx \left(\frac{1}{4\pi} \frac{e^4 Z_i^2 n_i}{\epsilon_0^2 m_e^2} \log \Lambda \right) \frac{1}{v_{Te}^3} \tag{1.48}$$

where $\log \Lambda = \log \left(\frac{12\pi \epsilon_0^{3/2} T_e^{3/2}}{n_e^{1/2} e^3} \right)$ is the Coulomb Logarithm and $v_{Te} = \sqrt{\frac{2T_e}{m_e}}$ is the electrons' thermal velocity.

Ideally one should consider the charge and concentration of each ion species composing the plasma, however this is mostly unknown and measurements (from visible Bremsstrahlung) provide only a mean ion charge of the plasma, weighted for each species by the proportion of electrons arising from that species:

$$Z_{eff} = \frac{\sum_s n_s Z_s^2}{\sum_s n_s Z_s} \tag{1.49}$$

where charge neutrality imposes

$$n_e = \sum_s n_s Z_s = n_i Z_{eff} \tag{1.50}$$

Typically, it is assumed that only a main ion species of charge Z_{main} and an impurity ion species of charge Z_{imp} compose the plasma. Consequently their respective concentrations $n_{i,main}$ and $n_{i,imp}$ can be determined as:

$$\begin{aligned} n_{i,main} &= \frac{Z_{imp} - Z_{eff}}{Z_{main}(Z_{imp} - Z_{main})} n_e \\ n_{i,imp} &= \frac{Z_{eff} - Z_{main}}{Z_{imp}(Z_{imp} - Z_{main})} n_e \end{aligned} \tag{1.51}$$

One should notice that the value of Z_{imp} is a strong function of the local plasma temperature (since it affects the ionization). In the experiments this is a quantity which is hard to measure and is often not spatially resolved and affected by large uncertainties.

1.2 Collisionless damping

When the phase velocity of the wave fields matches the particles velocity, energy and momentum can be exchanged between the two. This process results in collisionless damping of the wave. The generic wave-particle resonance condition is expressed as

$$\omega - k_\parallel v_\parallel - n\Omega/\gamma = 0 \tag{1.52}$$

where n is the order of the cyclotron interaction (zero for Landau/transit-time cases). Mathematically this effect appears as poles in the expressions for the dielectric tensor which is derived starting from a kinetic treatment of the wave problem, that is, by methods that take into account the motions of each and all of the particles.

The most widely used formulation of kinetic theory is the Boltzmann equation, for which the non-relativistic form is:

$$\frac{\partial f}{\partial t} + \frac{\partial f}{\partial \vec{x}} \cdot \frac{\partial \vec{x}}{\partial t} + \frac{\partial f}{\partial \vec{v}} \cdot \frac{\partial \vec{v}}{\partial t} = \left. \frac{\mathrm{d}f}{\mathrm{d}t} \right|_{\text{collisions}} \tag{1.53}$$

However, since in a hot plasma the wave propagation process involves time scales that are much shorter than the collision time scale, collisions can be to first order neglected, and the Vlasov equation

can be used instead

$$\frac{\partial f}{\partial t} + \frac{\partial f}{\partial \vec{x}} \cdot \frac{\partial \vec{x}}{\partial t} + \frac{\partial f}{\partial \vec{v}} \cdot \frac{\partial \vec{v}}{\partial t} = 0 \tag{1.54}$$

The Maxwell-Vlasov equations, together with the definition of space charge and plasma current

$$\sigma = \sum q_s \iiint d^3\vec{v} f_s(\vec{r}, \vec{v}, t) \tag{1.55}$$

$$\vec{J} = \sum q_s \iiint d^3\vec{v} f_s(\vec{r}, \vec{v}, t)\vec{v} \tag{1.56}$$

form a complete set of equations describing collisionless plasmas. The first step to derive the hot plasma dielectric tensor, starts by obtaining $f_1(\vec{x}, \vec{v}, t)$. We will then take the velocity moments to find the contributions to the first-order plasma current $j(\omega, \vec{k})$ for each species, and thus evaluate their susceptibilities.

The Vlasov equation may be solved by the so-called "method of characteristics", according to which Eq. 1.54 is solved by integrating particle orbits along the unperturbed (zeroth-order) orbits. The orbits are given by the equations of motion of a charged particle in a uniform external magnetic field $\vec{B} = B\hat{z}$:

$$\frac{\mathrm{d}\vec{x}}{\mathrm{d}t} = \vec{v} \tag{1.57a}$$

$$\frac{\mathrm{d}\vec{v}}{\mathrm{d}t} = \frac{q}{m}\left(\vec{E} + \frac{\vec{v} \times \vec{B}}{c}\right) \tag{1.57b}$$

Thus the rate of change of $f(\vec{x}, \vec{v}, t)$ along the zeroth order trajectory is given by

$$\frac{\mathrm{d}\vec{f}}{\mathrm{d}t} = \frac{\partial f}{\partial t} + \vec{v} \cdot \frac{\partial f}{\partial \vec{x}} + \frac{q}{m}\left(E + \frac{\vec{v} \times \vec{B}}{c}\right) \cdot \frac{\partial f}{\partial \vec{v}} = 0 \tag{1.58}$$

Since we are dealing with small amplitude waves, it is appropriate to linearize the Vlasov equation. Here, f_0 represents the equilibrium electron distribution, whereas f_1 represents the small perturbation due to the wave. The electric field is assumed to be zero in the unperturbed state ($\vec{E}_0 = 0$) and to zeroth order Eq. 1.58 is trivially satisfied. To first order Eq. 1.58 becomes:

$$\frac{\partial f_1}{\partial t} + \vec{v} \cdot \nabla f_1 + \frac{q}{m}\vec{v} \times \vec{B}_0 \cdot \nabla_v f_1 = -\frac{q}{m}\left(E_1 + \vec{v} \times \vec{B}_1\right) \cdot \nabla_v f_0 \tag{1.59}$$

1.3 RF current drive, collisional relaxation and quasilinear analysis

The dynamics of ordinary neutral gas are dominated by collisions. Because collisions dominate, the velocity distribution function for a neutral gas is close to a local thermal equilibrium. For a hot plasma instead, the ordering is inverted. Collisions are infrequent and the collisional relaxation toward a local Maxwellian may proceed on very long time scales. RF current drive and RF plasma heating are two examples in which the distribution function deviates from a Maxwellian and evolves under the coercive forces of the large RF fields and the relaxing influence of the Coulomb collisions. The mathematical tool for a complete description of the velocity-space multiple-scattering process is the Boltzmann equation with a collision term representing the accumulated effect of multiple two-particle Coulomb collisions that take place in a hot plasma. This term can be well modeled by a collision term of the Fokker-Planck type, which describes collisions in terms of diffusion in velocity space $\frac{\partial f}{\partial t} = \nabla \cdot (D\nabla f)$.

A simple model to describe the effect of high power RF waves on plasmas was suggested by Fisch [42] and consists of adding a diffusion term to the Fokker-Plank equation that tends to flatten the distribution function in the immediate vicinity of the resonant wave-particle velocity.

$$\frac{\partial f}{\partial t} = \left(\frac{\partial f}{\partial t}\right)_{\text{collisions}} + \frac{\partial}{\partial v} D_{\text{QL}} \frac{\partial f}{\partial v} \tag{1.60}$$

Since the rate of velocity space diffusion was found to be proportional to the squares of the amplitudes of the linear theory modes, this theory takes the name of "quasilinear theory".

The interaction between the waves and the distribution function can properly be described in terms of a diffusion process only when the wave-particle interaction is stochastic and is averaged over a time scale that is very long relative to a wave period. Validity of treating RF wave-particle interaction as quasilinear diffusion relies on the assumption that the spectrum of modes as seen by the particle, is sufficiently dense and broad that phase sensitive effects (such as particle trapping) disappear through destructive interference and phase mixing. Another requirement for the validity of the quasilinear theory is that the change of particle velocities during the wave-particle interaction is small and the interaction takes place over many wavelengths.

1.3.1 Quasilinear diffusion of a particle in a traveling wave

For the physical understanding of quasilinear diffusion, it is helpful to look at the 1D motion of a single particle in a traveling wave [32, p. 447]. For a wave field $\vec{E}(z,t) = \hat{z}E\cos(k\,z - \omega\,t)$ and a particle with velocity v and position z_0 at $t = 0$, one may write its 0^{th} and 1^{st} order motion as:

$$\begin{aligned} z &= v\,t + z_0 \\ m\frac{d}{dt}\Delta v &= qE\cos(k\,z_0 + k\,v\,t - \omega\,t) \end{aligned} \tag{1.61}$$

Integrating the 1^{st} order motion one can calculate

$$\Delta v = \frac{qE}{m}\frac{\sin(k(t\,v + z_0) - t\,\omega) - \sin(k\,z_0)}{\omega - k\,v} \tag{1.62}$$

and consequently, averaging over the initial positions z_0 [32],

$$\overline{(\Delta v)^2} = 2\left(\frac{qE}{m}\right)^2\left(\frac{\sin(t(\omega - kv)/2)}{\omega - kv}\right)^2 \tag{1.63}$$

For large wave-particle interaction time, Eq. 1.64 approaches a delta function. In the limit of quasilinear diffusion, only the resonant particles having $v = \omega/k$ feel a velocity-space diffusion that depends only on the amplitude (power) of the wave and takes the form of

$$D_v|_{t\to\infty} = \frac{\overline{(\Delta v)^2}}{2t} \approx \frac{\pi}{2}\left(\frac{qE}{m}\right)^2\delta(\omega - kv) \tag{1.64}$$

The same result was obtained by Kennel and Engelmann [43] by Fourier analysis on a fluid model, and extended to relativistic plasmas by Lerche [44].

1.4 Inhomogeneous Plasma

Uniform plasmas are an idealization which is rarely realized in most laboratory plasmas, where densities and magnetic fields vary to such an extent that it is sometimes difficult to estimate from

uniform plasma theory where the wave energy will go and whether it will reach specified regions.

The most rigorous approach for the solution of the wave propagation and damping in an inhomogeneous plasma, requires to solve the original wave Eq. 1.6 before the expansion in Fourier space. One therefore has to deal with partial integro-differential equations rather than algebraic equations, whose solutions are naturally much more difficult. When the spatial non-uniformity can be regarded as being in a single coordinate, then it is possible to Fourier analyze the problem in the remaining coordinates [4]. In this respect, in the dimensions where the plasma is nonuniform, one can still express any solution as a sum of Fourier modes, but these will in general be coupled together by the non-uniformities of the medium. In other words, fields of the form exp $i(\vec{k}\cdot\vec{x}-\omega t)$ will no longer separately satisfy Maxwell's equations. This approach is the one followed by spectral *fullwave* codes, which numerically solve for the superposition of Fourier modes which satisfy the wave equation.

An alternative, intermediate approach is the one followed by *ray-tracing* techniques, which assume the dielectric tensor varies little over a wavelength.

1.4.1 Ray-tracing

The ray-tracing technique is based on the solution of ray-tracing equations for position and wavevector, which stem from a Wentzel-Kramers-Brillouin (WKB) asymptotic solution of the wave equation. The solution of the first order equations essentially describes the evolution of the wavenumber inside the plasma, starting from the antenna position. The electric field amplitude of the propagating wave remains unsolved within this approximation and is calculated a posteriori via the energy conservation and the Poynting theorems.

Formulation

The ray-tracing formulation results from the first-order expansion in $k\,L$ of Eq. 1.6, where L is the smallest scale length inside of the plasma and k is the wavenumber. The wave trajectory and the evolution of their wave vector can be tracked by integrating the resulting system of equations [45]:

$$\begin{aligned}
\frac{d\vec{x}}{d\tau} &= \frac{\partial D}{\partial \vec{k}} \\
\frac{d\vec{k}}{d\tau} &= -\frac{\partial D}{\partial \vec{x}} \\
\frac{dt}{d\tau} &= -\frac{\partial D}{\partial \omega} \\
\frac{d\omega}{d\tau} &= \frac{\partial D}{\partial t}
\end{aligned} \tag{1.65}$$

where D is the dispersion function of the waves, which is a slowly varying function of $\vec{x}$ and t. In this expression τ is an arbitrary integration variable which is a measure of the distance along the trajectory of the ray. In the case of static plasma parameters $\frac{\partial}{\partial t}=0$ and Eq. 1.65 simplifies to:

$$\begin{aligned}
\frac{d\vec{x}}{dt} &= -\frac{\partial D/\partial \vec{k}}{\partial D/\partial \omega} \\
\frac{d\vec{k}}{dt} &= \frac{\partial D/\partial \vec{x}}{\partial D/\partial \omega}
\end{aligned} \tag{1.66}$$

In conjunction with the ray equations it is convenient to solve an evolution equation for the power P along each ray. The power is the determined by a damping rate γ, which is set by the imaginary

[4] This is the approach used for the study of LH coupling theory (see Sec. 2.3.2), and for toroidal mode number decomposition of the wave fields in a axisymmetric toroidal geometry

part of D and that can include the resonant damping terms and the damping due to collisions.

$$\frac{dP}{dt} = -2\gamma P \tag{1.67}$$

Validity and limitations of the WKB method

The ray-tracing formalism relies on the assumption that if the properties of the plasma vary sufficiently slow compared to the wavelength, then locally the wave can be thought of as propagating in an approximately uniform medium and, therefore behave as if all of the uniform plasma treatment applied. Thus, for any frequency and propagation, there is locally a well defined k and refractive index n corresponding to the values of the waves and plasma parameters. In laboratory plasmas this requirement is often well satisfied for ECH waves and not satisfied for ICH waves. Whether applying ray-tracing to LH waves is a valid approximation is still an open question.

A generally more stringent condition for the validity of the WKB approximation is based on the fact that we must be allowed to rigorously identify the gradient of the Eikonal function with the wave-vector. In principle, at a generic point $\vec{x}$ near a point $\vec{x}_0$, the phase of the wave $\angle\vec{E}$ can be expressed by the following relation [46]

$$\angle\vec{E}(\vec{x}) = \angle\vec{E}(\vec{x}_0) + \nabla\angle\vec{E}(\vec{x})\Big|_{\vec{x}=\vec{x}_0}(\vec{x}-\vec{x}_0) + \frac{(\vec{x}-\vec{x}_0)^2}{2}\nabla\cdot\nabla\angle\vec{E}(\vec{x})\Big|_{\vec{x}=\vec{x}_0} + \ldots \tag{1.68}$$

It is possible to define $\nabla\angle\vec{E} = \vec{k}$ only if the second term on the right-hand side of Eq. 1.68 is much smaller than the first term. This is the so called adiabatic-change criteria of the WKB theory and is equivalent to requiring

$$\left|\frac{\nabla\cdot\vec{k}}{k^2}\right| = \left|\frac{\nabla\cdot\nabla\angle\vec{E}}{k^2}\right| \ll 1 \tag{1.69}$$

At the edge of a Tokamak plasma, parameters such as density and temperature can have strong gradients. Furthermore, there are locations, such as at cutoffs or resonances, where the refractive index changes rapidly and the Eikonal ansatz is not satisfied by definition. A discussion of the validity limits of the WKB method is given in [46]. Recent efforts in numerical modeling are devoted to advancing beyond the WKB approach and benchmarking of existing ray-tracing codes have lead to more refined WKB-based methods [30, 47, 48].

Additional limitations of the ray-tracing formulation is that does not describe phenomena such as wave interference, focusing, diffraction and tunneling. Also, the application of this theory to fusion plasmas is further complicated by the fact that radiating structures do not provide boundary conditions compatible with the use of the Eikonal approximation. Instead, their close field has to be Fourier analyzed in the toroidal coordinate, and ray tracing has to be applied separately to each partial wave. The electric field at any given point in the plasma has then to be reconstructed by superposition of all partial waves illuminating that point.

Chapter 2

Lower hybrid wave physics

Lower Hybrid (LH) waves were originally proposed as a method for bulk ion heating. The idea was to launch LH waves and mode-convert them into ion Bernstein waves at the LH resonant layer $\omega = \omega_{\mathrm{LH}}$ [49, 50]. Unfortunately however, experimental performances have been rather inconsistent. Hence, since the earliest experiments in the 1980s the interaction of LH waves with ions was abandoned.

Around the same time LH waves started to gain considerable interest as a tool for driving non-inductive current in a tokamak plasma. In fact, if LH waves are launched preferentially in one toroidal direction (asymmetric $n_{\parallel}$ spectrum) around the tokamak, they can damp via electron Landau damping on electrons. When the wave is in resonance with high-velocity electrons (around 3 times their thermal velocity v_{Te}) an asymmetry in the electron distribution function is produced, which ultimately results in an electric current. Unlike the usual technique of driving the current inductively, with the plasma acting as secondary winding of a transformer, this can be done on a steady state basis. The LHCD scheme was successfully tested on the PLT tokamak in 1982 [51]. The LHCD efficiency in driving current was experimentally found to be much larger than those typical of tools based on launching waves in the ion- or electron- cyclotron frequency ranges [52]. On Tore-Supra a 6 *min*, 1 *GJ* plasma discharge was sustained using LH current drive alone [53]. Good reviews of LHRF and LHCD can be found in Refs. [54, 55, 56, 52, 57].

However, most experiments have demonstrated fully non-inductive LHCD, only at operating densities lower than the ITER requirements. In cases where LHCD operation was extended to high-density regimes, less positive results were obtained. In particular, recent experiments on Alcator C-Mod [58], ToreSupra [59], FTU [60] and JET [24] have observed a faster drop in Hard X-Ray emission (a proxy for LHCD) than what is expected by the LHCD efficiency $1/n_e$ scaling, across all densities. Understanding and making progress towards the solution of this problem is critical for Alcator C-Mod and possibly ITER, because the loss of current drive is particularly strong in diverted configurations and has so far impeded efforts to combine LHCD with significant bootstrap current in order to achieve optimized Advanced Tokamak (AT) regimes. This issue will be the focus of Chap. 6.

2.1 Lower hybrid waves within the cold uniform plasma approximation

Lower hybrid waves are those waves which satisfy the slow-wave branch (low $v_{\perp}$, high $n_{\perp}$) of the cold plasma dispersion relation for $n_{\parallel} = k_{\parallel}c/\omega > 1$ and at a frequency ω which lies between the ω_{ci} and ω_{ce}. Using the 2D slab geometry approximation described in Sec. 1.1.3, one can calculate the propagation ($n_{\perp}^2$) of the two roots of the cold plasma dispersion as a function of the plasma density, magnetic field and launched $n_{\parallel}$.

The graphical solution of Eq. 1.28 is shown in Fig. 2-1. In view of the fact that the density is higher in the core of a tokamak plasma, one can think of the abscissa to be the distance inside of the plasma from the launcher. It is assumed that a LH wave launched from an antenna in the vacuum region surrounding the plasma, tunnels through the thin evanescent region ($n_\perp^2 < 0$) at the plasma edge, where $n_e < n_s$. Here n_s stands for the cutoff density for the slow-wave. The wave propagation farther inside of the plasma can be studied by looking at the discriminant $C_2^2 - 4C_4C_0$ of the bi-quadratic equation Eq. 1.28.

If the discriminant of the bi-quadratic equation Eq. 1.28 is zero, then the two roots of the dispersion relation coalesce and *mode-conversion* takes place. A wave launched from the edge of the plasma would reach the first slow- fast- wave confluence point n_{T1}. Because of the short e-folding length of the evanescent wave in the region between n_{T1} and n_{T2}, the inaccessible LH wave is unable to tunnel through the region $n_{T1} < n_e < n_{T2}$ and will not propagate to higher density regions but will rather mode-covert to the fast-wave at n_{T1}.

2.1.1 Accessibility condition

The *accessibility condition* [61] is a requirement on the parallel refractive index $n_\parallel$ that insures a LH waves will reach the core of the plasma before being mode-converted into fast-wave. Mathematically, this condition corresponds to demanding that the discriminant $C_2^2 - 4C_4C_0$ of the bi-quadratic equation Eq. 1.28 remains always positive. Hence, this condition sets the minimum value of $n_\parallel$ for a given plasma density and magnetic field strength:

$$|n_\parallel| > \sqrt{1 - \frac{\omega_{pi}^2}{\omega^2} + \frac{\omega_{pe}^2}{\Omega_e^2}} + \frac{\omega_{pe}}{|\Omega_e|} = |n_{\rm acc}| \tag{2.1}$$

where the Stix parameters have been simplified to $S \approx 1 - \omega_{pi}^2/\omega^2 + \omega_{pe}^2/\Omega_e^2$, $D \approx \omega_{pi}^2/(\omega\Omega_i)$, and $P \approx -\omega_{pe}^2/\omega^2$ in view of the ordering $\omega \gg \Omega_i$, $\omega > \omega_{pi}$, $\omega \ll |\Omega_e|$ and $\omega < \omega_{pe}$ that holds for LH waves in the core of a tokamak plasma.

Figure 2-1 shows that the higher the value of $n_\parallel$, the farther the wave can penetrate into the plasma (at higher densities). When the accessibility condition is met $n_\parallel > n_{\rm acc}$, the slow and the fast-wave branches of the dispersion relation are completely separated and the LH waves can reach either the core of the plasma at a maximum density $n_{\rm max}$ or the LH resonant layer at a density n_{LH}, whichever comes first. In practice if thermal effects are taken into account, at the resonance layer the LH waves will mode convert to an ion plasma wave, a very short wavelength mode that is strongly damped in the plasma.

2.1.2 Lower hybrid resonance cones

An important property of the slow-wave arises from the nature of its group velocity [62, 63]. Starting from the electrons electrostatic dispersion relation of Eq. 1.40, we can assume $S \approx 1$ near the edge of the plasma ($\omega \gg \omega_{pi}$ and $\omega \gg \Omega_i$ for the ions, while $\omega \sim \omega_{pe}$ and $\omega \ll \Omega_e$ for electrons) and $P = 1 - \omega_{pe}^2/\omega^2$. One thus obtains:

$$\omega = \omega_{pe}\cos(\theta) = \omega_{pe}\frac{k_\parallel}{\sqrt{k_\perp^2 + k_\parallel^2}} \tag{2.2}$$

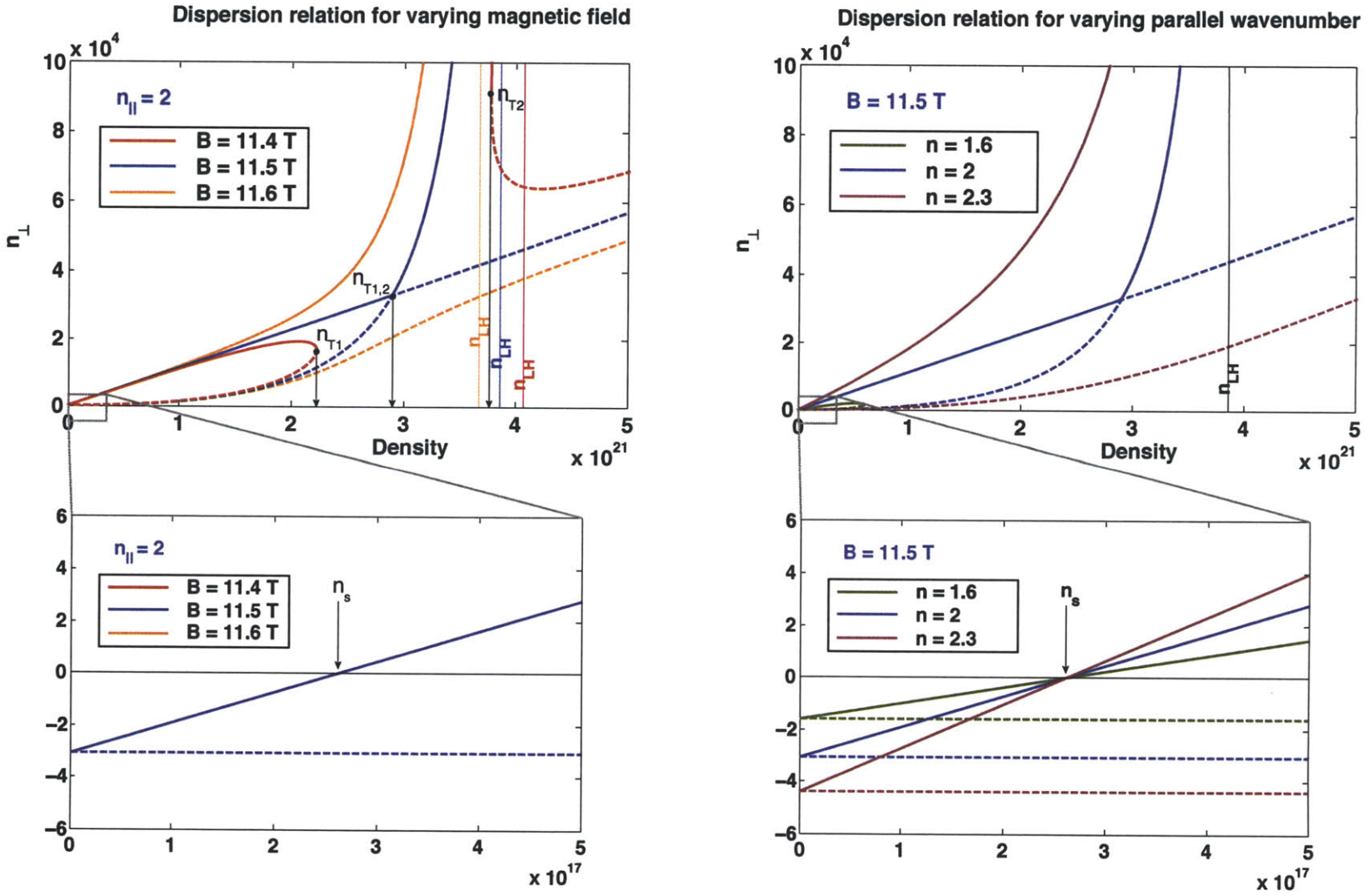

Figure 2-1: Graphical solution of Eq. 1.28, showing slow (solid lines) and fast-wave (dashed lines) as a function of density. The wave frequency is of 4.6 GHz and the plots are parametrized with respect to the magnetic field and the launched $n_{\|}$. For increased B and $n_{\|}$ the waves can propagate to higher densities (i.e. the accessibility improves). In the low density region, the wave propagation is insensitive to B. At 4.6 GHz the cutoff density for the slow-wave is at $n_s = 2.6 \times 10^{17}\ m^{-3}$ and is independent of the magnetic field. For higher $n_{\|}$ the waves are more evanescent in the region of plasma which is below cutoff density. For Alcator C-Mod parameters $\nu = 4.6\ GHz$, $n_e < 10^{21}\ m^{-3}$ and $B < 8\ T$ the slow- fast- wave confluence point n_{T2} is never reached.

The group velocity of the LH waves can be calculated to be:

$$\begin{aligned} v_{g\perp} &= \frac{\partial \omega}{\partial k_\perp} = -\frac{\omega_{pe} k_\parallel k_\perp}{k^3} \\ v_{g\parallel} &= \frac{\partial \omega}{\partial k_\parallel} = \omega_{pe} \frac{k_\perp^2}{k^3} \\ v_g &= \sqrt{v_{g\parallel}^2 + v_{g\perp}^2} = \omega_{pe} \frac{k_\perp}{k^2} \end{aligned} \tag{2.3}$$

Since $k_\perp \approx k_\parallel \omega_{pe}/\omega$ one sees that $v_{g\parallel}/v_{g\perp} = k_\perp/k_\parallel \approx \omega_{pe}/\omega$ which is independent of the wavenumber. Hence the notion of propagation along *resonance cones* inside of the plasma can be seen where the wave energy is propagating away from the antenna along critical angles which make a smaller and smaller angle with the magnetic field direction for increasing densities.

Additional characteristic properties of LH waves can be found by calculating the phase velocity $\vec{v} = \omega/\vec{k}$:

$$\begin{aligned} v_\perp &= k_\perp \frac{\omega}{k^2} \\ v_\parallel &= k_\parallel \frac{\omega}{k^2} \end{aligned} \tag{2.4}$$

It is then easy to show that $\vec{v} \cdot \vec{v}_g = 0$, meaning that the phase and the group velocity are orthogonal to one another. Also, LH waves are backward waves in response to the fact that $v_{g\perp}$ and $v_\perp$ have opposite signs.

2.2 Lower hybrid current drive

In his seminal paper, Fisch [42] showed that LH waves could be used to transfer parallel momentum to the electrons. In fact for electron Landau damping (ELD) the resonance condition is at $\omega - k_\parallel v_\parallel = 0$ and waves with sufficiently high power lead to the creation of a plateau in the velocity distribution function that results in a driven current. In practice the wave fields are composed of a whole spectrum of wavenumbers and the quasilinear plateau will extends from a few times the thermal velocity up to very relativistic velocities, depending on the range of resonant phases velocities in the wave spectrum.

2.2.1 Electron Landau Damping

Electron Landau Damping (ELD) is the process by which waves with sufficiently large values of $n_\parallel$ (low phase velocity) can damp in the core of a tokamak plasma and accelerate electrons. For the purposes of current drive with LH waves, the most important terms to retain are the cold plasma contribution and the electron Landau damping (ELD) term. Within this approximation, the ELD term depends only on the parallel component of the wave vector and contributes to the imaginary part of the parallel term of the dielectric tensor

$$\bar{\bar{\epsilon}}(k_z) = \bar{\bar{\epsilon}}_{\text{cold}} - i \begin{pmatrix} 0 & 0 & 0 \\ 0 & 0 & 0 \\ 0 & 0 & \epsilon_{\text{ELD}}(k_z) \end{pmatrix} \tag{2.5}$$

In principle, Landau damping is possible for both electrons and ions, however the ion absorption rate is typically negligible due to their lower thermal velocity. Also, FLR effects are significant only for large values of $k_\perp$, which is what happens to ions when close to the lower hybrid resonance. The crucial feature is the short perpendicular wavelength, which can bring the perpendicular phase

velocity down to the order of the ion thermal velocity. At this point we can therefore make several simplifying assumptions, which will ultimately lead to the expression for electron Landau damping alone.

First of all, we shall only consider electron motion, assuming that the ions form an immobile neutralizing background. This eliminates the summation over all species. Next, we have shown in Sec. 2.1.1 that LH waves in the core of the plasma are mostly electrostatic. This implies that they are longitudinal in nature and possess a perturbed electric field, but no perturbed magnetic field $\vec{B}_1 \sim 0$. With these assumptions, Eq. 1.59 becomes

$$\frac{\partial f_1}{\partial t} + \vec{v} \cdot \nabla f_1 + \frac{q}{m} \vec{v} \times \vec{B}_0 \cdot \nabla_v f_1 = -\frac{q}{m} E_1 \cdot \nabla_v f_0 \tag{2.6}$$

According to the "method of characteristics" both sides of Eq 2.6 can be integrated along the unperturbed orbits defined by Eqs. 1.57a and 1.57b. As a second approximation we will neglect all thermal effects in the perpendicular direction, thus $v_\perp = 0$ and $\vec{v} \times \vec{B}_0 = 0$. This approximation gets rid of cyclotron damping and all FLR effects and is mathematically equivalent to neglecting the presence of a background magnetic field. This approximation leads to:

$$\frac{\partial f_1}{\partial t} + \vec{v} \cdot \nabla f_1 = -\frac{q}{m} E_1 \cdot \nabla_v f_0 \tag{2.7}$$

which can be Fourier analysed to obtain:

$$-i(\omega - \vec{k} \cdot \vec{v}) f_1 + i \frac{q}{m} \phi \vec{k} \cdot \nabla_v f_0 = 0 \tag{2.8}$$

and therefore

$$f_1 = \frac{q}{m} \frac{\phi_1 \vec{k} \cdot \nabla_v f_0}{(\omega - \vec{k} \cdot \vec{v})} \tag{2.9}$$

At this point we make use Poisson's equation $\nabla^2 \phi = -\frac{\rho}{\epsilon_0}$ to derive the dielectric permittivity of the plasma. Substituting Eq. 2.8 into the Fourier transform of Poisson's equation one gets

$$k^2 \phi_1 = \frac{\rho}{\epsilon_0} = \frac{n}{\epsilon_0} \int_{-\infty}^{\infty} \mathrm{d}^3 v q \hat{f}_1(\vec{v}) \tag{2.10}$$

Dividing by $k^2 \hat{\phi}_1$ we conclude that

$$1 + \frac{\omega_p^2}{k^2} \int \frac{\vec{k} \cdot \nabla_v f_0}{\omega - \vec{k} \cdot \vec{v}} d^3 \vec{v} = 0 \tag{2.11}$$

and since $\vec{v} \equiv v_\parallel \equiv v_z$, by explicitly writing the velocity integrals, Eq. 2.11 becomes

$$1 + \frac{\omega_p^2}{k^2} \int_0^{\infty} 2\pi v_\perp \mathrm{d}v_\perp \int_{-\infty}^{\infty} \mathrm{d}v_\parallel \frac{k_\parallel \partial f_0 / \partial v_\parallel}{\omega - k_\parallel v_\parallel} = 0 \tag{2.12}$$

The singularity due to the vanishing denominator has to be evaluated in the Landau sense [64]:

$$\frac{1}{\omega - \vec{k} \cdot \vec{v}} = P \frac{1}{\omega - \vec{k} \cdot \vec{v}} - i\pi\delta \left(\frac{1}{\omega - \vec{k} \cdot \vec{v}} \right) \tag{2.13}$$

where P designates the *principal part* of the integral, and the contribution from the pole is accounted for by the *residual* (delta function). The principal part is obtained by removing an interval of length 2ϵ, symmetrical about the pole, $v_\parallel = \omega / k_\parallel$, from the range of integration, and then letting $\epsilon \to 0$.

The second term comes from the small semi-circle linking the two halves of the principal part integral in the complex plane. Note that the semi-circle is taken to deviate below the real $v_\parallel$-axis, rather than above, and the integral is calculated by letting the pole approach the axis from the upper half-plane in the $v_\parallel$-complex-space.

We can interpret Eq. 2.11 as the dispersion relation for purely electrostatic plasma waves, relating the wave-vector, $\vec{k}$, to the frequency, ω. If we compare the above results with those for a cold-plasma, where the dispersion relation is simply $\omega^2 = \omega_p^2$, we see firstly, that ω now depends on k (non-local). Secondly, we now have an imaginary part the dielectric tensor corresponding, since it is negative, to the damping of the wave. This damping is generally known as *electron Landau damping* and in the notation of Eq. 2.5 can be written as

$$\Im\{\epsilon_{zz}(k_z)\} = \epsilon_{\mathrm{ELD}}(k_\parallel) = -\frac{\omega_{pe}^2 2\pi}{\omega^2}\int_0^\infty v_\perp dv_\perp \left.\frac{\omega^2}{k_\parallel^2}\frac{\partial f}{\partial v_\parallel}\right|_{v_\parallel=\frac{\omega}{k_\parallel}} \tag{2.14}$$

A simplified expression can be obtained if the electron distribution function is a Maxwellian

$$f(v_\perp, v_\parallel) = \left[\frac{1}{\pi v_{Te_\perp}^2}\exp\left(-\frac{v_\perp^2}{v_{Te_\perp}^2}\right)\right]\left[\frac{1}{\sqrt{\pi}v_{Te_\parallel}}\exp\left(-\frac{v_\parallel^2}{v_{Te_\parallel}^2}\right)\right] \tag{2.15}$$

where $v_\perp^2 = v_x^2 + v_y^2$ and the thermal velocities are defined as $v_{Te}^2 = v_{Te_\perp}^2 = v_{Te_\parallel}^2 = 2T/m$. By substituting this electron distribution function in Eq. 2.14

$$\Im\{\epsilon_{zz}(k_\parallel)\} = \epsilon_{\mathrm{ELD}}(k_\parallel) = \sqrt{\pi}\frac{\omega_{pe}^2\omega}{|k_\parallel|^3 v_{Te}^3}\exp\left(-\frac{\omega^2}{k_\parallel^2 v_{Te}^2}\right) \tag{2.16}$$

These results are at the base of the LHEAF code, which is described in Chap. 6.

2.2.2 1D quasilinear theory and lower hybrid current drive efficiency

To illustrate the idea of quasilinear diffusion and understand the process of RF current drive it is of interest to study Eq. 1.60 in 1D. Axial symmetry about the magnetic field allows a reduction in the complexity of the problem from three to two velocity dimensions. The reduction from two to one velocity dimension is made under the assumption that the dependence of the electron distribution function on the perpendicular velocity is that of a Maxwellian with the bulk electron temperature. To further simplify the problem one can use as a collisional operator the Lenard-Berstein model [65]:

$$\frac{\partial f}{\partial t} = \frac{\partial}{\partial v}\left[\nu\left(vf + \frac{kT}{m}\frac{\partial f}{\partial v}\right)\right] + \frac{\partial}{\partial v}D_{\mathrm{QL}}\frac{\partial f}{\partial v} \tag{2.17}$$

where ν is the assumed collision frequency. This expression is qualitatively similar to the Fokker-Planck equation in one dimension for a Maxwellian plasma but admits exact analytic solution [52, 32].

For $D_{\mathrm{QL}}(v) \to 0$, the collision term relaxes the distribution function $f(v)$ towards stationary Maxwellian with an average energy $< nv^2/2 >= kT/2$, while for $D_{\mathrm{QL}}(v)$ finite, $f(v,t)$ approaches

$$f(v) \propto \exp\left(-\int dv \frac{mv}{kT_{\mathrm{eff}}}\right) \tag{2.18}$$

where $kT_{\mathrm{eff}} = kT + mD_{\mathrm{QL}}(v)/\nu$.

To first approximation one can take $D_{\mathrm{QL}}(v)/\nu$ piecewise constant or zero, depending on its magnitude compared to the thermal velocity v_{Te}. In this case $f(v)$ is a piecewise continuous function,

made Maxwellian distributions with an effective temperature kT_{eff}:

$$f(v) \propto \exp\left(-\frac{mv^2}{2kT_{\text{eff}}}\right) \tag{2.19}$$

The steady state RF power input can be estimated as

$$P = \int_{-\infty}^{\infty} dv \frac{mv^2}{2} \left.\frac{\partial f}{\partial t}\right|_{\text{RF}} = \frac{1}{2}\int_{-\infty}^{\infty} dv\ mv^2 \frac{\partial}{\partial v} D_{\text{QL}} \frac{\partial f}{\partial v} = \int_{-\infty}^{\infty} dv\ mv^2 \frac{mD_{\text{QL}}}{kT_{\text{eff}}} f \tag{2.20}$$

From this expression it is apparent the reduced RF absorption rate which is due to the quasilinear flattening of the distribution function in the presence of high power waves.

The steady-state macroscopic velocity $n < v >= \int f\ v\ dv$ introduced by the wave-plasma interactions can be calculated to be

$$n < v > \approx \frac{\omega}{k} f(\omega/k) \frac{m\delta_v D_{\text{QL}}}{\nu k T_{\text{eff}}} \tag{2.21}$$

after assuming that

$$D_{\text{QL}}(v)/\nu = \begin{cases} \text{constant}, & \left|\frac{\omega}{k} - v\right| \leq \delta_v/2 < v_{Te} \\ 0, & \text{otherwise} \end{cases} \tag{2.22}$$

And under the same conditions of $\delta_v < v_{Te}$, the power input is equal to

$$P \approx m\left(\frac{\omega}{k}\right)^2 f(\omega/k) \frac{m\delta_v D_{\text{QL}}}{kT_{\text{eff}}} \tag{2.23}$$

Combining the last two equations reveals a simple relation between the RF power and the induced macroscopic current j

$$P = \nu n m < v > \frac{\omega}{k} \approx \nu(\omega/k) \frac{m}{q} \frac{\omega}{k} j \tag{2.24}$$

which provides a rough basis for understanding the efficiency for RF-driven plasma current

$$\frac{j}{P} = \frac{q}{mv\nu(v)} \tag{2.25}$$

This would suggest that more current can be driven with low v (high k) electrons. However, because the coulomb cross section falls off with velocity as $\nu \propto n_e v^{-3}$, this rate can be significantly decreased by placing the resonant velocity, $v = \omega/k$, far out on the tail of the distribution. It follows that the high current drive efficiencies claimed by LHCD (and its attractiveness) resides in the creation of supra-thermal electrons. If this is the case, then we can rewrite Eq. 2.25 as

$$\frac{j}{P} \propto \frac{v^2}{n_e} \tag{2.26}$$

and since we can assume that these electrons were generated by resonant waves

$$\frac{j}{P} \propto \frac{1}{n_e n_\parallel^2} \tag{2.27}$$

In view of the ELD damping mechanism, it may appear that the most important velocity space dynamics is in the parallel rather than the perpendicular direction. In reality, important 2D effects (in velocity space) due to collisional pitch-angle scattering not only affect the perpendicular temperature in the plateau region but also lead to a heightening of the linear plateau that is enhanced

over that given by 1D linear theory, thus giving a higher current [66]. A more rigorous analysis of LHCD efficiency including the effects of both direct momentum and energy input [67] results in

$$\eta_{LH} = \frac{4}{5 + Z_{\text{eff}}} \frac{\hat{s} \cdot \nabla_v (v_\parallel v^3 / v_{Te}^4)}{\hat{s} \cdot \nabla_v v^2 / v_{Te}^2} \tag{2.28}$$

where $\hat{s}$ is the direction of velocity space displacement of the electrons and ∇_v is the gradient in velocity space. The surprising consequence of Eq. 2.28 is that the current arising from energy input is three times the amount arising from momentum input. The current drive efficiency which is usually cited for LH waves, is in the order of $\eta_{\text{LH}} \sim 0.1 - 0.2 \times 10^{20}\ m^{-2} MA/MW$. Also, it has been shown that the condition for Landau damping is that $v_\parallel = \omega / k_\parallel \leq 3\ v_{Te}$ where $v_{Te} = 2T_e/m_e$.

This perpendicular dynamics has been included in a one dimensional model as described in Ref. [68]. However, these models are only approximated and do not take into account particle trapping nor are good for perpendicular heating schemes. Ultimately, the rigorous solution of the Fokker-Planck equation with quasilinear diffusion in a non-homogeneous plasma is a complicated task which requires the use of numerical tools. An extensive description of the theory at the base of 2D/3D bounce averaged Fokker Planck quasilinear codes and their numerical implementation (with specific details of LH waves) is presented in Appx. B.

2.2.3 Lower hybrid density limits

In the context of LH waves, the term "density limit" has been used in reference to three different factors which limit effectiveness of the heating and current drive at higher densities. The first density limit is the *accessibility criterion* derived in Sec. 2.1.1 which has traditionally been thought to be the limiting factor for the penetration of LH waves to the core of a tokamak plasma at high density.

The second density limit refers to the appearance of *parametric decay* waves that has been observed in different experiments at the threshold of $\omega/\omega_{\text{LH}} \sim 2$. Parametric decay is a non-linear three wave interaction which has the effect of broadening the launched LH wave spectrum in velocity space (i.e. $n_\parallel$). The relation between the lack of LH power penetration into the high-density plasma core and strong parametric decay instability (PDI) produced spectral broadening that was observed for the first time in early experiments, which coupled LH power at high plasma densities (so that $\omega \approx \omega_{\text{LH}}$ in the core) with the aim of heating the core plasma ions [69]. In these experiments the coupled LH power produced only edge physics effects, consisting of PDI signatures in the frequency spectra of the signal received by radio-frequency probes located in the scrape-off layer. These spectra show a broadening in the LH operating line frequency (orders of magnitude higher than the line width of the RF power sources), more markedly for higher operating plasma densities, and sidebands shifted by harmonics of the ion-cyclotron frequency at the plasma edge, exhibiting a typical non-monotonic envelope for relatively high operating plasma densities. In these experiments, the resulting $n_\parallel$ spectral broadening was sufficient for bridging the gap between LH wave phase velocities and thermal velocities of the peripheral plasma ions, resulting in an ion tail formation.

The third density limit is the one that, more recently, several tokamak experiments have reported in association with the *anomalous loss of LHCD efficiency* that has been reported by several tokamak experiments including Alcator C-Mod [58], ToreSupra [59], FTU [60] and JET [24]. This effect is readily seen as sudden drop of the non-thermal bremsstrahlung (HXR) emission for increasing plasma densities, which is taken as a sensitive proxy for the population of fast electrons generated by LHCD. The LHCD is anomalous in the sense that it occurs at much faster rate than what predicted by the estimates discussed in Sec. 2.2.2 or conventional ray-tracing calculations for which the fast electron population (and consequently the amount of LH driven current and HXR emission) should be inversely proportional to plasma density $\sim n_e^{-1}$.

Although the reason for this effect is still an open debate, different theories agree that the SOL

region plays a key role in the loss of driven current. To date, these include electron-ion collisional absorption [25], ionization losses [70], wave scattering by density fluctuations [22] and parametric decay instability [24]. The very number of possible explanations shows how complex the problem is and the lack of any clear solution to this day is the situation compounded by the lack of experimental data pointing to any one explanation as being an outstanding candidate. In addition, it is also likely that in the experiments several factors operate simultaneously.

LHCD density limit on Alcator C-Mod

On Alcator C-Mod, several experimental campaigns have been devoted to the study of this phenomenon and a wide range of operational regimes have been scanned (including plasma current, toroidal field, launched $n_\parallel$ and power, plasma topology and species) [25, 26, 27, 58, 71]. Experimentally, the loss of LHCD manifest itself in several different ways. Besides the loop voltage not reacting to injection of LH waves (that is the quantity one ultimately cares), a sharp drop in the non-thermal Electron Cyclotron Emission (ECE) and Hard X-Ray (HXR) emission are also observed. Associated to the loss of LHCD, are several effects in the SOL which are well documented in Refs. [25, 71].

Figures 2-2 and 2-3 compares the drop in loop voltage as a function of the normalized power

$$\tilde{P} = P_{\rm LH}/\bar{n}_e I_p R_0 \; W\, m^2/A \tag{2.29}$$

for the cases of a power and a density scan. Such relationship was first proposed in Ref. [72] to estimate the LHCD efficiency and was used in Ref. [73] to investigate the dependency of the LHCD efficiency as a function of launched power and $n_\parallel$ on Alcator C-Mod. Assuming that the plasma current is composed of three pieces, an underlying ohmic part proportional to the loop voltage and independent of the RF power, an RF part proportional to the LH power and independent of the loop voltage and a nonthermal component proportional to both the voltage and LH power, change in loop voltage can be written as

$$-\frac{\Delta V}{V} = \frac{(\eta_0 + \eta_1)\tilde{P}}{1 + \eta_1 \tilde{P}} \tag{2.30}$$

where η_0 is the LHCD efficiency

$$\eta_0 = \frac{1}{5 + Z_{eff}} \frac{1}{n_\parallel^2} \tag{2.31}$$

and η_1 is related to the non-thermal conductivity

$$\eta_1 = \frac{Z_{eff}}{5 + Z_{eff}} \frac{1}{n_\parallel^4} \frac{I_p}{n_e T_e^{3/2}} \tag{2.32}$$

In order for this method to yield useful results, the underlying ohmic conductivity should be a constant (i.e. $I_p/n_e T_e^{3/2}$ should be held constant). Although a direct comparison between Figs. 2-2 and 2-3 can not be done (different $n_\parallel$ and $I_p/n_e T_e^{3/2}$ is not constant among the two plots) it is important to notice that in the case of a density scan, the loop voltage drop crosses zero for non-zero LH power, clearly indicating that $\eta_0 \to 0$ as the density increases.

In general however, the HXR emission is the most sensitive measurement to the presence of fast-electrons and is the method of choice to diagnose the LHCD performance. Figure 2-4 shows that the HXR emission from the Alcator C-Mod core plasma over the energy range of 40 to 200 keV drops by over four orders of magnitude by tripling the line averaged density. Initial studies [25, 26, 27] suggested the presence of a break-in-slope in the HXR emission occurring around the line average density $\bar{n}_e = 10^{20}\ m^{-3}$. However, latter implementation of an advanced Pulse Height Analysis (PHA) analysis (described in detail in Appx. C) showed that the break-in-slope was an artifact of pileup and baseline drift effects on the HXR signals at the lowest densities. As a result, it was

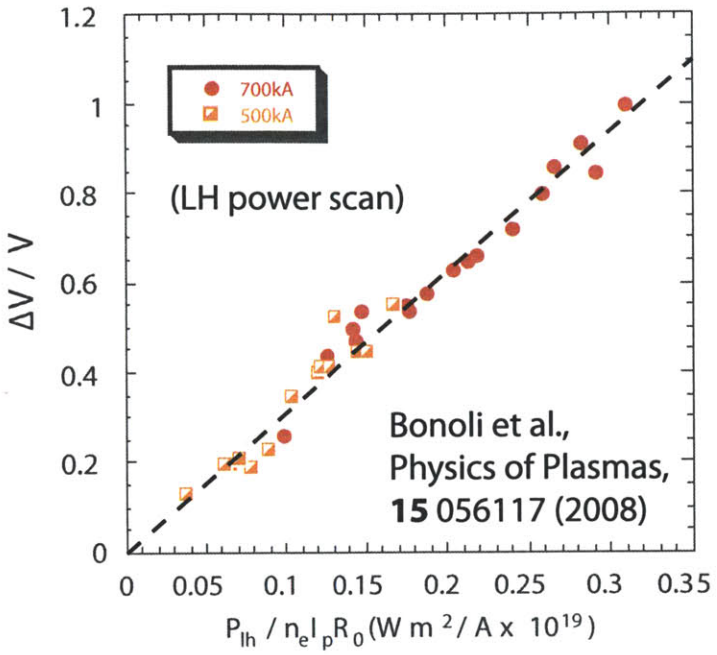

Figure 2-2: The drop in loop voltage follows a linear relation as a function of the normalized LH power, when a power scan at low density is performed. Figure adapted from Ref. [73]

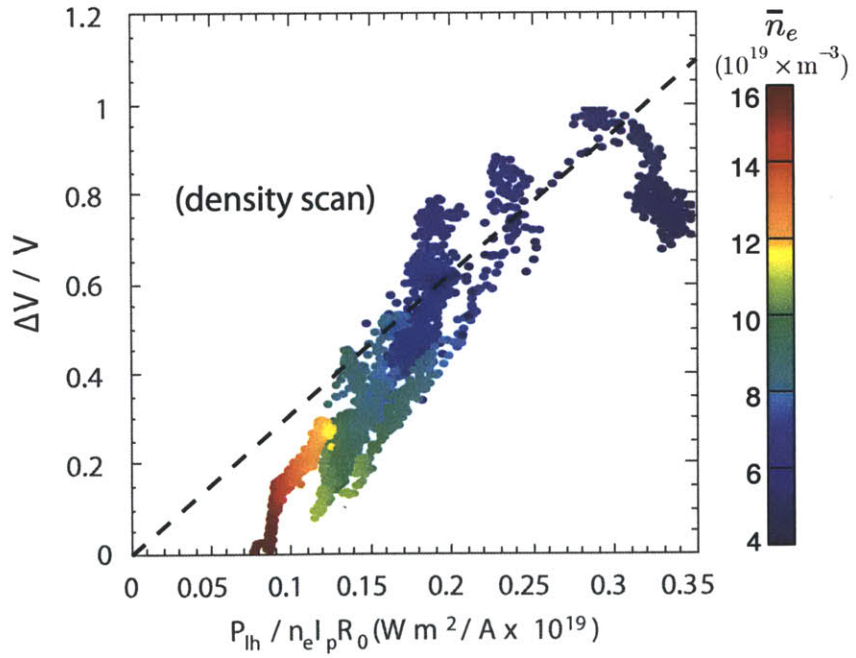

Figure 2-3: When the density is scanned the drop in loop voltage does not follow the expected current drive efficiency. Plot of several discharges with $B = 5.4\ T$, $I_P = 800\ kA$, $n_{\|} = 1.9$.

realized that the drop of HXR emission is steady across all densities, implying that the nature of the process involved is not sudden and, differently from what previously suggested, there is nothing special about the density of $\bar{n}_e = 10^{20}\ m^{-3}$.

On Alcator C-Mod, using ray-tracing Fokker-Planck modeling, Wallace found that good agreement with the experimental results could be obtained when a strongly collisional SOL was included in the model [26]. The LHCD density limit on Alcator C-Mod is analyzed in detail in Chap. 7 with the aid of a newly developed fullwave code named LHEAF. A new physics picture is proposed, according to which it is a strong upshift in the $n_\parallel$ spectrum that makes the overall LHCD efficiency low by allowing the waves to Landau damp near the edge.

2.3 Lower hybrid waves in non-uniform plasmas

2.3.1 Evolution of the $n_\parallel$ spectrum induced by toroidicity

According to quasilinear theory, the RF fields cause particles to diffuse in velocity space, thus producing a plateau in the electron distribution function. In order to have a significant population of fast electrons (pull a significant fast electron tail), the wave fields should fill the entire region from $3\,v_{Te} < v_\parallel < v_{\mathrm{maxacc}}$ with a significant amount of power. Wave fields with low phase velocity are necessary to make the distribution function deviate where there is a large number of electrons, while wave fields with high phase velocity are necessary to sustain the non-thermal population to relativistic speeds. Lack of any spectral components in between these extremes can results in a strong degradation of current drive. A puzzling result of LHCD experiments is that the parallel phase velocity of the injected LH waves is much greater than the phase velocity required for electron landau damping to occur. The question of how these high phase velocity waves are able to interact with plasma electrons and thus transfer their momentum and energy is called the *spectral gap* problem.

Of the many mechanisms which have been proposed to bridge this velocity gap (including nonlinear instabilities, density fluctuations, magnetic ripples), the upshift induced by toroidal geometry effects [39] is the only one which is universally recognized and has been successful in showing that the toroidal variation of $n_\parallel$ during the wave propagation can in many cases fill the spectral gap. The toroidally induced upshift (or a downshift) of the wave spectrum was first studied using ray-tracing techniques [74, 75, 76, 77].

In a toroidal equilibrium, the evolution of the $n_\parallel$ wave spectrum can be formalized by expressing Eq. 1.66 in the toroidal coordinates (r, θ, Φ), with r the minor radial position, θ the poloidal angle, and Φ the toroidal angle. In toroidal coordinate the canonical wave momenta are given by (k_r, M, N), with k_r the radial wavenumber, $N = Rk_\Phi$ the toroidal mode number and $M = rk_\theta$ the poloidal mode number. Hence,

$$\begin{aligned}
\frac{dr}{dt} &= -\frac{\partial D/\partial k_r}{\partial D/\partial \omega} \\
\frac{d\theta}{dt} &= -\frac{\partial D/\partial M}{\partial D/\partial \omega} \\
\frac{d\Phi}{dt} &= -\frac{\partial D/\partial N}{\partial D/\partial \omega} \\
\frac{dk_r}{dt} &= \frac{\partial D/\partial r}{\partial D/\partial \omega} \\
\frac{dM}{dt} &= \frac{\partial D/\partial \theta}{\partial D/\partial \omega} \\
\frac{dN}{dt} &= \frac{\partial D/\partial \Phi}{\partial D/\partial \omega} = 0
\end{aligned} \tag{2.33}$$

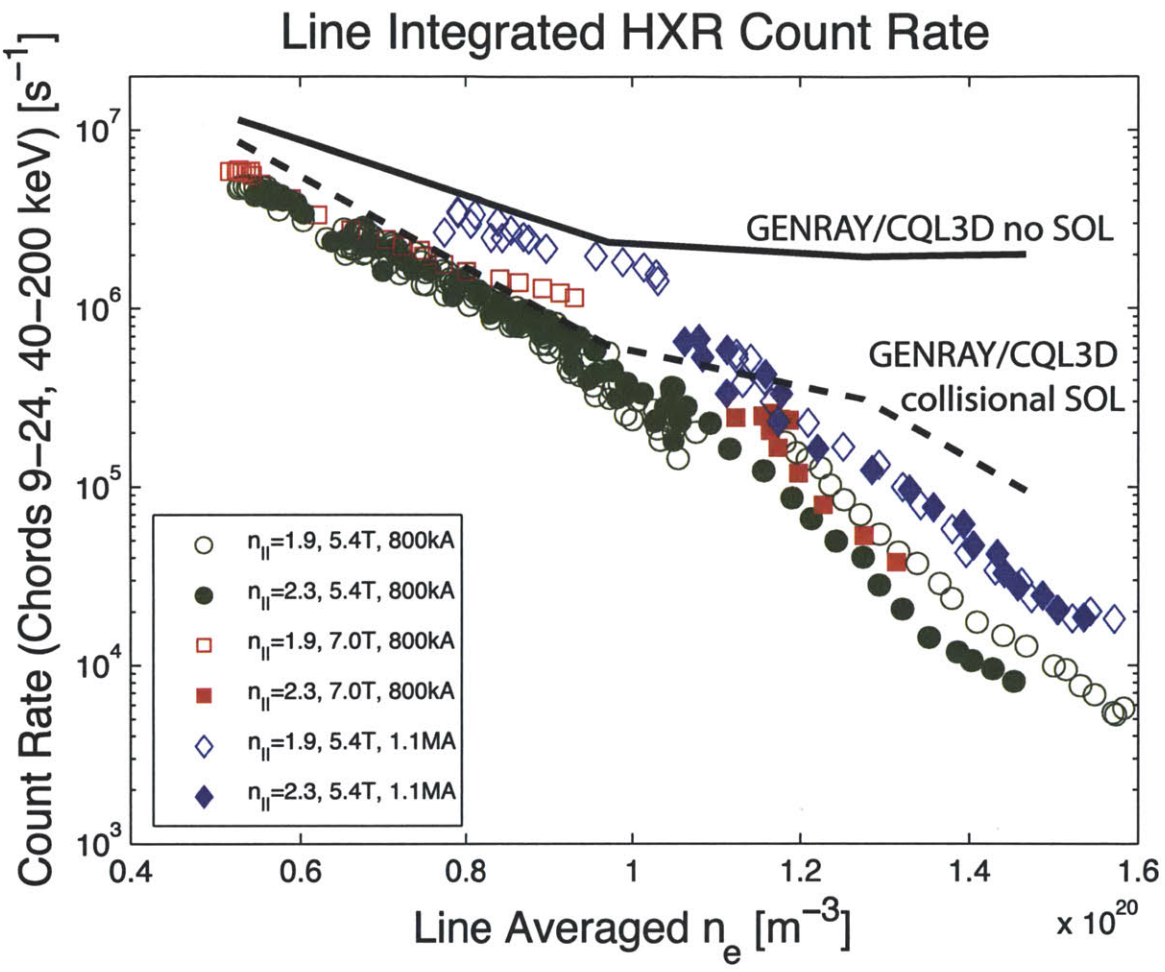

Figure 2-4: Fast electron bremsstrahlung emission as measured by the HXR camera diagnostic on Alcator C-Mod for different discharges. In this plot, HXR from the core (from chord 9 to chord 24) with energy ranging from 40 to 200 keV are considered. All discharges plotted are single null. The lines represent HXR emission as predicted by LH GENRAY/CQL3D without a SOL (solid) and with a SOL (dashed) for $n_{||} = 1.9$, 5.4 T, 800 kA. Figure from Ref. [71].

While the toroidal mode number $N = Rk_\Phi$ is conserved, this is not the case for the wave poloidal mode number $M = rk_\theta$. This is due to the poloidal inhomogeneities of the magnetic field $\vec{B}(r,\theta)$ (momentum conservation requires M to vary in presence of poloidal gradients). Expressing $\vec{k}$ and $\vec{B}$ in toroidal coordinates:

$$\vec{k} = \hat{e}_r k_r + \hat{e}_\theta (M/r) + \hat{e}_\Phi (N/R) \tag{2.34}$$

$$\vec{B} = \hat{e}_r B_r + \hat{e}_\theta B_\theta + \hat{e}_\Phi B_\Phi \tag{2.35}$$

one finds that

$$k_\parallel = \frac{\vec{k}\cdot\vec{B}}{|\vec{B}|} = \frac{[k_r B_r + (M/r)B_\theta + (N/R)B_\Phi]}{|\vec{B}|} \tag{2.36}$$

Since in general for a tokamak equilibrium $B_r \ll B_\theta \ll B_\Phi$

$$k_\parallel \approx \frac{[(N/R)B_\Phi + (M/r)B_\theta]}{|\vec{B}|} \tag{2.37}$$

From this expression it is evident how in variation to $k_\parallel$ are due to the combined effects of toroidicity (M variation) and magnetic shear (B_θ variations). In view of the dependency of M with poloidal gradients of D, one can expect poloidal inhomogeneities due to the plasma equilibrium (elongation, triangularity, Shafranof shift, flux expansion, etc.) to play a significant role in the evolution of $n_\parallel$. As the waves change their value of $n_\parallel$ (upshift or downshift) their accessibility as well as their damping conditions are affected.

When ray-tracing LH waves, close to the center of the plasma the rays can become tangent to a magnetic surface and undergo radial reflection. At these locations $k_r = 0$, that is the condition for the formation of a caustic or of a focal point. This effect occurs when $n_\parallel$ is high enough to satisfy the accessibility condition, so that the waves do not mode convert to the fast-wave branch of the dispersion relation.

More details about the evolution of the $n_\parallel$ spectrum for the specific case of the Alcator C-Mod geometry can be found in Appx. A.

2.3.2 Lower hybrid wave coupling

Coupling is the process by which RF power propagates and possibly tunnels from an antenna to the plasma. Several important remarks about LH wave coupling can be drawn from the low density region of Fig. 2-1. First one can notice the wave is evanescent ($n_\perp^2 < 0$) in the low density region at the edge of the plasma which is below $n_{\text{cutoff}} \approx \omega^2 \epsilon_0 m_e / e^2$. If such low density layer is thin enough, then it is possible for energy to tunnel through it. It is worth pointing out that below cutoff the higher the value of $n_\parallel$ the faster the wave field E decays in the perpendicular direction $\hat{x}$ (more evanescent):

$$E = E_0 \exp(ik_\perp x) = E_0 \exp\left(-(\omega/c)\left|\sqrt{1-n_\parallel^2}\right| x\right) \tag{2.38}$$

For typical $n_\parallel \approx 2$ and $\omega \approx 2\pi 10^9$ rad/s the e-folding length is in the order of a few mm and LH antennas are charged with the difficult mission of delivering high powers while being close to the plasma. In these prohibitive conditions of thermal and mechanical stresses, obtaining good wave coupling is a major challenge for the applicability of these systems in a fusion reactor.

Lower hybrid linear coupling theory

In general the calculation of the coupling efficiency of an antenna requires the solution of the full-wave fields at the antenna-plasma interface. For the case of grill launchers the fields inside of the waveguides these can be expressed in terms of waveguide modes. For the simple case of a 2D slab geometry with a single $n_\parallel$ and a linear density gradient, the reflection coefficient can be calculated

analytically. Assuming that $n_\Phi = n_\parallel$, one can set $E_y = 0$ in Eq. 1.25 [1] so that:

$$\begin{bmatrix} S + \frac{c^2}{\omega^2}\frac{\partial^2}{\partial z^2} & \frac{c^2}{\omega^2}\frac{\partial^2}{\partial x \partial z} \\ \frac{c^2}{\omega^2}\frac{\partial^2}{\partial x \partial z} & P + \frac{c^2}{\omega^2}\frac{\partial^2}{\partial x^2} \end{bmatrix} \cdot \begin{bmatrix} E_x \\ E_z \end{bmatrix} = 0 \tag{2.39}$$

Assuming a solution of the form $\exp(ik_\parallel z)$ in the $\hat{z}$ direction, one can substitute $\frac{\partial}{\partial z} = ik_\parallel$ and solve for the perpendicular electric field E_x as a function of the parallel electric field E_z to obtain

$$E_x = \frac{ik_{||}E_z'}{\frac{\omega^2 S}{c^2} - k_{||}^2} \tag{2.40}$$

where the prime denotes a derivative with respect to x. Substituting Eq. 2.40 in Eq. 2.39 one gets:

$$E_z'' - \frac{\omega^2}{c^2} P \frac{n_{||}^2 - S}{S} E_z = 0 \tag{2.41}$$

Near the edge of the plasma $\omega \gg \omega_{pi}$ and $\omega \gg \Omega_i$ for the ions, while $\omega \sim \omega_{pe}$ and $\omega \ll \Omega_e$ for electrons. Substituting the approximate expressions of the dielectric components in Stix notation:

$$\begin{aligned} S \approx & 1 - \omega_{pe}^2/\Omega_e^2 + \omega_{pi}^2/\omega^2 \sim 1 \\ P \approx & 1 - \omega_{pe}^2/\omega^2 = 1 - \frac{n_e}{n_{\text{cutoff}}} \end{aligned} \tag{2.42}$$

results in

$$E_z'' + \frac{\omega^2}{c^2}(1 - n_{||}^2)\left(1 - \frac{n(x)}{n_{cut}}\right) E_z = 0 \tag{2.43}$$

The solutions to this differential equation for a linear $n(x)$ are linear combinations of the Airy functions Ai and Bi [78]. It is interesting to note that with good approximation the coupling is independent of the magnetic field strength.

Assuming that the antenna structure imposes $E_z = E_z(0)$ at the boundary $x = 0$, then knowledge of $E_z'(0)$ makes it possible to construct an input impedance of the plasma (using Ampere's law Eq. 1.1b) as

$$Z_{\text{p}}(n_\parallel) = \frac{E_z(0)}{H_y(0)} = -i\omega\mu_0 \frac{E_z}{E_z'\left(1 + \frac{n_\parallel^2}{S - n_\parallel^2}\right)} \tag{2.44}$$

which can be used to estimate the reflection coefficient of the antenna as

$$\Gamma(n_\parallel) = \frac{Z_{\text{p}}(n_\parallel) - Z_{\text{ant}}}{Z_{\text{p}}(n_\parallel) + Z_{\text{ant}}} \tag{2.45}$$

where Γ is the ratio of reflected to forward field amplitude and Z_{ant} is the antenna vacuum impedance.

In theory if the $n_\parallel$ spectrum of the antenna is known, the antenna reflection coefficient can be evaluated as a linear superposition of the $\Gamma(n_\parallel)$ weighted by the power at a particular $n_\parallel$. However, the wave field at the antenna-plasma interface (and consequently the launched spectrum) is usually not known a priori and depends on the plasma itself. A self-consistent evaluation of the wave fields requires the use of numerical codes (see Sec. 2.5.2).

From this discussion it is evident how the launched spectrum which is imposed by the antenna structure is key to the physics of the wave coupling problem. The antenna spectrum is calculated

[1] Setting $E_y = 0$ implies that there is no fast-wave, which is in any case very poorly radiated in view of the left hand cutoff which is farther inside of the plasma. The fast wave component but can influence the spectrum in the vicinity of $n_\perp^2 = 1$ and the overall coupling efficiency of the launcher

at the boundary between the antenna and the plasma and is defined as the two dimensional Fourier transform of the wave fields tangential to such fictitious boundary. As an example, assuming a 2D geometry as introduced in Sec. 1.1.3, the spectrum can be expressed in terms of the electric field parallel ($n_{\parallel} \equiv n_z$) and perpendicular ($n_{\perp} \equiv n_y$) components with respect to the magnetic field

$$E_{\tan}(k_y, k_z) = \mathfrak{F}(E_{\tan}(y,z)) \equiv \int_{-\infty}^{\infty}\int_{-\infty}^{\infty} e^{-i(k_z z + k_z z)} E_{\tan}(y,z) dy dz \tag{2.46}$$

Lower hybrid wave coupling in the non-linear regime: ponderomotive force theory

Experiments have show that the linear theory of LH waveguide coupling begins to break down if the RF power flux exceeds approximately 0.3 MW/m^2 [79]. In this regime the high power RF waves interact strongly and modify the edge plasma which in turn affects the wave propagation itself, thus making the overall problem non-linear. Even though all current drive experiments ultimately operate at high power, the wave coupling in the non-linear regime is still poorly understood and a definitive theoretical model is missing.

Experimental evidence and modeling [9] have pointed to *ponderomotive forces* as the leading candidate to explain this observation. Ponderomotive forces push charged particles that are in an inhomogeneous oscillating electromagnetic field towards the weaker field areas. In a plasma this results in a depletion of the density where the wave fields are high. The ponderomotive force has been extensively discussed in Ref. [80] in the context of radio-frequency confinement of plasmas, and later developed by several authors explicitly for the case of LH waves [9, 10, 11].

The easiest way tor derive this non-linear force is to consider the motion of an electron in the oscillating $\vec{E}$ and $\vec{B}$ fields of a wave [80]. Neglecting the DC E_0 and B_0 fields, the equation of motion for the electrons is

$$m\frac{d\vec{v}}{dt} = -e\left[\vec{E}(\vec{x}) + \vec{v} \times \vec{B}\right] \tag{2.47}$$

This equation is exact if $\vec{E}$ and $\vec{B}$ are evaluated at the instantaneous position of the electron. The nonlinearity comes partly from the $\vec{v} \times \vec{B}$ term, which is second order because both $\vec{v}$ and $\vec{B}$ vanish at the equilibrium, so that the term is no larger that $\vec{v}_1 \times \vec{B}_1$, where $\vec{v}_1$ and $\vec{B}_1$ are the linear-theory values. The other part of the non-linearity, as we shall see, comes form evaluating $\vec{E}$ at the actual position of the particle rather than its initial position. Now, let's assume a wave electric field of the form

$$\vec{E} = \vec{E}_s \cos(\omega t) \tag{2.48}$$

where $\vec{E}_s$ contains the spatial dependence. In first order, the $\vec{v} \times \vec{B}$ term in Eq. 2.47 may be neglected and one can evaluate $\vec{E}$ at the initial position $\vec{x}_0$, so to obtain:

$$\begin{aligned} m\, d\vec{v}_1/dt &= -e\vec{E}(\vec{x}_0) \\ \vec{v}_1 &= -(e/m\omega)\vec{E}_s \sin(\omega t) = d\vec{x}_1/dt \\ \vec{x}_1 &= (e/m\omega^2)\vec{E}_s \cos(\omega t) \end{aligned} \tag{2.49}$$

It is important to note that in a non-linear calculation, one cannot write $e^{i\omega t}$ and take its real part later. Instead, one has to write the real part explicitly as $\cos(\omega t)$. This is because the products of oscillating factors appear in non-linear theory, and the operations of multiplying and taking the real part do not commute.

Going to second order, we expand $\vec{E}(\vec{x})$ about $\vec{x}_0$:

$$\vec{E}(\vec{x}) = \vec{E}(\vec{x}_0) + (\delta\vec{x}_1 \cdot \nabla)\vec{E}\Big|_{x=x_0} + \ldots \tag{2.50}$$

We must now add the term $\vec{v}_1 \times \vec{B}_1$, where $\vec{B}_1$ is given by Maxwell's equation:

$$\begin{aligned} \nabla \times \vec{E} &= -\partial \vec{B}/\partial t \\ \vec{B}_1 &= -(1/\omega)\nabla \times \vec{E}_s\Big|_{x=x_0} \sin(\omega t) \end{aligned} \tag{2.51}$$

To this order then, the second part of Eq. 2.47 is

$$m\, d\vec{v}_2/dt = -e\left[(\delta\vec{x}_1 \cdot \nabla)\vec{E} + \vec{v}_1 \times \vec{B}_1\right] \tag{2.52}$$

Substituting the expression for the first order terms and averaging over time, we have

$$m\left\langle \frac{d\vec{v}_2}{dt} \right\rangle = -\frac{e^2}{m\omega^2}\frac{1}{2}[(\vec{E}_s \cdot \nabla)\vec{E}_s + \vec{E}_s \times (\nabla \times \vec{E}_s)] = f_P \tag{2.53}$$

Here we have used $< \sin^2(\omega t) >=< \cos^2(\omega t) >= 1/2$. The double cross product can be written as the sum of two terms, one of which cancels the $(\vec{E}_s \cdot \nabla)\vec{E}_s$ term. What remains is:

$$\vec{f}_P = -\frac{1}{4}\frac{e^2}{m\omega^2}\nabla E_s^2 \tag{2.54}$$

This is the effective non-linear force on a single electron. The force per m^{-3} is f_P times the electron density n_0 which can be written in terms of ω_{pe}^2. Since $E_s^2 = 2 < E^2 >$, we finally have the ponderomotive force formula

$$\vec{F}_P = -\frac{\omega_{pe}^2}{\omega^2}\epsilon_0 \nabla \frac{< E^2 >}{2} \tag{2.55}$$

If the wave is electromagnetic, the second term in Eq. 2.53 is dominant, and the physical mechanism for $\vec{F}_P$ is as follows. Electrons oscillate in the direction of $\vec{E}$, but the wave magnetic field distorts their orbits. That is, the Lorentz force $-e\vec{v} \times \vec{B}$ pushes the electrons in the direction of $\vec{k}$ (since $\vec{v}$ is in the direction of $\vec{E}$, and $\vec{E} \times \vec{B}$ is in the direction of $\vec{k}$. The phases of $\vec{v}$ and $\vec{B}$ are such that the motion does not average to zero over an oscillation, but there is a secular drift along $\vec{k}$. If the wave has uniform amplitude, no force is needed to maintain this drift; but if the wave amplitude varies, the electrons will pile up in regions of small amplitude, and a force is needed to overcome the space charge. This is why the effective force $\vec{F}_P$ is proportional to the gradient of $< \vec{E}^2 >$. Since the drift for each electron is the same, $\vec{F}_P$ is proportional to the density, hence the factor $\frac{\omega_{pe}^2}{\omega^2}$ in Eq. 2.55.

If instead the wave is electrostatic, the first term in Eq. 2.53 is dominant. Then the physical mechanism is simply that an electron oscillating along $\vec{k} \parallel \vec{E}$ moves farther in the half-circle when it is moving from a strong-field region to a weak-field region than viceversa, so there is a net drift.

Although, $\vec{F}_P$ acts mainly on the electrons (in view of their lower mass), the force is ultimately transmitted to the ions, since it is a low-frequency or DC effect. When electrons are bunched by $\vec{F}_P$, a charge separation field $\vec{E}_{cs}$ is created. The total force felt by the electrons is

$$\vec{F}_e = -e\vec{E}_{cs} + \vec{F}_P \tag{2.56}$$

Since the ponderomotive force on the ions is smaller by the mass ratio m_e/m_i, the force on the ion fluid is approximately

$$\vec{F}_i \approx -e\vec{E}_{cs} \tag{2.57}$$

Summing up the last two equations, we find that the force on the plasma is $\vec{F}_P$.

To evaluate the effect on the plasma density it is advantageous to introduce the concept of a ponderomotive potential Φ_P (defined as $\vec{F}_P = -\nabla\Phi_P$). At equilibrium the density of each species

follows the Boltzmann distribution and Φ_P has to balance the electrostatic potential Φ_{cs} which is due to charge separation:

$$n = n_0 \exp\left(-\frac{e(\Phi_{cs} + \Phi_P)}{\kappa T}\right) \tag{2.58}$$

In theory ponderomotive force acts on all species in the plasma, also on the ions, however in view of the inverse proportionality to the mass of the particle, this effect is mostly relevant for electrons. Imposing quasi-neutrality eliminates Φ_{cs} and one can expand the electron density as $n_e \approx n_{e0}(1+\delta n)$, where

$$\delta n = -\frac{e(\Phi_{Pe} + \Phi_{Pi})}{\kappa(T_e + T_i)} \tag{2.59}$$

The ponderomotive potential Φ_P for a uniform magnetized cold plasma can be derived by integrating Eq. 2.53. However this is not a simple undertaking. An alternative approach derived in Ref. [81], based on the Hamiltonian of the particles oscillation center in an electromagnetic wave field gives as a result:

$$\Phi_P = \frac{e}{m}\left[\frac{|E_z|^2}{\omega^2} + \frac{|E_x|^2 + |E_y|^2}{\omega^2 - \Omega^2} + \mathrm{Im}\left\{\frac{\Omega(E_y * Ex - E_x * E_y)}{\omega(\omega^2 - \Omega^2)}\right\}\right] \tag{2.60}$$

where it is assumed that $\mathbf{B} = B_0\hat{z}$.

Worth pointing out is that the net effect of the wave fields on the plasma density depends on the ratio between the ponderomotive and the kinetic potentials. As it will be stressed in Chap. 5, the plasma temperature is an important feedback mechanism for ponderomotive effects, since the injection of high power RF waves tends to heat the plasma in the vicinity of the launcher through collisional damping.

2.4 Lower hybrid wave launching structures

In order to excite an electrostatic LH wave, a launcher (antenna) having a slow-wave structure needs to be located close to the plasma. Very different antenna designs have been employed depending on the machine parameters. Conventional tokamak experiments (Alcator C-Mod, JET, FTU, Tore Supra, JT60, etc.) employ so called grill launchers, whereas other designs have been used for spherical tokamaks or reverse field pinch experiments (e.g. combline, interdigital, and dielectric loaded grill). Also, over the years the conventional grill design has evolved to improve the coupling performance (e.g. multijunction), handle higher powers (e.g. PAM), or improve the transmission efficiency (e.g. four-way-splitters). In the following sections the main antenna designs are introduced. An excellent review of LH coupling structures (and more) is given in Ref. [82].

Classical grill

The launching of LH waves in the low GHz frequency range is most commonly achieved by a phased array of waveguides, the "grill" [5]. These waveguides are operated in the fundamental TE_{10} mode and are oriented such that the wave electric field in the waveguide is nearly parallel to the background magnetic field in the plasma so to ensure that only the slow-wave branch of the dispersion relation is excited.

Usually, the relative phases among the waveguides can be easily adjusted so that the electric field pattern at the grill mouth has a characteristic $n_\parallel$ spectrum, which might be peaked at a typical value of $n_\parallel \approx 2$. Two, four, six, eight waveguides were common in early experiments, but many more are used in more recent experiments. The larger the number of waveguides in the toroidal direction, the narrower the $n_\parallel$ spectrum that can be made.

A simplistic way to estimate the launched $n_\parallel$ spectrum for these type of antennas is to assume

that at the grill mouth only the TE_{10} mode of the waveguides is present, although in reality other guided modes are excited at the waveguide plasma interface. With this assumption, it is possible to calculate that for N waveguides of width w, septa of width δ and a relative phase difference of $\Delta\phi$, the $n_{\|}$ power spectrum becomes

$$P(n_{\|}) = P_0 \frac{\sin^2(n_{\|}\frac{w\omega}{2c})}{n_{\|}^2} \frac{\sin^2(N\alpha/2)}{\sin^2(\alpha/2)} \tag{2.61}$$

where

$$\alpha = \left(\Delta\phi + n_{\|}\frac{\omega}{c}(w+\delta)\right) \tag{2.62}$$

and P_0 is a normalization constant. A convenient formula for the peak of the $n_{\|}$ spectrum is

$$n_{\|} = \frac{c\Delta\phi}{\omega(w+\delta)} \tag{2.63}$$

Multijunction

Grill antennas can obtain the relative phasing among adjacent waveguides either in the transmission line feeding of the antenna or directly inside the antenna with built-in phase shifters. Multijunction designs [4] use the latter approach and exploit multiple waves reflections at the mouth of the launcher to improve the coupling efficiency and are inherently load resilient. In fact, for specific phase shifts the waves can be made to destructively interfere at the input waveguide (as long as adjacent columns see the same plasma load).

The load resilience characteristic is of particular importance for long distance coupling (i.e. when the launcher is located deep in the limiter shadow, as expected on ITER), however comes at the expense of higher power densities in the last section of the launcher, which can be thought of as a cavity resonator. Other engineering advantages of these launchers is that they are compact and significantly simplify the antenna feeding structure. However, since the waveguide phasing is set by built-in phase shifters, the launched spectrum can not be changed and tends to be more complicated compared to the traditional grill antenna (due to the multiple wave reflections at the grill mouth).

PAM

Passive-Active Multijunction (PAM) launchers [83, 84] are an extension of the fully active multijunction concept. This design alternates waveguides which are connected to the microwave source, with waveguides which are shorted (hence the name passive). The idea behind this concept is that passive waveguides can reflect microwave power back to the plasma which is coupled from the adjacent active waveguides. This design has shown to work well near the cutoff density where the inter-waveguide coupling, which is characteristic of grill launchers in the presence of a plasma, is strongest. Key to this design is the distance of the short inside of the passive waveguide, which is optimized so that the waves which are radiated with the correct phasing to produce a clean $n_{\|}$ spectrum. Passive-Active Multijunction designs are particularly attractive for multi-megawatt antenna suitable for ITER and reactor like tokamaks because cooling channels can be installed behind the passive waveguides to efficiently dissipate the heat which would otherwise accumulate at the front of the grill [85].

Poloidal-splitter

One of the main drawbacks of multijunction antennas is that these are not able to operate over a wide parallel wavenumber range. This freedom is necessary to fully explore the LH wave physics, including coupling, accessibility, damping and current drive. The poloidal-splitter concept was first implemented on Alcator C-Mod and designed to distribute the microwave power in four ways in the

poloidal direction (hence the name *4-way-splitter antenna*) [1]. This design was proved to improve the transmission efficiency and simplify the feeding structure with respect to traditional LH grill launchers, while overcoming the aforementioned limitation of the multijunction designs. More details about the design and benchmarking of this antenna will be given in details in Chap. 3 and 4.

Other antennas

In order to satisfy the condition $\omega < \omega_{LH}$, devices which have small static magnetic field (such as ST Tokamaks or RFP) need to operate at a wave frequency which is lower than what is normally used in standard Tokamaks. Also, these devices may have a different magnetic field topology. In turn, these differences require antenna structures different from the classical phased waveguide arrays.

2.5 Existing numerical tools for lower hybrid waves

In the following sections the main numerical tools for LH waves which are referred throughout this thesis are introduced.

2.5.1 Wave propagation and damping

In Sec. 2.2 and 2.2.2 it was shown that LH waves tend to distort the electrons velocity distribution function, which in turn affects the wave absorption itself. Since these two effects are coupled to one another the problem is non-linear and its solution requires the iterative use of two simulation codes. In general, a wave code is used to determine the location and amplitude of the waves in the plasma. From this information, the RF diffusion coefficient is calculated and used in a Fokker-Planck code to calculate the perturbed electron distribution function. Since the absorption of the waves, and consequently the wave electric field strength, is a function of the electron distribution through the local wave damping, the perturbed distribution function is then passed back to the wave code, which recalculates the quasi-linear diffusion coefficient with the new distribution function. The process is repeated until the result converges.

Until recently numerical modeling of LHCD has consisted, for the most part, of toroidal ray-tracing codes and Fokker-Planck solvers. The ray-tracing approach is appealing because it is computationally straightforward and has been successful at correctly modeling some of experimental results of LHCD [39]. Nonetheless, ray-tracing inherently excludes some wave physics, and the eikonal approximation used to justify ray-tracing can break-down at cutoffs and caustic surfaces, as discussed in Sec. 1.4.1. These limitations have have lead to more efforts in numerical modeling. These include the development of more refined WKB-based models, so called WKBp or beam-tracing methods [30, 47, 48], which expand the wave Eq. 1.6 to second order in $k\,L$; and of fullwave models, which completely describe the wave propagation by directly solving Maxwells equations.

GENRAY

GENRAY is a ray-tracing code that allows for the simulation of waves in axisymmetric toroidal plasma through the use of the geometrical optics approximation. When used for LH waves, the rays are launched from a location in the plasma close to and slightly above the cutoff density, and are independently followed until they reach a damping threshold, at which point each ray is terminated. This likely happens when the parallel wavenumber is sufficiently high to satisfy the Landau resonance condition for wave absorption. If the rays traverse to the edge of the plasma prior to fully damping, then they are reflected either from of a cutoff layer or a conducting surface located at the plasma edge. Ray-tracing modeling is constantly affected by the uncertainty related to the initial conditions of the rays.

GENRAY uses a two dimensional SOL profile for plasma density and a one dimensional SOL profile for plasma temperature [2]. The temperature and density profiles consist of exponentially decaying profiles based on the distance from a point in the SOL to the separatrix, with the e-folding length chosen by the user. The e-folding length for density may be defined as a function of poloidal angle.

GENRAY interfaces with the Fokker Planck code CQL3D to self-consistently take into account the non-maxwellian distribution function. The GENRAY/CQL3D package [86] has been used extensively to interpret LHCD experiments. Because this simulation model has been used so widely, it is a natural choice for comparing more sophisticated full-wave calculations against.

Paraxial beam-tracing

Paraxial beam-tracing [30, 47, 48] involves following the path of a ray, but expanding the parameters around the axis of the beam so that it has a Gaussian envelope whose width reflects the effects of diffraction on the beam. Like ray-tracing, beam-tracing is also affected by the uncertainty related to the initial conditions of the beam.

TORIC-LH

TORIC-LH [87, 88, 15] uses a spectral decomposition along the poloidal and toroidal directions and finite elements are used in the minor radius in a torus. The TORIC code assumes zero ion Larmor radius effects, but does retain the effect of finite electron Larmor radius and thus electron damping due to transit time magnetic pumping.

Like GENRAY, the TORIC-LH code also iterates with the CQL3D Fokker-Planck code, but in this case the RF induced quasilinear diffusion coefficient is calculated starting from the full-wave fields. In view of the domain discretization within the code (spectral in the poloidal direction), TORIC allows only the inclusion of a simple SOL model, in which the flux surfaces have to be conformal to the last closed flux surface and must have constant temperature and density. In TORIC the wave field excitation is done by imposing a known wave field distribution (in terms of poloidal modes) at the boundary of the simulation domain.

AORSA

In addition to the toroidal spectral decomposition which is typical of fullwave solvers, AORSA [89] uses a cartesian spectral decomposition in the poloidal direction. AORSA is the only code which can treat finite ion Larmor radius effects, although these are not relevant for the LHCD case. Also the AORSA code employs the CQL3D Fokker-Planck code to self-consistently take into account the non-maxwellian distribution function. Recently, a SOL model has been implemented in the AORSA code with density and temperature profiles calculated by the SOLPS code [90].

CQL3D

The electron distribution function in the presence of RF wave fields is calculated by the CQL3D (Collisional Quasi-Linear 3D) [91] Fokker-Planck code starting from a quasi-linear diffusion which is constructed on the basis of either ray-tracing or fullwave calculations. The CQL3D code iterates with ray-tracing or fullwave codes to find a self-consistent solution for the wave damping and for the bounce averaged $f(v_\perp, v_\parallel, \rho)$ distribution function. This code is equipped with a rich set of synthetic diagnostic tools which make possible direct comparison with experimental data collected by different diagnostics.

[2] Recently, a newer version of GENRAY under testing allows for arbitrary 2D SOL profiles to be specified on a cartesian grid.

2.5.2 Linear coupling codes for grill antennas

The prediction of power deposition and driven current profiles are the primary goals of numerical modeling. However, numerical tools are also needed to calculate the fields inside the launcher and in the first few centimeters in front of it in the presence of the plasma. These tools are essential for understanding, and thus controlling, the interaction between the launcher and the plasma, and are often the starting point of other numerical calculations. Also, since the main technological challenge in LHCD is to place the waveguide array near the plasma edge in order to prevent large reflection due to the unavoidable edge cutoff region, LHCD antennas have to be carefully designed and optimized.

The antenna determines the boundary conditions of the wave propagation inside the plasma. Hence, common practice is to model the antenna-plasma coupling of a LH grill antenna by splitting the problem into two parts: the vacuum side and the antenna-plasma interface. The two simulations are then combined by cascading the scattering matrices of the two parts, following the well known network approach [92]. Usually, the electromagnetic field scattered by the antenna is assumed to be dissipated far away from the coupling region so that the coupling problem is treated as a problem of radiation in a semi-infinite medium independent of the absorption in the core plasma. In such a modeling, the propagation into the plasma core is not calculated.

At the vacuum-plasma interface, the boundary conditions are expressed through the plasma surface impedance, a rank-2 tensor linking the tangential components of electric and magnetic fields at the interface. In most cases, the analysis of grill antenna has been primarily done by matching the wave field solution at the interfaces between plasma, vacuum, and antenna regions (mode matching codes). Examples of these codes include GRILL [5], FELHS[93] ALOHA and ALOHA2D [94], GRILL3D [95]. The disadvantage is restriction to slab geometries, which makes it difficult to use this method for more complicated non-grill like structures. To address these types of problems, the TOPLHA code [2, 96], which originated from the TOPICA [3] code for ion cyclotron antennas, has been developed for LH launcher analysis and allows for the description of complicated antenna geometries.

The modeling flexibility given some codes, often comes at the expenses of solving large numerical problems, which can be time and resource consuming. For example, the simulation time can range from few seconds on a desktop computer (e.g. GRILL) to several hours on an HPC cluster (e.g. TOPLHA). By assuming somewhat simplified geometries, mode matching codes have often been shown to be fast and reliable tools for the prediction of the performances and radiated spectrum of the launcher. Their usage is especially convenient when many simulations are required, such as during the initial stages of an antenna design or for routine modeling of experiments. The use of larger more sophisticated code should be left as a validation exercise or to the cases when simpler and faster codes is simply not applicable.

GRILL

The GRILL code assumes a 1D slab plasma geometry. The density in front of the grill is assumed to be linear (see Fig. 5-1). This assumption greatly simplifies the evaluation of the plasma surface impedance, which is a scalar function of the parallel wavenumber (no fast-wave) and can be expressed analytically in terms of an Airy function. The vacuum electric and magnetic fields inside of the grill antenna is described in terms of waveguide transverse modes. The overall solution of the problem is obtained by applying the appropriate boundary conditions between the electric and magnetic field at the waveguide openings. This technique is usually referred to as "mode-matching" [97] and is common to other codes including ALOHA, FELHS.

Advanced LOwer Hybrid Antenna (ALOHA)

The ALOHA code has been developed to improve the modeling of the coupling of LH waves while keeping a fast tool. In ALOHA the plasma coupling is calculated from a fast classical model that

describes the effect of the slow-wave only (ALOHA 1D) or from a more advanced model that considers the contribution of both fast and slow-waves (ALOHA 2D). The evaluation of the plasma surface impedance has been implemented both numerically or in terms of Airy (slow-wave) and Whittaker (fast-wave) functions. Worth mentioning is that ALOHA describes the SOL by means of a single-layer or a two-layer electron density profile, but does not allow the addition of a vacuum layer in front of the grill.

The scattering matrix at the grill mouth itself is obtained with the mode matching method used for the standard grill. For the grill description, ALOHA accepts as an input the scattering matrix of an antenna which can be calculated using electromagnetic simulation tools or measurements. In addition ALOHA can evaluate the scattering matrix of a grill launcher in the presence of ideal waveguide splitting (E-junctions) and other discontinuities, based on the mode-matching method.

Finite Element Lower Hybrid Solver (FELHS)

FELHS includes the evaluation of the coupling and the radiated power spectrum for traditional grills and active and passive-active multijunction. The scattering matrix at the grill mouth itself is obtained with the mode matching method used for the standard grill and, similarly to ALOHA, the code is able to internally model multijunction antennas by a mode-matching formulation. The code considers waveguides of finite height and can take into account both the slow and the fast-wave. Density profile and magnetic field shear can be specified arbitrarily, and a vacuum layer between the grill mouth and the plasma surface can be included in the model. The plasma surface impedance is then obtained by numerically integrating the full wave equations using a finite element approach in slab geometry.

Torino Politecnico Lower Hybrid Antenna (TOPLHA)

TOPLHA is a boundary element code in which the antenna is discretized using linear vector functions defined over a triangular surface mesh. The plasma description, currently incorporates the plasma surface impedance which is calculated by some other code. Currently TOPLHA is coupled to the 1D plasma code FELHS for modeling the plasma response. TOPLHA was originally developed to address the problem of LH wave coupling including a realistic antenna shape. However, worth pointing out is that since the code is coupled to a 1D plasma code, effects such as the launcher curvature are included by an ad-hoc formulation as reported in Ref. [3] (so called 1.5D formulation).

The TOPLHA code has been verified against the ALOHA code [2, 98]. Comparisons have been made for several plasma scenarios on different antenna designs: an array of independent waveguides, a multi-junction antenna and a passive/active multi-junction antenna. When simulating the same geometry and plasma conditions the two codes compare remarkably well both for the reflection coefficients and for the launched spectra. The different approaches of the two codes to solving the same problem strengthens the confidence in the final results.

COMSOL Multiphysics

The commercial software COMSOL Multiphysics [99] uses Finite Element Methods (FEM) to solve arbitrary systems of partial differential equations. This code is extremely versatile and works for 1D, 2D and 3D geometries. The RF module of this code is able to describe the propagation of electromagnetic waves in materials with anisotropic complex dielectric tensors, which is what is needed for the calculation of LH wave coupling. The FEM approach leaves absolute freedom in the description of the antenna geometry and of the plasma within the collisional cold plasma approximation. In particular, spatial variations of any given quantity is permitted, thus allowing the freedom to specify realistic magnetic equilibria, arbitrary density distributions, poloidal and toroidal asymmetries, etc.

The use of a FEM code to model antenna-plasma wave coupling was first reported in Ref. [14]. The capability of handling the complicated antenna structure and simulating the wave field inside

the plasma provides a unique opportunity for analyzing non conventional LH launchers, such as the MST interdigital antenna [100] and the TST2 combline antenna [101]. Worth pointing out is that the COMSOL Multiphysics package has also been the workhorse for the design of the ICRF rotated antenna on Alcator C-Mod [102, 103].

2.5.3 Non-Linear coupling codes for grill antennas

Most of the coupling analysis tools self-consistently calculate the effect of high power RF waves on the edge plasma, but assume that the density profile which is input into the code is already self-consistently at equilibrium with the wave fields. The codes [9, 11] which evaluate the effect of ponderomotive forces on the density profile do not (and can not) focus on the coupling problem itself, since in addition to considering only slow-wave propagation and low density, they assume a monochromatic wave spectrum.

2.6 Numerical tools developed throughout this thesis

For this thesis two fullwave numerical codes based on a finite element approach (FEM) have been developed. The *POND* code solves non-linear coupling problem including the effect of the ponderomotive forces on the edge plasma density. In POND the non linear coupling between the wave electric fields and the density depletion by ponderomotive forces is taken into account via the iterative approach. The *LHEAF* code solves the wave propagation for realistic fusion plasma parameters in the LH range of frequencies. A newly developed efficient iterative algorithm takes into account the electron Landau damping effects of a hot plasma in a FEM code. An in-depth description the LHEAF and POND codes, together with simulation results and comparisons to the Alcator C-Mod experiment will be discussed in Chap. 5 and 6. Both of these codes are based on the commercial software COMSOL Multiphysics [99].

Chapter 3

Alcator C-Mod and the four-way-splitter lower hybrid antenna

The Alcator C-Mod tokamak [104] is a compact (major radius $R_0 = 0.68\ m$, minor radius $a = 0.22\ m$) diverted tokamak with the ability to run high toroidal magnetic field ($B_t = 5 - 8\ T$), high plasma current ($I_P = 1.5\ MA$) and high electron density $\bar{n}_e \approx 0.5 \times 10^{20}\ m^{-3}$ plasmas. The inner vessel walls are covered with molybdenum and tungsten tiles. Alcator C-Mod shares many of the properties of ITER, but on a smaller scale. Characteristic of this experiment is the high RF power density, which is provided by two two-strap ICRF antennas at 80 MHz (D and E ports) and one four-strap antenna with a variable frequency source between 50 and 80 MHz (J port). Additionally, a LH system at 4.6 GHz is available for non-inductive current drive. Figures 3-1 and 3-2 show cutout CAD schematics of the Alcator C-Mod tokamak with the location of the heating systems and the main diagnostics.

The goal of the LHCD experiment is to demonstrate and study the full non-inductive high performance tokamak operation using the parameters close to that envisioned for ITER in terms of LHCD frequency and magnetic field. Previously, up to 1.2 MW of microwave power at 4.6 GHz has been successfully coupled for 0.5 s using a traditional grill launcher (LH1). To explore wider parameter regimes using higher power and longer LHCD pulse, the second LHCD launcher (LH2) was designed, constructed and successfully installed in May 2010. In this chapter, the details of the LH2 launcher design and its integrated RF design and antenna-plasma coupling is presented. At the end of the chapter, the diagnostic systems which are relevant for this thesis are briefly overviewed.

3.1 Four-way-splitter antenna

Since the development of the first grill launchers [5], the multijunction [84] and PAM [83] concepts have enabled the design of multi-megawatt antennas suitable for reactor like tokamaks. However, multijunction antennas are not able to operate over a wide parallel wavenumber range, which is necessary to fully explore LH wave physics, including coupling, accessibility, damping and current drive.

For this reason LH2, an innovative LH launcher based on a novel four-way-splitter concept [1] has been employed as a final stage power splitting component. Similarly to a multijunction design, in a four-way-splitter antenna the power splitting is done at the front of the launcher, resulting in a simple low loss feeding network. However, since the power splitting is done poloidally the launched parallel wave spectrum can be changed with the same flexibility of conventional grill antennas

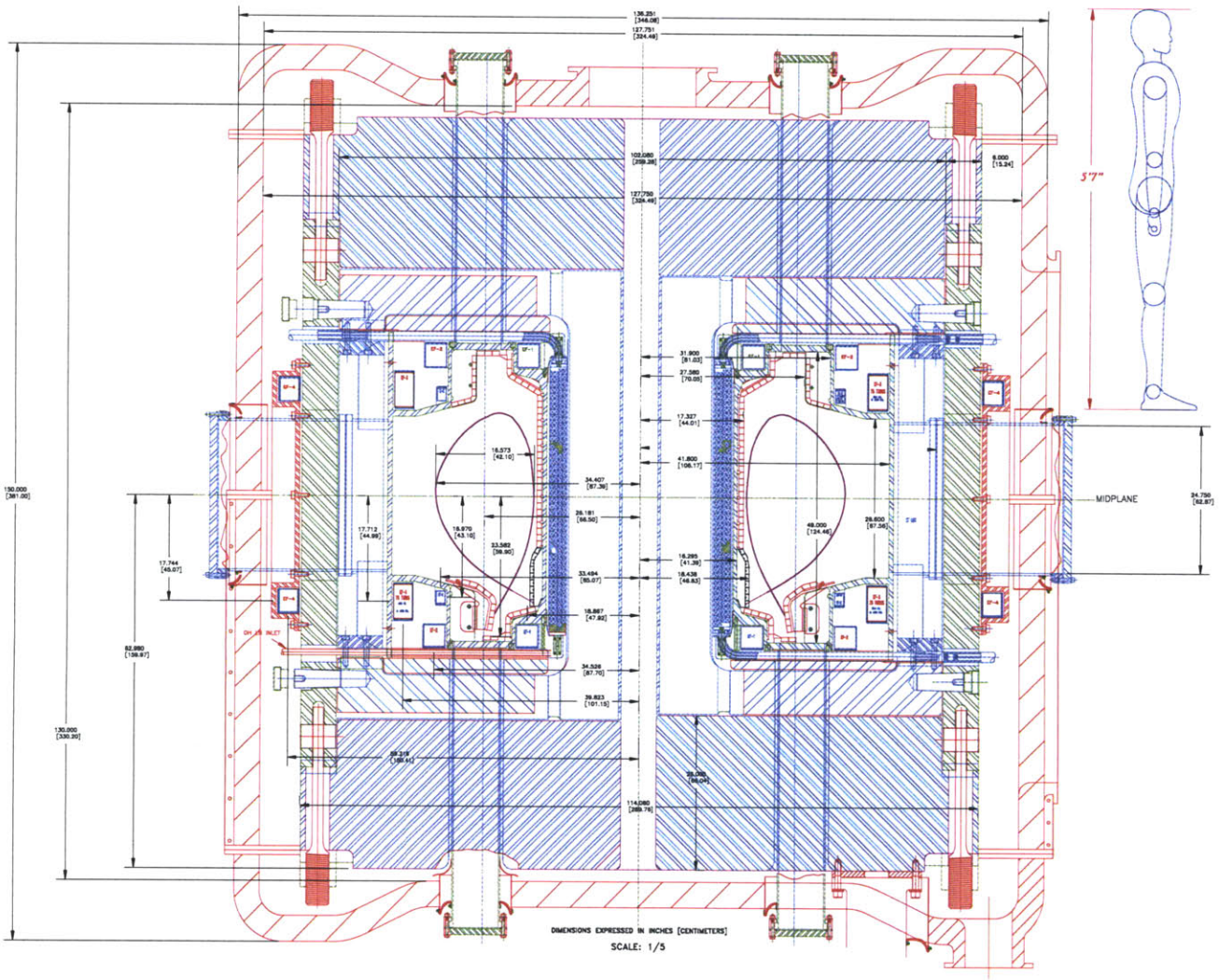

Figure 3-1: Side cross-sectional CAD view of the Alcator C-Mod tokamak reporting the most relevant dimensions. The compact design of the machine and the cryostat enclosing the vacuum vessel and magnetic field coils make access challenging. For reference, a typical 5'7" graduate student is shown.

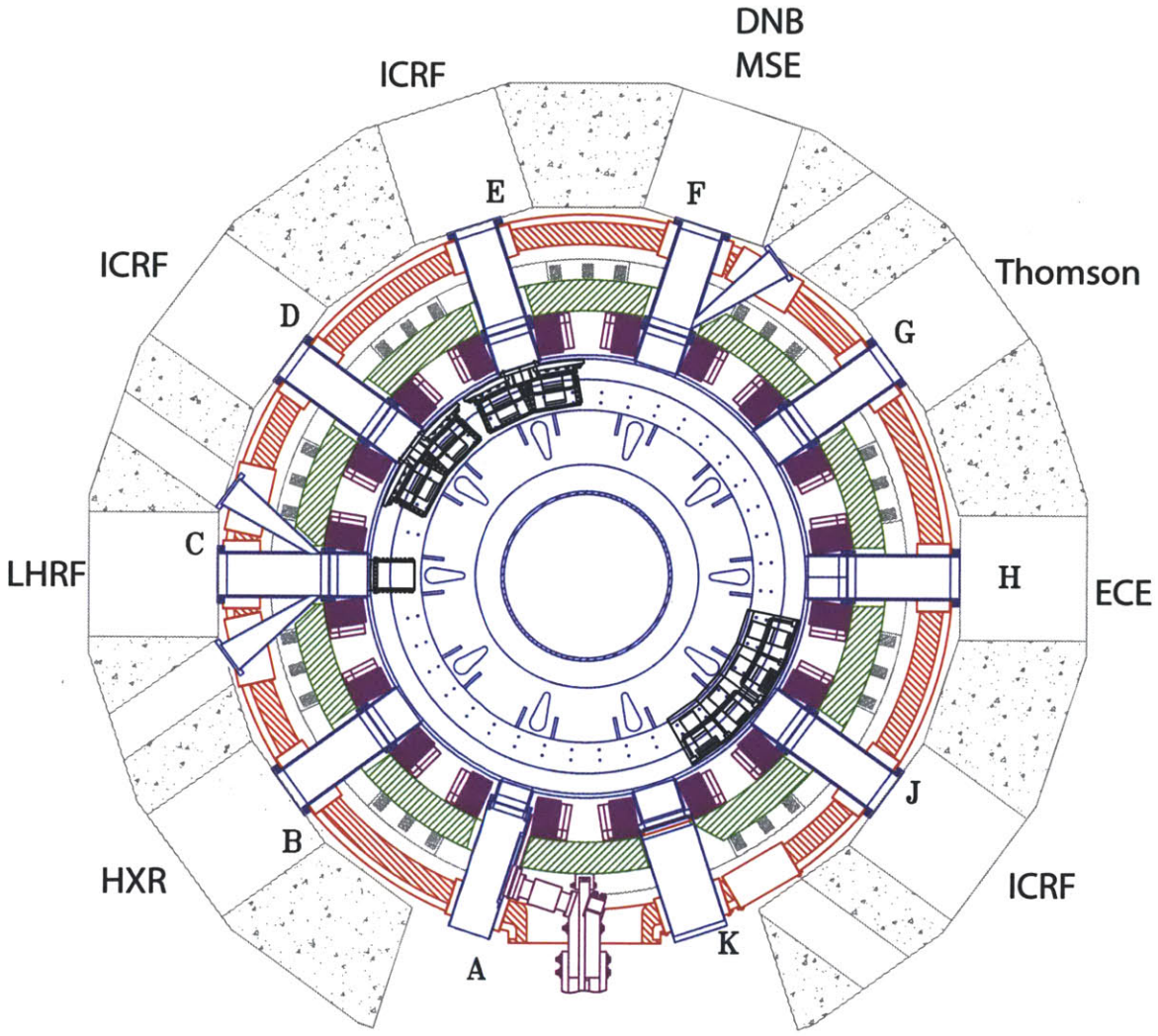

Figure 3-2: Top-down CAD view of the Alcator C-Mod tokamak. Key heating and diagnostic systems are labeled at their respective ports. Ten horizontal ports exist on the out-board side, along with top and bottom ports at the same toroidal positions. Ports are named A through H and J and K; two outboard limiters are installed, a full limiter in the GH sector and a split limiter in the AB sector. The toroidal magnetic field and plasma current are always in the same direction and clockwise in normal operation.

($-3.8 < n_{\|} < 3.8$). In this respect the four-way-splitter design overcomes the major limitation for multijunction antennas. For the same reason, the directivity of the antenna is not affected by the plasma load, another known issue of multijunction antennas.

Figure 3-3 shows, the plasma facing part of the forward waveguide assembly (the coupler assembly), which presents to the plasma a grill made of 16 columns of 4 waveguides. This is made of 16 four-way-splitter modules which are stacked in the toroidal direction. Each of the waveguides is 60 *mm* in height and 7 *mm* in width and they are spaced 1.5 *mm* toroidally and 21 *mm* poloidally. A total of 8 passive waveguides (one on each side of each row) are installed to reduce the reflection on the edge columns [84].

Each four-way-splitter module (Fig. 3-4) splits the microwave power in four ways in the poloidal direction. This is accomplished by openings in the narrow side of the main waveguide. The four-way-splitter can be explained in terms of transmission line theory as four parallel impedances which are spaced by one guide wavelength. One shorted stub at the end of the splitter is three quarters of a guide wavelength away from the last waveguide and acts as an open circuit. The microwave power is redistributed depending on the plasma load on each row of the four-way-splitters. If the load on each waveguide is the same, the power splitting is even among rows.

As a consequence of the poloidal curvature, the radial locations of the top and bottom output waveguides differs by 4 *cm* with respect to the middle output waveguides. Phase shifters compensate for the longer length of the top and bottom waveguides and ensure even power splitting for equal loads at the waveguides-plasma interface. Vacuum windows are placed at 2.5 *in* from the mouth of the grill, allowing the whole four-way-splitter structure to be pressurized with Nitrogen to prevent arcing and ensuring short high RF power conditioning time. Each splitter is made from stainless steel and four short sections of copper on which Alumina vacuum waveguide windows are brazed. The air side inner-wall of the splitter is copper plated to reduce the low transmission loss. The splitters are connected to standard WR-187 waveguides via a transformer and a feeding network connects the launcher with the transmission line from the klystrons. This transformer can be thought of as a double stub tuner that matches the impedance of the splitter to the one of the feeding network.

Figure 3-5 shows a schematic of the whole LH2 launcher, which consists of the forward waveguide assembly anad the rear side waveguide assembly. The phase difference between the columns is controlled by a combination of mechanical phase shifters and by independent phasing of the klystrons. Ten 250 *kW* klystrons feed the antenna at the rear side waveguide assembly. The four centermost columns are directly fed by one klystron, whereas the other columns share one klystron in pairs. The phase relation between these columns is set to 90 degrees by fixed phase shifters. Under normal operation the klystrons feeding the centermost columns run at half power of the other klystrons, so as to have uniform power density at the grill front. The maximum power density at the launcher achieved to date is 50 MW/m^2, which exceeds an empirical weak conditioning limit [105] given by 0.32 $f^2 b = 41\ MW/m^2$, where f is the source frequency in GHz and b is the waveguide short dimension in *cm*, and is about 83% of the scaling law shown in Ref. [106].

A major objective for the LH2 antenna was to reduce the transmission losses and to improve the over-all reliability as compared to LH1. The fabrication process was revised and optimized for this purpose. Poor electrical contact, which resulted in the increase of dissipation of high frequency surface current on LH1, was carefully eliminated. The number of components, joints, and gaskets in the feeding network were also significantly reduced. Moreover, all waveguides were pressurized to a higher pressure than LH1 to prevent arcing. These efforts resulted in a reduction of transmission losses by 30% (from 35% to 24%), rapid commissioning and reliable LHCD operation.

The new Alcator C-Mod LH launcher is equipped with a rich suite of diagnostic tools. These include microwave probes, to measure the forward and reflected power at the grill mouth and characterize the LH2 performance; three sets of two Langmuir probes of different lengths (1 *mm* and 2 *mm*), to point measure the edge density and estimate its scale length; and an X-mode SOL reflectometer, to measure the time evolution of the density profile in front of the launcher. In addition, 16 directional couplers are used to measure the forward and reflected power at the input of each

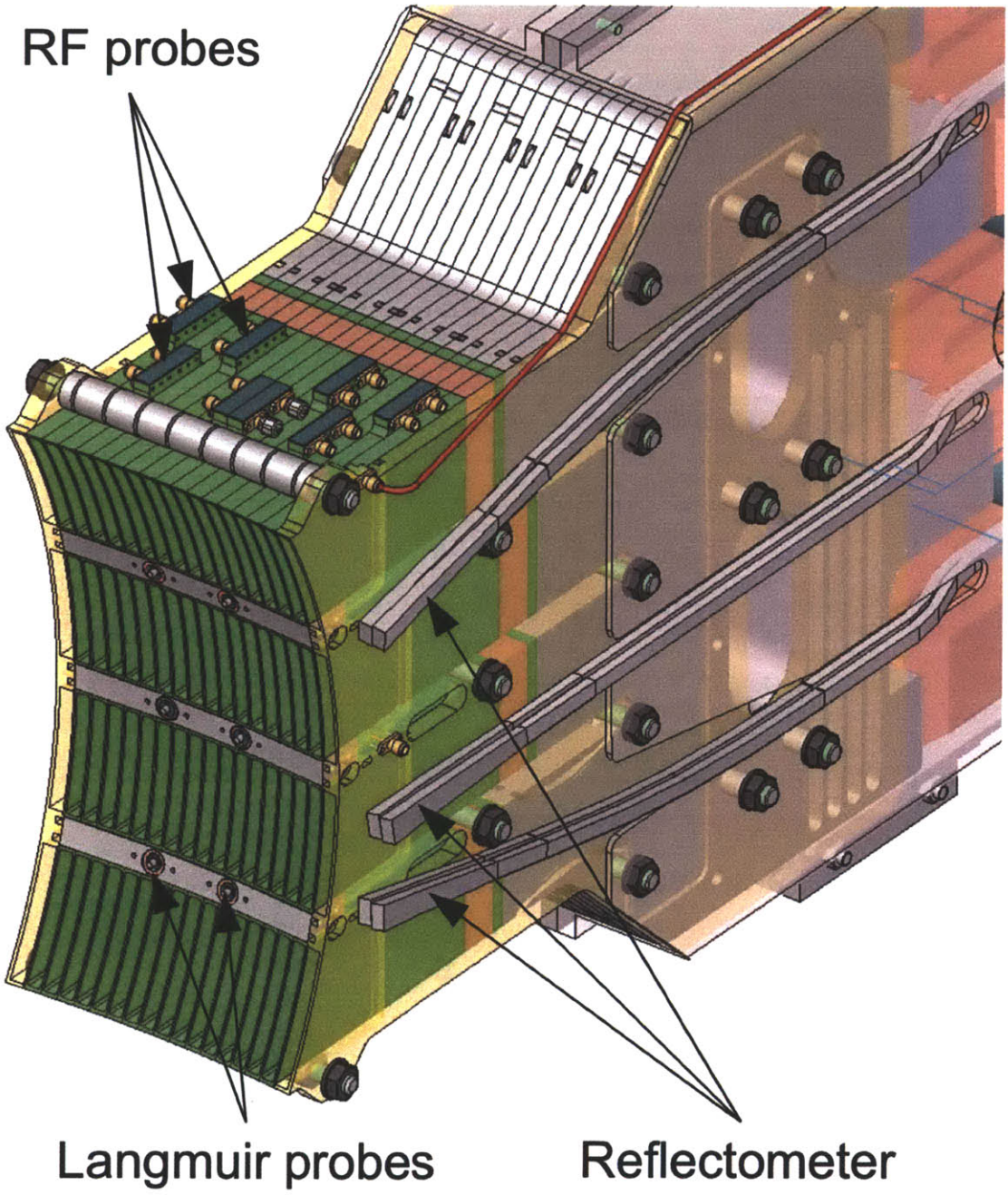

Figure 3-3: CAD schematics of the coupler waveguide assembly and dedicated diagnostics.

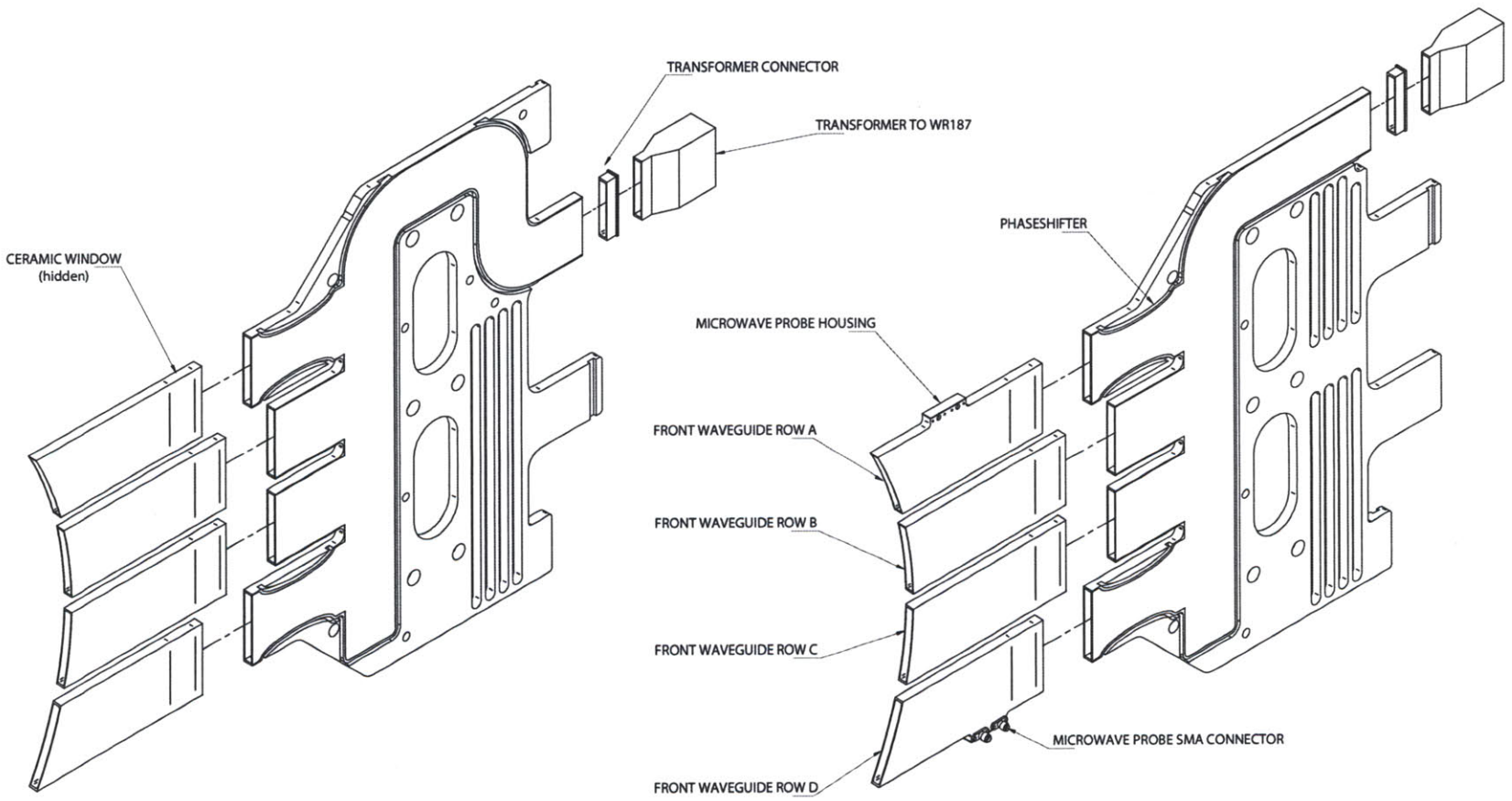

Figure 3-4: CAD explosion of the S-bend feed and straight feed four-way-splitter assemblies.

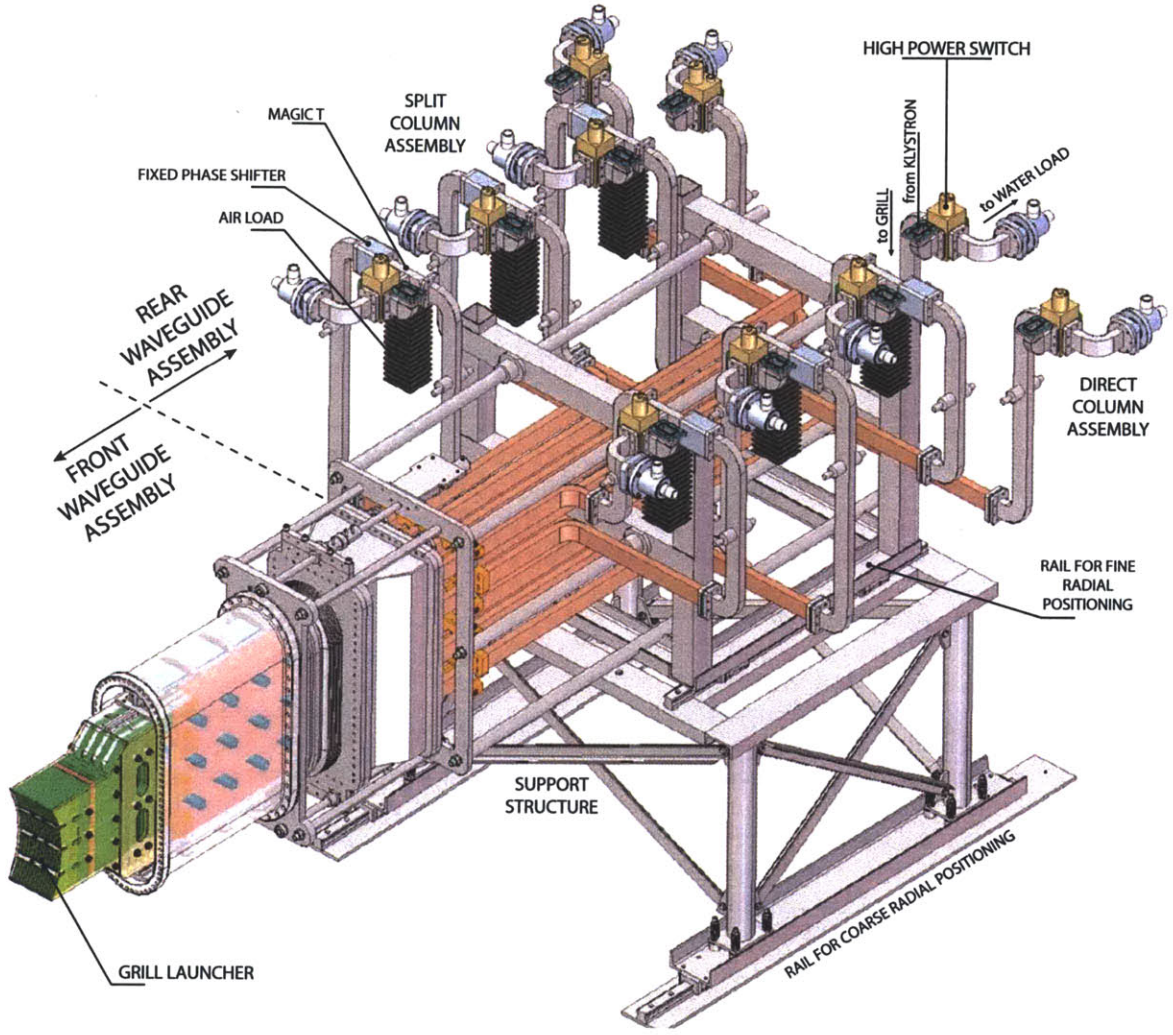

Figure 3-5: CAD schematics of the LH2 system including the feeding network up to the high power switches.

four-way-splitters.

Finally, the LH launcher is radially movable, and is usually operated between 2 mm and 0.1 mm behind local protection limiters which are mounted fixed on the vacuum vessel. This characteristic is quite unique since other LH experiments have private limiters which are fix mounted to the launcher. This feature was found to have important repercussions for the wave coupling performance since it limits how far inside of the plasma the launcher can be pushed and ultimately affects the flexibility of operation. Starting from the 2011/2012 campaign, a new limiter design which is fix mounted to the launcher has been implemented. The private limiters for the 2010/2011 campaign were located 0.5 mm behind the main limiters and the ICRF limiters. Figure 3-6 shows the launcher as it appeared just after installation inside of the Alcator C-Mod vessel.

3.1.1 Four-way-splitter antenna design

Despite the possibility of designing the splitters when facing any arbitrary plasma load, the antenna was designed assuming matched loads on the output waveguides. For this task the geometry of the splitters was optimized using the commercial software Microwave Studio (MWS) [107] so to ensure equal power and phase splitting and low reflection coefficient at 4.6 GHz. Figure 3-7 shows the power and phase splitting characteristic of a four-way-splitter. This conservative design choice was driven by the uncertainty of the density profiles in front of the launcher.

To predict how the four-way-splitter behaves when facing a plasma, the Alcator C-Mod LH antenna was designed based on an integrated model using the LH wave coupling code TOPLHA [108, 2, 109, 3] (development throughout the authors' Master thesis [108]) and MWS. In this approach, TOPLHA solves the antenna-plasma coupling problem assuming a stratified plasma, and MWS solves the EM problem of the vacuum region. The RF characteristics of the two problems are expressed using scattering matrices (S-matrices) [110], which relate the electric field of the forward waves and the backward waves at ports of an RF circuit. The former region has 64 ports (the number of active waveguides), and the solution is expressed by a 64×64 S-matrix, S_p, representing the plasma response. The latter problem is an EM problem in an array of 16 four way splitters, each of which has 5 ports, and the solution is expressed by a 80×80 S-matrix, S_v, representing the LH2 structure. The overall RF characteristic of the four way splitter is then calculated by cascading the S-matrices from these simulations [92]. Subsequently, the COMSOL Multiphysics code has been used to self consistently take into account the electromagnetic-thermal-structural interactions. This comprehensive and predictive analysis has proven to be valuable at understanding the behavior of the system when facing the plasma and has profoundly influenced several design choices of the LH2.

In design stage, a simple linear density profile, as defined in Sec. 2.5.2, has been used. In particular the profiles had no vacuum gap, a fixed gradient $dn/dx = 10^{20}\ m^{-4}$ and variable edge density n_0. This choice was based on LH1 coupling simulations at high density using the GRILL code [26].

Particular attention was given to the study of the peak fields in the waveguide, since the antenna operates at a power density of 5 kW/cm^2, above the weak conditioning limit [82, 106]. Hence, the Alcator C-Mod design has been optimized to minimize the standing wave ratio within the antenna structure. Key parameters for this optimization are the so called *common* and *differential* phase lengths of the AD and BC output waveguides, as depicted in Fig. 3-8. These lengths have been designed for the phases of the reflected waves coming from the plasma to interfere constructively at the input waveguide when the plasma impedance is the same at the four plasma facing waveguides. Lowering the recirculating power in each of the splitters comes at the expense of higher reflection coefficients (Fig. 3-9), a well known tradeoff also for multijunction designs. This design choice was based on considerations relating the available source power and the threshold for the weak/hard conditioning limits. Experimentally it was observed that indeed the operational limits dictated by the power density at the front of the coupler is similar to the one set by the available source power. Also, a reduced number RF breakdowns was observed compared to LH1.

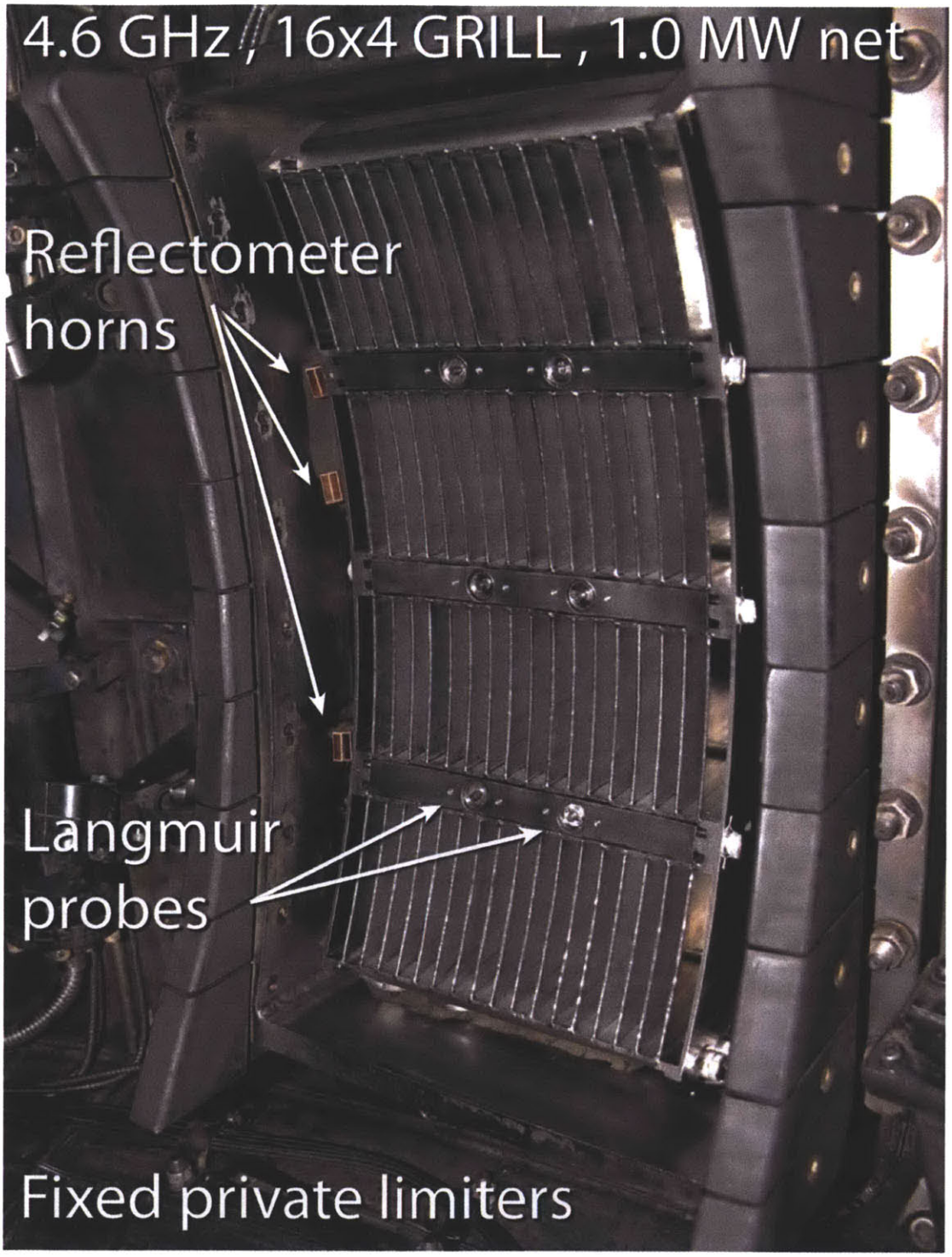

Figure 3-6: Plasma side view of the LH2 launcher installed on Alcator C-Mod. The grill is composed of 16×4 active waveguides and 8 passive waveguides on each side of the launcher. The local protection limiters can be seen surrounding launcher.

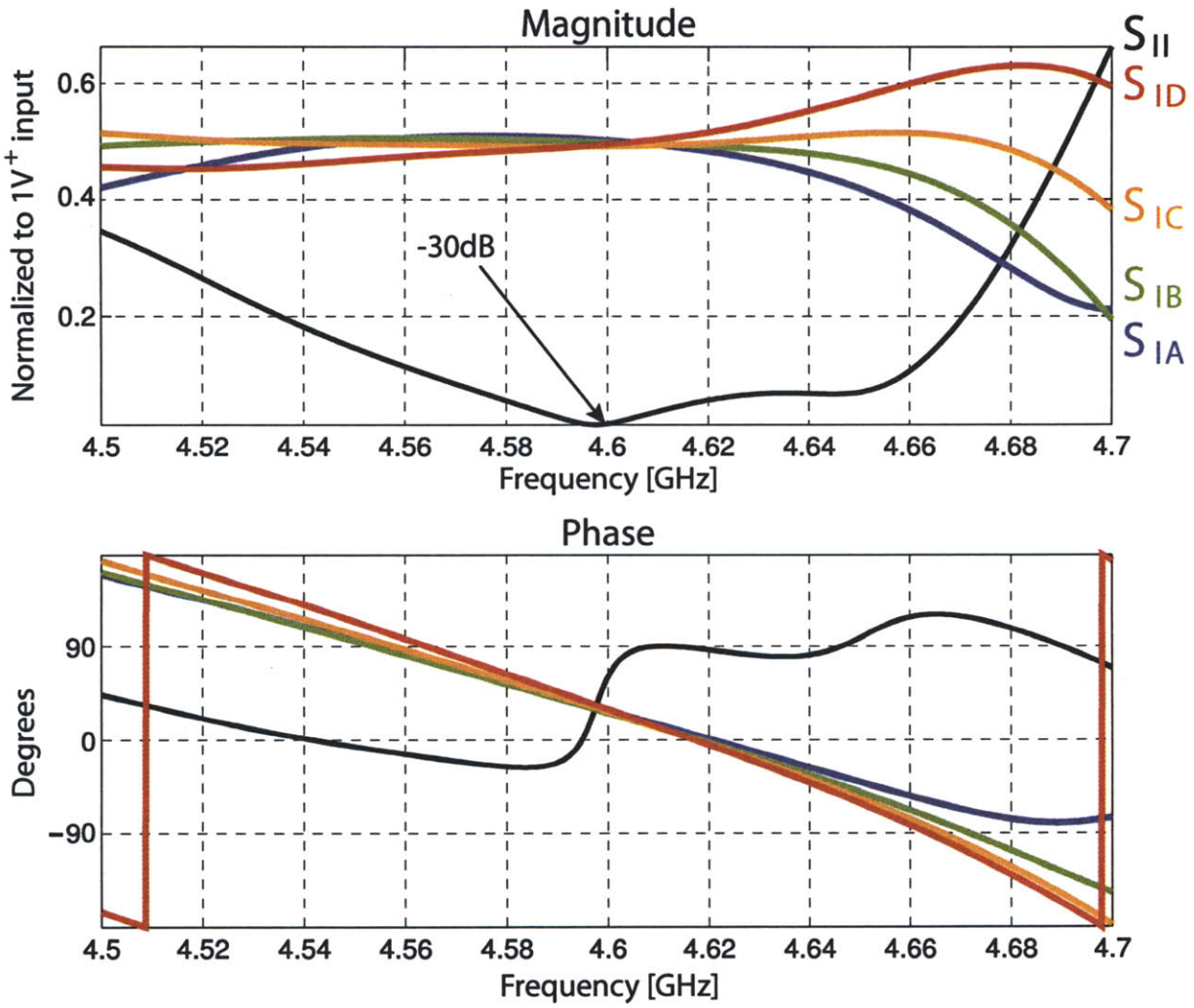

Figure 3-7: The four-way-splitter scattering parameters were optimized in MWS for equal power and phase splitting at 4.6 GHz (0.5 V^+ on each output waveguide, equivalent to 1/4 of the forward power). The transformer has been designed to minimize the reflection coefficient for the case of mathed loads at the output waveguides $|S_{\mathrm{II}}| \approx -30\ dB$.

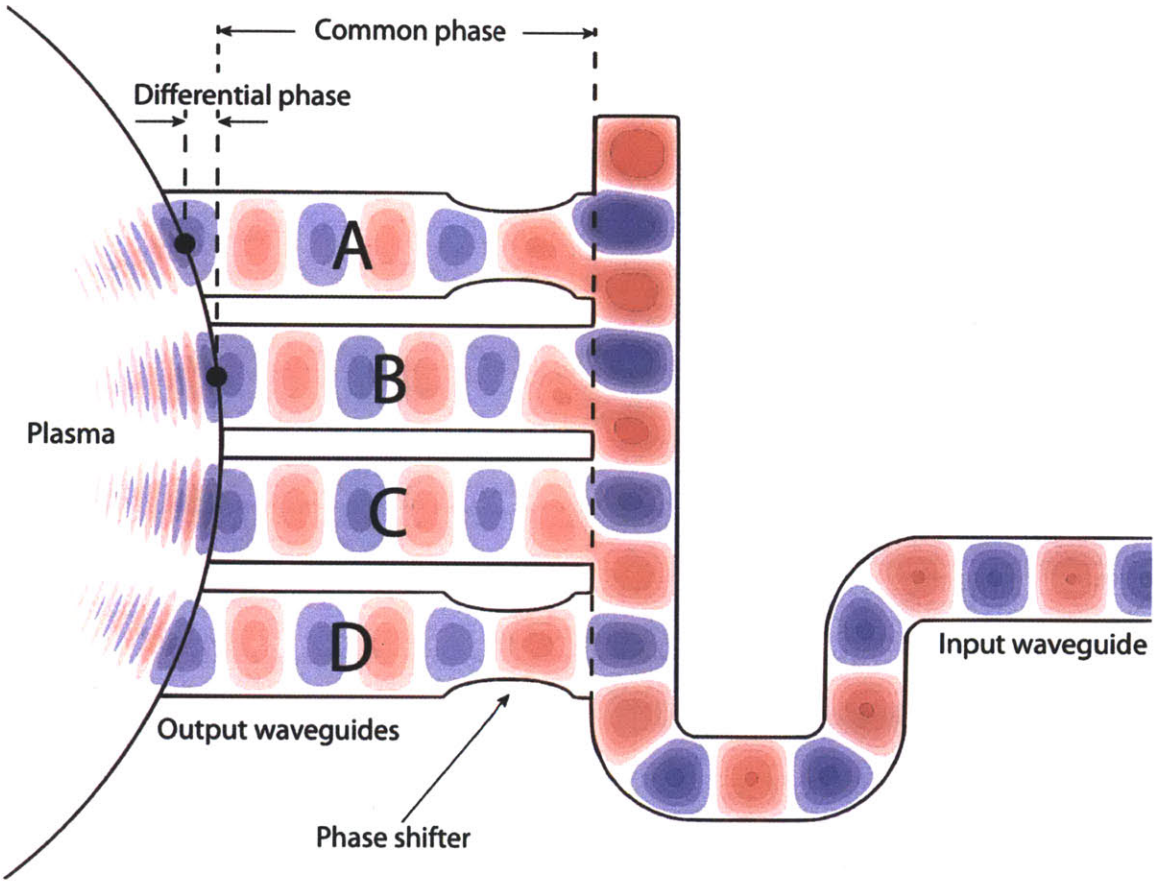

Figure 3-8: COMSOL simulation showing the wave fields inside of the four-way-splitter. RF power enters from the input waveguide and is distributed poloidally among the A, B, C, D output waveguides. Phase shifters on the A and D rows ensure zero poloidal phase difference at the grill mouth (0 differential phase).

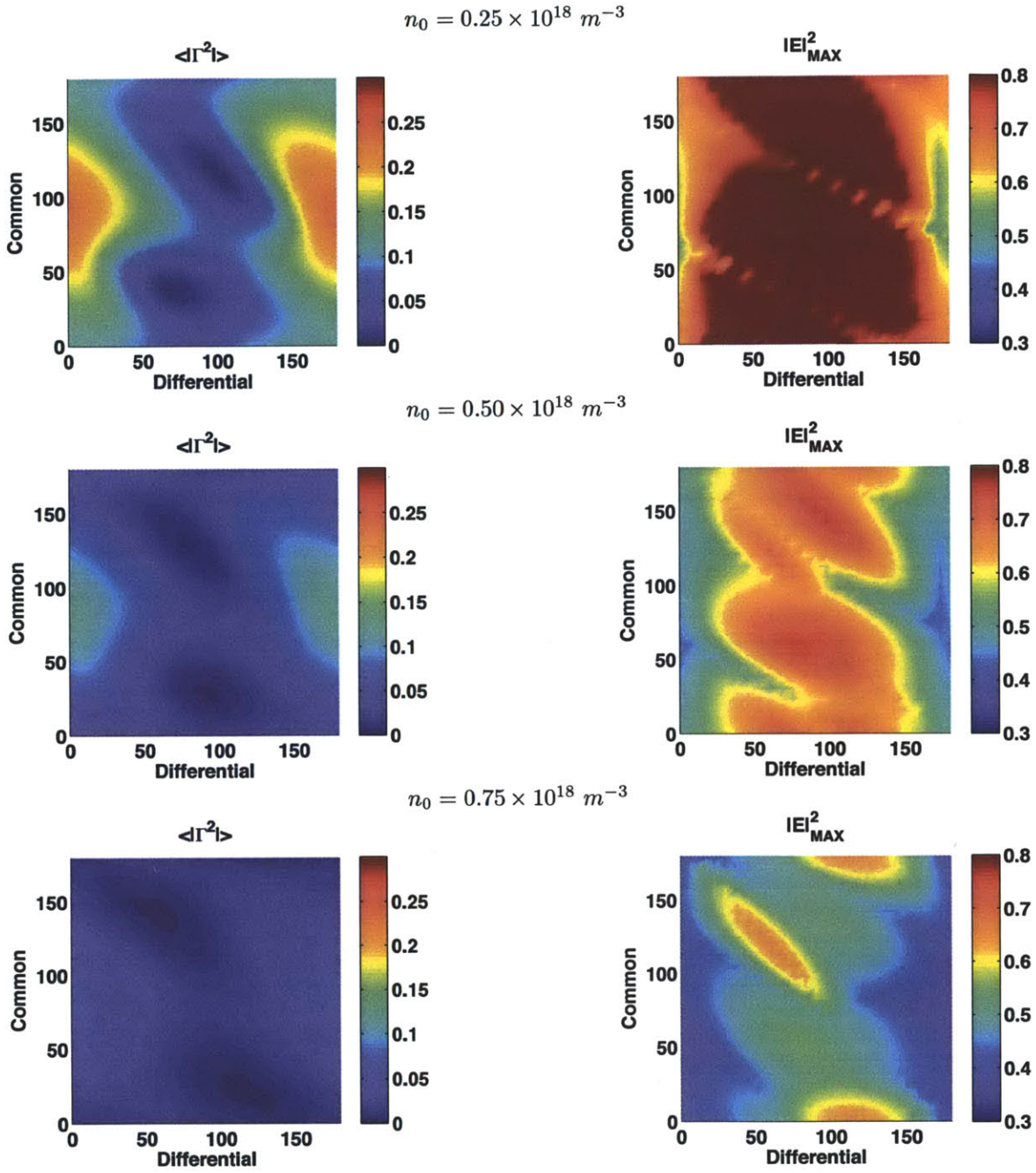

Figure 3-9: Average antenna reflection coefficient $|\Gamma|^2$ and maximum electric field $|E|^2_{\max}$ at the grill mouth as a function of the common and differential phase between the AD and BC rows. Low reflection coefficient trades off with high electric fields at the grill mouth. In this plot the LH2 antenna design is at 0 common and 0 differential phase. Plots are made for different edge plasma densities and a launched $n_\parallel$ of 1.9. At the lowest densities, high reflection coefficients are expected (see Fig. 3-10(a)) and consequently also higher fields.

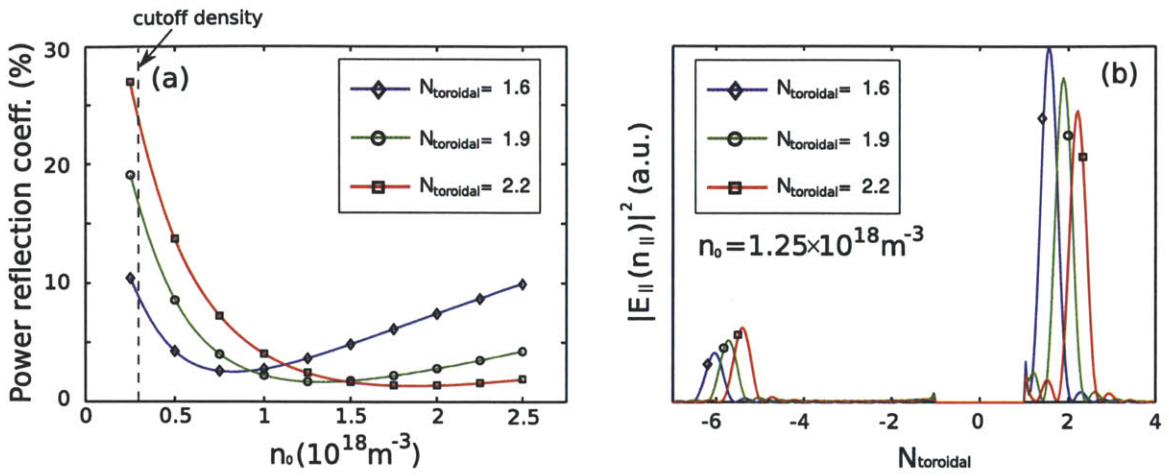

Figure 3-10: (a) The power reflection coefficient as a function of n_0, and (b) the launched spectrum, when the plasma load is uniform in the poloidal direction ($n_0 = 1.25 \times 10^{18}\ m^{-3}$).

As reported in Ref. [111, 112] simulations predicted good coupling (less than 10% reflected power) and a clean launched parallel wave spectrum over a wide range of n_0. Figure 3-10 shows the predicted reflection coefficient as a function of n_0 for different launched $n_\parallel$ and the associated $n_\parallel$ spectrum for the cases of n_0 of $1.25 \times 10^{18}\ m^{-3}$. In these simulations the density profiles in front of all four rows of launcher are assumed to be same.

However, on Alcator C-Mod the launcher has a comparable size with respect to the plasma, and in a real experimental condition, the density in front of the launcher was often observed to not be uniform in the poloidal direction. Hence the impact of having a different plasma impedance on each row of the launcher was surveyed. This effect was tested by assuming different density profiles in front of different rows. A typical case is shown in Fig 3-11. As an example of non-uniform density profile, $n_0 = 0.5 \times 10^{18}\ m^{-3}$ for top and bottom rows and $n_0 = 1.25 \times 10^{18}\ m^{-3}$ for the middle rows were used. Very little adverse effect was found on the reflection at the four-way-splitter input (Fig. 3-11(a)). The non-uniform case (blue) is in between the two uniform cases (red and green). Since the power splitting is done in the poloidal direction, the $n_\parallel$ spectrum is also not adversely affected. The major impact of the poloidal asymmetry of the density is the uneven power splitting in the poloidal direction (Fig. 3-11 (b)). In this case, more power was injected from the middle rows.

These modeling results suggested the importance of characterizing experimentally the behavior of the four-way-splitter antenna and was the major drive for the installation of the microwave probes diagnostic which is discussed in detail in Chap. 4.

3.2 Alcator C-Mod diagnostics

Alcator C-Mod is a very well diagnosed device, with a rich set of instruments measuring plasma parameters of interest [113]. In particular the line integrated average plasma density $\bar{n}_e$ is measured by a two color interferometer (TCI) system. A Thomson scattering (TS) diagnostic is used to measure both the electron density n_e and temperature T_e profile in the core plasma. The standard between-shot magnetic equilibrium reconstruction is done with EFIT [114], using only the magnetic diagnostics data. For more specialized applications, EFIT is also run with pressure contraints from kinetic diagnostics and, in a few cases, Motional Stark Effect (MSE) measurements, which constrain the pitch angle of the magnetic field line in the plasma [115]. In the following, the additional diagnostic which were involved in analyses presented in this thesis are briefly introduced.

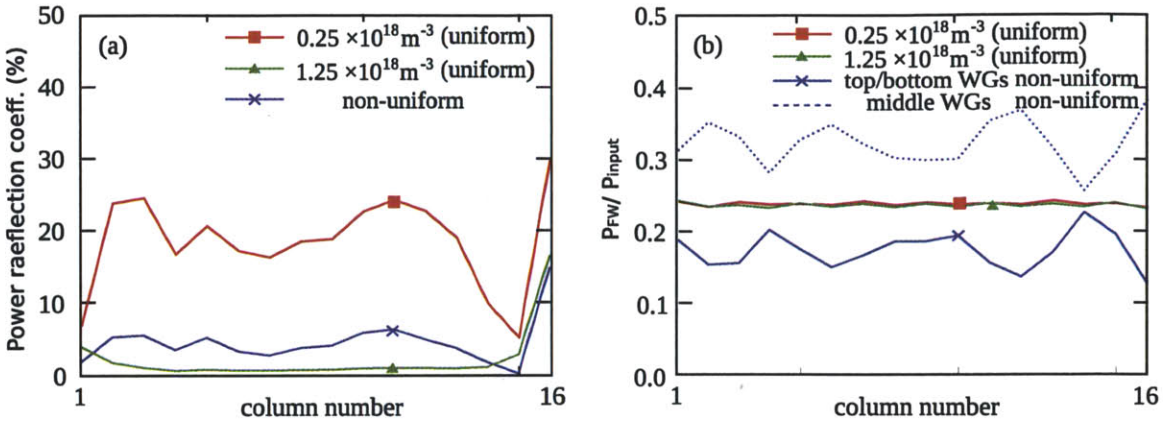

Figure 3-11: The impact of poloidal asymmetry of the density in front of the grill. The power reflection coefficient at the input port of four-way-splitter on each column (a), and the normalized forward power on rows (b). In these simulations $n_{\parallel} = 1.9$.

3.2.1 Hard X-Ray camera

This diagnostic measures the non-thermal bremsstrahlung emission in the Hard X-Ray (HXR) region (typically 40 to 200 keV) which occurs when fast electrons accelerated by LH waves via ELD interact with ions or bulk electrons and radiate. Under the assumption that the local emissivity will change in accordance with the location of the wave damping, the HXR diagnostic is the major diagnostic workhorse for LHCD discharges since it yields information about the spatial and energetic distribution of LHCD driven fast electrons [19]. Measurements can then be compared to Fokker-Planck codes which use a synthetic HXR camera diagnostic.

On Alcator C-Mod the HXR diagnostic is composed of 32 detectors arranged in a fan configuration around a pinhole which views a poloidal cross section of the plasma from a midplane horizontal port, as shown in Fig 3-12. Each channel consists of 2.0 mm thick cadmium-zinc-telluride (CdZnTe) detectors and a preamplifier and shaper convert the pulses into a digitizable form. A 1 mm aluminum vacuum window and stainless steel plates of variable thickness provide shielding for low energy photons. All electronics are mounted together in a box that is mounted inside a 1.5 in-thick lead gamma ray shield. An extensive description of the diagnostic is given in [116, 21].

The system makes use of fast digitization, which offers great flexibility for data processing and reduction. Pulses are digitized at a rate of 10 MHz for the entire shot. The raw pulse data is then analyzed for pulses (Pulse Height Analysis, or PHA) to determine the energy and time of each incident photon. This approach allows the raw pulse information to be re-binned thus allowing for photon counting statistics to be balanced against time and energy resolution. Details of an improved pulse height analysis routine are presented in detail in Appx. C. The chordal measurements for a given energy can be inverted to give the radial emissivity profile [117].

3.2.2 SOL measurements on Alcator C-Mod

On Alcator C-Mod the SOL density and temperature profiles are measured by several diagnostics. These include fixed Langmuir probes, fast-scanning Langmuir probes and reflectometer systems. Their arrangement in the Alcator C-Mod poloidal cross section is shown in Fig. 3-13.

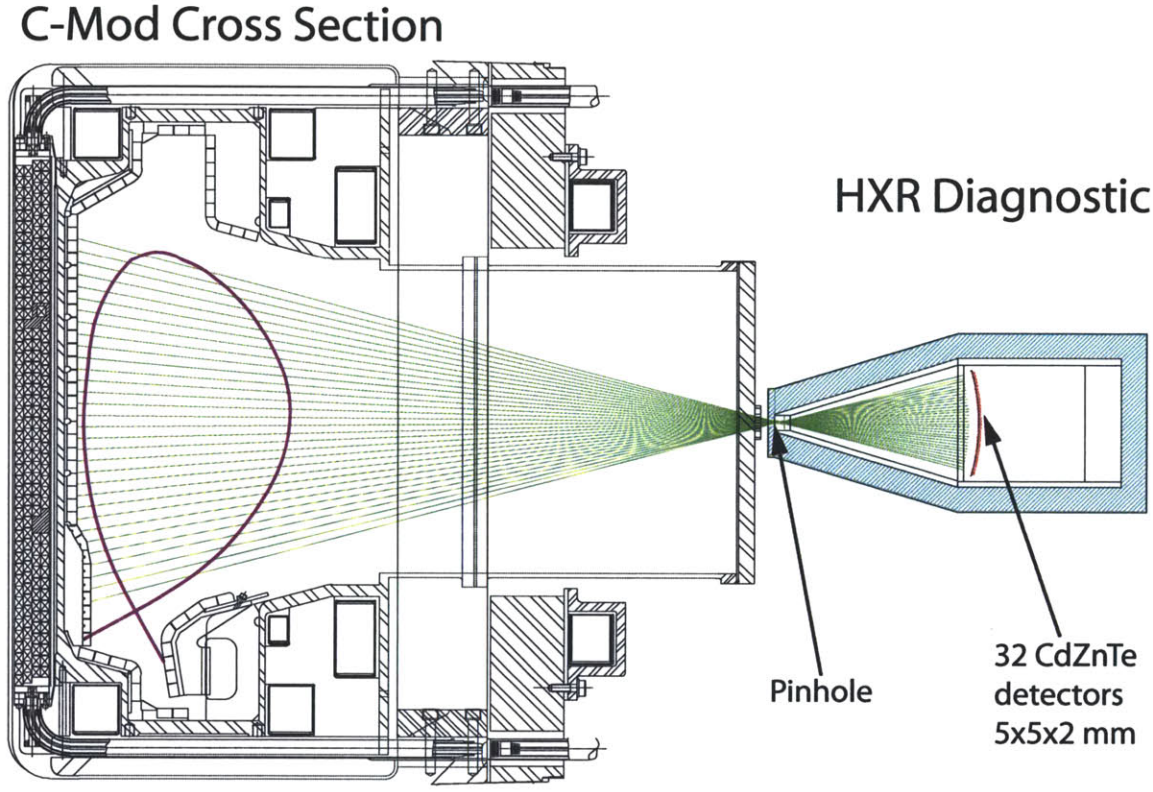

Figure 3-12: CAD drawing of the Alcator C-Mod HXR camera viewing chords geometry. The CdZnTe detectors are numbered from 1 to 32 starting from the top of the diagnostic. Figure from Ref. [21].

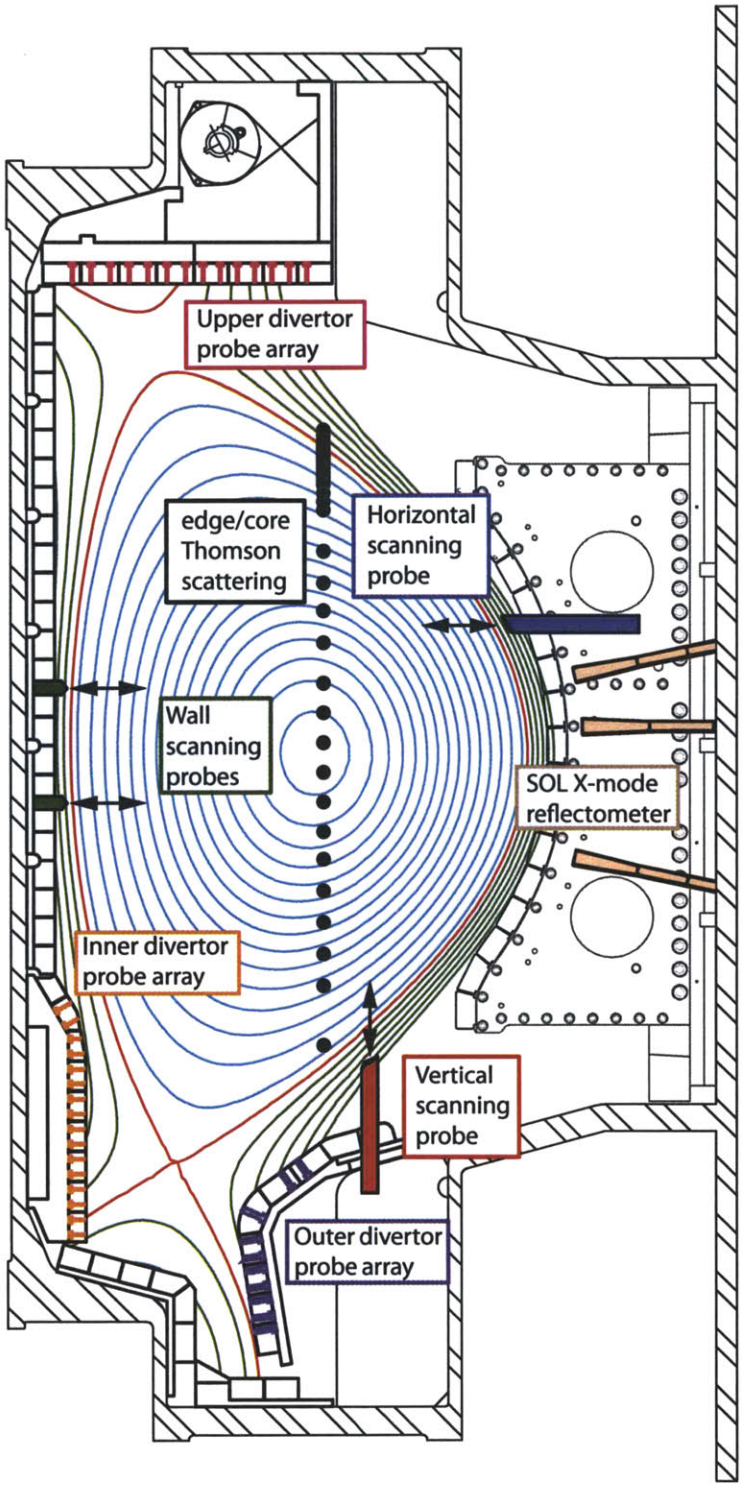

Figure 3-13: CAD drawing of the SOL diagnostics on Alcator C-Mod that are referred throughout the thesis.

Reciprocating Langmuir probes

There are two scanning probes that can be plunged into the plasma up to the last closed flux surface. The A-port scanning probe (ASP) extends horizontally 11 cm above the midplane on A horizontal port in a location that is not magnetically connected to the LH antenna at C-port. The F-port scanning probe (FSP) extends vertically from the F bottom vertical port. In addition, inner-wall scanning probes embedded in a C-Mod inner-wall tile module, allow profile measurements on the high field side. All of these probes support multiple electrodes and can scan three times per shot to a pre-specified depth. The details about the design and operation of the scanning probes can be found in Ref. [118] and [119].

Divertor Langmuir probes

A rich set of forty Langmuir probes is embedded in Alcator C-Mod in the lower-inner, lower-outer and upper divertor tiles. These probes consist of ceramic-coated Mo or W pins which are operated with swept voltage waveforms allowing the measurement of electron temperature and density, and floating potential. This allows us to measure divertor profiles in both lower-null (LN) and upper-null (UN) magnetic topologies. Each of the three embedded probe arrays is arranged to provide radial SOL profiles which can be compared with profiles provided by the scanning probes.

Lower hybrid Langmuir probes

A total of six Langmuir probes are installed on the front of the LH grill, in between the rows of waveguides which compose the grill. As shown in Fig. 3-6, these probes are arranged in three pairs, each at a different poloidal height. Most of the time these probes are operated with swept voltage waveforms allowing the measurement of electron temperature and density, but occasionally they are run with a DC negative voltage to measure the ion saturation current. In each pair of the probes pins have different lengths (~ 1 mm and ~ 2 mm) in order to estimate the profiles scale length in front of the launcher in addition to the point measurements. Measurements using the X-Mode SOL reflectometer have shown that a more reliable way of estimating the density gradient at the grill mouth is to linearly interpolate the density measured by either Langmuir probes to the edge-most point of the Thomson scattering system.

X-Mode SOL reflectometer

Reflectometry has been widely used to measure density profiles and fluctuations in fusion machines. In reflectometry, millimeter waves are launched toward the plasma and reflected at the cutoff layers. By comparing the signal amplitude and phase of the reflected waves with those of the launched waves, density profiles, fluctuation levels, and turbulence correlation lengths can be determined.

Alcator C-Mod has been recently equipped with a swept-frequency X-mode reflectometer to measure the scrape-off layer density profiles at the top, middle, and bottom locations in front of the LH2 launcher. This diagnostic was not available for LH1 launcher. Additional reflectometer horns are planned to be installed adjacent to the new ICRF rotated antenna.

The system operates between 100 and 146 GHz at sweep rates from 0.01 ms to 1 ms, and will cover a density range of approximately 10^{16} to 10^{20} m^{-3} at $B_0 \sim 5$ T. As discussed in Sec. 1.1.3, the propagation of X-mode waves in a plasma depends the magnitude of the static magnetic field. Errors on the order of 0.1% in the magnetic equilibrium from EFIT can easily result in radial shifts in the reconstructed density profiles of the order of millimeters. To constrain the reflectometer density profiles at the edge, the measurements from the Langmuir probes are used. This minimizes reflectometer radial error bars to $\sim mm$ scale and is the largest uncertainty of this measurement. The same consistent assumption is done for all measurements taken by this diagnostic. More details about the diagnostic and the profile inversion technique can be found in Ref. [7, 8].

Chapter 4

Microwave probe diagnostic

Poloidal variations of edge density are predicted to affect the evenness of the poloidal power splitting, suggesting the necessity of the forward and reflected power measurements at each row of the launcher. For this reason, a new antenna diagnostic based on the microwave probe concept [6] has been installed on the four-way-splitter launcher. This diagnostic is composed of a set of 32 microwave probes that nonperturbatively monitor the forward and reflected power in a carefully selected set of waveguides composing the grill. The probes are installed in pairs in 15 of the 64 active waveguides which compose the LH grill and by themselves in 2 of the 8 passive waveguides on the sides of the grill. The phase and amplitude of the signal coming from each probe is measured with off-the-shelf homodyne I/Q detectors and subsequently digitized at 250 KHz. A novel approach for calibrating the diagnostic and the four-way-splitter antenna has been developed.

4.1 Description of the microwave probe diagnostic

In each of the monitored grill waveguides, two probes displaced by one quarter of the guided wavelength λ_g sense the total wave field (both amplitude and phase) in the waveguide (Fig. 4-1). Since the location of each probe is known, the amplitude and phase measurements of the total wave field at the probes location can be then deconvolved, and the amplitude and phase of the forward and reflected waves deduced. In the following we will use the network analyzer convention $\exp(i(-k\,x-\omega\,t))$ [1] and will indicate with a subscript F (*forward*) the probes which are closest to the plasma and a subscript R (*rear*) to denote the probes which are closest the the vacuum windows.

The measured total field at the probe locations are:

$$\begin{aligned} E_F &= E_+ e^{-ik\Delta} + E_- e^{ik\Delta} \\ E_R &= E_+ + E_- \end{aligned} \tag{4.1}$$

where k is the axial wave-vector of the TE_{10} mode. By solving this system of equations, the forward and reflected waves traveling inside of each waveguide can be expressed as a linear combination of the total fields:

$$\begin{aligned} E_+ &= \frac{E_R + iE_F}{2} \\ E_- &= \frac{E_R - iE_F}{2} \end{aligned} \tag{4.2}$$

where the distance $\Delta = \lambda_g = \pi/(2k)$ is chosen to maximize the signal to noise ratio. In a similar

[1] The choice of this sign convention is such that the wave propagation for positive ω takes place in the $-k$ direction.

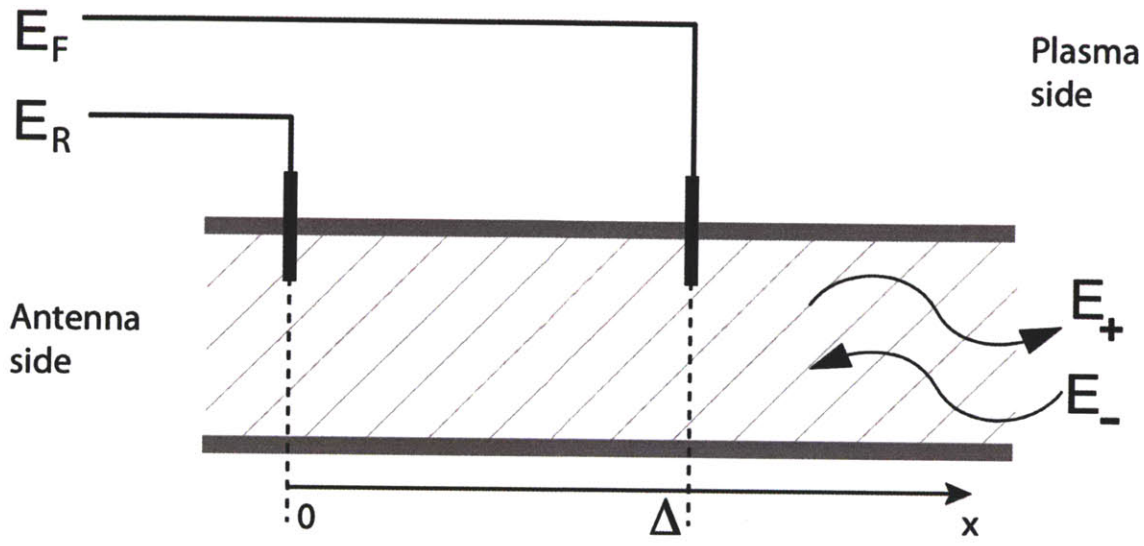

Figure 4-1: Schematic depicting the incident and reflected wave measurement setup in the grill waveguides.

way, passive waveguides can be monitored by a single probe located at $\lambda_g/4$ from the short at the end of the waveguides. In this case we can use the same exact equations but set $E_R = 0$, which corresponds to a reflection coefficient of 100%.

In Alcator the grill waveguides are named using letters (A,B,C,D) for the rows and numbers for the columns (1 to 16). On the LH2 15 of the 64 active waveguides have probes installed, as schematically shown in Fig. 4-2. The probes are arranged to measure the waves in the two centermost columns and on every other waveguide of the bottom row of grill. This arrangement scheme was chosen to maximize the flexibility of the system.

The microwave probe system can be macroscopically split into two parts: the *probe assembly* and the *I/Q detector assembly.*

4.1.1 Probe assembly

Microwaves are coupled to the probe through a small circular coupling hole located on the narrow side of the waveguides. The probe itself is a stainless steel field-replaceable SMA with Teflon dielectric. The central conductor of the probe is a stainless steel step wire and is connected (tack welded) to the opposite side of the probe housing by forming a small electrical loop (*current loop probe*). An EMI gasket seals the interface between the probe and its housing and ensures low pickup noise. Figure 4-3 shows the individual components of a probe assembly, an assembled probe and a probe installed in a waveguide housing.

The resulting current loop probe samples the H_z field of the fundamental TE_{10} mode, where the coordinate system is rotated such that the long side of the waveguide opening is aligned along $\hat{x}$ and the short one along $\hat{y}$. Microwaves are coupled to the probes through a small circular coupling hole located on the narrow side of the waveguides, where the H_z field is maximum. The H_z field is proportional to the E_y field, which is what we are ultimately interested in. Following the notation from Ref. [110]:

$$H_z = H_0 \cos\left(\frac{\pi x}{a}\right) e^{i(\omega t - kz)} \tag{4.3}$$

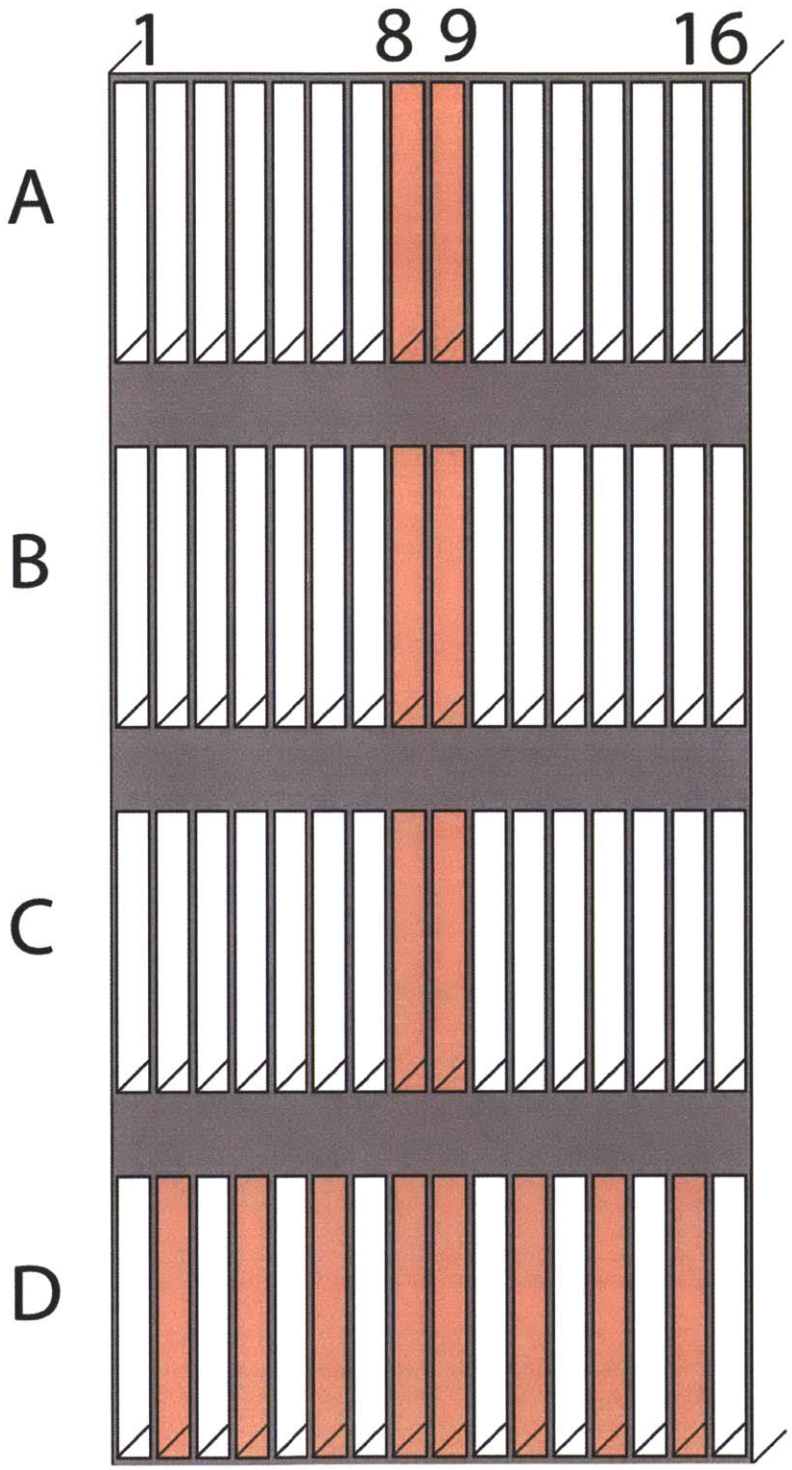

Figure 4-2: The waveguides monitored by the microwave probes diagnostic are highlighted in red.

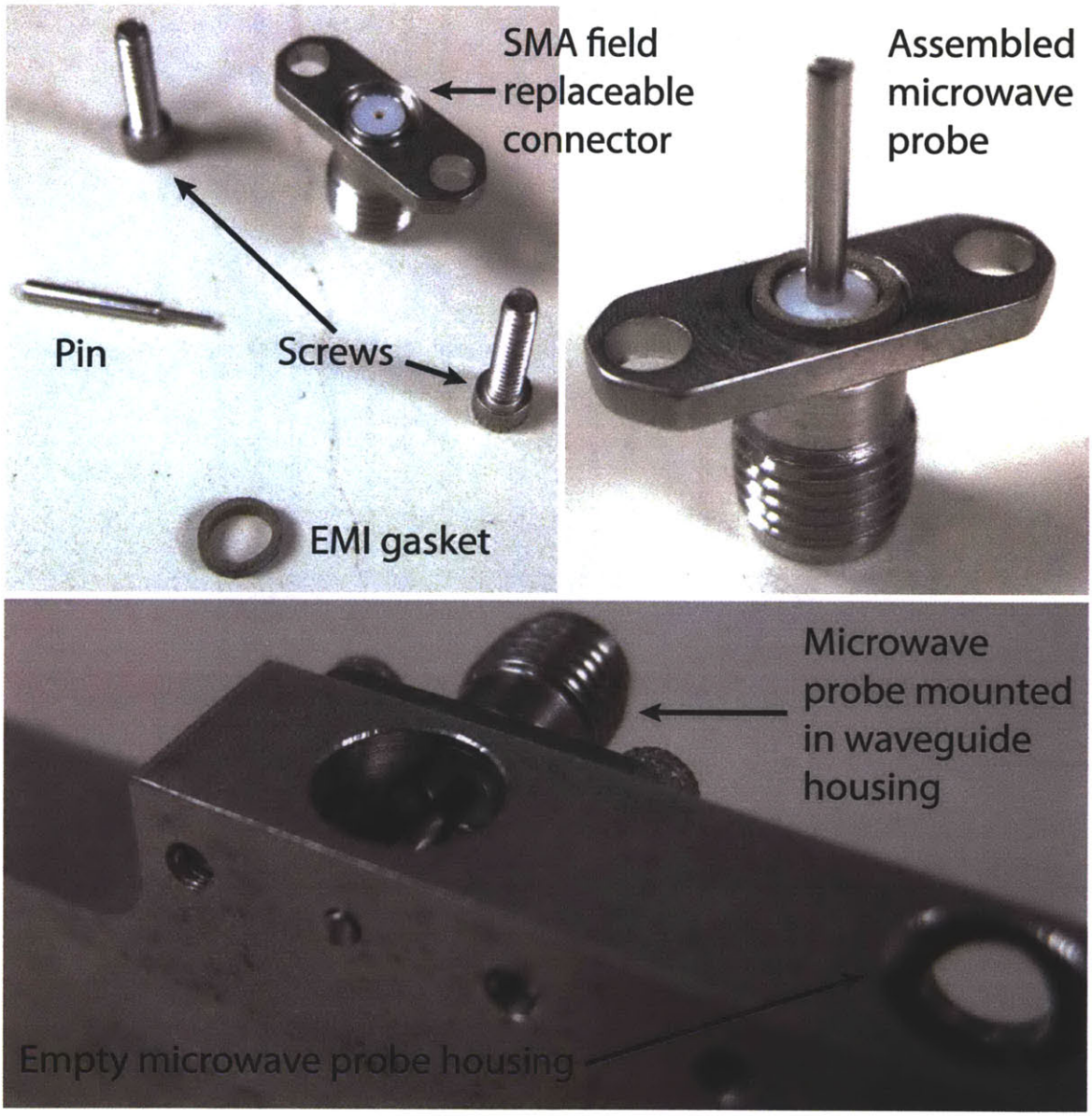

Figure 4-3: Clockwise: components of the probe assembly (SMA field replaceable connector, pin, EMI gasket and screws); assembled microwave probe; microwave probe mounted in waveguide housing and empty microwave housing.

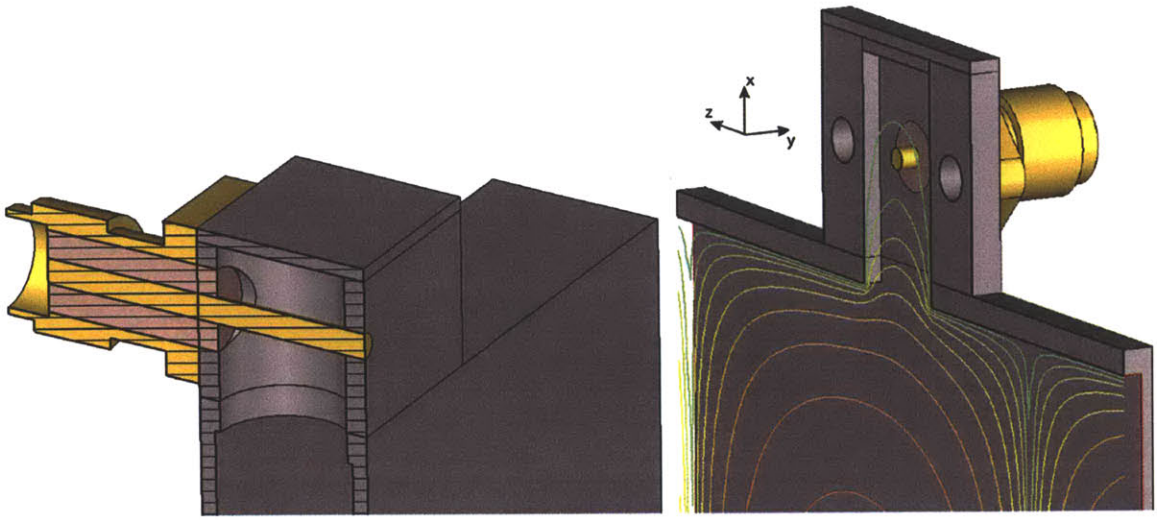

Figure 4-4: Cross section of the probe assembly and simulation in CST Microwave Studio, showing the contour plot of the magnetic field H_z as it leaks through the coupling hole and is picked up by the loop probe.

$$E_y = E_0 \sin\left(\frac{\pi x}{a}\right) e^{i(\omega t - kz)} = -i\omega\mu_0 \frac{a}{\pi} H_0 \sin\left(\frac{\pi x}{a}\right) e^{i(\omega t - kz)} \tag{4.4}$$

This design has proven to be robust, reproducible and in agreement with the simulations which were done at the design stage using CST Microwave Studio (Fig. 4-4). The measured coupling coefficient is $\approx -65 \pm 2\ dB$.

In each waveguide, the probe housing is located at a minimum distance of 2 cm from both the alumina vacuum window and the grill mouth. Such distance is enough to ensure that the higher order evanescent modes which are excited at the grill mouth are not picked up by the probes. Modal analysis using ALOHA [94] show that the highly evanescent TM modes are the ones which are primarily excited at the grill mouth and their effect becomes negligible within few centimeters off the discontinuity.

Silicon-Dioxide (SiO_2) cables $0.142''$ in diameter (see Fig. 4-6) are used in-vessel to connect the probe assembly to the vacuum feedthroughs located in the back of the launcher. The connection scheme at the vacuum feedthroughs is reported in Fig. 4-7. This type of cable is vacuum compatible and ensures low losses and excellent phase stability with respect to temperature variations. Once on the air side, the cables are made of expanded polyethylene for dielectric, which also has better phase stability with temperature than teflon. In general, all cables coming from a pair of probes installed on the same waveguide are kept in close proximity to one another, so to minimize effects of temperature variations on the measurements.

4.1.2 I/Q detector assembly and signal digitization

The phase and amplitude of each probe signal is then finally measured with off-the-shelf homodyne I/Q detectors and are digitized at 250 KHz. Orion Microwave integrated circuit allows I/Q detection in the 3 GHz to 6 GHz frequency range, with IF ranging from DC to 300 MHz. For our application the RF signal is the one coming from the probes, the LO signal is taken from the 4.6 GHz master oscillator which drives the Klystrons.

Before entering the RF port of the I/Q detectors, the signal coming from each probe is filtered and attenuated, as shown in Fig. 4-8. The output I and Q signals of each I/Q detector (for a total

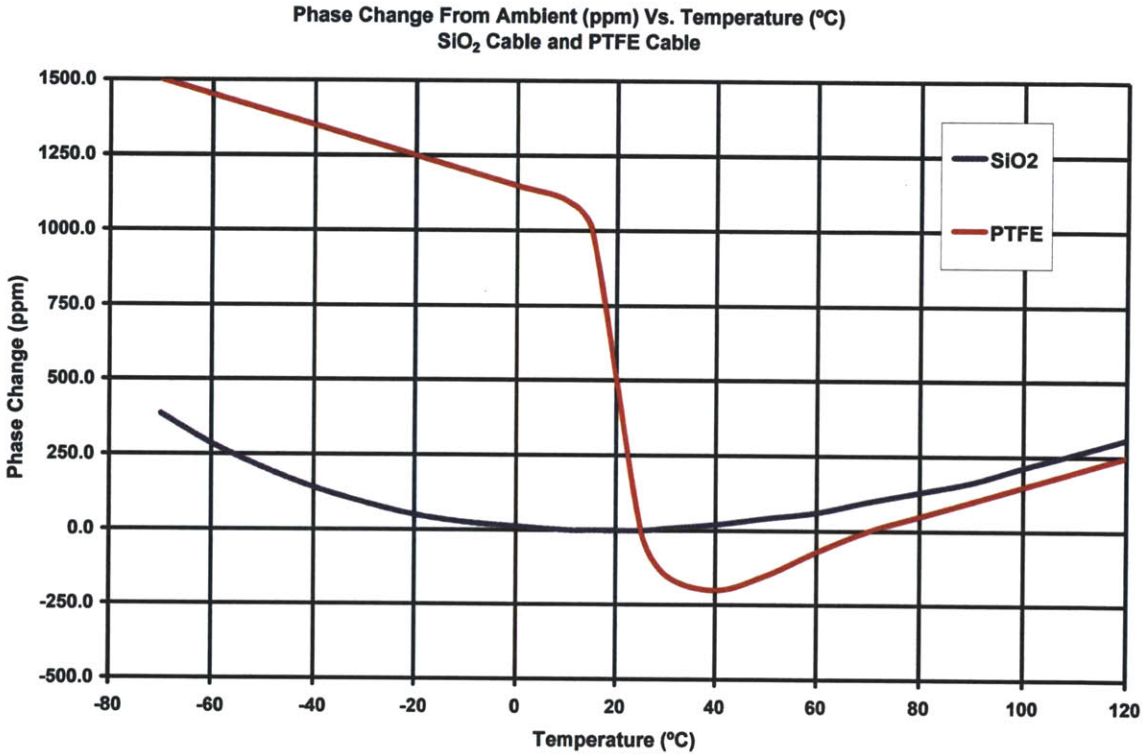

Figure 4-5: Phase change from variations off the ambient temperature of 25 $°C$ for the SiO_2 and the teflon (PTFE) 0.142″ diameter cables at 2 GHz. The strong phase response to temperature variations of the latter material was of concern for invessel installation, where high temperature gradients can be expected ($< 25\ °C$ in the cryostat region and $> 25\ °C$ in the vicinity of the plasma). Figure courtesy of www.stablecables.com.

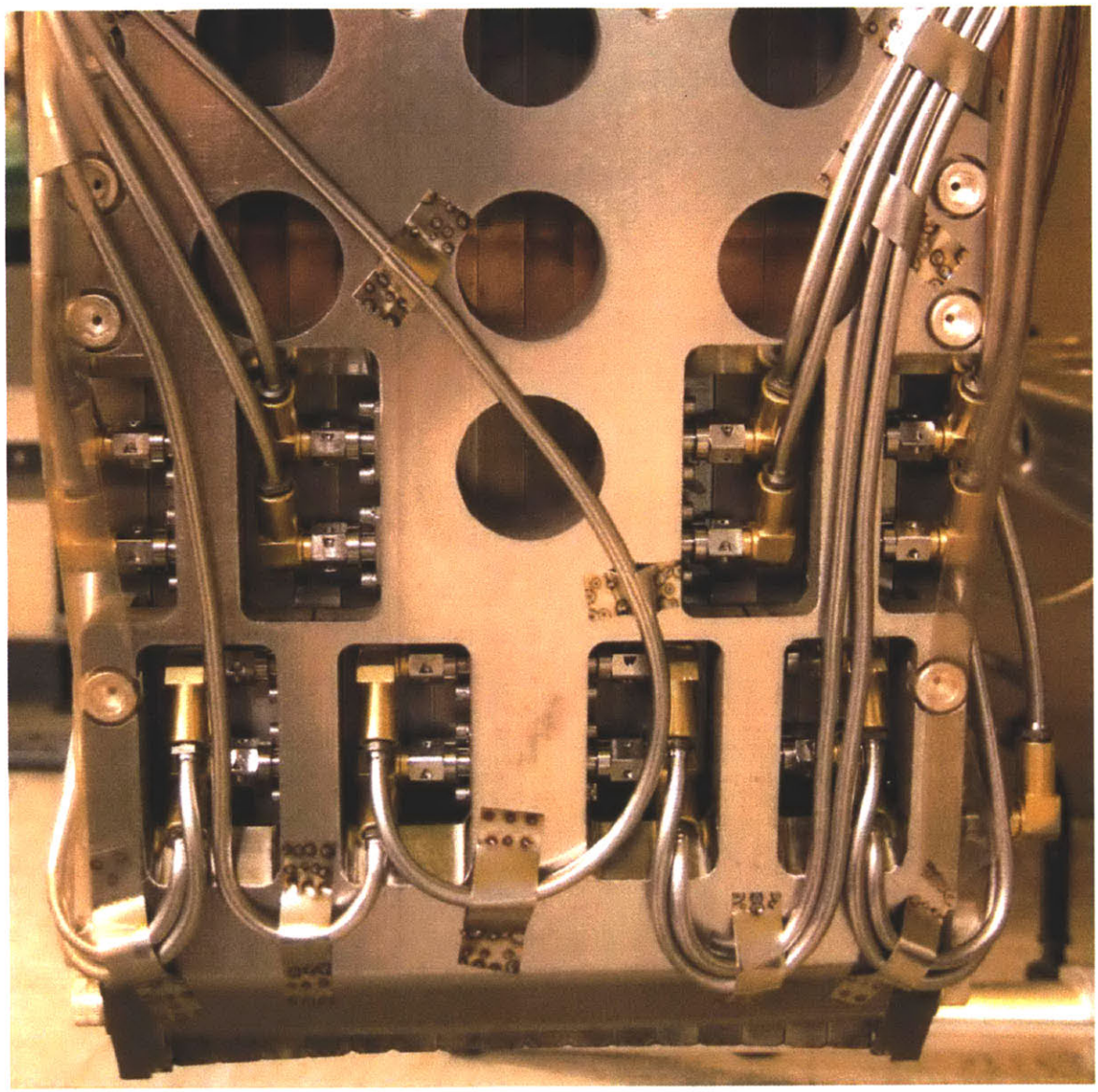

Figure 4-6: Bottom view of the LH2 launcher, where most of the probes are installed. The SiO_2 cables at the bottom of the launcher connect to the microwave probes with a right-angle SMA type connection. The SiO_2 cables are held in place by small pieces of shim-stock which are tack-welded to the launcher.

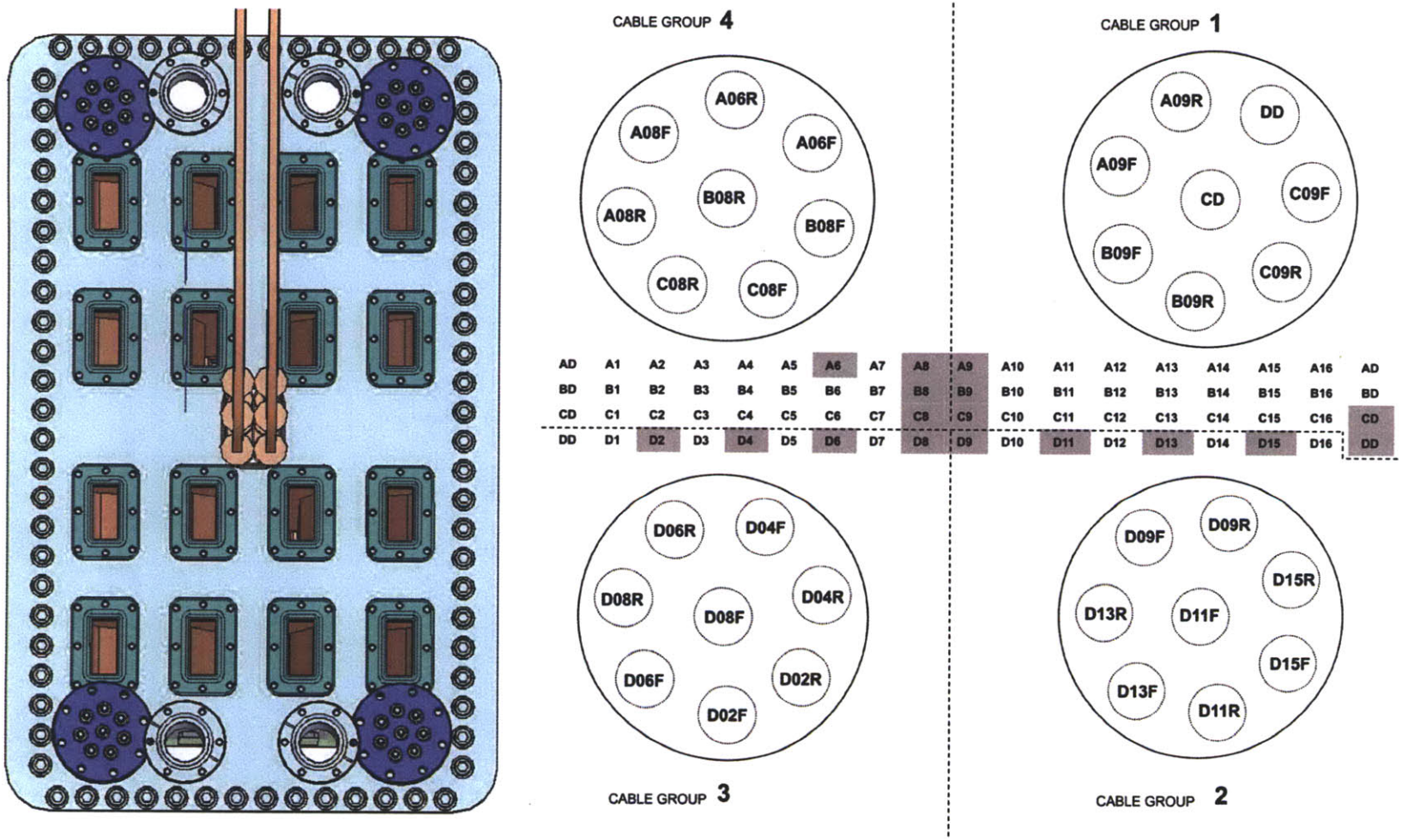

Figure 4-7: On the left is a CAD view of the LH antenna backplate, showing the 16 WR-187 waveguides which feed the 4-way-splitters, four flanges with 8 SMA vacuum feedthroughs for the microwave probes (at the plates corners) and the 6 reflectometer waveguides which are connected to the respective feedthroughs at the center of the plate. On the right is the LH microwave probe vacuum feedthrough arrangement as seen from the air-side.

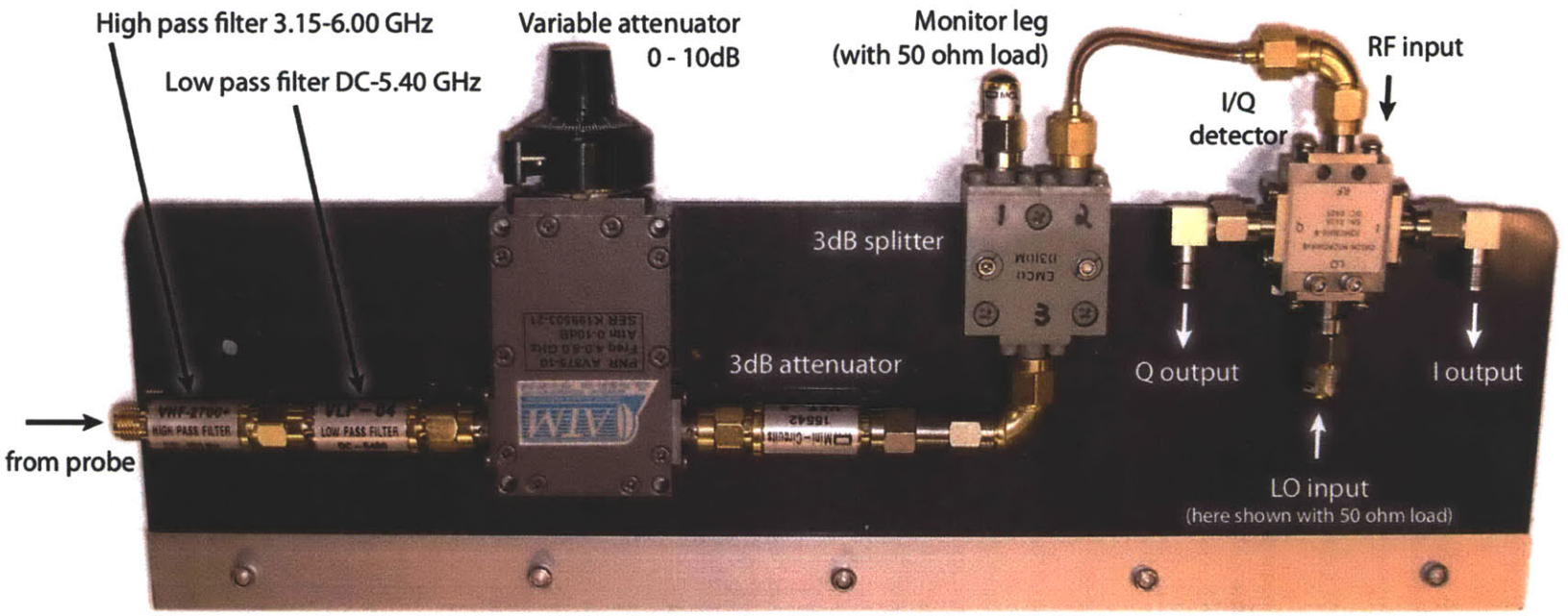

Figure 4-8: One of the 32 microwave boards which filters and attenuates the 4.6 GHz signal coming from a mictowave probe, before feeding it to the off-the-shelf homodyne I/Q detector.

of 64 channels) is then amplified and buffered before being digitized (12 bit, 100 kHz). Figures 4-9 and 4-10 show the electronic circuit schematic and a printed circuit board featuring 16 channels. The microwave components and the electronics for the microwave probe diagnostic are hosted in a metal box which is connected to the side of the launcher, shown in Fig. 4-11. The calibration of the microwave system is done on the signals measured by the digitizers.

4.2 Microwave probes and antenna calibration procedure

The calibration of the microwave probe system has been done in two stages. First we calibrated the (passive) in-vessel components (probe assembly, SiO_2 cables, feedthrough). Second we calibrated for the I/Q detector assembly (I/Q detectors, LO amplifiers, attenuators, filters, DC breaks). The calibration of the whole launcher is done by using the same components which were designed for the calibration of the in-vessel components of the system. An remote calibration procedure has also been developed.

4.2.1 In-vessel components

The calibration of the in-vessel components is done by inserting a matched load in each of the fingers of the four-way-splitter and measuring the signal (incident wave) from each of the probes of the splitter. For the calibration of the launcher, waveguide loads are made of a radiation absorbent material and they are machined in the shape of a wedge. However, this shape can not be used for the microwave probes calibration, since the presence of the long wedge perturbs the fields at the probe location. Hence, a new matched load was designed using COMSOL Multiphysics. The new load, which is commonly referred to as the *Obsorber* (Fig. 4-12), features piramidal shapes which have been inspired by anechoic chamber designs and has been proven to be very effective at ensuring low reflections (-30 dB designed, -27 dB measured) while filling only the first section (≈ 2 cm) of the reduced waveguide composing the grill. This load is made by water-jet cut of solid ECCOSORB 117 sheets (a radiation absorbent material) which have been subsequently grind by hand so to obtain the pyramidal shape.

An absolute calibration of the probes was obtained by measuring the amplitude and phase of the incident wave in each of the reduced waveguides. For this purpose, a reduced waveguide to WR187 adaptor was designed using CST Microwave Studio. This adaptor, commonly referred to as the *Odaptor* (Fig. 4-13), is designed to present a low insertion loss (-30 dB) at 4.6 GHz. The final component has been Electrical Discharge Machined (EDM) to ensure a perfect fit when the component is inserted in the reduced waveguides which form the curved grill of the launcher.

A phase reference plane common to all probes was set by using a fixture which forces the adaptor to be inserted always at the same depth. The four legs of the fixture are designed to slide in the passive waveguides and expand as the screws are tightened. This fixture, is commonly referred to as the *Oframe* (see Figs. 4-14 and 4-15).

4.2.2 I/Q detectors calibration

The calibration of the I/Q detector assembly consists of a back-mapping procedure, which allows to compensate for non-linear effects of the I/Q detector assembly (e.g. DC offsets, I/Q gain balance, saturation, etc.). Such procedure requires measuring the amplitude and phase output for a broad set of known amplitude and phase input signals, possibly covering the whole signals dynamic range that will be encountered during operation. Worth pointing out is that knowledge of the input signal requires the calibration of the measurement setup itself, which is commonly referred to as the "*drive leg*". The calibration of the I/Q detectors has been done in two independent ways, for ensuring redundancy and the best possible measurement accuracy.

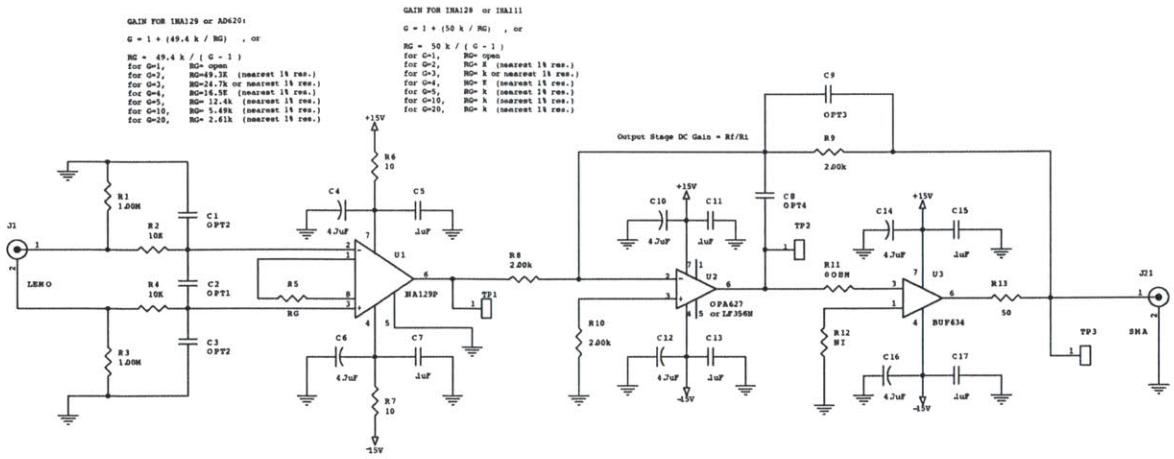

Figure 4-9: Circuit schematic of the amplifier/buffer of a microwave probe channel.

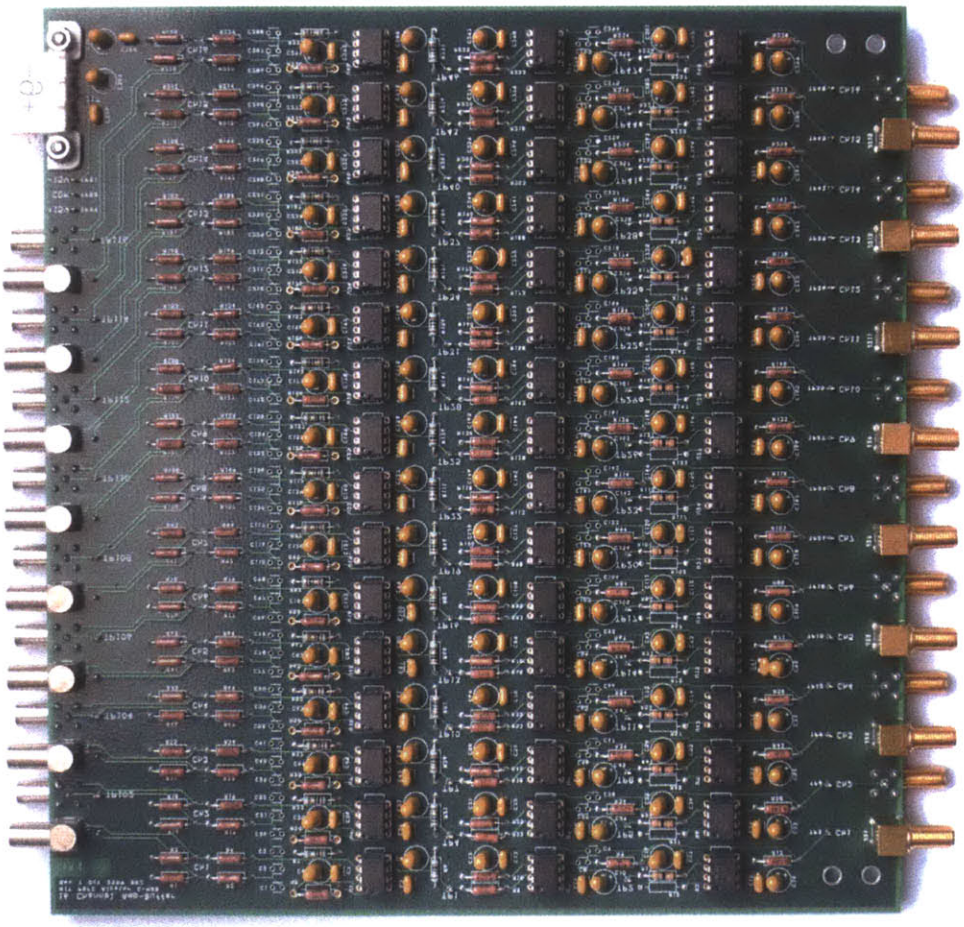

Figure 4-10: One of the four 16 channel amplifier/buffer printed circuit boards. The LEMO connectors for the IF signal coming from the I/Q detectors are located on the left of the figure, while the SMA connectors for the amplified signal going to the digitizers are on the right.

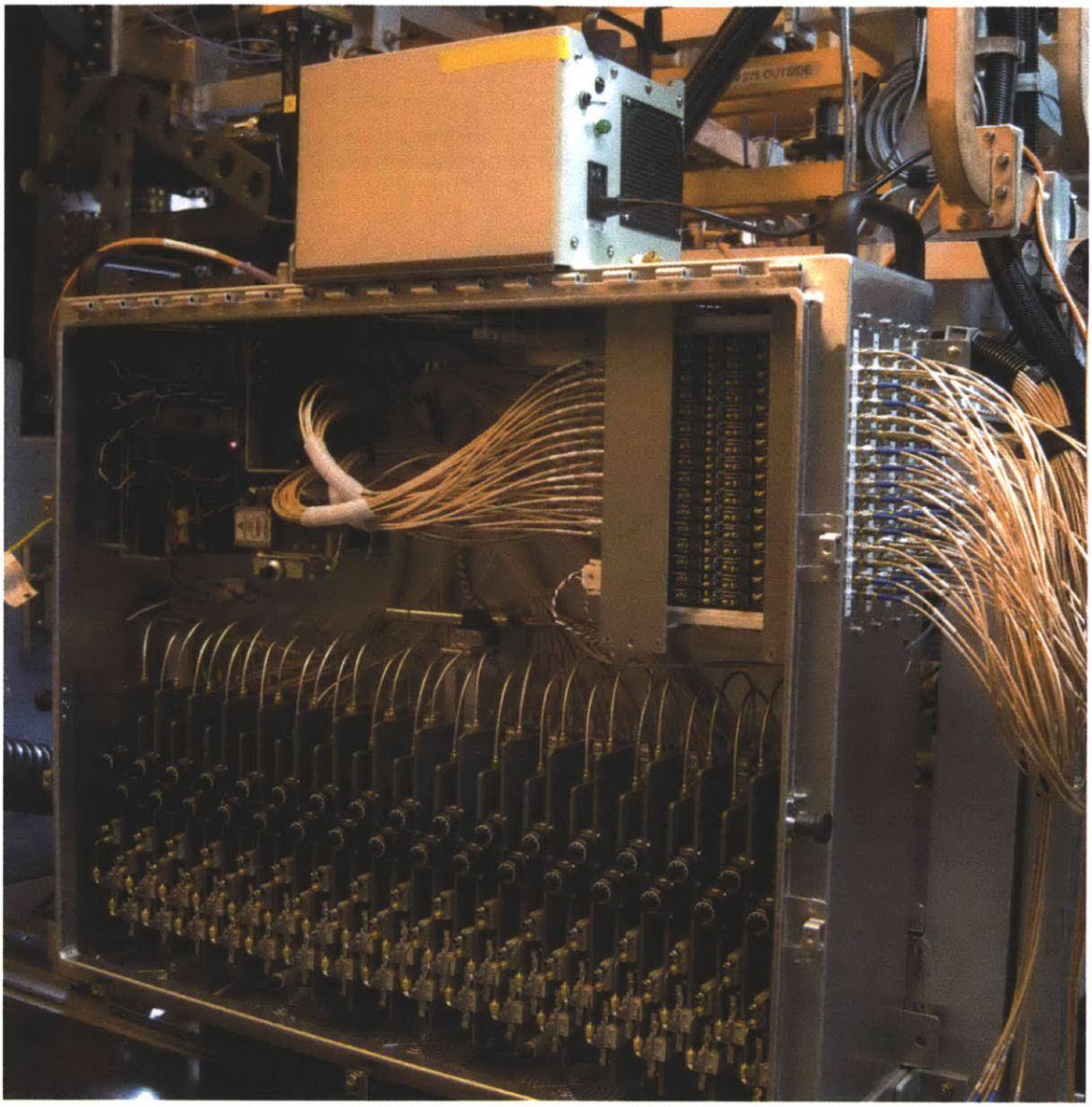

Figure 4-11: The microwave components and electronics for 32 microwave probe channels are hosted in a metal box which is connected to the laucher support structure. Also located in the box, is the LO amplifier and its splitting network.

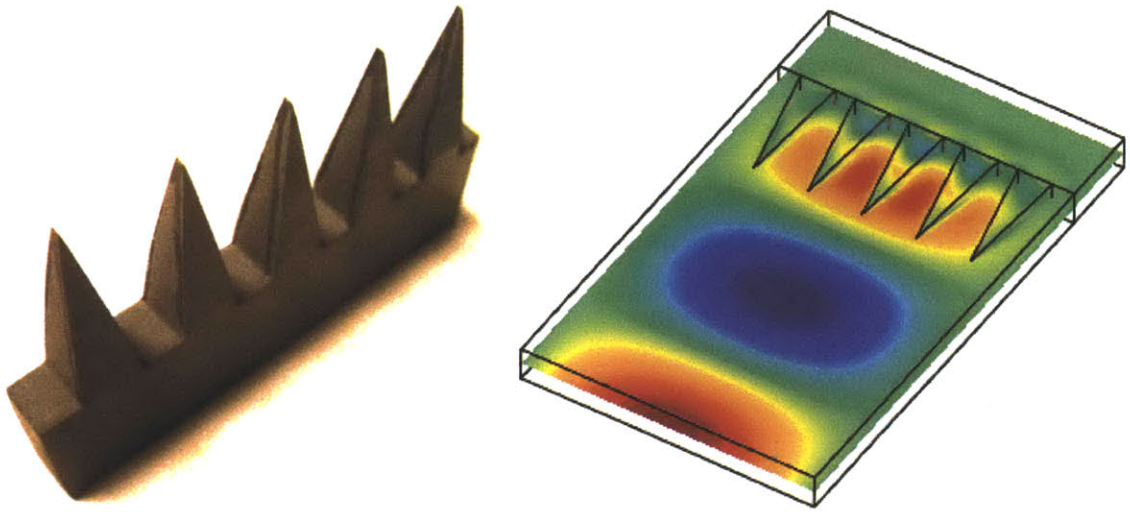

Figure 4-12: The *Obsorber* and COMSOL Multiphysics simulation showing how $\Re\{E_y\}$ decays inside of the conic absorbing structure.

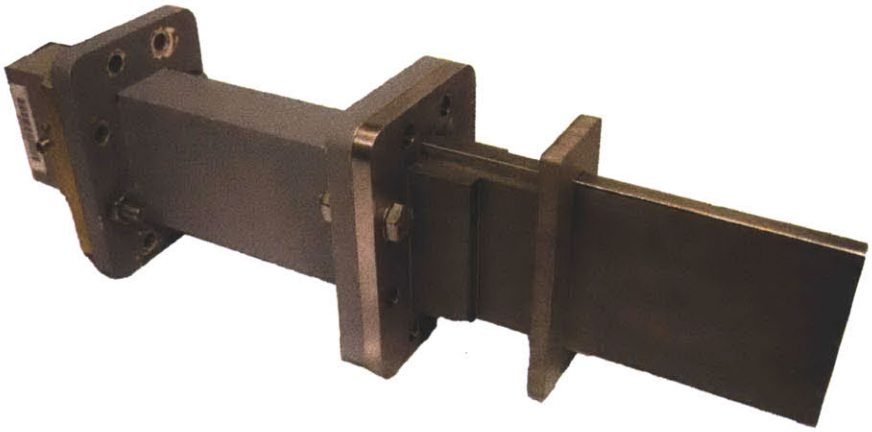

Figure 4-13: The *Odaptor* allows a transition from a reduced waveguide to a standard WR187 waveguide with low insertion loss.

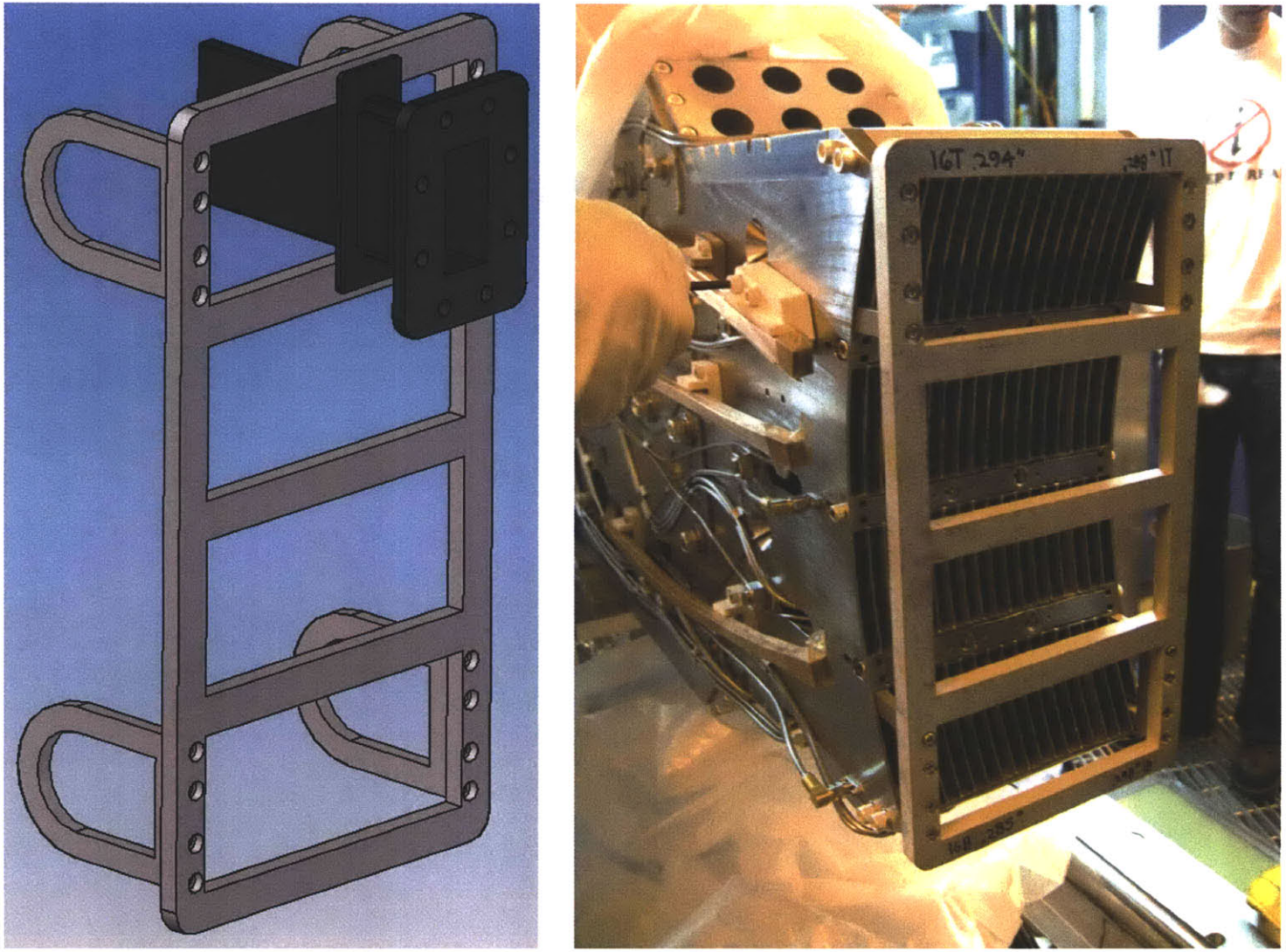

Figure 4-14: On the left, CAD drawing of the *Oframe* which is used to set the reference plane for the phase measurements on the launcher. Shown in black is also the *Odaptor*, as it would be used in combination with the fixture. On the right, the fixture once is installed on the launcher.

Figure 4-15: In this picture, the *Oframe* and the *Odaptor* in place, during an in-vessel calibration, at the end of the 2010/2011 campaign. While the amplitude and phase are measured by means of the *Odaptor*, wedge loads are inserted in the other waveguides.

The first method involves the use of vector modulators to scan the amplitude and phase of the RF signal in raster and recording the corresponding IF signals. Vector modulators work by adding known phase shift and amplitude modulation to the LO signal. The use of vector modulators is convenient because they can be digitally programmed to allow an absolute calibration of each channel. However, these components are known to become inaccurate at low power levels and impose the drive leg to be non-linearly characterized both in amplidute and phase, thus adding complexity to the calibration procedure.

An alternative calibration scheme that does not require the use of vector modulators was developed to overcome their numerous limitations. This calibration setup is depicted in Fig. 4-16 and relies on the use of a 4.6 GHz generator for the RF input which is different from the one used for the LO. Since the frequency of the two generators differs by some small but finite amount ($\sim 400\ Hz$) this frequency difference ultimately appears as a phase change in time, thus describing circles in the I/Q plane. By modulating the amplitude of the RF signal generator one can describe spirals (hence the name *spiral* calibration technique) which fill the I/Q plane and therefore characterize the response of the I/Q detector. All of the non linearities in the system (AM, 4.6 GHz signal generator, amplifiers, ...), require the drive let to be non-linearly calibrated only in its amplitude, which can be achieved by monitoring its output with a high accuracy power detector. A phase reference (i.e. the orientation of the spiral) can be set by using the LO signal itself as the RF signal for all I/Q detectors. Figure 4-16 summarizes the signals of the spiral calibration technique as measured

As a benchmark of the two calibration procedures, a 4.6 GHz sinusoidal signal with a known measured power of 15.64 dB has been used as the RF input of the I/Q detectors. Since the signal has a constant amplitude and the benchmark setup differs from the calibration drive leg of the spiral calibration procedure, this signal constitues a valid test also for the spiral calibration procedure. As shown in Fig. 4-18, the comparison of the two calibration methods indicates that the spiral technique leads to a more precise evaluation of the RF input power. In view of the better accuracy, this is the method of choice for the calibration for the I/Q detectors.

4.2.3 Remote calibration of the microwave probe diagnostic

A remote calibration scheme of the microwave probes installed on the 4-way-splitters 8 and 9 was developed. Since for these two splitters the forward and reflected waves are measured at all ports, it is possible to set up a minimization problem based on simple power balance considerations which allows to find the coupling coefficients of each probe. This routine is extremely useful since it allows an evaluation of the precision of the existing on-site calibration. Also, with this approach it is possible to evaluate possible changes in the diagnostic which could happen either by accident (e.g. loose cable) or systematically (e.g. temperature variation).

Given the scattering matrix $\bar{\bar{S}}$ of the 4-way-splitter

$$\bar{\bar{S}} = \begin{pmatrix} S_{II} & S_{IA} & S_{IB} & S_{IC} & S_{ID} \\ S_{AI} & S_{AA} & S_{AB} & S_{AC} & S_{AD} \\ S_{BI} & S_{BA} & S_{BB} & S_{BC} & S_{BD} \\ S_{CI} & S_{CA} & S_{CB} & S_{CC} & S_{CD} \\ S_{DI} & S_{DA} & S_{DB} & S_{DC} & S_{DD} \end{pmatrix} \tag{4.5}$$

and following the naming convetion of Fig. 4-19, the magnitude of the reflected wave V_{ref} at the 4-way-splitter input can is written as:

$$|V_{ref}| = \left| (S_{II}, S_{IA}, S_{IB}, S_{IC}, S_{ID}) \cdot (V_{inc}, V_{A,ref}, V_{B,ref}, V_{C,ref}, V_{D,ref})^{\mathrm{T}} \right| \tag{4.6}$$

The forward and reflected waves are measured by directional couplers which are located at the input of the four-way-splitters. The amplitude and phase of the forward wave is also measured by means

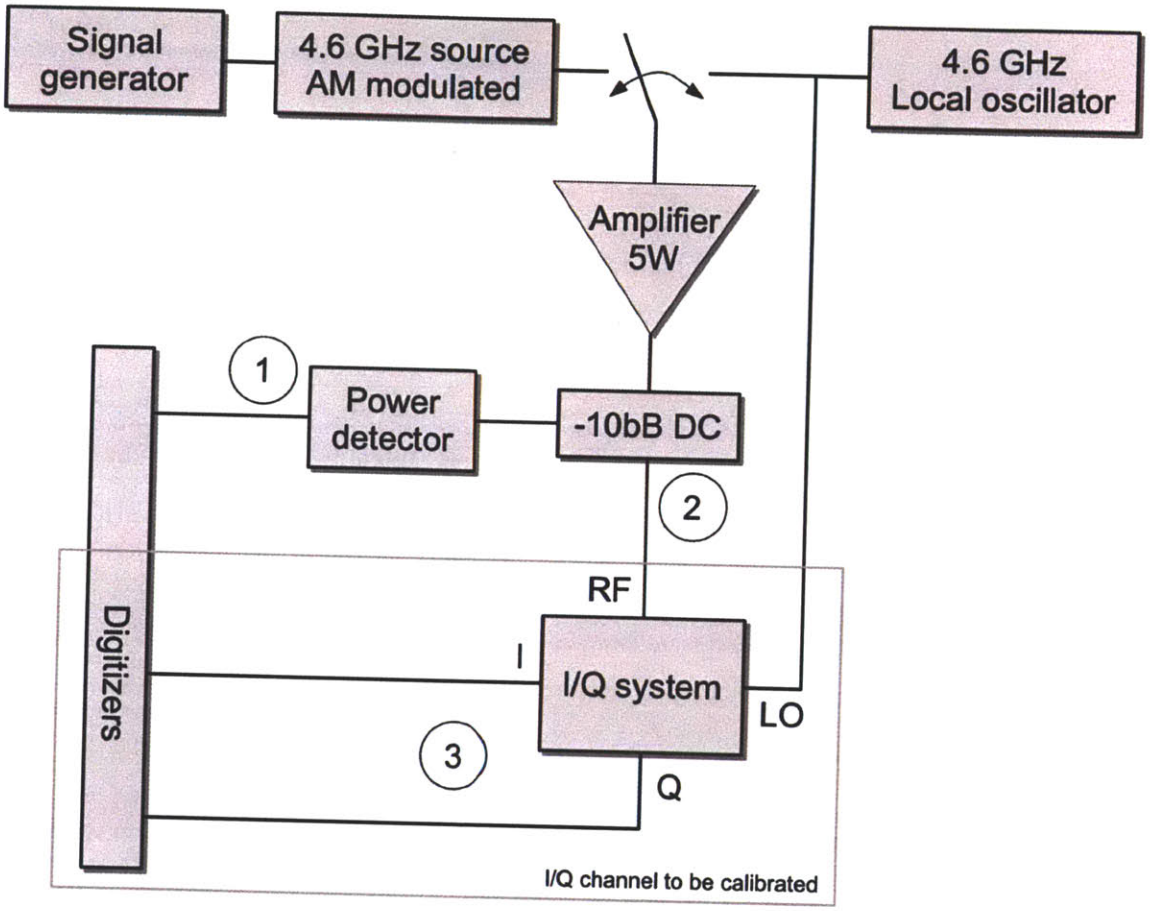

Figure 4-16: Calibration setup for I/Q detectors using the spiral technique. The LO signal is common to all of the probes. A sample of the signals that would be measured at the locations ①, ② and ③ is reported in Fig. 4-17.

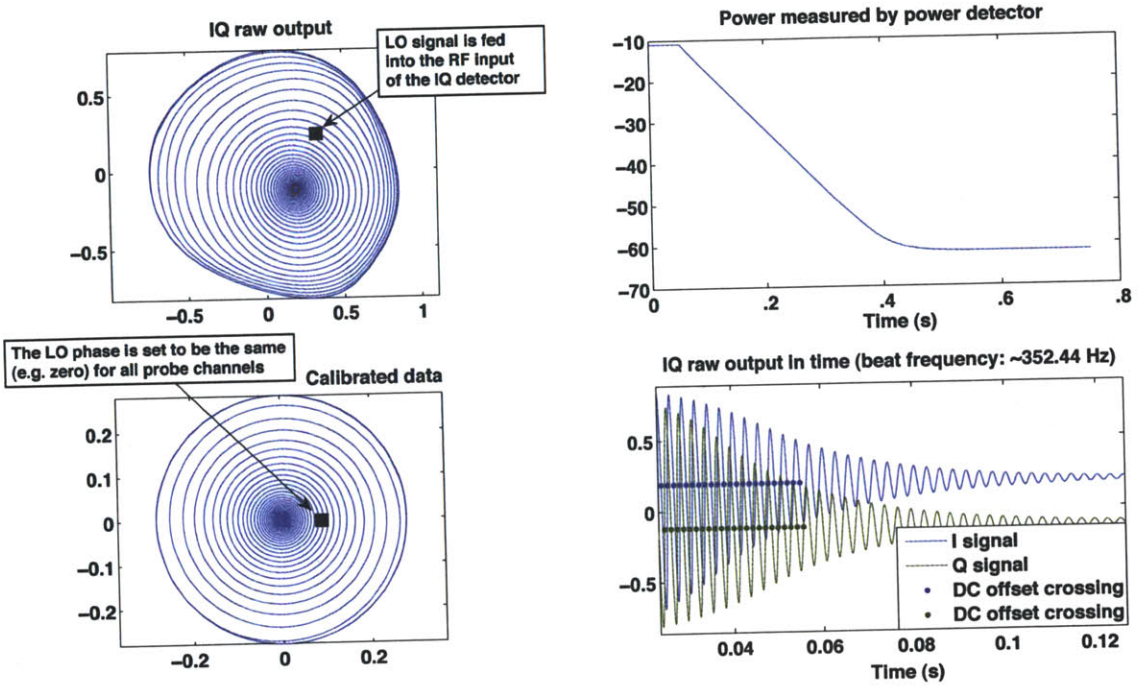

Figure 4-17: Calibration signals for I/Q detectors calibration using the spiral calibration technique. The I/Q raw output signal shows clear signs of non-linear distorsion at the edges of the calibration domain. The calibration converts the voltage measured by the digitizers to power measured at the output of the vacuum feedthroughs.

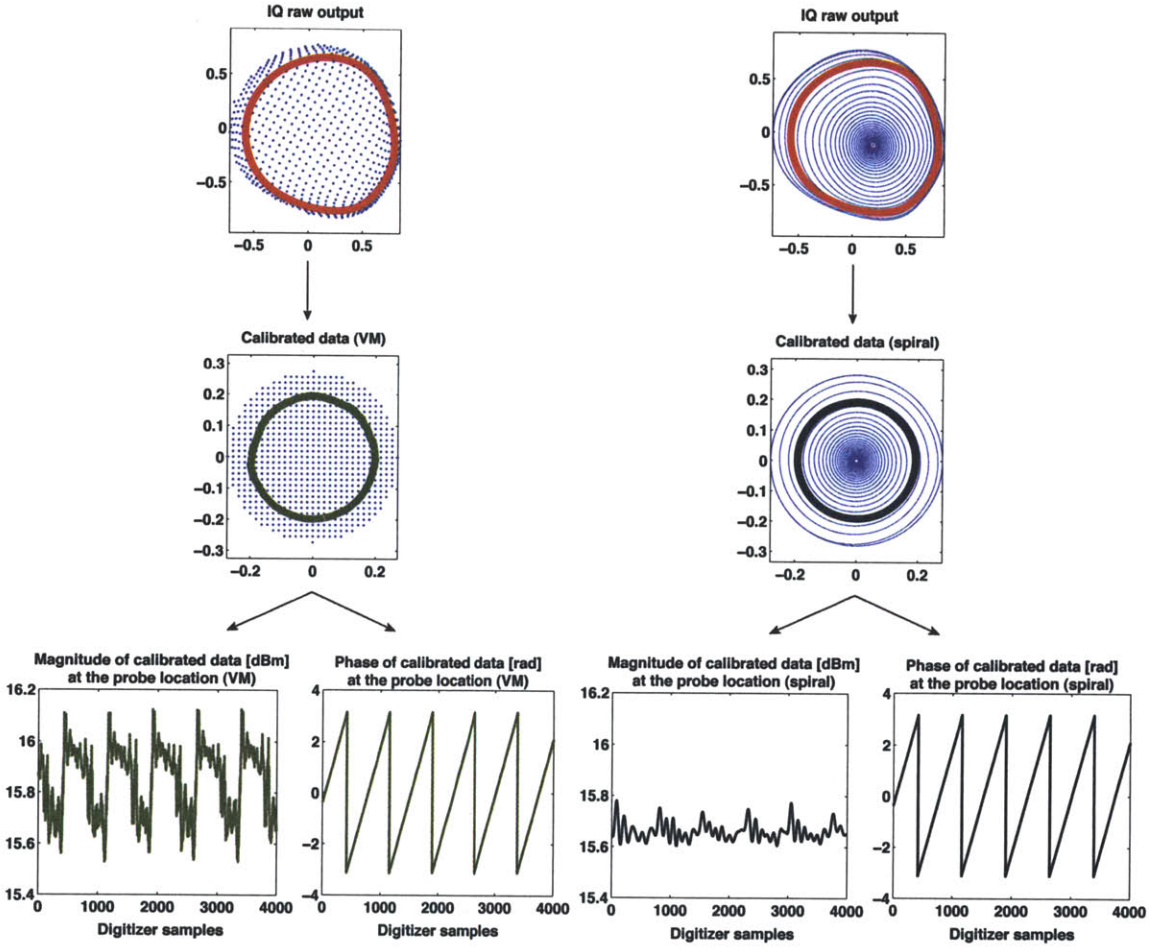

Figure 4-18: Benchmark of the vector modulator and spiral calibration techniques for channel D06R. A constant amplitude signal is fed into the I/Q detector system with a linearly changing phase. Even for relatively high signal amplitudes, the spiral calibration technique measures can measure with better accuracy the input signal. It is however at low input power that this scheme outperforms the vector modulator calibration technique.

of I/Q detectors at the Klystron outputs.

If in the previous equation we substitute the reflected waves $V_{A,ref}, V_{B,ref}, V_{C,ref}, V_{D,ref}$ with the measured values from the microwave probe system $\tilde{V}_{A,ref}, \tilde{V}_{B,ref}, \tilde{V}_{C,ref}, \tilde{V}_{D,ref}$, then we have an estimate of what the reflected wave at the input of the splitter should be:

$$|\tilde{V}_{ref}| = \left| (S_{II}, S_{IA}, S_{IB}, S_{IC}, S_{ID}) \cdot \left(V_{inc}, \tilde{V}_{A,ref}, \tilde{V}_{B,ref}, \tilde{V}_{C,ref}, \tilde{V}_{D,ref} \right)^{\mathrm{T}} \right|. \tag{4.7}$$

The remote calibration is then done by introducing eight complex coefficients, one for each probe, so that the reflected waves at the microwave probe locations are expressed as:

$$\tilde{V}_{A,ref} = \frac{C_{RA} V_{RA} - i\, C_{FA} V_{FA}}{2} \tag{4.8}$$

$$\tilde{V}_{B,ref} = \frac{C_{RB} V_{RB} - i\, C_{FB} V_{FB}}{2} \tag{4.9}$$

$$\tilde{V}_{C,ref} = \frac{C_{RC} V_{RC} - i\, C_{FC} V_{FC}}{2} \tag{4.10}$$

$$\tilde{V}_{D,ref} = \frac{C_{RD} V_{RD} - i\, C_{FD} V_{FD}}{2} \tag{4.11}$$

where the subscript R and F stand for *rear* or *forward* probe.

The value of the calibration coefficients are then found by minimizing the least square difference between the measured reflection coefficient at the intermediate coupler and the one evaluated according to Eq. 4.7. Since Eq. 4.7 is valid at any moment in time, we can always construct an overdetermined system. It is worth pointing out that for all matter and purpose no distinction can be made between an error in the microwave probes calibration or in the 4-way-splitter scattering coefficients.

The cost function of the non-linear minimization problem is defined as:

$$R = \left\langle \left(\tilde{V}_{ref}(t) - V_{ref}(t) \right)^2 \right\rangle_t \left[\alpha + \frac{1}{8} \sum_{k=\{RA,FA,\ldots,RD,FD\}} |1 - C_k|^2 \right] \tag{4.12}$$

The first part of the cost function R is the time averaged least square deviation between the amplitude of the reflected wave calculated according to Eq. 4.7 ($\tilde{V}_{ref}$) and the one measured by the directional coupler at the input of the splitter (V_{ref}). The second part of the cost function R is defined in such a way to make more expensive larger deviations from the original calibration. Here, the coefficient α is a parameter set by the user which allows to relax (higher α) or tighten (smaller α) this latter constraint.

If we assume that the calibration coefficients are constant in time[2], then one can use discharges with different (orthogonal) behavior to ensure a well conditioned minimization process. As an example, Figs. 4-20 and 4-21 show the comparison between the coupling measurements prior and post the new calibration procedure. In this example the eight complex calibration coefficients defined in Eqs. 4.8 - 4.11 have been computed to be:

[2]This assumption has been assesed by calculating the calibration coefficients for discharges taken during different shots and verifying their constancy.

Coefficient	Amplitude	Phase (deg.)
C_{RA}	0.944	-3.663
C_{FA}	0.980	4.446
C_{RB}	1.096	7.113
C_{FB}	1.090	-2.131
C_{RC}	1.126	6.040
C_{FC}	0.980	-4.020
C_{RD}	0.974	-5.278
C_{FD}	1.086	-2.506

A significant improved agreement between V_{ref} and $\tilde{V}_{ref}$ can be obtained with deviations from the original calibration of the order of few percent in the amplitude and no more than 10 degrees in the phase. Such a result gives confidence in the calibration procedure described in Sec. 4.2 and in the calibration of the four-way-splitter antenna itsef.

4.3 Assessment of antenna performances with microwave probe diagnostic

4.3.1 Launched toroidal spectrum

The toroidal array of probes was used to confirm the correct phasing of the launched waves. Figure 4-22 shows the measurement of the phase of the incident wave, the small differences with respect to the nominal phasing being attributed in the recirculating power in the four-way-splitters. The associated reconstructed toroidal spectrum can be deduced by taking the Fourier transform of the incident waves fields as measured by the toroidal probes array. This process assumes that the unmonitored columns have the same power and 90 degrees phase shift with respect to the measurement in the adjacent monitored waveguide. A clean launched toroidal spectrum was confirmed for different antenna phasing.

4.3.2 Power splitting

Numerical simulations predict the LH2 to be sensitive to poloidal nonuniformities. The two poloidal arrays of probes installed on columns 8 and 9 have been used to measure the poloidal power redistribution and the amount of recirculating power in the four-way-splitters. To highlight the poloidal power splitting characteristic of the four-way-splitter design, the power redistribution has been forced by shaping and moving the plasma.

Vertical displacement

Figure 4-23 shows the measurements of the microwave probes installed in column 8, for an intentional plasma vertical displacement. In this experiment the net power measured at rows A and D rows clearly tracks the plasma movement and is higher when the plasma is placed in front of each row. Row C shows the least change in the net power, and this is in agreement with the observation that the equilibrium does not change dramatically in front of this row. Finally the net power tracks the behavior of row D and becomes negative after 0.95 s. This is consistent with the observation that the plasma separatrix is touching the LH private limiters, since in this condition one can expect most of the power to be reflected and more to be coupled through the adjacent column. A directional coupler at the input of the splitter measures the coupling fluctuations to be less severe than what is observed at the grill mouth.

$$|\tilde{V}_{ref}| = \left|(S_{II}, S_{IA}, S_{IB}, S_{IC}, S_{ID}) \cdot \right.$$
$$\left. \cdot (V_{inc}, V_{A,ref}, V_{B,ref}, V_{C,ref}, V_{D,ref})^T \right|$$

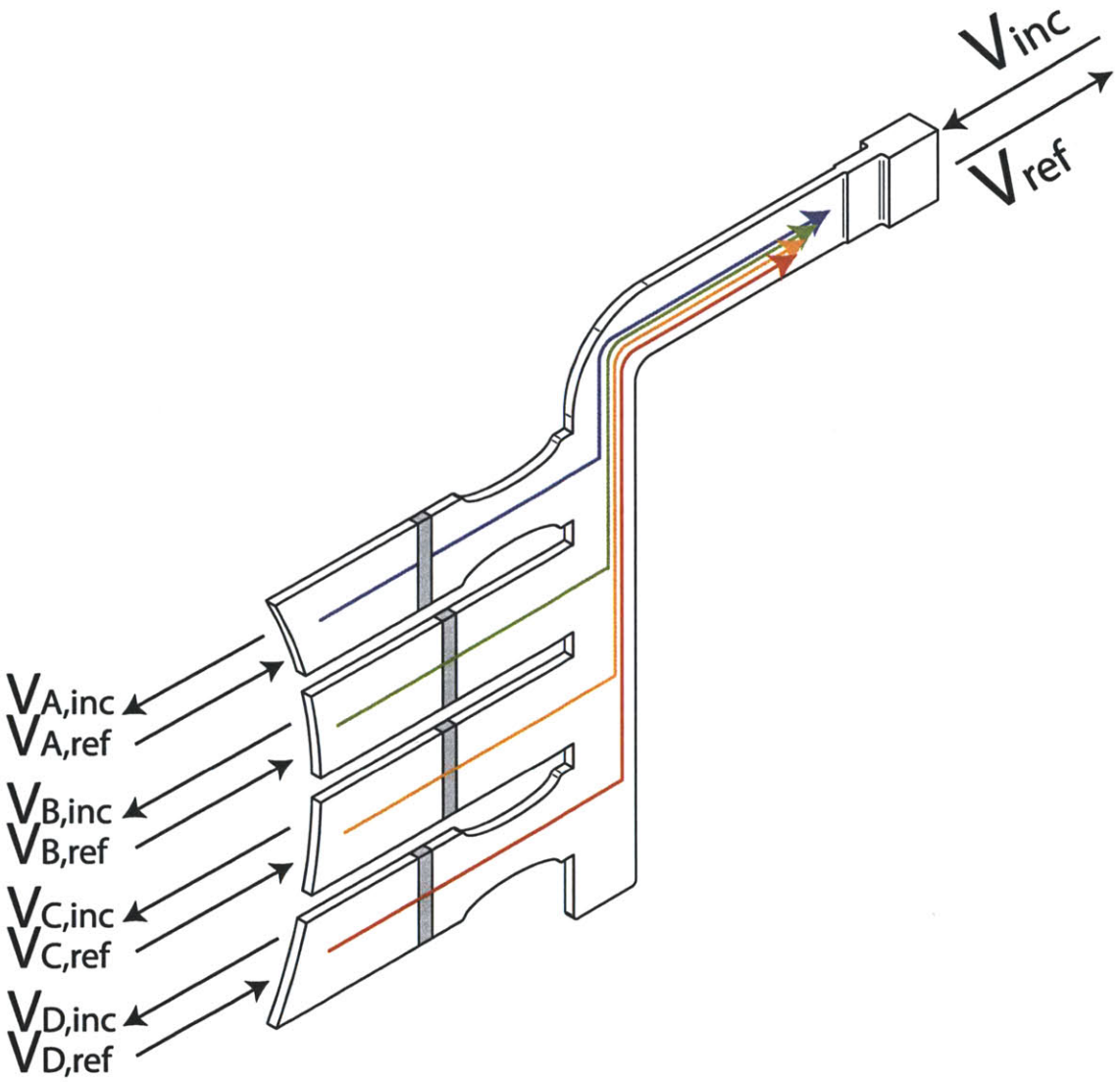

Figure 4-19: Schematic and nomenclature for the remote calibration of microwave probes. For the splitters where the forward and reflected waves are measured at all ports, the probes coupling coefficients can be found by imposing that conservation of energy is satisfied at all times. This calibration procedure works even when power is coupled through adjacent columns, since the subsrcipts *inc* and *ref* simply indicate the direction of the group velocity of the wave, independent of their origin.

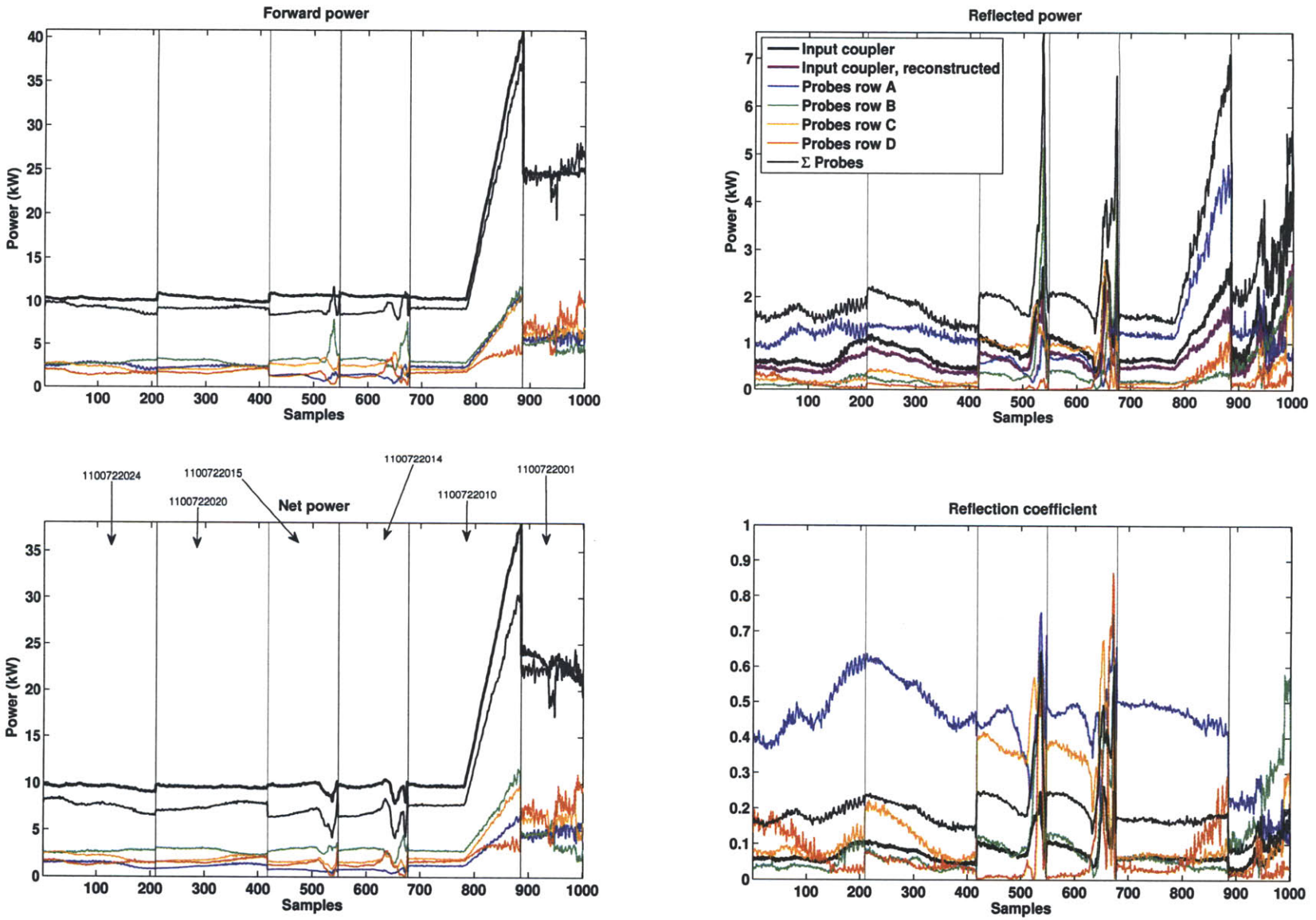

Figure 4-20: Coupling measurements of column 9 prior the remote calibration procedure. One thousand samples from different shots during the run day of the 22^{nd} of July 2010 is shown. In these shots the plasma has different shapes, is displaced radially and vertically, and different LH power and phasings are used. Some difference can be observed between the amplitude of the reflected wave calculated according to Eq. 4.7 ($\tilde{V}_{ref}$) and the one measured by the directional coupler at the input of the splitter (V_{ref}).

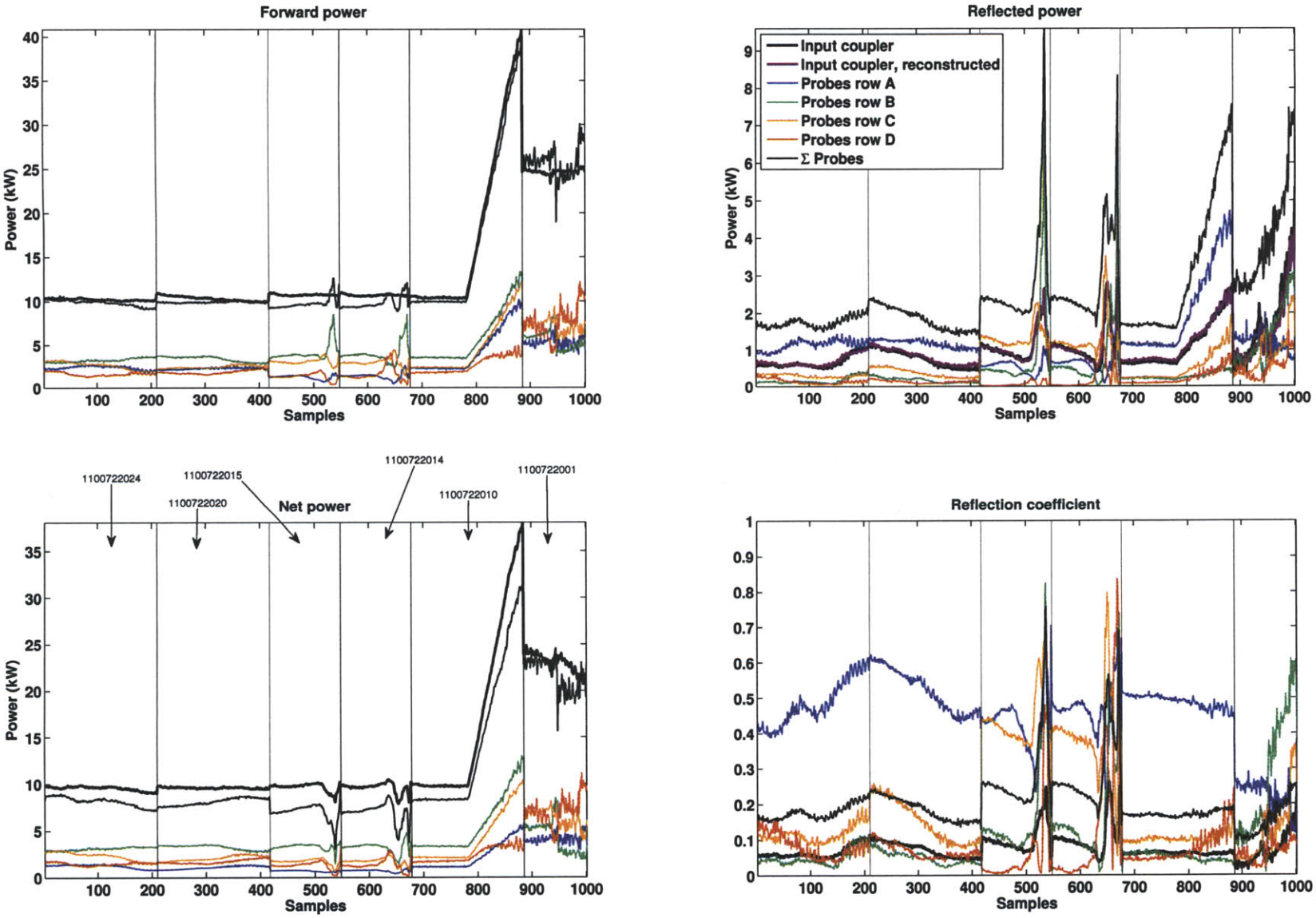

Figure 4-21: Same as Fig. 4-20 but after the remote calibration procedure. Compared to Fig. 4-20, the amplitude of the reflected wave calculated according to Eq. 4.7 ($\tilde{V}_{ref}$) agrees well with the one measured by the directional coupler at the input of the splitter (V_{ref}).

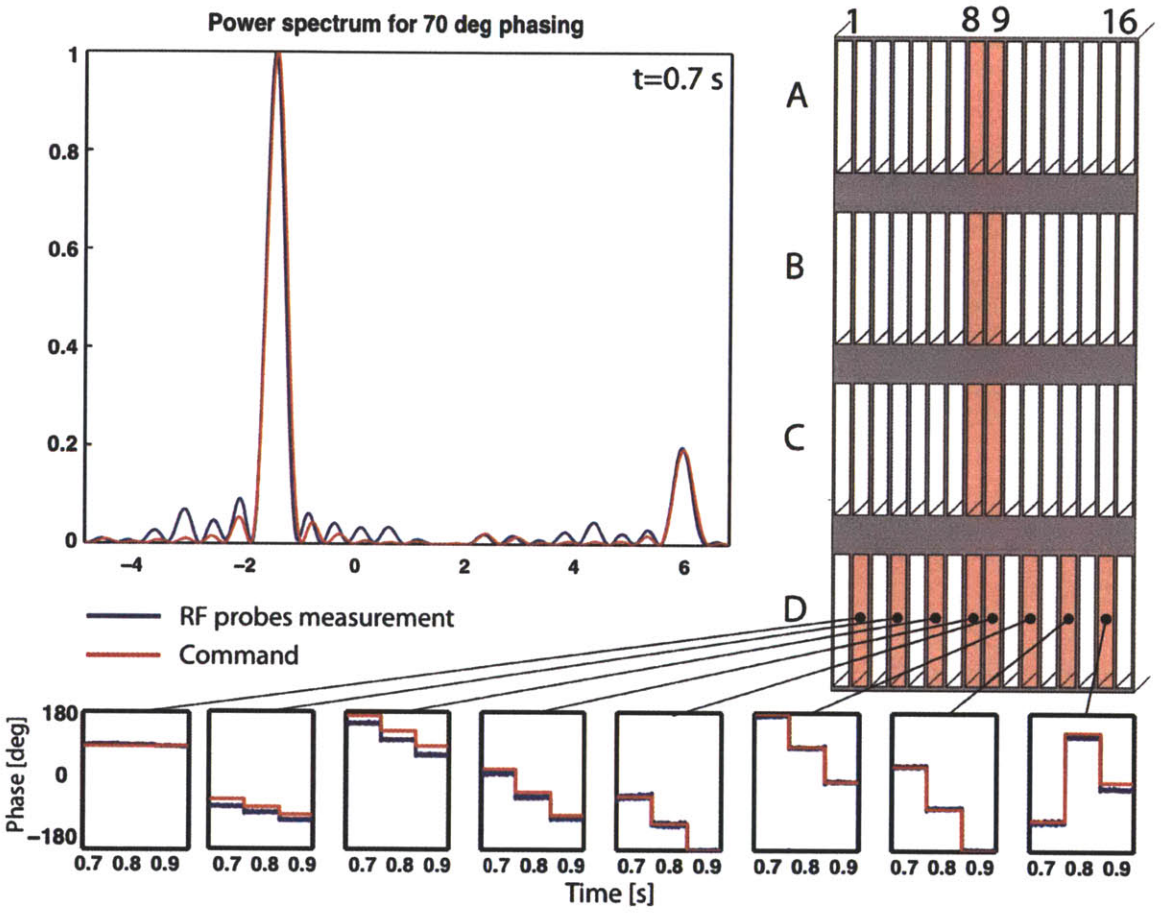

Figure 4-22: Monitored waveguides (shaded), measure the phase of the incident wave during a shot in which the LH phase is scanned from 70 to 90 to 110 degrees. The reconstructed $n_{\|}$ spectrum for 70 degrees phasing is shown and is in good agreement with the expected one. Shot number is #1100715017.

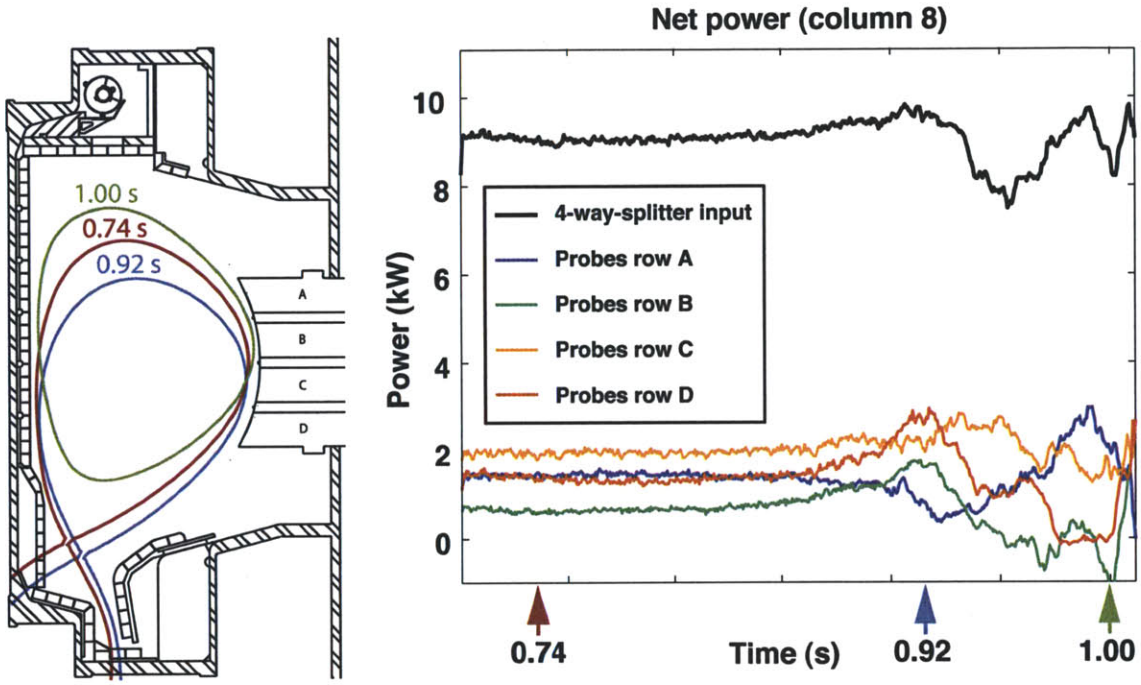

Figure 4-23: Plasma equilibrium at three different times and net power as measured by the microwave probes installed in column 8 and the directional couplers at the input of the four-way-splitter. Shot number is #1100722016.

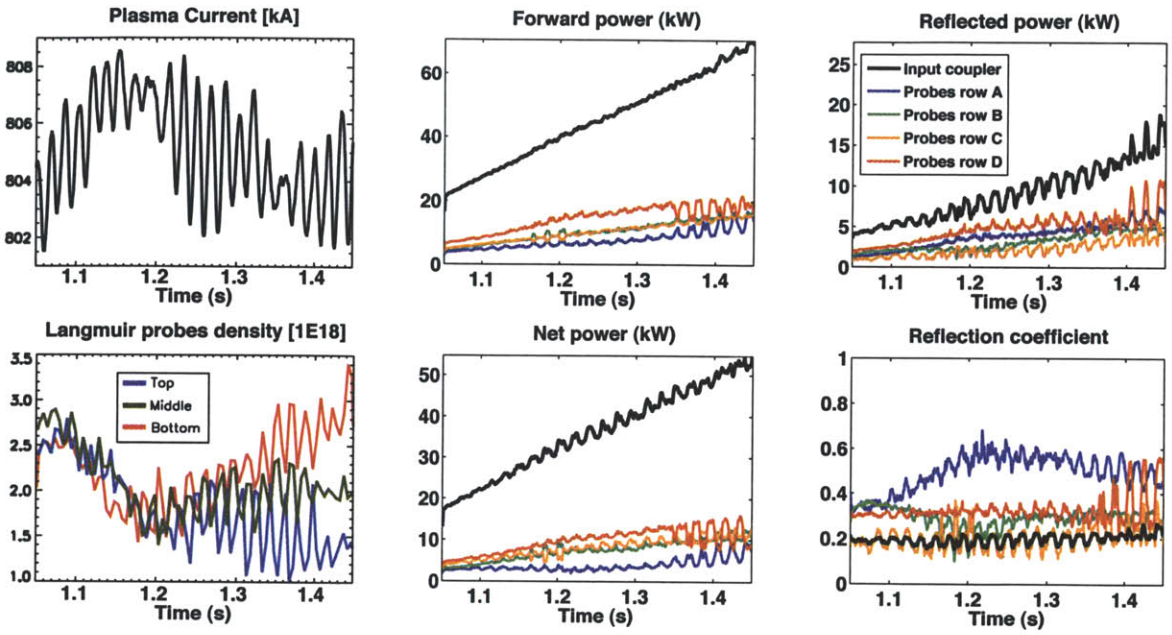

Figure 4-24: In shot #1101028030 a vertically unstable plasma during a LH power ramp highlights the power splitting characteristics. In this figure, are shown the microwave probe traces of column 9.

Vertically unstable plasma

Another interesting example of poloidal power redistribution is shown in Fig. 4-24. The plasma current, the toroidal field and the control coils exhibit an oscillatory characteristic. The out-of-phase behavior of the density recorded at the Langmuir probes suggest that the plasma exhibits vertical jogs. This is a perfect opportunity to study the power partioning of the splitter. The microwave probe measurements show that, in agreement with the density measurements, the top (A) and bottom (D) rows are more affected and their behaviour is also out of phase. The center rows (B, C) instead show much milder variations (also in agreement with the density measurements). Worth noticing is how the reflection coefficient at the input of the splitter is more resilient than the one measured at each individual output waveguide.

Chapter 5

Lower hybrid wave coupling on Alcator C-Mod

Linear coupling theory for LH waves [5] has been validated in several experiments but has been shown to break down at high power densities. The power density threshold for the transition from the linear to the non-linear coupling regimes is not well defined, even though all current drive experiments ultimately operate in this regime. Some experiments [5] reported that above a power density threshold of 0.5 to 4 KW/cm^2, the reflection coefficient decreases and becomes roughly independent of the phase between adjacent waveguides. On the contrary, previous experiments on ASDEX [120] showed a degradation of the coupling at high power. High power (400 kW to 1 MW) operation on the first C-Mod LH launcher (2006, 2007, 2008 campaigns) did not show any apparent trend, even though reflection coefficients are significantly higher (20% to 30%) than at lowest power levels. During the 2006 campaign, at best $\sim$ 15% power reflection coefficient was achieved at the grill mouth, after optimizing the equilibrium of the plasma to be conformal to the shape of the antenna. Also, a moderate dependency on phasing was reported (90 degree phasing showing best coupling, followed by 60 and 120 degree phasing). Understanding of LH wave coupling at high power will be essential for the LHCD system envisioned for ITER.

Lower hybrid wave coupling strongly depends on the details of the density profile in the proximity of the antenna mouth. Historically, simple linear density profiles were used, so to allow for parametric studies while ensuring the existence of analytic solutions. The most refined versions of such linear profiles have the form:

$$n_e = \begin{cases} n_{e0} + \frac{\mathrm{d}n}{\mathrm{d}x}(x - \Delta_{GAP}) & \text{, if } x \geq \Delta_{GAP} \\ 0 & \text{, if } x < \Delta_{GAP} \end{cases} \tag{5.1}$$

where the launcher is assumed to be at $x = 0$, n_{e0} is the density pedestal, $\frac{\mathrm{d}n}{\mathrm{d}x}$ is the density gradient, and Δ_{GAP} is a vacuum region between the launcher and the plasma. This type of profile was first proposed in Ref. [10] and analyzed in detail in Ref. [121]. A graphical representation of such a profile is shown in 5-1.

Another practical reason which historically limited theorists to the use of linear profiles was that in the experiment the edge density profile was not well diagnosed. The absence of a density profile measurement of the first few mm in front of the antenna while this one was operating, left no other choice but to use the parameters of the linear density model to fit coupling simulations to the experimental measurements. Weakness of such method is that even when good consistency between experiments and calculations was obtained, one could not say if this was due to the accuracy of the physics model or the ambiguity of the density profile.

Noticeable is the role of the millimetric vacuum gap which has often been invoked to exist in front

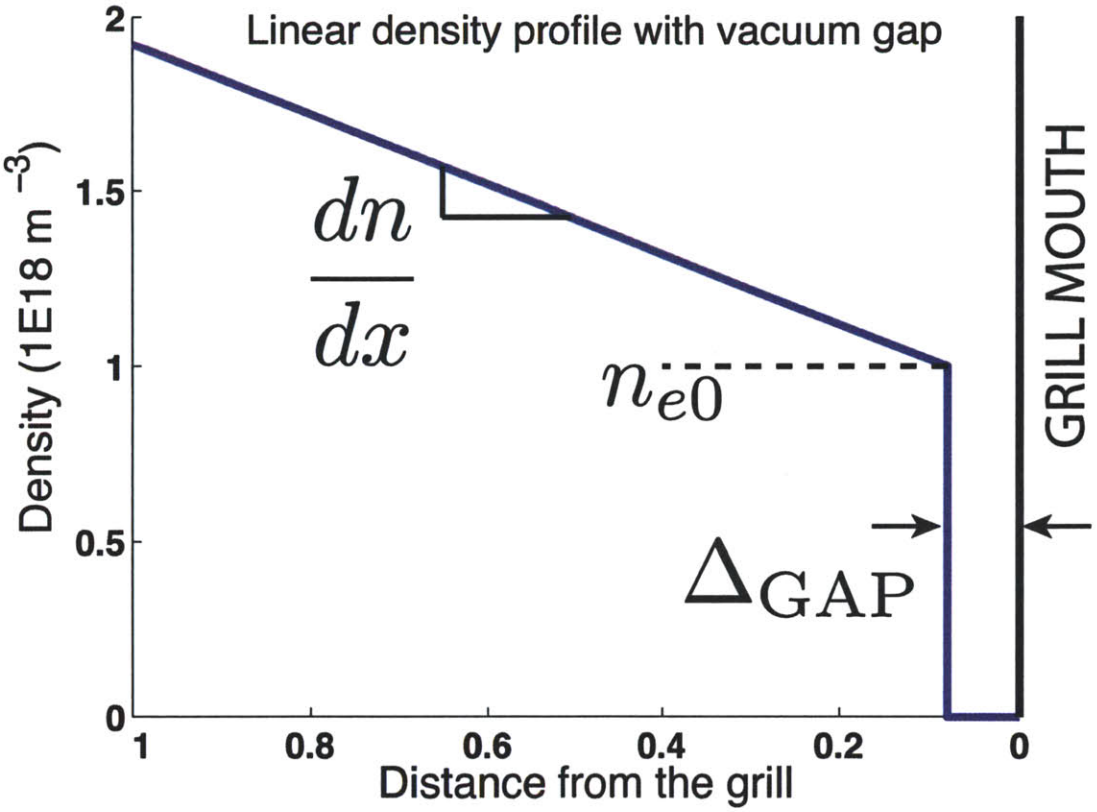

Figure 5-1: Linear density profile that is for example used in the GRILL code. It is customary to define the density scale length as $\lambda_n = \frac{n}{dn/dx}\ m$.

of LH launchers, in order for simulations to agree with experimental measurements, as summarized in Table 5.1. Worth pointing out is how LH coupling simulations on ITER were done for vacuum gaps ranging up to 1 *cm*, leading to very different results [122]. Coupling measurements with the first LH launcher on C-Mod were explained by means of linear coupling theory codes which used different density profiles in front of the grill depending on the density measured by the edge Langmuir probes. Two regimes were identified [26]. The first one, at low density, required the presence of a vacuum gap, fixed density gradient, and different density pedestal. The second one, at high density, required no vacuum gap, a changing gradient and fixed density pedestal.

A density profile with presence of such gap has never been directly measured, and different theories have been put forward to justify its possible existence. These include: modification of the transport phenomena during LH [123], misalignment of the grill [124], limiter shadowing in front of the waveguides or an improper match between plasma and grill curvature [124]. However, the most plausible cause is that the plasma is pushed away under the action of ponderomotive forces acting on the plasma surface [10, 121, 11, 125], resulting in an effective shift of the density profile in the radial direction, thus creating a low density region where LH waves are evanescent and increasing the reflection coefficient. It is clear that a definitive theoretical model in this regime is still missing; experimental observations are often contradictory and additional experimental information is therefore essential.

Device	Gap	Code	Reference
C-Mod LH1	$0 - 0.5\ mm$	Brambilla	[26]
T'edV	$1\ mm$	SWAN	[123]
Tore Supra	$0\ mm$	ALOHA	[94]
WEGA	$0\ mm$	N/A	[126]
JET	$1\ mm$	N/A	[127, 128]
FTU	$0\ mm$	Brambilla	[129]
FTU-PAM	N/A	SWAN Grill3D	[130, 131, 106]
ASDEX	$2\ mm$	Brambilla	[120]
ITER	$0 - 1\ cm$	SWAN ALOHA TOPLHA Grill3D	[122, 85]
JT60	$0\ mm$	N/A	[132]
PBX-M	$1\ mm$	Stevens	[124]

Table 5.1: The presence of a vacuum region between the grill and the plasma was often found to be necessary to reproduce the experimental data. This table summarizes the vacuum gap used in different experiments using different coupling codes.

The new Alcator C-Mod LH launcher is now in a unique position to study LH wave coupling. In fact the LH launcher is not only equipped with three sets of two Langmuir probes of different lengths, but also has an X-mode SOL reflectometer to measure the actual density profile in front of the launcher at three poloidal locations. The availability of accurate density profile measurements eliminates these free parameters and enable a characterization of the antenna coupling performance and a self-consistent validation of LH wave coupling codes. In this thesis we found that the experimental results support the existence of a density depletion in the presence of high power RF and modeling showed that this is compatible with what is expected by ponderomotive forces.

5.1 High power coupling

On the Alcator C-Mod tokamak, although the average reflection coefficient measured during high power operations ($> 1\ MW/m^2$) at the input of the splitters can be reduced to be as low as $\sim 15\%$ in optimized conditions, its amplitude is usually higher than simulations predicted at the design stage for typical SOL density parameters [111]. To address this issue, a systematic survey of the coupling properties of the launcher has been carried out.

Presented here are two sets of three discharges at 70, 90 and 110 degrees phasing, one set for the launcher being $\delta = 0.1\ mm$ behind the protecting limiter, the other for $\delta = 1\ mm$. In these experiments the plasma equilibrium was kept constant while the density was swept during the LH pulse by gas puffing. Figure 5-3 shows the power reflection coefficient as a function of average edge density as measured by the Langmuir probes embedded into the LH antenna. The experiments were carried out at magnetic field of $5.4\ T$ and peak core densities of $2.0 \times 10^{20}\ m^{-3}$, so the wave LH waves were fully accessible throughout the whole plasma. For reference, the time evolution of the plasma parameters for shot #1100818004 are shown in Fig. 5-2.

In this experiment, the measurements of the power reflection coefficient shows the typical trend predicted by linear coupling theory [5], the reflections rapidly increasing for densities close to the cutoff density and reaching a minimum, which is more pronounced at lower phasing. The reflection coefficient is observed to increase at higher phasing. Also, reflections are systematically lower when

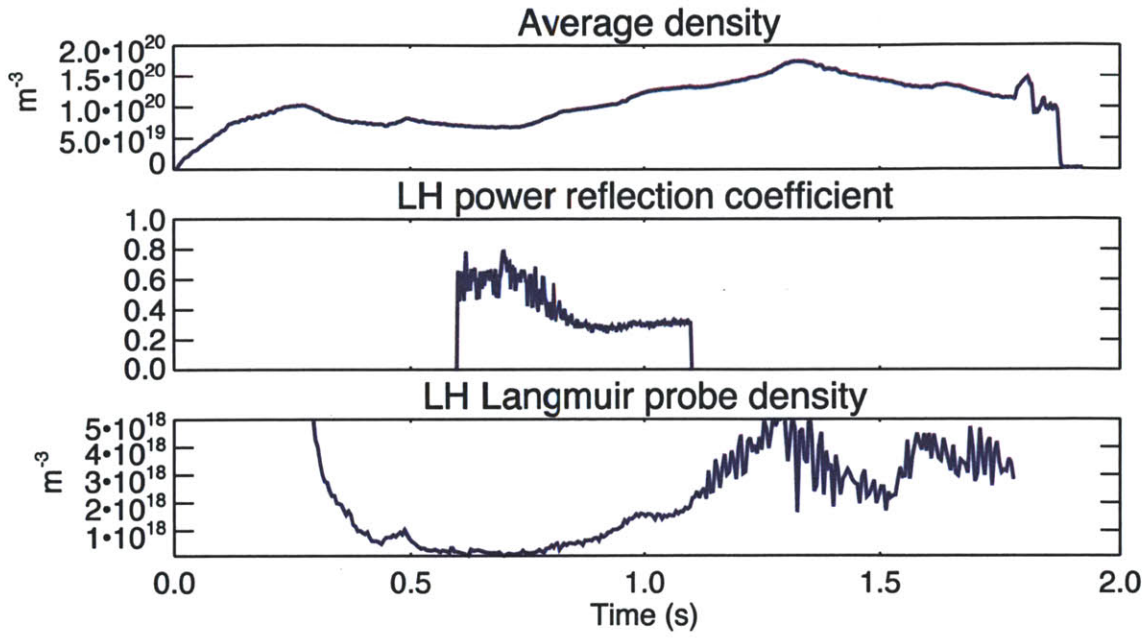

Figure 5-2: Average plasma density, power reflection coefficient and density measured by Langmuir probes for shot #1100818004.

the launcher is pushed farther towards the plasma.

LH wave coupling simulations have been carried out using the density measurements from the Langmuir probes installed in front of the launcher. A wide range of experimental observations were reproduced with the GRILL code [5] (black dots in Fig. 5-3), provided that the density profiles included the presence of a vacuum gap of the order of 1 mm. The density at the coupler is measured by the Langmuir probes while the density gradient is estimated by taking the edge-most channel of the Thomson scattering system. This density model is supported by the observation that the reflection coefficient is observed to increase at higher phasing, suggesting that the waves tunnel through an evanescent region. However, it was not possible to reproduce the experimental measurements using a single vacuum gap value across the whole density scan. Hence, a new variable density gap was used in the density model of Eq. 5.1,

$$\Delta_{GAP} = \Delta_{GAP0}(1 - \alpha n_{e0}) \tag{5.2}$$

the idea being that the vacuum gap reduces proportionally as the edge density increases. The parameters Δ_{GAP0} and α were chosen so to best reproduce the experimental measurements and were found to be $\Delta_{GAP0} = 1\ mm$ for $\delta = 0.1\ mm$ and $\Delta_{GAP0} = 1.3\ mm$ for $\delta = 1\ mm$. In both cases $\alpha = 2 \times 10^{-20}\ m^3$. This model is an extension of the model which has been used so far to explain LH wave coupling on several machines [10, 121]. This model is able to predict the measurements, and is in line with the two coupling regimes (with and without vacuum gap) that were identified for the LH1 launcher on Alcator C-Mod [26].

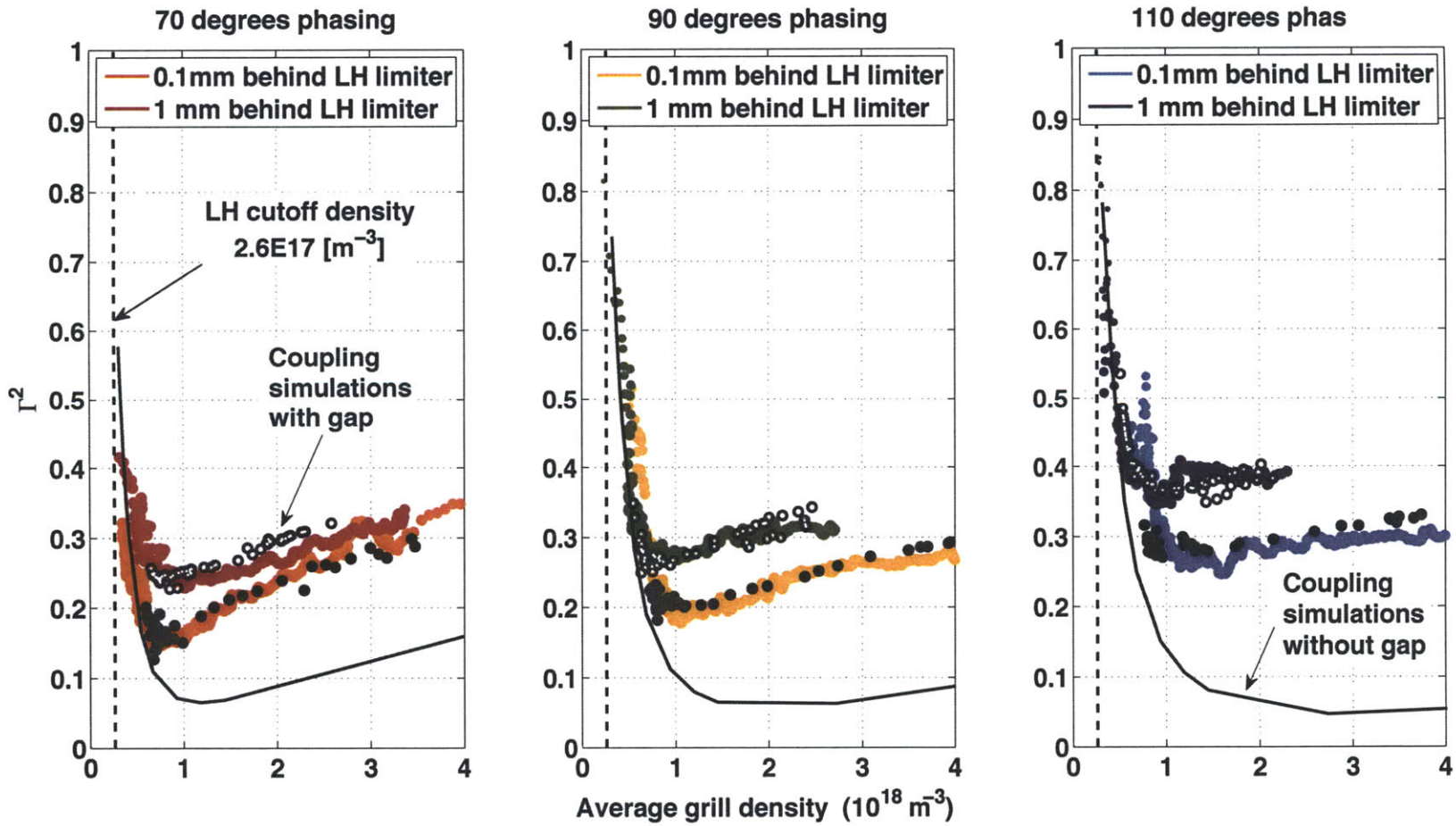

Figure 5-3: Power reflection coefficient as a function of average probe density for different phasing and launcher radial positions behind the private limiters. Data from shots: #1100818003 (70 deg, 1 *mm*), 1100818004 (90 deg, 1 *mm*), 1100818005 (110 deg, 1 *mm*), 1100818008 (70 deg, 0.1 *mm*), 1100818009 (90 deg, 0.1 *mm*), 1100818010 (110 deg, 0.1 *mm*). The filled black circles and the open black circles are coupling simulations using the Brambilla code and the density model with variable vacuum gap.

n_{e0}	$0.8 \times 10^{20}\ m^{-3}$	$1.0 \times 10^{20}\ m^{-3}$	$1.4 \times 10^{20}\ m^{-3}$
Γ^2 experiment	29%	29%	28%
Γ^2 simulation (LH phase)	34%	27%	30%
Γ^2 simulation (OH phase)	20%	11%	10%

Table 5.2: Comparison of the power reflection coefficients between experiment and simulation for the density profiles of Fig. 5-6.

5.2 Density measurements by SOL X-mode reflectometer and Langmuir probes

On Alcator C-Mod, for the first time the depletion of the density profile in front of the launcher was directly measured with the SOL X-mode reflectometer diagnostic [7, 8] which was introduced in Sec. 3.2.2. Such an effect is best evident for LH power modulation experiments as reported in Fig. 5-4. The Langmuir probes also register a reduction of the electron density and an increase of the electron temperature. The latter is of particular interest because the temperature increase can act as an important feedback mechanism for ponderomotive effects.

The following study focuses on three power modulation experiments which have three different line averaged densities. The SOL density profiles are reported in Fig. 5-5. These are spline fits to the data collected during the *LH on* and *LH off* periods of the modulation experiment; thus allows an increase in the measurement statistics. From the measurements it is immediately clear that a density depletion by LH waves in the very proximity of the launcher is always present. These profiles are also in qualitative agreement with the variable gap model of Eq. 5.2 that we introduced in the previous section. From these profiles one can also observe that the density tends to rise about 2 *cm* away from the launcher. On ASDEX SOL X-Mode reflectometer has measured the density increase farther inside of the plasma, but not the density depletion close to the launcher [133]. This difference is most probably due to the fact that in the case of Alcator C-Mod the reflectometer horns are placed in the shadow of the LH private limiters. On ToreSupra instead the SOL X-Mode reflectometer was unable to measure density profiles during LH due to electron cyclotron emission radiation created by supra-thermal electrons generated by the LH waves [134].

2D coupling simulations using the reflectometer density profiles reported in Fig. 5-5 were performed using COMSOL and the results are reported in Table 5.2. The simulated reflection coefficients are more sensitive to the details of the profiles than what has been actually measured. Nonetheless, simulations were found to agree within a few percent of the experimental measurements, that is quite remarkable considering that the 3D structure of the SOL and of the launcher was completely neglected. For reference, simulations were run also for the ohmic profiles (i.e. when LH was *off*). In this case the reflection coefficients were found to be systematically lower. Comparing the simulation results for *LH on* and *LH off*, suggests that both a low density at the grill (especially in the presence of an evanescent layer) and a steep density gradient contribute negatively to the wave coupling.

A word of caution has to be said regarding the calibration of the reflectometer profiles. This in fact relies on the EFIT magnetic equilibrium reconstruction to locate the position of the X-Mode cutoff, which is used as the starting point for the inversion of the raw data. Errors in the magnetic field of the order of 0.1% result in errors of the order of 1 *mm* in the radial location of the reflectometer profiles. This is by far the largest uncertainly in this system. By comparison the shape of the profile is instead a robust quantity. To reduce this uncertainty the measurements by the Langmuir probes (average measurements from the B port and D port probes) have been used to constrain the radial shift of the measured reflectometer profiles. Although the length of the Langmuir probes is of the order of a *mm* and therefore it does not necessarily reduce the absolute error in the shift of the profiles, the same consistent assumption has been done for all of the measurements presented in this

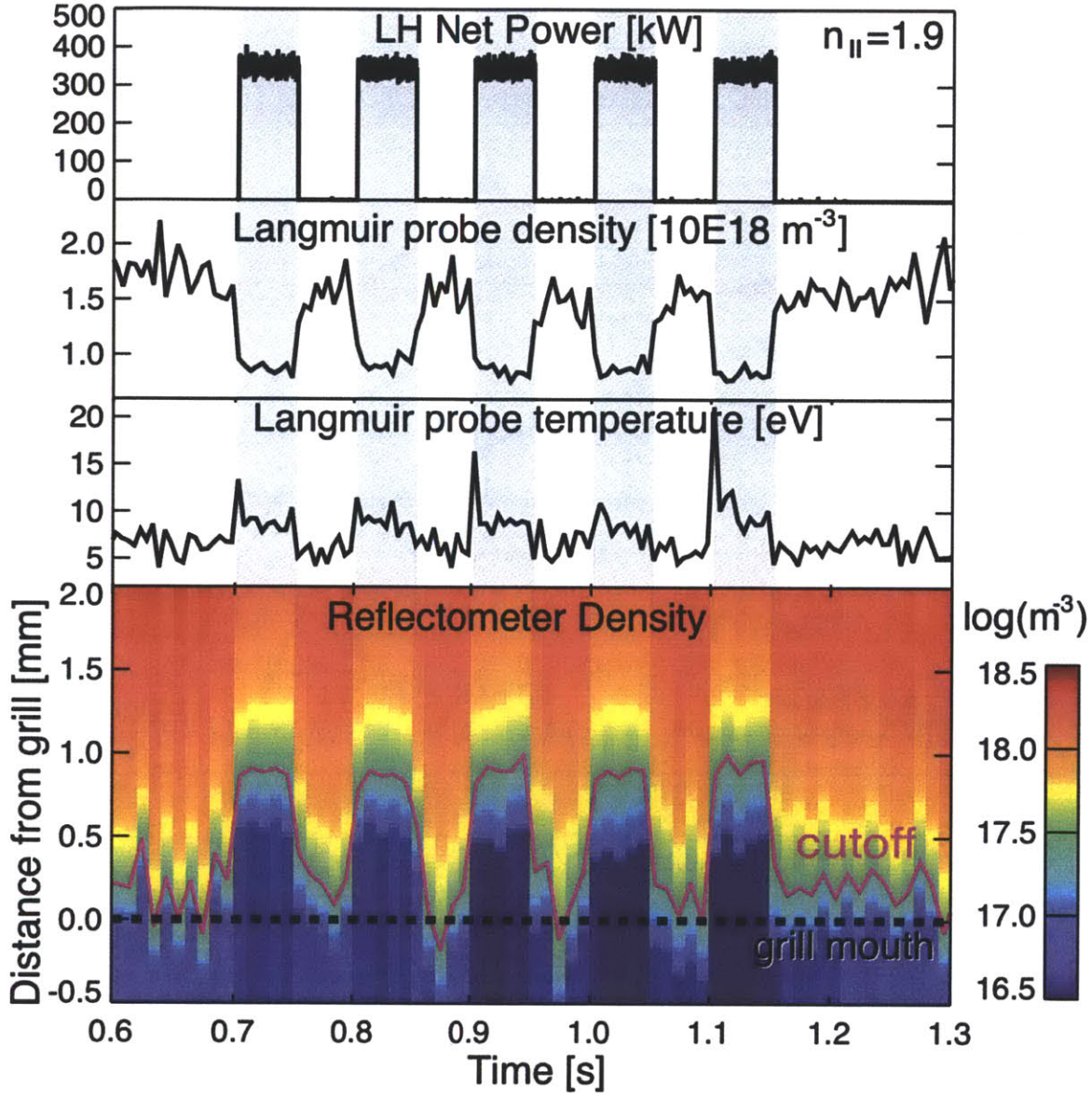

Figure 5-4: SOL measurements during a power modulation experiment (shot #1101118003) show clear indication of density depletion in front of the launcher when LH power is on. This type of experiment has been used to generate the average density profiles of Fig. 5-5.

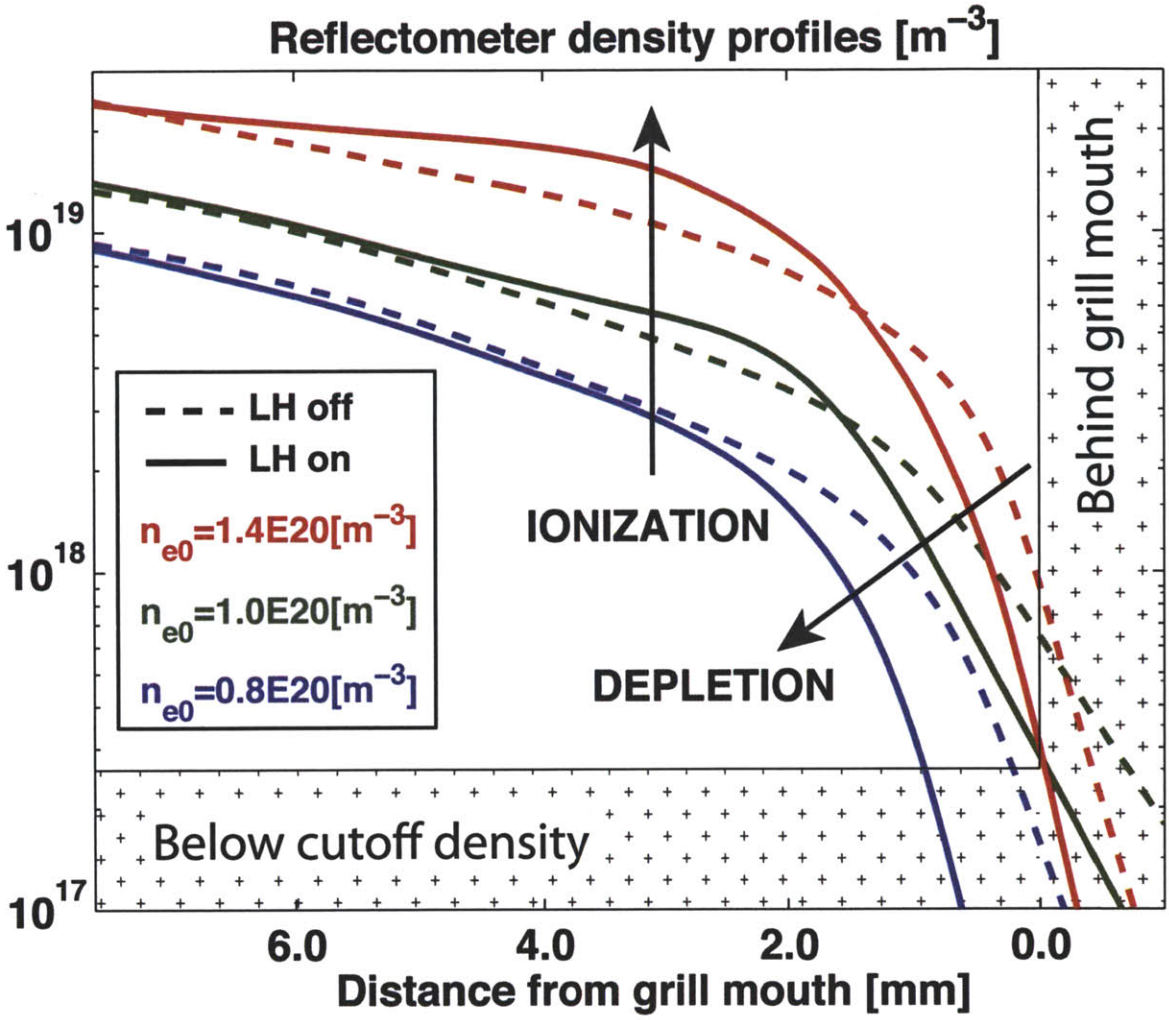

Figure 5-5: Density profiles measured by reflectometer for shots #1101118003 (0.8×10^{20} m^{-3}), #1101118008 (1.0×10^{20} m^{-3}) and #1101118014 (1.4×10^{20} m^{-3}). Solid and dashed lines represent the profiles in presence and absence of high power LH waves, respectively.

thesis.

In general, in presence of high power LH waves the SOL exhibits 3D structures which are apparent when looking at the LH launcher with a visible camera. Figure 5-6 shows glowing striations which are routinely observed above waveguide rows during high power operation. This 3D structure is also confirmed by the Langmuir probe measurements. Such effect was also observed in the first generation launcher on Alcator C-Mod and in other experiments [26]. In particular, Ref. [133] attributed a similar observation on ASDEX to the formation of vortices (or convective cells) in front of the plasma [79]. Although there is clear experimental evidence of these convective cells and numerical tools such as COMSOL allow the description of arbitrary 3D non-uniformities of the plasma parameters, for the time being we retain these vortices as a second order effect and assume that the plasma is an infinite slab medium allowing only variations in the radial direction.

5.3 Coupling at low power

A non-perturbative low power experiment was setup mid-way into the 2010/2011 campaign to verify that the measured high reflection coefficients were due to the presence of high power LH waves interacting with the SOL profiles. In this setup, the high power klystron feeding network is substituted with a low power feeding network. Which network to operate is selected by means of a high power switch (the same switch which is used to connect the klystrons either to the launcher or to the high power water loads). For the low power network, the 4.6 GHz waves coming from a signal generator are amplified to $\sim 5\ W$ and then fed at the switches. Each leg of the low power feeding network is setup to mimic the corresponding leg of the high power network. The power is split into 16 ways (of which only 10 are used), and an additional $-3\ dB$ attenuator is used for the direct fed columns. The phase of each leg is individually set by mechanical phase shifters so as to obtain 90 degree phasing at the columns of the grill. Directional couplers ($-10\ dB$), located at the input of the splitter, measure the amplitude of the reflected waves. In view of the arrangement, the comparison of the reflection coefficients of the direct fed columns is possible.

The low power measurements shown in Fig. 5-7 were collected in piggyback and were therefore not done in the same plasma conditions of the high power experiments reported in the previous sections. Nonetheless, at low power the reflection coefficient is observed to be much lower than what has ever been measured during high power operations. Also, the minimum of the reflection coefficient appears to be broader and occurring at higher densities. In this case, coupling simulations that based on the reflectometer density measurements had no vacuum gap, were found to agree well with the measurements. For comparison, simulations with an additional 1 mm vacuum were also calculated and found to have a higher reflectivity than the one observed in low power experiments.

This is a very important test which gives confidence in the reflectometer profile measurements. Since coupling was found to be a strong function of the injected LH wave power, effects such as local limiter shadowing and mismatching of the plasma/antenna curvatures [124, 123] are most likely not the main contributors to the high reflectivity observed on C-Mod. This ultimately points to ponderomotive forces as the leading candidate to explain this observation [9, 10, 11].

5.4 Modeling of SOL modification by ponderomotive forces

Ponderomotive force is the force that charged particles experience in an inhomogeneous oscillating field which makes them drift toward the weaker field area. In Sec. 2.3.2 the ponderomotive force was derived by considering the non-linear force acting on an electron in the oscillating $\vec{E}$ and $\vec{B}$ fields of a wave and we introduced the concept of a ponderomotive potential Φ_P.

The density perturbation and wave propagation are coupled to one another in a non-linear way (the former depends on the wave fields and the latter depends on the dielectric tensor which is a function of the plasma density). Following the derivation from [10], the analytical formulation of

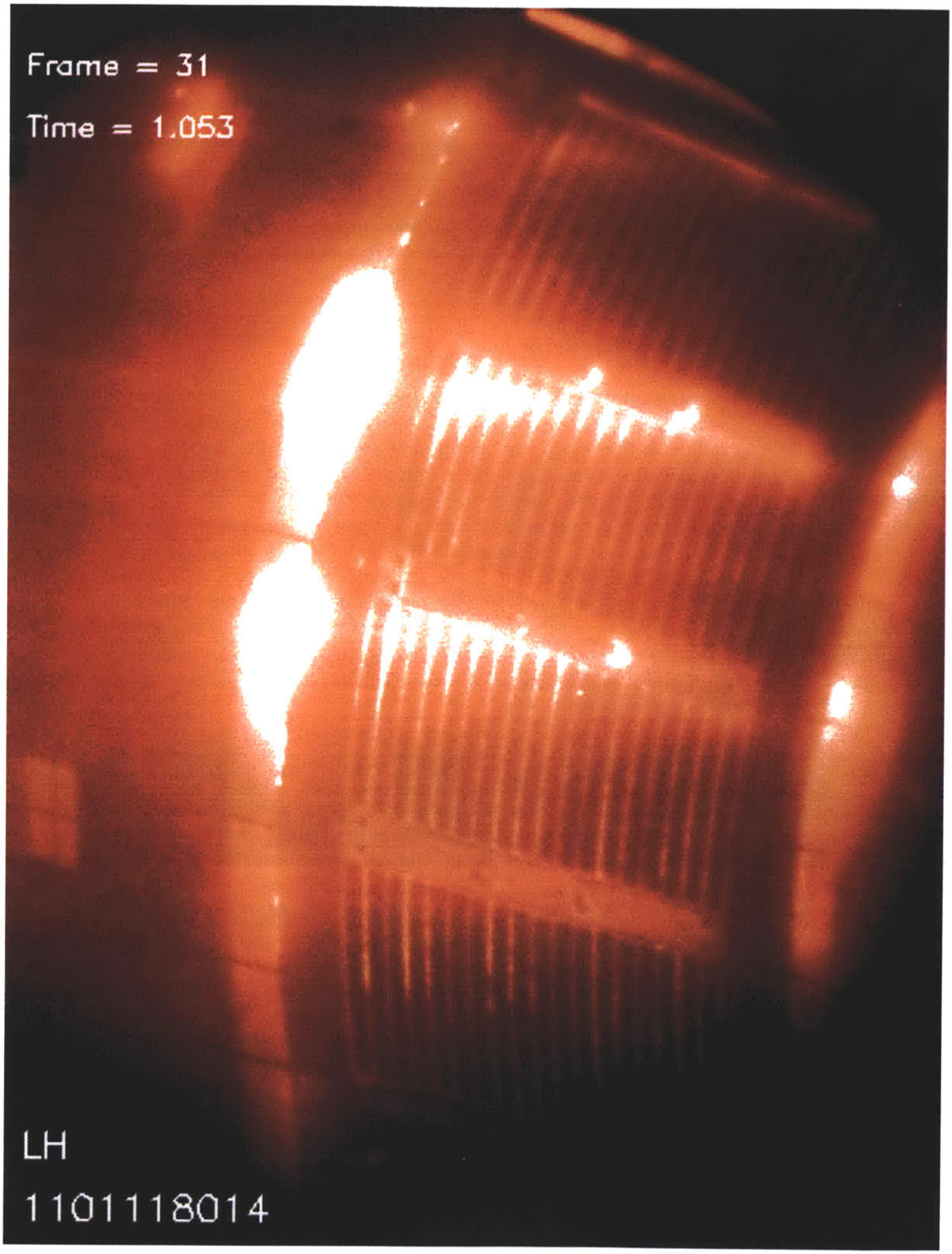

Figure 5-6: Visible camera frame, showing glowing striations which are routinely observed above waveguide rows during high power operation.

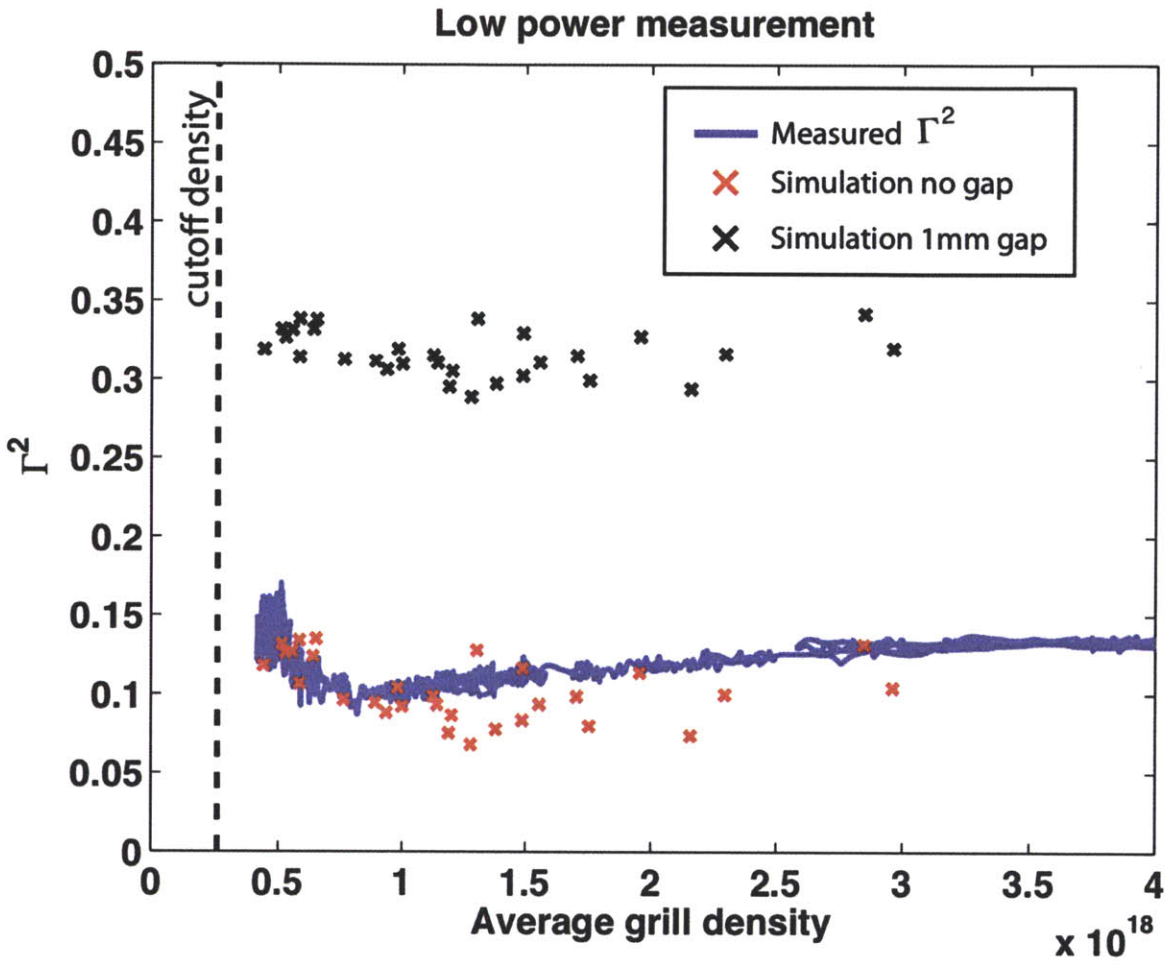

Figure 5-7: Reflection coefficients of the direct fed columns (7, 8, 9 and 10) for the low power measurements (90 deg. phasing, launcher 0.1 *mm* behind the limiter). Data collected during shot #1110204021.

the non-linear problem employs the conventional cold plasma wave equation where the density is modified by the ponderomotive potential. To find an analytic solution to the problem, previous work have further simplified Eq. 2.60 by considering only 1D geometries, often assuming only slow wave propagation and expanding the equation under the assumption of a monochromatic wave spectrum [9, 10, 11]. For our analysis instead, the solution was found by means of a fullwave finite element method (FEM) simulation in which the non linear coupling between the wave electric fields and the density depletion by ponderomotive forces is taken into account via an iterative approach. The new code has been named POND.

5.4.1 The POND code

POND solves the non-linear problem via the iterative approach depicted in Fig. 5-8. To start, the wave electric field is calculated by the FEM software COMSOL from the radial density profile in absence of the LH waves. The density perturbation is then calculated in MATLAB according to Eqs. 2.59 and 2.60 and averaged in the parallel direction. The resulting radial density profile is then used for the new iteration step, until the wave fields and the perturbed density profile reach equilibrium.

As we shall see, the overlapping of the LH resonance cones produces a 2D structure of the density depletion in front of the grill. In the experiment, one can expect the 2D structure of the density depletion to be blurred out by the effect of parallel particle transport, the perpendicular transport being assumed to be $D_\perp \ll D_\parallel$. As an order of magnitude estimate of $D_\parallel$, one can assume the edge temperature to be $\sim 10\ eV$, which corresponds to an electron speed of $v_e = \sqrt{\frac{2kT_e}{m_e}} \sim 2 \times 10^6\ m/s$, and translates to a distance $D_\parallel \sim v_e/f \sim 0.4\ mm$ traveled by the electrons in one wave cycle with a frequency of $f = 4.6\ GHz$. In other words, one can expect electrons to travel across about one waveguide in the time period of 20 wave oscillations. In the following study the density along the magnetic field line is assumed to be constant and equal to the average of the density calculated according to Eq. 2.59. This is not a limitation of the code itself (which allows the density to be specified arbitrarily at any point in space) but rather a simplifying assumption that avoids the problem of trying to pin down an accurate value for $D_\parallel$ and $D_\perp$.

It should be said that this problem could be solved within the COMSOL software itself. However, numerically this is not advantageous because averaging (i.e. integrating) the density perturbation in the parallel direction couples many of the unknowns in the system, which ultimately results into an hybrid sparse-dense algebraic system not suited for neither sparse nor dense matrix solvers. Performing such averaging procedure in MATLAB significantly speeds up the solution process, at the cost of iterating with COMSOL. Nonetheless this comes at no additional cost, since the process is non-linear also solving the whole problem within COMSOL requires stepping through iterations to solve the problem.

POND has been verified in 1D against the results published in Ref. [9]. In particular the density profile modification as a function of power was well reproduced, as show in Fig. 5-9. These authors also predicted the critical power for the onset of the nonlinear behaviour, defined as when the ponderomotive potential equals the kinetic potential, which for the Alcator C-Mod parameters one can calculate to correspond to a power density of $\sim 0.2\ kW/cm^2$ and a net forward power of $\sim 70\ kW$.

It is worth pointing out that the POND code is very generic and relies only on the assumption (in view of the expansion of Eq. 2.59) that the wave power is of the same order of the temperature, so that $\epsilon_0|E|^2/n_eT_e \sim O(1)$. Hence, even if in the following we restrict our analysis to LH waves, this method could in principle be used to investigate the effect of ponderomotive forces in other frequency ranges. The main advantage of using a FEM scheme is the possibility of extending the numerical simulations to 2D or even 3D. Also, FEM allow the electron density to be uniquely specified at any point in space thus allowing for the description of complicated geometries or non-uniformities in the

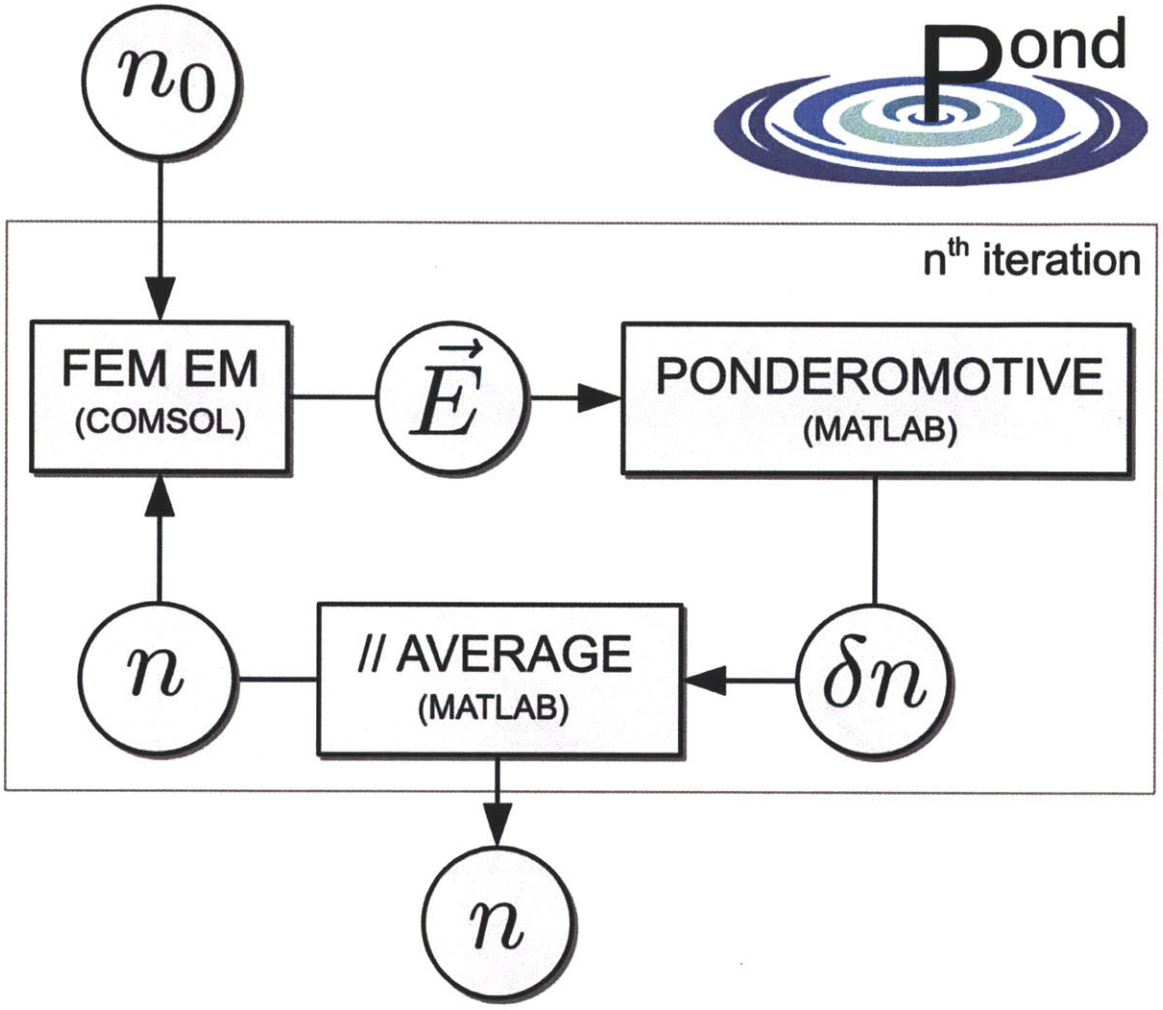

Figure 5-8: The POND procedure starts from the density profile in absence of LH waves and iterates between the EM solver COMSOL and Eq. 2.59, until the solution converges.

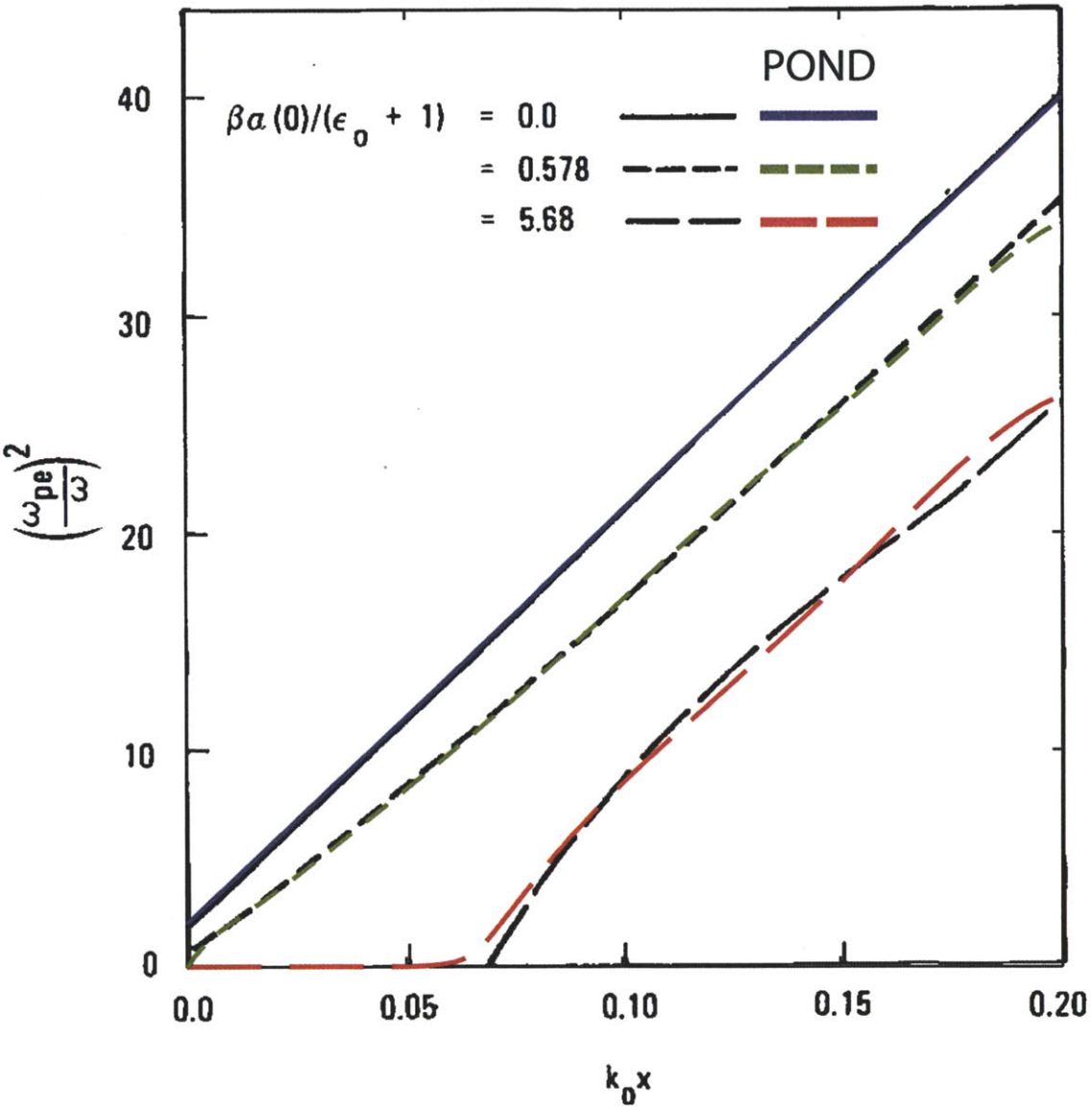

Figure 5-9: Comparison of the FEM approach with existing work. In this simulation only a single spectral component ($n_\parallel = 10$) is considered, only slow wave is present (both its electromagnetic and electrostatic components), $T_e = 10\ eV$, $T_i \sim 0$ and 2 power levels are compared. The starting density profile is linear. Plots have been normalized to allow over-plotting with published data from Ref. [9].

plasma.

An alternative approach for modeling the effect of ponderomotive forces in front of a grill antenna would be to use a Particle In Cell (PIC) code. In this type of codes individual particles (or fluid elements) are tracked in continuous phase space, whereas moments of the distribution such as densities, currents and fields are computed simultaneously on stationary mesh points. PIC codes have been already successfully applied to estimate near field effects of LH waves [135] and ponderomotive effects should be a natural byproduct of such calculation (although not pointed out by the authors). Nonetheless, PIC simulations are very computationally demanding. By comparison the FEM approach implemented in POND is significantly more efficient and scalable.

5.4.2 Comparison of POND with the Alcator C-Mod experiment

Using this exact same model the modification of the density profiles as measured on Alcator C-Mod was simulated. Starting from the density profile measured by reflectometer during ohmic phase, the density perturbation by ponderomotive forces was calculated and compared with the density profile measured by reflectometer during LH phase. Worth pointing is that the number of free parameters in this validation process is very limited. In the model, the LH net power density is set to be equal to average value in the experiment. The temperature is set to decay exponentially from 70 eV at the separatrix to the temperature measured by Langmuir probes at the edge.

The simulation results are shown in Fig. 5.4.2 as black traces. By comparing the modeling results to the experimental density profiles at the very edge of the plasma, one can state that these are consistent with the theory of ponderomotive forces being the cause of the density depletion measured in front of the launcher. The density depletion model of Eq. 2.59 only allows for the density to be reduced by the presence of the ponderomotive potential. The increase of density which is observed in the experiment cannot be reproduced by this model and additional processes must be included in the model.

As previously stated, the main advantage of using a FEM approach is that the same formulation can be seamlessly applied to more complicated geometries and is readily extendable to 2D or 3D. In particular, the extension to 2D or 3D allows more physics to be taken into account, namely the effect of a realistic $n_{\|}$ spectrum and the inclusion of higher order modes at the waveguides' openings (in view of the 2D nature of the model only modes which have no poloidal ($\hat{y}$) variations can exist (TEM, TM and TE_{x0}), which however are the ones known to have the largest contribution [94]). Also, other effects which could be seamlessly included in the analysis are $\vec{B}$ tilt, curvatures, and poloidal/toroidal non-uniformities.

The simulation results of the *first* iteration step of a 2D simulation corresponding to shot #1101118003 are shown in Fig. 5-10. In this simulation a grill composed of 16 active and two passive waveguides launches LH waves into the plasma.

Figure 5-10(A) shows the $\Re E_z$ component of the waves electric field along the magnetic field direction. The most striking feature of this picture are the resonance cones (main lobe going right, high $n_{\|}$ reverse lobes going to the left) that the wave forms inside of the plasma. An artificial damping term is used close to the boundaries of the plasma, away from the launcher, to avoid reflection at the boundaries of the simulation domain. Also visible are the higher order waveguide modes which are excited at the interface between the grill and the plasma. These modes are highly evanescent and decay fast for distances longer than the waveguide openings. The passive waveguides at each side of the launcher reflect the power which is coupled through the plasma with the addition of a phase difference of 90 degrees. Under the assumption that most of the power comes from the adjacent waveguide, the phasing of this waveguide is therefore consistent with a 90 degree phased waveguide array. This wave field results in the density depletion $\delta_n = (n_e - n_{e0})/n_{e0}$ depicted in Fig. 5-10(B).

A striking difference in respect with the 1D simulation results is an enhanced density depletion, driven by the standing wave pattern of the resonance cones in front of the grill. At the crossing

point of the forward and reverse resonance cones the wave fields become higher, ultimately resulting in a higher ponderomotive potential Φ_P (Eq. 2.60) and a larger δn (Eq. 2.59). This effect is the result of considering a realistic $n_\parallel$ spectrum to be launched into the plasma. By contrast, in the 1D simulation all of the power was assumed to be in a single $n_\parallel$ component of the spectrum. Worth pointing out is that for slab/toroidal geometries with uniform density along the field lines, instead of using a FEM code the 2D/3D wave fields could be obtained by the superposition of different $n_\parallel$ and n_y spectral components, of which the weighting coefficient should be provided by a coupling code.

Finally, a 3D simulation has been run to assess the effect of considering the finite height of the waveguides. The density profiles reported in Fig. 5.4.2 are evaluated at the waveguide midplane, that is the region of highest field. Little difference is observed between the 2D and the 3D simulation results. In a sense this result comes as no surprise, since the 2D simulations already includes the effect of the most important higher order modes at the antenna-plasma interface.

The final outcome of this extensive analysis in agreement with existing work [136, 9, 10, 11, 137]. The density depletion measured in front of the launcher is compatible with the effect induced by ponderomotive forces of LH waves. The innovative modeling method used in the POND code and the availability of SOL density depletion profiles have allowed an unprecedented strong validation of the ponderomotive theory.

Finding methods for controlling the electron density in front of the coupler are ultimately needed to obtain good coupling. Since the beginning of LH operations in 2005, the Alcator C-Mod LH system has been operating with private limiters which were installed fixed to the vacuum vessel walls, while the launcher was able to move independently of these. The results presented in this chapter have driven the design of a new set of LH launcher private limiters, which are mounted to the launcher itself, have been installed for the 2011-2012 campaign. As reported in Fig. 5-3, characterization of the LH2 coupling performances, showed that the reflection coefficient is a sensitive function of the radial position of the launcher, especially at higher phasing. Best coupling is systematically obtained when the launcher is closest to the plasma, and consequently, for most of that campaign the launcher has operated ~ 1 mm behind the protecting limiters or less. The minimum absolute radial position of the launcher has been realized to be a limiting factor for the coupling of LH waves on Alcator C-Mod. Furthermore, the old limiter design often imposed shaping constraints on the plasma in order to adjust for the antenna-plasma coupling. The new limiters will be movable with the launcher instead of being fixed to the vessel wall, thus allowing a greater flexibility in the positioning in the launcher with respect to the plasma. Also, by this design the LH launcher can be placed in front or behind the main limiters and other structures (e.g. ICRF antennas), allowing strong changes in the density scale lengths in front of the launcher. This aspect has been reported to be important for non-linear coupling effects on ToreSupra [138, 137]. The possibility to access higher temperature regions in the SOL plasma should also play a positive role at reducing the importance of non-linear effects.

(A)

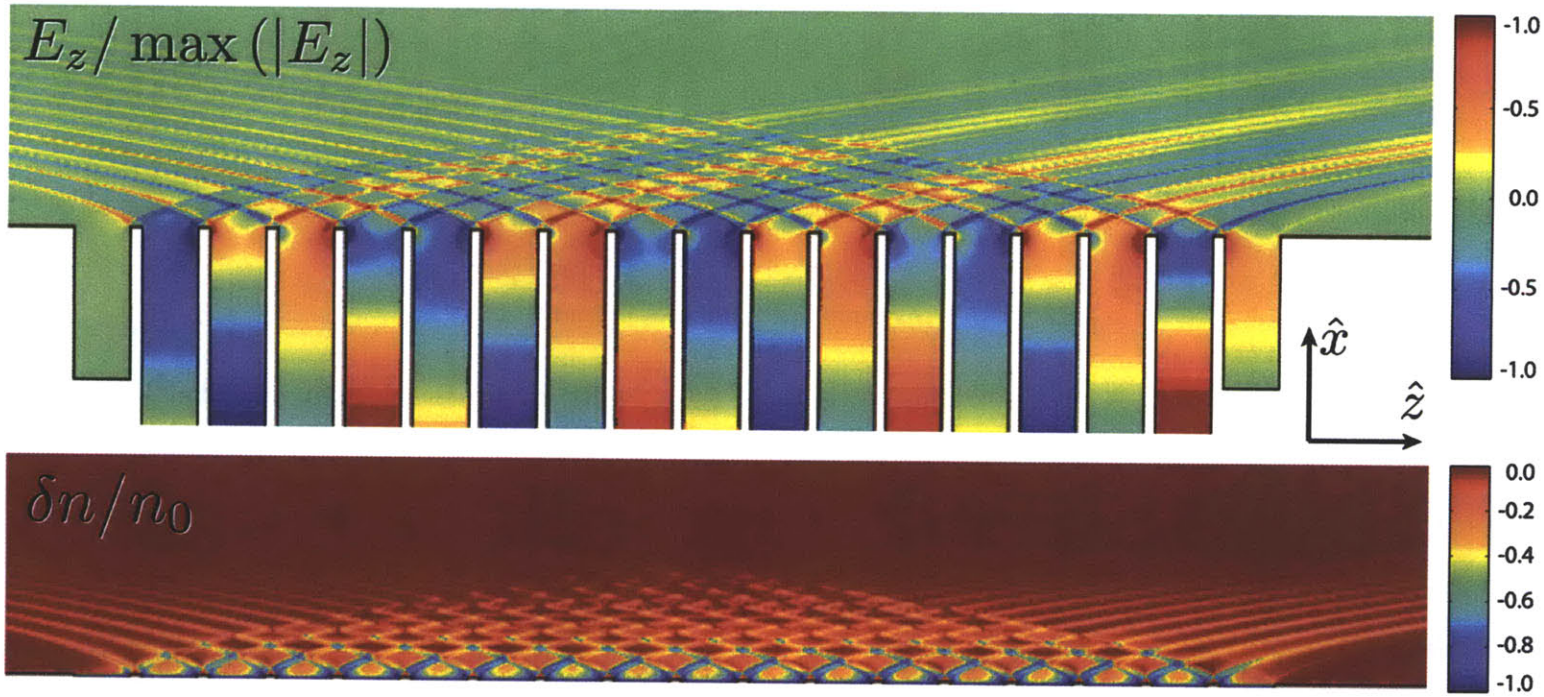

(B)

Figure 5-10: The electric field E_z (A), and density depletion $\delta_n = (n_e - n_{e0})/n_{e0}$ (B) are shown at the first step of the iteration of the 2D simulation corresponding to the low density case (shot #1101118003).

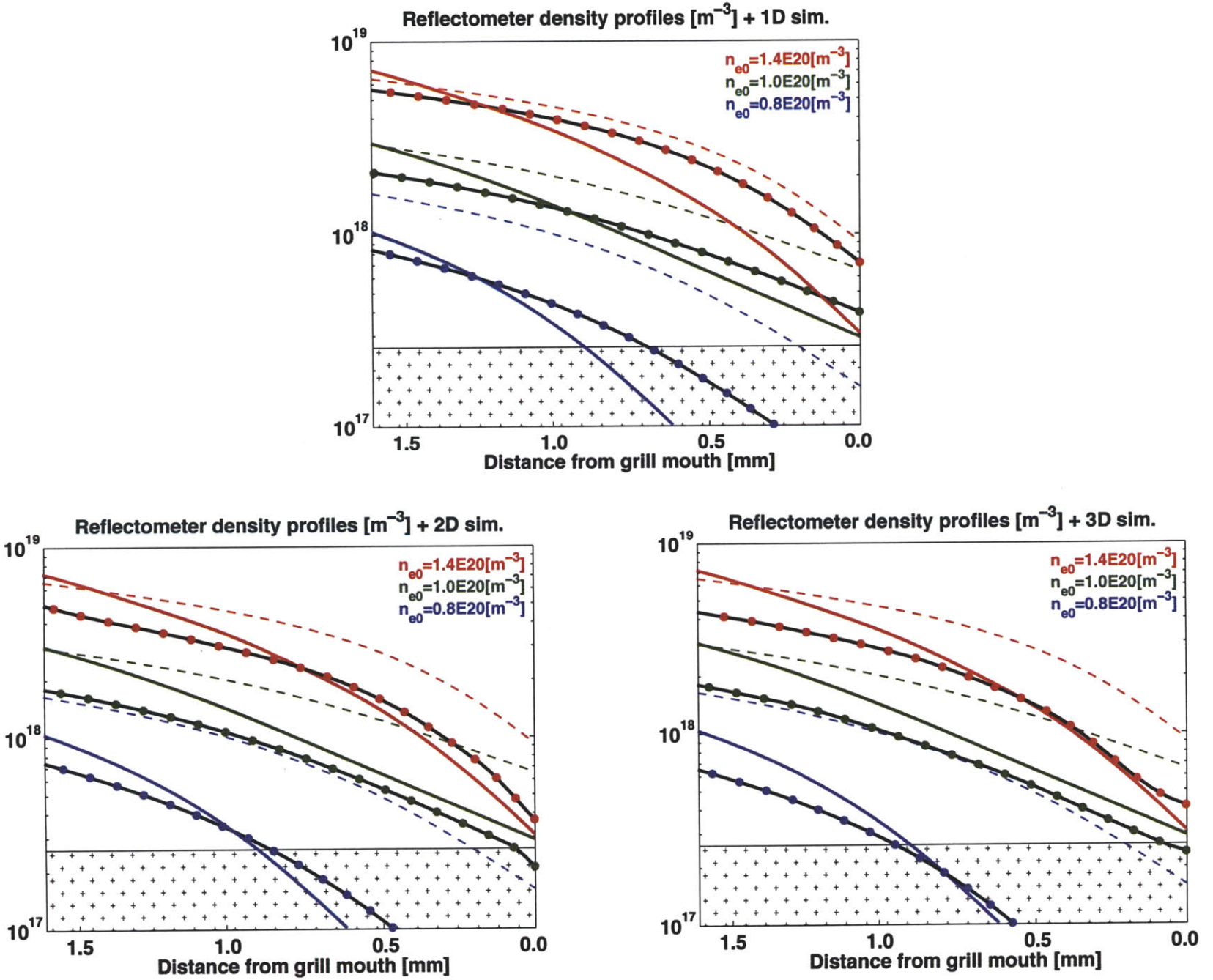

Figure 5-11: Dashed and solid lines represent the measured profile for *LH off* and *LH on*, respectively. The black lines with colored dots represent the respective density profile as calculated at final stage of 1D, 2D and 3D POND simulations.

Chapter 6

Integrated LHCD modeling with LHEAF

In the past, the analysis of the propagation and absorption of the LH wave has mostly relied on the ray-tracing technique which was introduced in Sec. 1.4.1. A variety of features of LH waves can be explained by ray-tracing, such as the increase and broadening of the parallel refractive index due to the toroidal geometry effect. In some regimes, good agreement with experimentally measured driven current profiles has been reported by coupling ray-tracing codes with Fokker-Planck solvers [139, 73].

At first the ray-tracing approach would seem to be entirely adequate, since the characteristic length of LH waves in plasma is several tens of times smaller than the dimensions of the system. However, rather marked fullwave effects may occur when the transverse dimension of the resonance cones becomes comparable with the wavelength. Such condition occurs both at the periphery of the plasma and in caustics. This causes the ray method to break down, with consequent diffractional blurring of the wave beams in both configurational space and spectral space. Whether fullwave effects can play an important role on the waves power absorption an current drive has been a long standing question and has motivated the development of fullwave simulation codes. The full wave approach properly treats wave behavior in regions where the WKB approximation is not satisfied and describes physical phenomena correctly such as partial reflections, interference, and scattering which are not addressed by ray-tracing. Also, the full wave approach allows evanescent fields to exist in regions where the plasma density is below cutoff.

In dispersive media, such as a hot plasma, the Helmholtz equation has the form of an integro-differential equation. Since a convolution integral in the real space domain can be expressed as a product in the spectral domain, the Helmholtz equation has an algebraic form, and for this reason the spectral domain has been the natural choice for implementing fullwave codes. This approach has achieved great successes in modeling plasma waves in the ICRF frequency range and in the Alfvèn wave frequency range [140, 141, 89]. However, in the LH frequency range, the characteristic short wavelength of the waves makes the electro-magnetic problem so large that the number of unknowns can become intractable even when modeling small devices. Although recent progress in computational technology has softened these limitations to a large degree, the spread of the wave spectrum is so wide that massive parallel computing is required to address the problem [142, 143, 15]. In addition, since spectral solvers represent the solution in terms of basis functions, they have difficulty in accurately representing the tokamak vessel or the launching antenna structure, and their use is mostly limited to the description of the core plasma.

In this chapter, a different approach to solve Maxwells equations directly in the real space is presented. For this purpose, a numerical code named LHEAF (Lower Hybrid wavE Analysis based on FEM) [12, 13] has been developed. The main benefits of this code are a significant reduction

of the computation requirements and a seamless handling of the SOL and launcher regions. First the formulation at the base of LHEAF and some details about its numerical implementation are presented. LHEAF simulations are then compared with ray-tracing calculations for a Maxwellian tokamak plasma with a circular cross-section and for an ITER plasma. Next, the coupling to Fokker-Planck codes is explained and the code validation for an Alcator C-Mod discharge is shown. In the last chapter of this thesis, LHEAF is finally used to investigate the origin of the LHCD density limit.

6.1 LHEAF formulation

The propagation of LH waves is well described by the magnetized cold plasma approximation, while their absorption is governed by the electron landau damping (ELD) process. Within the cold plasma approximation the time harmonic wave equation is a conventional Partial Differential Equation (PDE). However, the ELD term depends on the parallel wave number k_z, meaning that this effect is non-local and consequently, the wave equation has an integro-differential form. Directly solving this equation corresponds to solving a large dense matrix and requires a large computational effort.

LHEAF deals with this issue by adopting two analysis techniques. First, the convolution integral is treated in an explicit manner by splitting the original integro-differential equation into two coupled equations which are solved iteratively, the idea being that the ELD term is approximated by an effective local damping. The resulting electromagnetic problem has the form of a conventional PDE which can be efficiently solved by a conventional 3D FEM solver. Second, assuming that the tokamak plasma axisymmetric, the electric field is decomposed into its toroidal mode numbers. This is a standard technique used by fullwave spectral codes [140, 144] and is known as *single mode analysis*. However its implementation in a 3D FEM code is new [14] and it is based on the use of periodic boundary conditions to specify the toroidal mode number.

The LHEAF code has been developed based on the RF module of COMSOL Multiphysics [99] and the MATLAB [145] technical computing environment. One of the main advantages of using a commercial software package is the availability of a well established platform. Developers of commercial software packages are committed to updating and optimizing their software for the latest computing technologies (e.g. new solvers, new algorithms, multi-core parallelism, massively parallel computing, etc.) as this helps to ensure successful market share for that product. The user can therefore focus on the study of the physics of the problems, leaving aside the difficulty of coding and debugging a piece of complex simulation software.

6.1.1 Iterative solution for the inclusion of ELD

In general, the plasma dielectric tensor depends on the wave vector $\vec{k}$ and the wave equation Eq. 1.7 expressed in the real space results in the integro-differential equation:

$$\nabla \times (\nabla \times \vec{E}) + \frac{\omega^2}{c^2} \frac{1}{(2\pi)^{(3/2)}} \int d\vec{x'} \bar{\bar{\epsilon}}(\vec{x} - \vec{x'}) \cdot \vec{E}(\vec{x'}) = 0. \tag{6.1}$$

In Chap. 2 it was shown that the propagation of the LH waves is well described by the magnetized cold plasma approximation, while their absorption is governed by the electron landau damping. Within this approximation, the ELD term depends only on the parallel component of the wave vector and contributes to the imaginary part of the parallel term of the dielectric tensor as described in Sec. 2.2.1. For a Maxwellian plasma $\epsilon_{\mathrm{ELD}}(k_\parallel)$ has an analytic expression:

$$\epsilon_{\mathrm{ELD}}(k_\parallel) = \sqrt{\pi} \frac{\omega_{pe}^2 \omega}{|k_\parallel|^3 v_{Te}^3} \exp\left(-\frac{\omega^2}{k_\parallel^2 v_{Te}^2}\right) \tag{6.2}$$

whereas, for a generic distribution function:

$$\epsilon_{\mathrm{ELD}}(k_{\parallel}) = -\frac{\omega_{pe}^2 2\pi}{\omega^2}\int_0^{\infty} v_{\perp}dv_{\perp}\,\frac{\omega^2}{k_{\parallel}^2}\frac{\partial f}{\partial v_{\parallel}}\bigg|_{v_{\parallel}=\frac{\omega}{k_{\parallel}}} \tag{6.3}$$

where non-Maxwellian electron velocity distribution arising from the interaction of the LH waves with the plasma, must be self-consistently calculated by a means of Fokker-Planck codes, as explained in Sec. 6.5.

In the following expressions the background magnetic field is assumed to be in the $\hat{z}$ direction, but the general expression for an arbitrary direction of the magnetic field lines can be obtained by an appropriate coordinate system rotation.

Directly solving the original integro-differential equation Eq. 6.1 corresponds to solving a large dense matrix and would require large computational power [89]. Instead, in LHEAF the problem is split into two coupled equations which are solved iteratively. The workflow of the LHEAF code, for a Maxwellian plasma is shown in Fig. 6-1. The main idea behind this approach is that the ELD term can be approximated by an effective local damping $\bar{\bar{\epsilon}}_{\mathrm{ELDeff}}$ [1]. The resulting equation is a conventional PDE which can be solved by a conventional 3D FEM solver. The value of the effective local damping is then found iteratively, by successive refinements of an initial guess. According to this scheme, at the N^{th} step of the iteration loop, the electric field $E^{(\mathrm{N})}(z)$ is computed by solving:

$$\nabla\times(\nabla\times\vec{E}^{(\mathrm{N})}(\vec{x})) + \frac{\omega^2}{c^2}\left(\bar{\bar{\epsilon}}_{\mathrm{cold}} + \bar{\bar{\epsilon}}^{(\mathrm{N})}_{\mathrm{LEDeff}}\right)\cdot\vec{E}^{(\mathrm{N})}(\vec{x}) = 0 \tag{6.4}$$

Subsequently, an updated value of $\bar{\bar{\epsilon}}^{(\mathrm{N+1})}_{\mathrm{ELDeff}}$ is computed as a one dimensional convolution integral along the magnetic field lines:

$$\bar{\bar{\epsilon}}^{(\mathrm{N+1})}_{\mathrm{ELDeff}} = \frac{-i}{E^{(\mathrm{N})}}\frac{\hat{z}\hat{z}}{\sqrt{2\pi}}\cdot\int dz'\epsilon_{\mathrm{ELD}}(z-z')E_z^{(\mathrm{N})}(z') \tag{6.5}$$

and is substituted into Eq. 6.4 to find the electric field at the next step of the iteration. This procedure is repeated until the power deposition converges. An initial value for $\bar{\bar{\epsilon}}^{(1)}_{\mathrm{LEDeff}}$ is calculated, by assuming that there is no spread of the parallel wavenumber and that the parallel wavenumber k_z in Eq. 2.16 is equal to the toroidal wavenumber k_{tor}. Here, the value of $\epsilon_{\mathrm{ELD}}(z)$ is evaluated by taking the numerical FFT of $\epsilon_{\mathrm{ELD}}(k)$.

$$\epsilon_{\mathrm{ELD}}(z) \equiv \int dk_z \mathrm{Im}(\epsilon_{zz}(k_z))e^{-ik_z z} \tag{6.6}$$

Figure 6-3 shows the normalized $\mathrm{Im}(\epsilon_{zz}(k_z))$ and the associated $\epsilon_{\mathrm{L}}(z)$ for temperatures of 1 keV and 10 keV. It is noteworthy to point out how the wide spread of $\mathrm{Im}(\epsilon_{zz}(k_z))$ in the spectral domain translates into the limited domain of $\epsilon_{\mathrm{L}}(z)$ in the real space domain. For the temperature range of interest for tokamak plasmas, the domain over which $\epsilon_{\mathrm{L}}(z)$ has non negligible value is always in the range of few centimeters.

Alternatively[2], the convolution integral of Eq. 6.5 can be cast into a product in Fourier space that is subsequently inversely-Fourier transformed to real space

$$\int dz'\epsilon_{\mathrm{ELD}}(z-z')E_z^{(\mathrm{N})}(z') = \int dk_z \mathrm{Im}(\epsilon_{zz}(k_z))E_z^{(\mathrm{N})}(k)e^{-ik_z z} \tag{6.7}$$

[1] An alternative interpretation of $\bar{\bar{\epsilon}}_{\mathrm{ELDeff}}$ in therms of wavelet analysis is given in Sec. D.2.2

[2] Both of these methods (convolution integral in real space and product in spectral space) have been implemented and their numerical equivalence successfully tested.

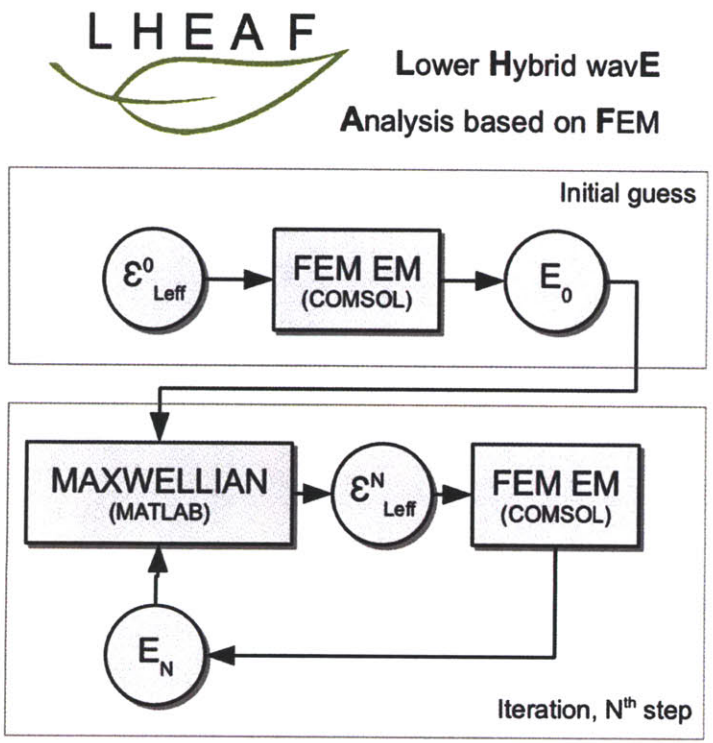

Figure 6-1: Schematic of the iterative procedure for a Maxwellian plasma, as it has been implemented using COMSOL for the solution of the wave equation and MATLAB for the evaluation of the effective local damping term $\bar{\bar{\epsilon}}_{\mathrm{ELDeff}}$.

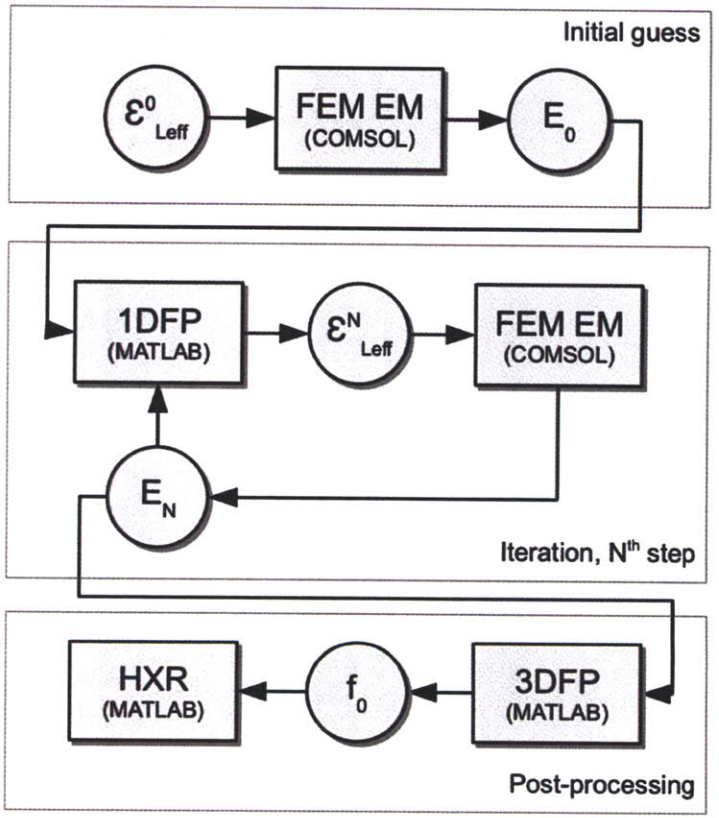

Figure 6-2: For the case of a non-Maxwellian plasma, a 1DFP code is included in the iteration loop to account for the effect of an electron distribution function distorted by the RF fields on the wave absorption. A 3DFP code is used as a postprocessing to evaluate the distribution function in 2D velocity space. An HXR synthetic diagnostic allows a direct comparison with the experiments.

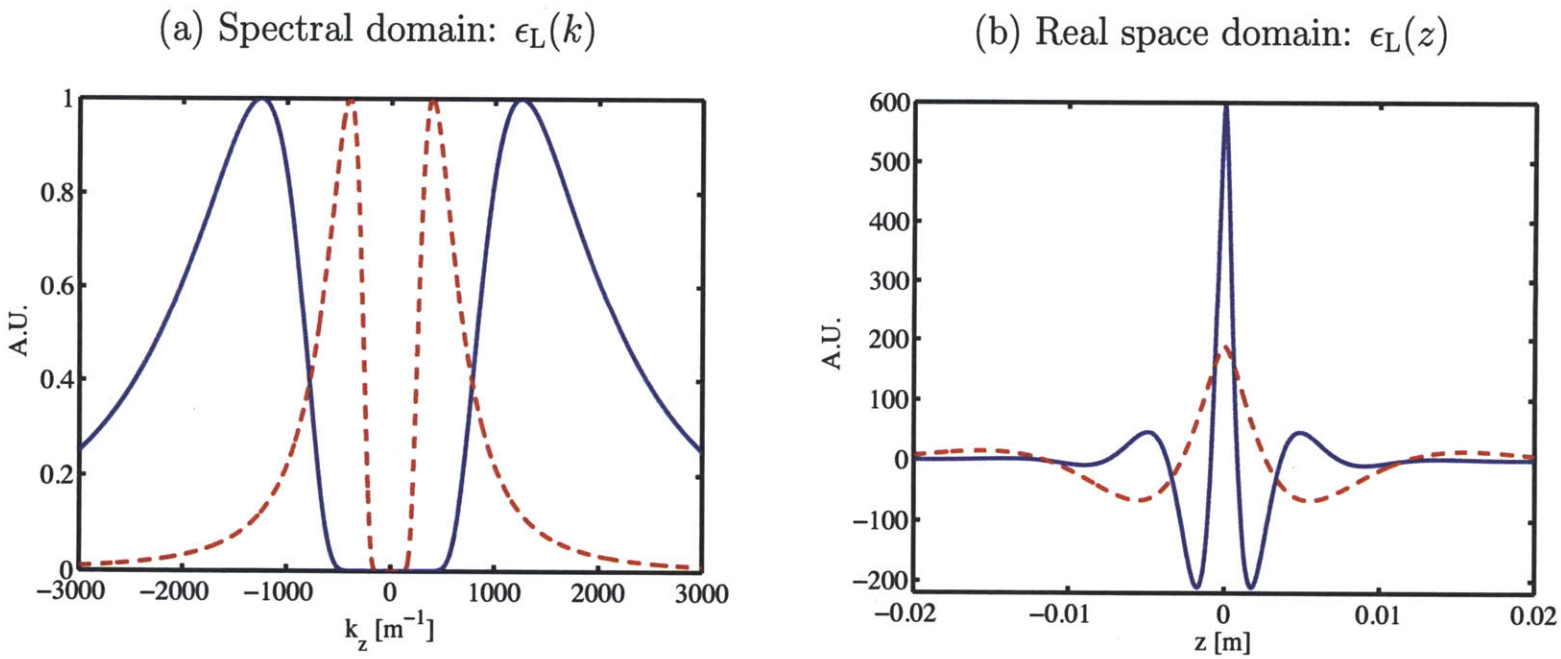

Figure 6-3: (a) The imaginary parallel component of the dielectric tensor in the spectral domain $\mathrm{Im}(\epsilon_{zz})$, and (b) the corresponding convolution kernel in the real space domain $\epsilon_L(z)$ for the electron temperature of 1 keV (blue-solid) and 10 keV (red-dashed). In these figures the wave frequency is 4.6 GHz.

where $E_z^{(N)}(k)$ is the Fourier transform of the parallel electric field along the magnetic field line. Numerically, this approach is significantly faster $O(N \log N)$ compared to a numerical convolution $O(N^2)$ in view of the higher numerical efficiency of the Fast Fourier Transform (FFT) algorithm.

6.1.2 Toroidal symmetry and single toroidal mode analysis in 3D FEM

Tokamaks are characterized by an azimuthal (rotational) symmetry which allows a Fourier analysis of the electromagnetic fields in the toroidal direction

$$\vec{E}(x,y,\phi) = \sum_{n=-\infty}^{\infty} \vec{E}_n(x,y) e^{-in_\phi \phi} \tag{6.8}$$

where n_ϕ is the toroidal mode number.

Theoretically, a wave with a single toroidal mode number could be launched in a tokamak geometry by an infinite number of infinitesimally thin phased waveguides. LHEAF exploits this simple idea to solve for the wave electric field of a single toroidal mode in a 3D FEM solver [114]. However in the actual numerical implementation the waveguides must be allowed to have a finite toroidal extent. The penalty for this approximation is a small spread in the toroidal mode of the waves which are allowed to propagate inside the torus. A plot of the toroidal spectrum as a function of the number of waveguides around the torus of is shown in Fig. 6-5. As the waveguides become thinner and their number increases, the spectrum of the main lobe narrows and the toroidal mode number of the side lobes increases.

If a single toroidal mode is allowed to propagate inside of the torus, there is a known phase relationship of $e^{-in_\phi \Delta\phi}$ between the fields at two different toroidal locations which are $\Delta\phi$ radiant apart from each other. In a 3D FEM solver, such a relationship can be imposed by applying *Floquet-Bloch* periodic boundary conditions [146] at the sides of the toroidal slice.

6.2 Numerical implementation

Our current implementation uses the RF Module of COMSOL Multiphysics and MATLAB. In this integrated environment, the former solves the EM problem at each step, while the latter sets up the iterative solution and calculates the effective local damping. COMSOL allows the definition of the full 3D dielectric tensor of a spatially varying media which is necessary to model the harmonic propagation of waves in a cold magnetized plasma. With COMSOL the exact shape of the tokamak first wall and of the antenna launching structure are included in the model. Also, the toroidal helical magnetic field topology and the plasma density can be directly input from experimental measurements.

6.2.1 Boundary conditions

The boundary conditions used in COMSOL are here described based on a sample geometry similar to the one highlighted in red in Fig. 6-4. The Floquet-Bloch periodic boundary conditions (green and blue boundaries in the Fig. 6-6a) have been implemented by means of extrusion coupling variables and perfect magnetic conductor boundary conditions. This technique was validated using a known analytic solution, as reported in [114]. Other boundary conditions used in the models are the Perfect Electric Conductor (PEC), the continuity of the tangential fields, and the input port (i.e. the incident wave launched in the waveguide), as shown in the following Fig. 6-6b,c,d respectively.

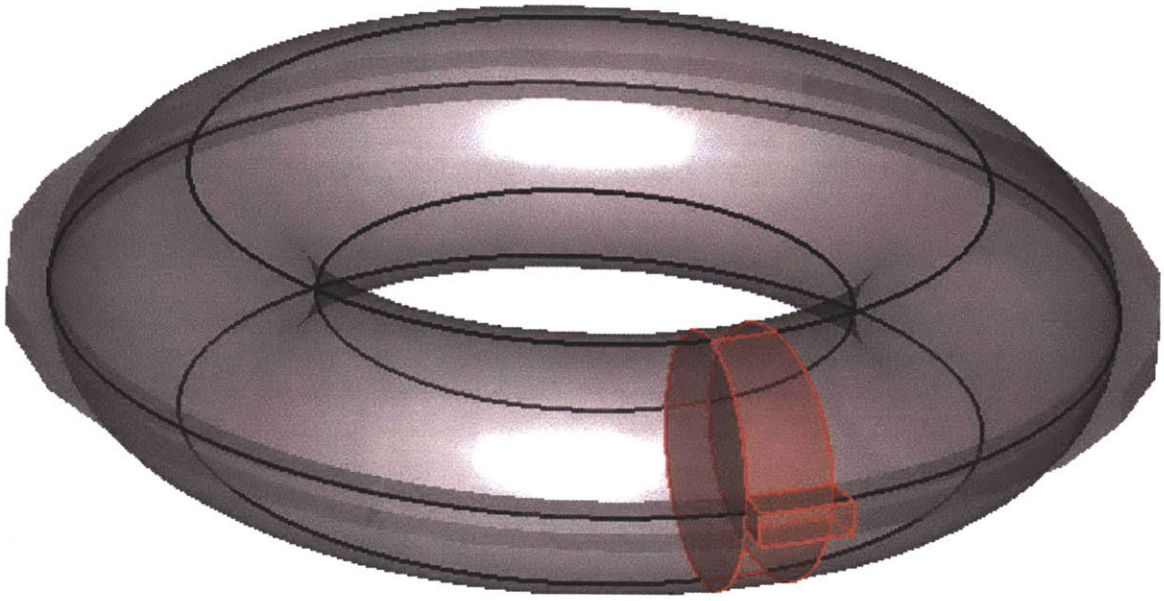

Figure 6-4: Schematic of a tokamak having a circular cross section and a waveguide launching structure on the low field side. A sector including the tokamak vessel and its associated waveguide are highlighted.

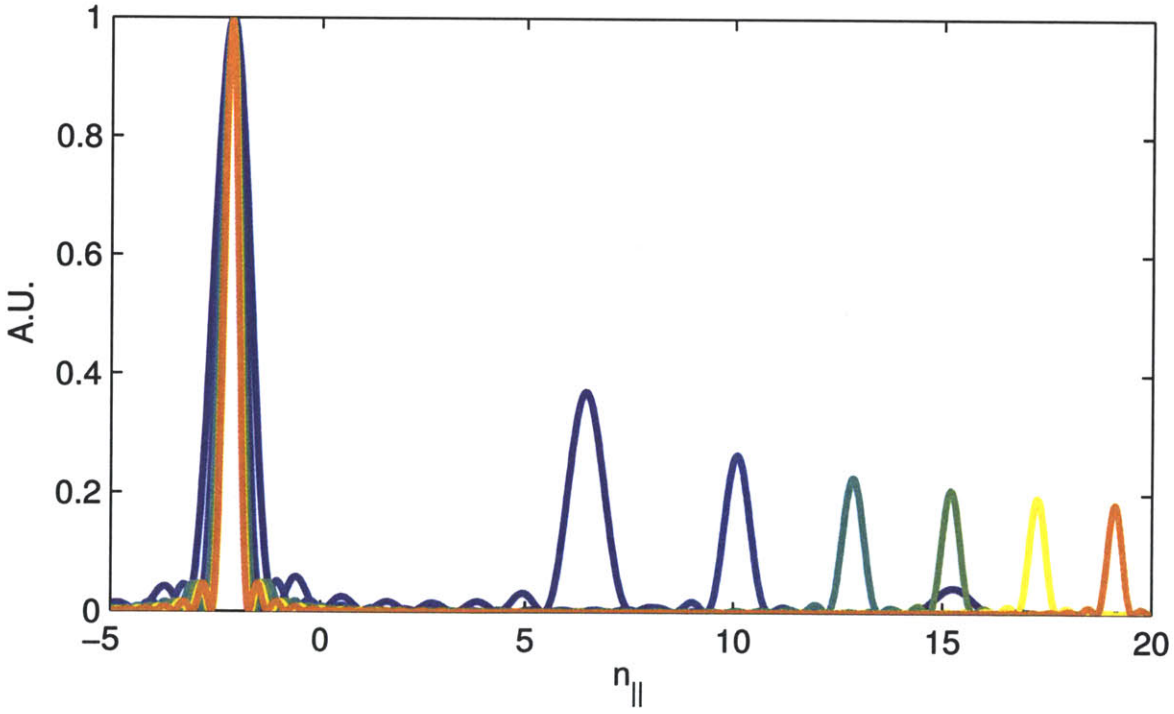

Figure 6-5: The launched spectrum tends to a delta function as the angular extent of the sector becomes thinner (main lobe becomes more peaked and the side lobes move to higher $n_{\|}$ and their energy content becomes smaller). The phasing among the waveguides in each sector is modified such to keep the main $n_{\|}$ lobe to be constant.

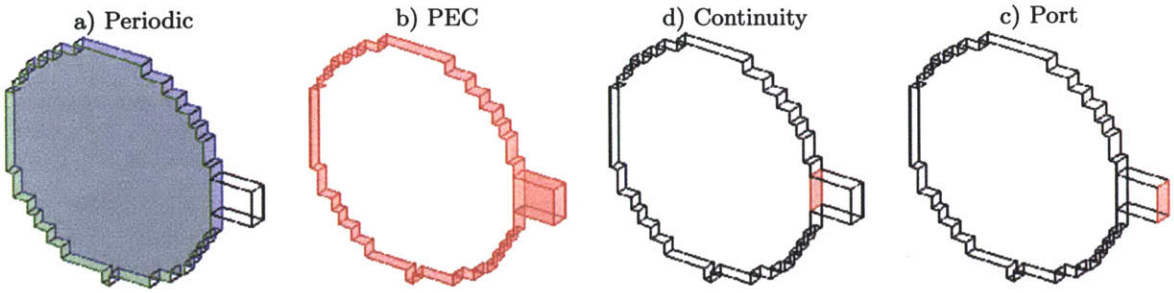

Figure 6-6: Boundary conditions used in the COMSOL model to solve for single toroidal mode propagation of LH waves launched by a grill antenna.

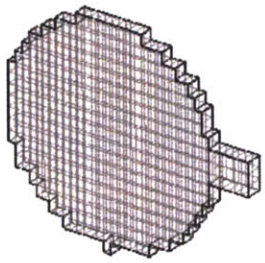

Figure 6-7: Sample of a cubic mesh used in LHEAF. The mesh is only one element thick in the toroidal direction. For the sake of illustration the mesh element size is much larger than the one used in actual simulations, where the cubic element sides are usually $< 1\ mm$.

6.2.2 Meshing

In COMSOL, the electromagnetic problem solved on a 1^{st} order polynomial vector finite elements, associated to a uniform hexahedral (or cubic) mesh. In the case of electromagnetic waves propagating into an anisotropic medium (the magnetized plasma) FEM methods lead to sparse, complex, non-symmetric linear systems. When doing single toroidal mode analysis in COMSOL a single mesh element is used to discretize the infinitesimally thin sector in the toroidal direction. Since the relationship between the solution on the two sides of the slice is known, the 3D problem effectively reduces to a 2D problem, meaning that the number of unknowns is almost cut in half. For the sake of illustration, a sample (very coarse) cubic mesh of the poloidal cross-section highlighted in the geometry of Fig. 6-4 is shown in Fig. 6-7.

To properly resolve the waves, the grid size and/or mode resolution used in the numerical method must be adequate to resolve the shortest wavelength in the system. In the particular case of LH waves, the wavelength arising from the propagation in plasmas is rather short ($\sim mm$) compared to the device size ($\sim m$), thus making the electromagnetic problem very large. Consequently in general these models require a large number of Degrees of Freedom (DoF) for the wave fields to be solved correctly. We studied the scalability of the LHEAF approach, and we investigated the possibility of using massive parallel computer for solving extremely large problems.

6.2.3 Scalability of the LHEAF approach

In LHEAF the numerical solution of the EM problem corresponds to the solution of a cold plasma propagation and hot plasma effects are treated iteratively. The resulting numerical problem scales more favorably to large scale plasmas when compared with spectral techniques. In the following the

scaling of different fullwave approaches is evaluated as a function of the linear size of the device (i.e. its major radius R, assuming a constant aspect ratio $\epsilon = a/R$). The scaling of the solution time of solvers other than FEM is deduced under the conservative assumption that the computational requirements are dominated by the inversion time of the linear system and not by the filling of the system itself.

A common way to solve large sparse linear systems is to use iterative techniques. However we opted for using direct solvers, the reason being that electromagnetic problems in plasma lead to ill conditioned linear systems (due to the high contrast of refractive index) thus making the convergence rate slow. Furthermore, it is known that iterative methods to not converge at all when "Floquet-Bloch" periodic boundary conditions were present. For these reasons we opted for a direct solution of the linear system for single toroidal mode analysis problems.

The time required for inverting a sparse matrix strongly depends on the fill-in of the system. Sparse linear system solvers such as UMFPACK [147], PARDISIO [148] and MUMPS [149] use advanced pre-ordering algorithms to minimize the fill-in. We compared the time required to solve the problem with the MATLAB UMFPACK solver with and without the Approximate Minimum Degree (AMD) [150] pre-ordering scheme. We found the solution time to scale almost linearly $O(N_{\mathrm{DoF}}^{1.12})$ with the number of DoF when AMD is used. The PARDISIO and MUMPS solvers gave similar or better results than UMFPACK with pre-ordering. Since the number of DoF is proportional to the cross-sectional area, we conclude that the FEM approach scales as R^2, where R is the major radius of the device. Figure 6-8 shows the time required to assemble and solve the linear system as a function of the DoF on a desktop computer equipped two 3.0 GHz quad-core CPUs and with 96 GB of RAM. On such configuration we routinely solve problems with more than 30 million unknowns. For these models with a larger number of unknowns use of massive parallel computing resources is necessary. In these cases the linear system is assembled on the aforementioned Desktop computer and then sent to the National Energy Research Scientific Computing Center (NERSC) where they are inverted by aid of the MUMPS library.

6.2.4 Scalability of spectral based approaches

Spectral domain solvers represent the solution in terms of basis functions which are defined over the computational domain they are applied to, thus resulting in linear systems which are full. A fully spectral approach, as implemented in the AORSA [89] code, uses a spectral basis set that is (k_x, k_y), and will result in full linear system. For a matrix of size $N \times N$, the cost of performing Gaussian elimination is equal to $2/3\,N^3$. Consequently we can expect the solution time to scale as R^6, the number of DoF being proportional to R^2 and the solution time of a full linear system scaling as the cube of the number of matrix elements. On the other hand, a semi-spectral code such as TORIC-LH [88], is based on an (r, m) basis set and uses a 1D finite element approach in the radial direction and a 1D spectral approach in the poloidal direction. The resulting numerical system for this approach is block-diagonal. The computational work to solve such a system scales as $N_f M^2$, where N_f is the number of flux surfaces and M is the number of poloidal modes used to represent the solution. Since the number of poloidal modes required to represent the solution with a given spatial accuracy scales linearly with the size of the device, we can deduce that this approach scales as R^3.

6.3 Alcator-C mockup model for a Maxwellian plasma

The first step for the validation of the LHEAF code has been to model a simple mockup experiment which could be easily compared among other codes. With this in mind, we modeled a tokamak plasma based on the parameters of the Alcator C experiment [151, 152]. The model has a major radius of 0.64 m, a circular cross section with minor radius 0.17 m and close fitting perfectly conducting walls. The toroidal field is 8 T, the plasma current is 400 kA, and the central electron density is 5×10^{19} m^{-3}. The density and temperature profiles are parabolic. A single 6 cm high

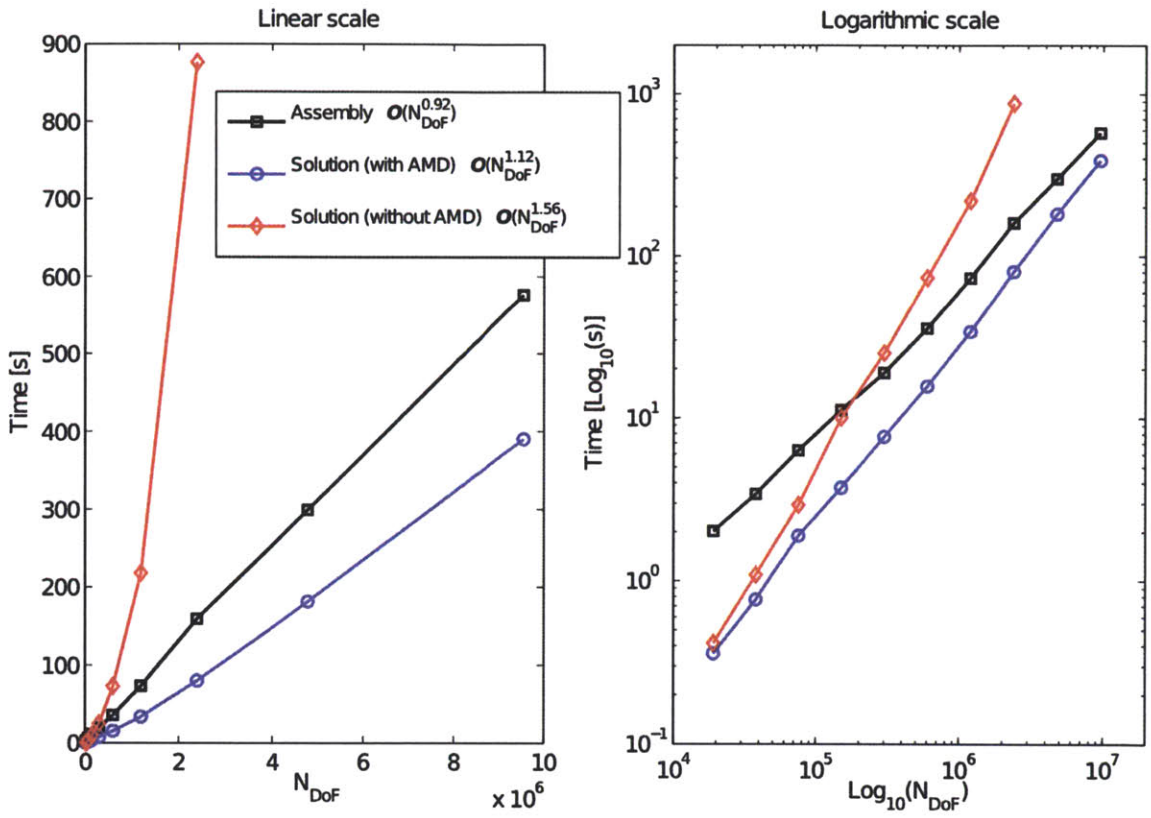

Figure 6-8: Linear and logarithmic plot of the time required for assembly and for the solution of the FEM problem as a function of the number of DoF. We compared the time required to solve the problem with the MATLAB UMFPACK solver with and without the Approximate Minimum Degree (AMD) pre-ordering scheme. We found PARDISIO and MUMPS to give similar result to UMFPACK with pre-ordering.

wave guide located on the low field side of the torus couples the microwave power at 4.6 GHz with a toroidal refractive index $n_{\rm tor}(= ck_{\rm tor}/\omega)$ of 2.5. This model has been used to cross validate several LH codes including LHEAF and a ray-tracing code [12], TORIC-LH [13] and AORSA [15].

Figure 6-9 shows the fullwave calculation of the wave electric field from LHEAF and the ray trajectory as calculated by a ray-tracing code. Three rays are launched: from the top, middle, and bottom of the wave guide. The comparison indicates good agreement between the wave field and the ray trajectories.

Figure 6-10 shows the dependency of the parallel electric field on the temperature, and it can be seen that as the temperature increases, the wave damping becomes stronger. Figure 6-11 shows the flux surface averaged power absorption profile corresponding to the four cases of Fig. 6-10. In Fig. 6-11 (a), overlaid are the power deposition profiles as calculated by the ray-tracing code. It can be seen that as the temperature increases the deposition profiles clearly shift towards the plasma edge, consistent with the physical picture where less k_z up-shift is required for the wave damping as the temperature increases. We also compared our result with the spectral code TORIC-LH [15] in Fig. 6-11 (b). The results from the three codes show good agreement. Those three codes are designed to implement essentially the same physics model, namely the wave propagation by the cold plasma and the absorption by ELD, but all based on different approaches, and their agreement strongly suggests that the physics model was implemented correctly. A small discrepancy remains between the codes for the lowest temperature case, which is not in the single pass absorption regime, as shown in Fig. 6-10. Although the ray approximation may be questionable in this case, the difference between LHEAF and TORIC-LH must be investigated in future work.

Several convergence studies have been carried out and this method has been proven to be resilient to the initial solution, though a reasonable first guess ensures a fast convergence. In all cases reported, five iterations have been enough to reach a converged solution. Each complete iteration required about 20 minutes on a desktop computer with two quad-core 3 GHz Intel Xeon processors and 16 GB of RAM.

6.4 ITER advanced scenario for a Maxwellian plasma

We present the single toroidal mode simulation of LH waves as they propagate in a poloidal cross section of the ITER tokamak. For the first time a fullwave simulation of LH waves in a realistic ITER plasma has been done, proving the scalability and flexibility of the LHEAF code.

The ITER LHCD system is planned to operate at 5 GHz and launch 20 MW into the plasma via a Passive Active Multijunction (PAM) antenna [153] with a parallel launched spectrum peaked at $n_{\|} = 2 \pm 0.1$. The ITER LH launcher will be made of 4 identical PAM blocks containing 12 rows of waveguides each. Each row will consist of 24 active waveguides (9.25×58 mm) alternating with 25 passives waveguides (7.25×58 mm). All waveguides are separated by 3 mm toroidal and 1 cm poloidal septa. With this arrangement, the forward power density is of about 11 MW/m^2.

In ITER the distance from the last closed magnetic flux surface ($R_{\rm LCFS} \approx 8.18$ m) to the first wall will be at least 12 cm in order to avoid excessive heat load from the plasma. The wide SOL is expected to play an important role in the coupling and propagation of the LH waves. At the launcher location, the electron density is expected to be below the cutoff density of the slow wave ($n_{\rm c} = 3.1 \times 10^{17}$ m^{-3} at 5 GHz). Experiments on ASDEX [120] and JET [154, 155, 156] used local gas injection in the SOL to increase the electron density in front of the launcher above the slow wave cutoff density and improve the slow wave coupling. Similar techniques are likely to be used in ITER.

In the following we will focus on only one top part of the antenna system (12 top rows), as proposed for the first phase of the ITER LH system [157]. The design of the LH launcher is still under way and for this simulation we assumed the launcher profile to be conformal to the flux surfaces and to be located at $R_{\rm ANT} = 8.3$ m at the midplane, 12 cm away from the LCFS. For this

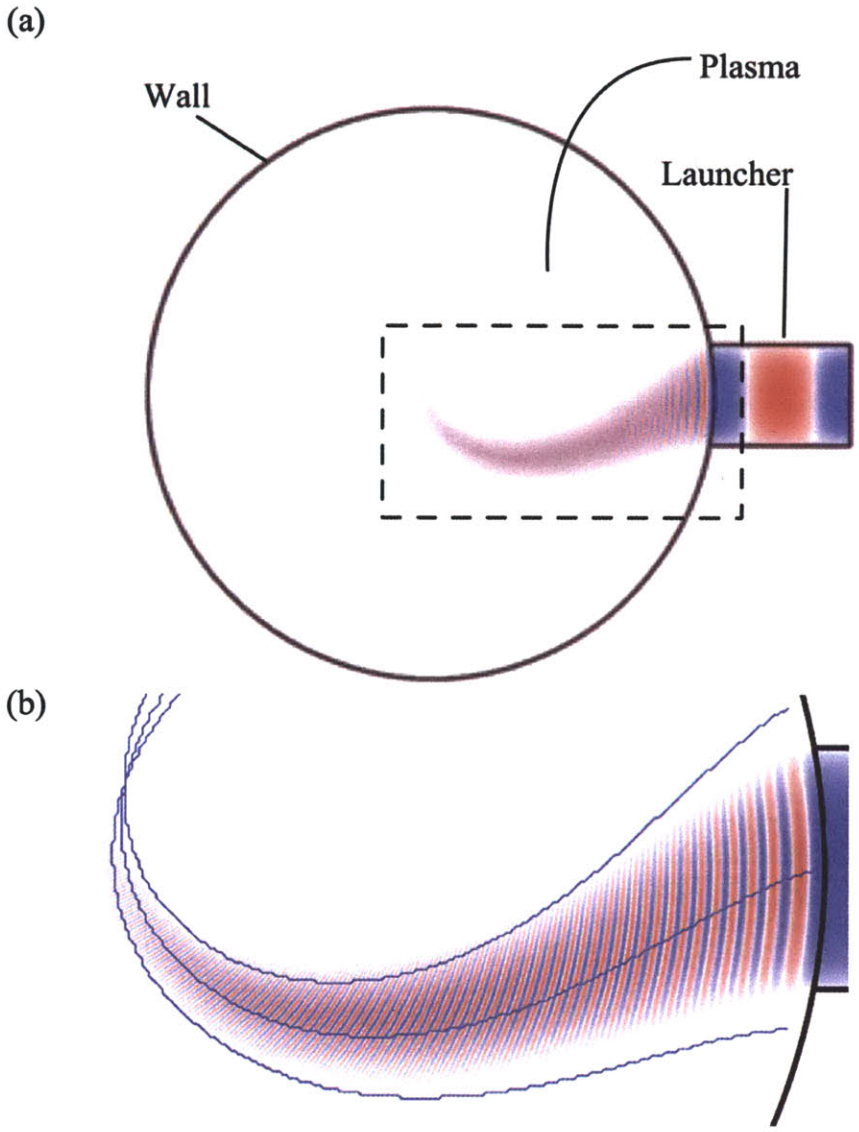

Figure 6-9: (a) In the fullwave simulation, the waves propagate through the wave guide structure as TE_{10} mode. The seamless handling of the coupler and the plasma regions allows one to take into account the reflection from the plasma. (b) Detail, showing a snapshot of the parallel electric field as calculated by the fullwave code and the ray trajectories as calculated by the ray-tracing code.

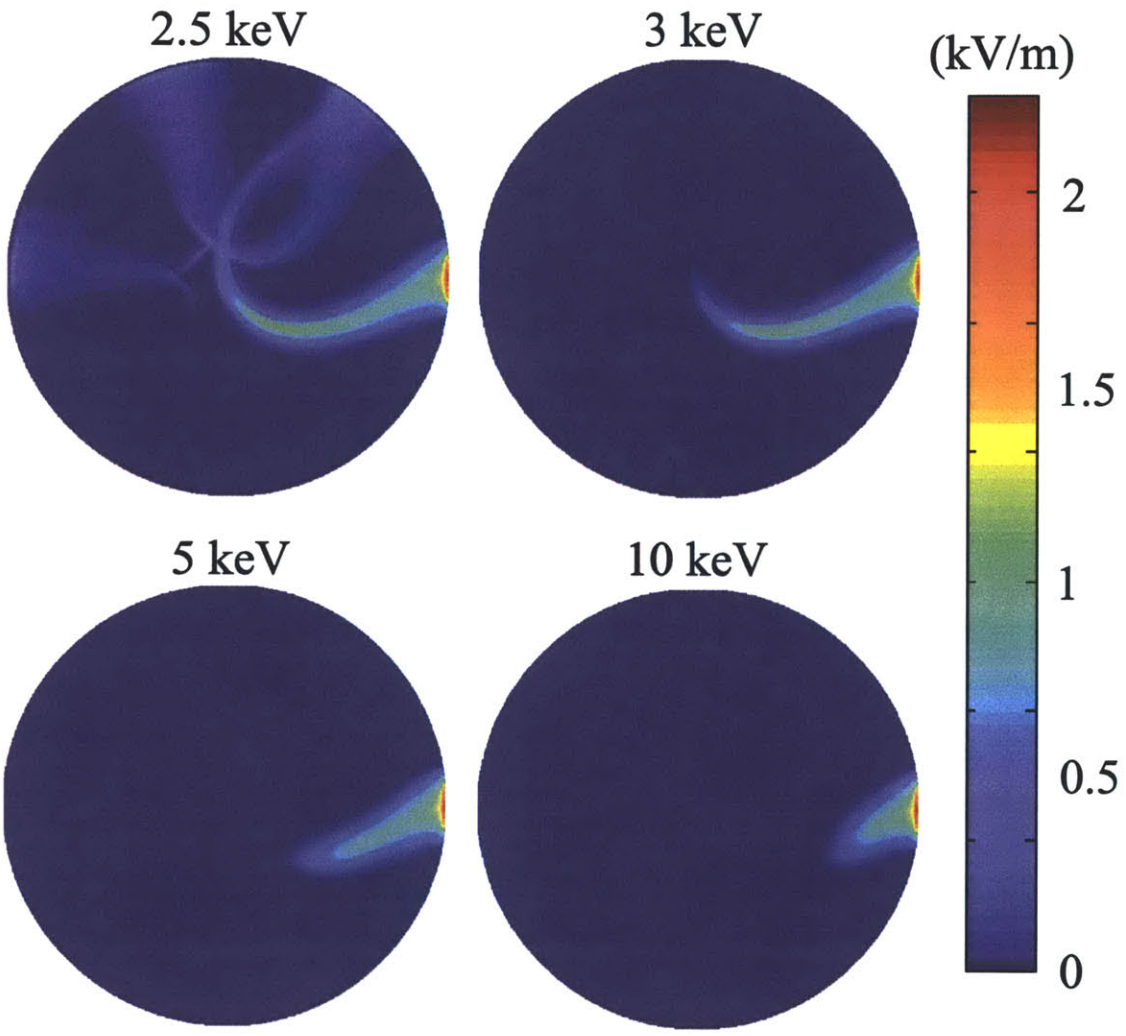

Figure 6-10: Poloidal cross sectional plot of $|E_{\|}|$ of the plasma region for the central temperature of 2.5 keV, 3 keV, 5 keV and 10 keV. For all cases the input power is 1 kW and the reflection from the plasma is constant and equal to 4%.

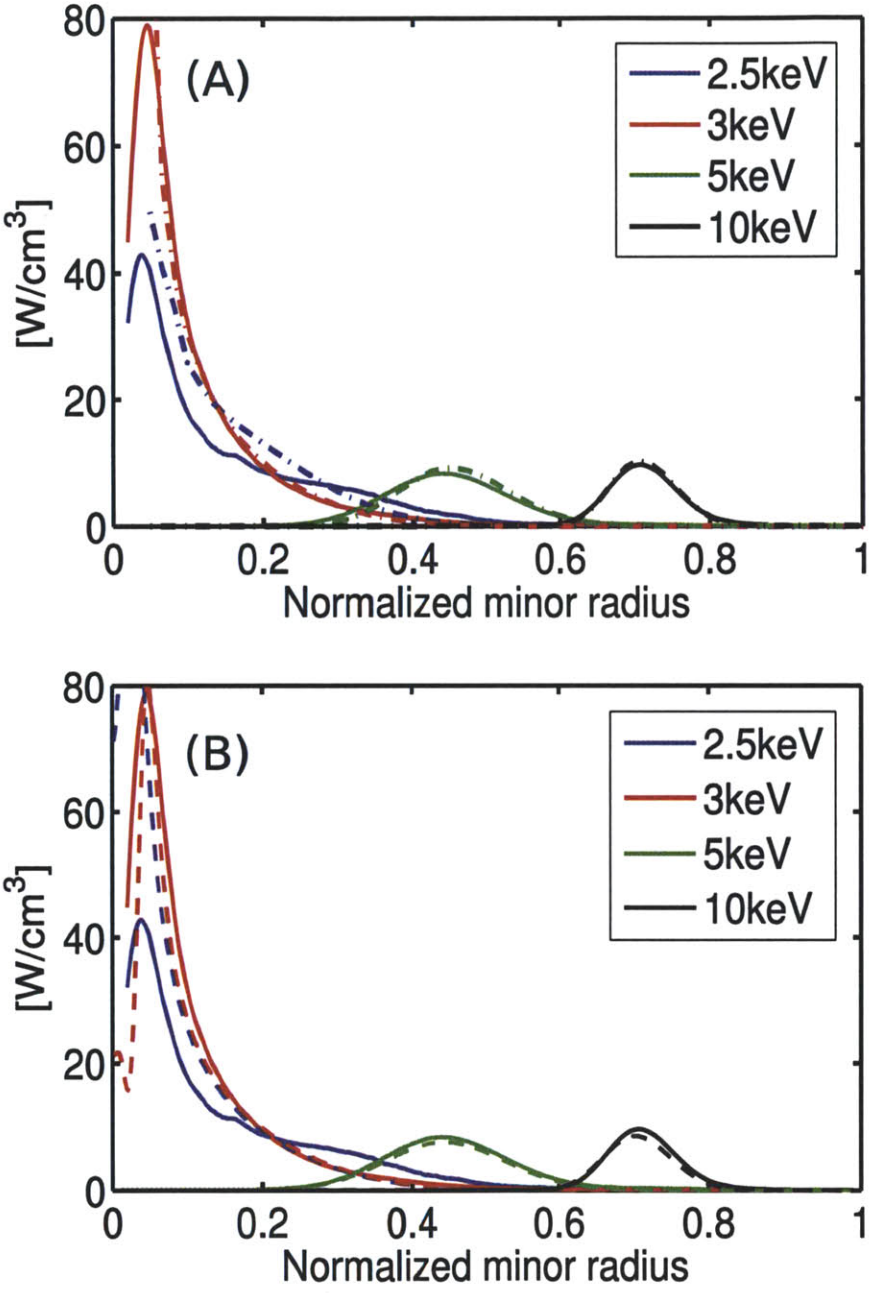

Figure 6-11: (a) Normalized radial power deposition profile as calculated by LHEAF (solid lines) and the ray-tracing (dashed lines), and (b) by LHEAF (solid lines) and TORIC-LH (dashed lines) for different temperatures. The launched power is 600 kW.

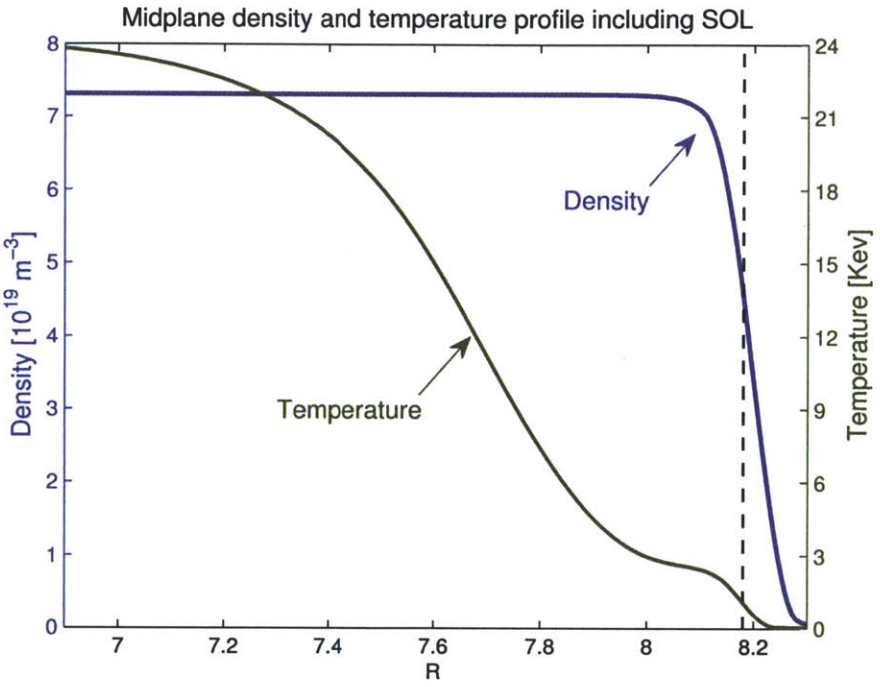

Figure 6-12: Midplane density and temperature profiles for the ITER LH scenario, including SOL.

simulation the plasma is assumed to be Maxwellian, and the power absorption is self consistently retained in the simulation by means of LHEAF iterative routine. For our simulations we used the magnetic equilibrium and the core density and temperature profiles for the LH scenario [158] as provided by the ITER-LH task force (Shown in Fig. 6-12). Assuming that gas puffing will be used in ITER to improve long distance coupling, we used the SOL profiles consistent with the results from JET and the ITER PAM coupling studies. In particular an exponential falloff of the density and temperature with a scale length of $\frac{n_e}{dn_e/dx} = 2\ cm$ was used.

In ITER scale plasmas, LH waves having $n_{\|} \approx 2$ are expected to be strongly damped and to be localized in the outer region of the plasma. Hence one can take advantage of the flexibility of the FEM approach, by considering only the region of plasma where the wave fields are expected to be non-zero. In our simulations, the spatial localization of the LH waves was inferred prior of the fullwave calculation by means of ray-tracing. By this approach the original problem size was reduced by a factor of 12, from $\sim 25.5\ m^2$ to $\sim 2.0\ m^2$.

Figure 6-13 shows the logarithmic plot of the parallel wave electric fields propagating through the final section of the launcher, through the SOL into the core plasma, where they are finally absorbed by ELD. Contour plots of the magnetic flux surfaces and of the fullwave computational domain are over plotted. About 6% of the power is reflected at the waveguide-plasma interface, resulting in a standing wave pattern in the waveguide section. Figure 6-14 shows that the radial power deposition profile is peaked at $\rho = r/a \approx 0.7$ in agreement with ray-tracing simulations. The power reflected accounts for the slight difference in the absolute magnitude of the radial power deposition profile between LHEAF and ray-tracing. This modeling work shows that ray-tracing and LHEAF agreement is good in the case of strong single pass absorption.

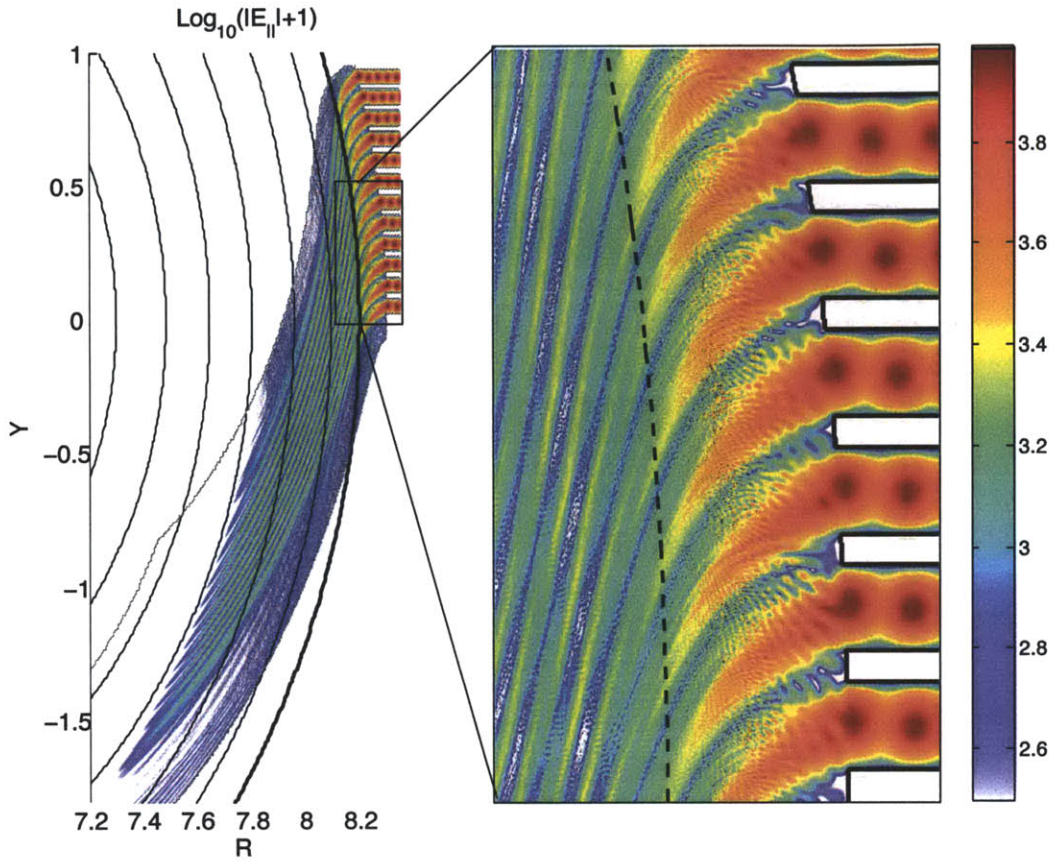

Figure 6-13: Logarithmic magnitude of the electric field of LH waves as they propagate in an ITER poloidal cross section. The thick black line indicates the last closed flux surface. The area delimited by the gray line represents the computational domain of the LHEAF simulation. The reflection coefficient is relatively high, as it can be inferred by the large standing wave ration of the electric field inside of the waveguides.

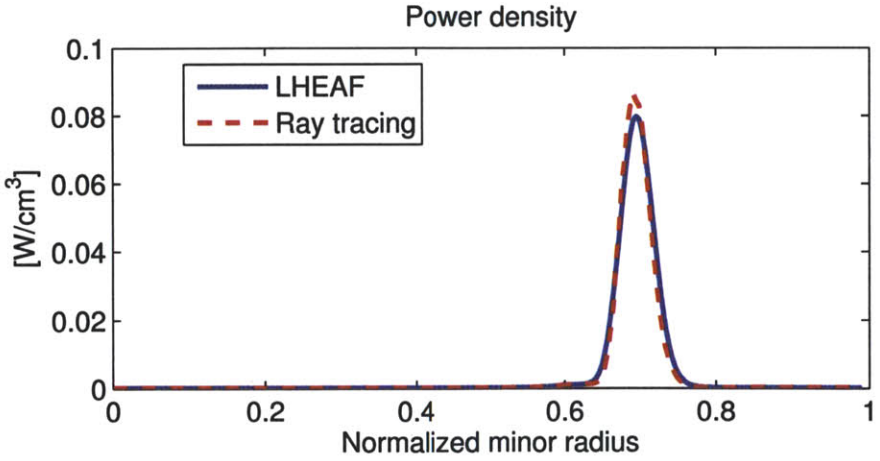

Figure 6-14: The radial power deposition profile calculated by LHEAF and ray-tracing shows good agreement, with most of the power being damped at $\rho \approx 0.7$.

6.5 Coupling to Fokker-Plank codes

The non-Maxwellian electron velocity distribution arising from the interaction of the LH waves with the plasma is taken into account by a 1D Fokker-Planck code which is included in the iteration loop. The 2D electron distribution function resulting from the balance between collisions and RF quasilinear diffusion in a toroidal geometry, is obtained by postprocessing the LHEAF solution using VERD, a relativistic 3D ($v_\parallel$, $v_\perp$, r) bounce averaged Fokker-Planck solver [13]. Once the distribution function is known, the plasma current and the bremsstrahlung emission resulting from the LHCD driven fast electrons can be calculated. The workflow of the LHEAF code, including its Fokker-Planck modules is show in Fig. 6-2.

In practice nothing impedes to substitute the $\text{LHEAF}_{\text{FP1D}}$ module with the 3DFP module VERD inside of the iteration loop. However this is not done, since using a 1DFP solver in the iteration loop is enough to evaluate the LH power absorption while significantly reducing the computational burden. An in depth discussion about the validity of the approach followed in LHEAF is presented in Appx. B.5.

6.5.1 LHEAF 1D Fokker-Planck module : $\text{LHEAF}_{\text{FP1D}}$

To evaluate the deformation of the distribution function, a 1D Fokker-Planck code was included in the LHEAF iteration loop. The 1DFP code is integrated in LHEAF by updating the parallel distribution function at each step of the iteration, before the effective local damping is calculated. At the end of the iteration process, the resulting electron distribution function is in a self-consistent state with the wave fields. The model $\text{LHEAF}_{\text{FP1D}}$ module is based on Refs. [66, 159] and is here briefly summarized.

Starting from the single particle picture introduced in section 1.3.1, the quasilinear diffusion coefficient is calculated using the amplitude of the parallel electric field, $E_\parallel$. First the wave electric field from fullwave code is Fourier decomposed into discrete modes

$$D_{\text{QL1D}}(v_\parallel) = \frac{\pi e^2}{2m_e^2} \sum_{k_\parallel=-2\pi n/L}^{2\pi n/L} \left| \frac{E_{k\parallel}(k_\parallel)}{L^2} \right|^2 \delta(\omega - k_\parallel v_\parallel), n = 0, \pm 1, \pm 2, ... \tag{6.9}$$

and assuming an infinitely dense mode spectrum (i.e. $L \to \infty$) one gets:

$$\lim_{L\to\infty} D_{\text{QL1D}}(v_\parallel) = \frac{\pi e^2}{2m_e^2} \frac{2\pi}{L} \int_{-\infty}^{\infty} |E_{k\parallel}(k_\parallel)|^2 \delta(\omega - k_\parallel v_\parallel) dk_\parallel = \frac{\pi e^2}{2m_e^2} \frac{2\pi}{L v_\parallel} \left| E_{k\parallel}\left(\frac{\omega}{v_\parallel}\right) \right|^2 \tag{6.10}$$

The stationary solution of electron distribution function is evaluated by

$$f(v_\parallel) = \frac{1}{\sqrt{2\pi v_{\text{th}}^2}} \exp\left(- \int_0^{v_\parallel} \frac{\nu_{\text{e}}(v'_\parallel) v'_\parallel}{D_{\text{c}}(v'_\parallel) + D_{\text{QL}}(v'_\parallel)} dv'_\parallel \right) \tag{6.11}$$

where v_{th}, $D_{\text{c}}(v'_\parallel)$ and $\nu_{\text{e}}(v'_\parallel)$ are the electron thermal velocity, the collision operator for Maxwellian background electrons, and the electron-ion collision frequency, respectively. Detailed expressions for them can be found in [159].

The power absorption density is calculated by

$$P_{\text{FP}} = -n_{\text{e}} m_{\text{e}} \int v_\parallel D_{\text{QL}}(v_\parallel) \frac{\partial f(v_\parallel)}{\partial v_\parallel} dv_\parallel, \tag{6.12}$$

where n_{e} is the electron density on the given flux surfaces. In order to obtain self-consistent solutions of the distribution function and the wave field, we scaled D_{QL} so that the power absorption from

Eq. 6.12 and the power absorption from the fullwave code are equal. Usually, this process takes a 2 to 3 step iteration of 1D Fokker-Planck calculation.

6.5.2 LHEAF 3D Fokker-Planck module: VERD

A 3D Fokker-Planck ($v_\parallel$, $v_\perp$, r) code named **VE**locity and **R**adial **D**iffusion (VERD) is used to post-process the fullwave fields resulting from the iteration of the EM solver with the $\text{LHEAF}_{\text{FP1D}}$ module. The newly developed 3D Fokker-Planck solver calculates the steady state electron distribution function and the driven current profile, while the synthetic HXR diagnostic module calculates the resulting HXR radiation spectrum. An in-depth description of the relativistic 2D bounce-averaged Fokker-Planck equation under a zero banana width approximation solved by this code is given in Appx. B. For convenience, a short summary is also provided here.

The Fokker-Planck equation solved by the 3DFP module VERD is:

$$\frac{\partial(\lambda f_0)}{\partial t} = -\nabla_{\text{p}}\Gamma_{\text{p}} - \nabla_{\text{r}}\Gamma_{\text{r}} + \langle S(f_0)\rangle \tag{6.13}$$

where f_0 is the mid-plane distribution function, $\lambda = \tau_{\text{B}} p_\parallel / m_{\text{e}}$ (τ_{B} is the bounce time), Γ_{p} is the momentum space particle flux due to Coulomb collisions, the LH waves (Γ_{LH}) and the Ohmic electric field, and Γ_{r} is the flux in the real space radial direction. The Belaiev-Budker's linearized relativistic collision operator was implemented associated with the source term $\langle S(f_0)\rangle$ for electron-electron collisions and the classical collision operators for electron-ion collisions [160]. Numerical implementation of the Fokker-Planck code was tested against previously published results [161].

A fast electron radial diffusion model [162, 73] is used

$$D = D_{rr}\frac{v_\parallel}{v_{te}\gamma^3}\ m^2/s \tag{6.14}$$

The velocity space diffusion equation resulting from quasi-linear theory of LH waves is expressed as:

$$\nabla_{\text{p}}\Gamma_{\text{LH}} = \frac{\partial}{\partial p_\parallel}\left(-D_{\parallel\parallel}^{(\text{LH})}\frac{\partial f_0}{\partial p_\parallel}\right) \tag{6.15}$$

The evaluation the diffusion coefficient $D_{\parallel\parallel}^{(\text{LH})}$ is based on the calculation of transit-acceleration of test particles during one bounce time, taking into account the RF electric field from the fullwave simulation. Following p.447 of Ref. [32] and taking into account electron banana orbits, the acceleration during one banana bounce motion was evaluated from

$$\delta u = \oint \frac{ds}{v_\parallel}\frac{qE_0(s)}{m_{\text{e}}}\exp\left(i\Lambda(s) - i\omega t(s)\right). \tag{6.16}$$

where s and Λ are the length and the phase of the LH wave along the field line, respectively, and $\Lambda(s) - \omega t(s)$ is the wave phase as viewed by electrons. In this equation, the integration along the particle trajectory is approximated as the integration along the guiding center and the effective parallel electric field, which is expressed as

$$E_0(s) \sim E(s)J_0\left(\frac{k_\perp(s)v_\perp(s)}{\Omega(s)}\right) \tag{6.17}$$

where the Bessel function is a correction due to the perpendicular wave length of the LH waves. The argument of the Bessel function is evaluated using the "local" perpendicular wave number defined as $k_\perp = \frac{d\Lambda}{ds}\sqrt{-\frac{P(s)}{S(s)}}$, where $P(s)$ and $S(s)$ are the Stix notation [32]. $D_{\parallel\parallel}^{(\text{LH})}$ is evaluated using $\delta p^2/2\tau_{\text{B}}$. This approach reduces the $D_{\parallel\parallel}^{(\text{LH})}$ calculation to a simple line integration along the field line, which

is easy to implement in LHEAF, since the wave electric field is readily expressed in real space.

6.6 HXR synthetic diagnostic module: $LHEAF_{\mathrm{XHR}}$

Once the distribution function is known from the 3DFP module VERD, it is possible to solve for the bremsstrahlung emission from the plasma. The Hard X-Ray (HXR) spectrum provides a direct and sensitive measurements of the high energy tail of the electron distribution function. The HXR synthetic diagnostic module implemented in LHEAF is based on Ref. [19] and for convenience is summarized it in the following.

The differential count rate observed at the detector may be written as

$$\frac{dN_E}{dtdE} = \int_0^\infty \eta_A(k)(1-\eta_D(k))G(k,E)\frac{dN_k(t,k)}{dtdk}dk \tag{6.18}$$

where E denotes the actual measured energy and k is the photon energy emitted from the plasma. For Alcator C-Mod, $\eta_A(k)$ represents the fraction of photons transmitted through a 1.0 mm thick aluminum vacuum window and a stainless steel shielding plate of variable thickness. The $(1-\eta_D(k))$ term is the fraction of photons that are stopped within the CZT detector. The $G(k,E)$ function represents the detector response and is normalized so as to conserve energy when integrated over k.

Since the étendue of the system ε is small, then the differential number of photons $dN_k/dtdk$ emitted by the plasma is expressed as an integral over the chord length within the plasma $l_{max}-l_{min}$, according to

$$\frac{dN_k(t,k)}{dtdk} \simeq \int_{l_{min}}^{l_{max}} \varepsilon \frac{dn_k(t,k,\overline{x},\hat{b}\cdot\hat{d})}{dtdkd\Omega}dl. \tag{6.19}$$

In the HXR synthetic diagnostic module of LHEAF, one specifies the geometry of the chordal measurements of the HXR diagnostic. The contributions of the HXR emission seen along each chord is then calculated as a function of the photon energy. In particular the angle of the magnetic field line and the direction of observation must be known to evaluate the bremsstrahlung cross sections. The distribution function at each point along the viewing chord is known by projecting the distribution function f_0 that the 3D Fokker-Planck module calculated at the midplane.

The $n_k = dN_k/dV = n_k^{ei} + n_k^{ee} = \sum_i dN_k^{ei}/dV + dN_k^{ee}/dV$ term is the photon density which arises from both electron-ion (summation for all ion species) and electron-electron collisions. Ion-electron collisions dominate at lower energies while electron-electron collisions become significant at the highest energies in the range of interest. The n_k^{ei} and n_k^{ee} terms can be expressed in terms of the known differential bremsstrahlung cross sections [163] and the velocity moment of the electron distribution function.

For the case of Alcator C-Mod, the existing HXR data analysis suffered from pulse pileup and baseline drift which occurred for highly non-inductive discharges. An improved analysis technique for the experimental data collected by the HXR camera has been developed to more accurately evaluate the HXR flux and allow a reliable comparison with the results obtained by the LHEAF synthetic HXR diagnostic. Details of the Alcator C-Mod HXR camera diagnostic are given in Sec. 3.2.1, while the improved analysis technique is described in Appx. C.

6.7 LHEAF validation with the Alcator C-Mod LHCD experiment

Several LHCD experiments have been carried out on the Alcator C-Mod tokamak. In the following section the simulated current density profiles and the HXR radiation predicted by LHEAF are

compared with measurements for a set of discharges which encompass a broad range of operating regimes.

To improve the accuracy of the magnetic equilibrium, and consequently of the driven current profile, in addition to the external magnetic measurements kinetic measurements and motional Stark effect (MSE) pitch angle measurements (when available) have been used to constrain the EFIT equilibrium reconstruction. For discharges with good LHCD, instead of low order polynomial functions, spline functions with 5 to 6 knot points are used for better representation of the pressure and current profiles. The EFIT computation grid is set to 129 × 129 data points.

6.7.1 Benchmark discharge #1080320017

The discharge #1080320017 has a special meaning for the LHEAF code because it has been used to benchmark the code since the early stages of the development. This discharge was chosen because it was the best LHCD shot of the 2008 campaign, that is when the development of LHEAF started. For this comparison the discharge parameters at 1 s have been used, 400 ms after the onset of the LH, so to ensure that the LHCD current is well penetrated and the conditions are steady state (current penetration time $\tau_J \sim 150\ ms$). The results presented in this section have been published in Ref. [164, 18].

Figure 6-15 shows the logarithmic color plot of the parallel electric field amplitude. For this simulation the plasma separatrix is treated as a conducting boundary from which the waves are specularly reflected. Four waveguides inject 900 kW of RF power in the plasma from the low field side of tokamak with a toroidal spectrum of $n_\phi = 1.9$. For this simulations $Z_{\text{eff}} = 2.5$. This discharge is in a "moderate" multi-pass regime, since most waves undergo multiple reflections before being absorbed without however filling up the entire plasma cross-section.

Plots of the electron distribution function and the associated momentum diffusion coefficient are shown in Fig. and Fig. 6-17, respectively. As it can be seen the quasi-linear plateau and the distribution function that develops become asymmetric with respect to $U_\perp$ due to the LH induced velocity space diffusion plotted in Fig. 6-17.

Current profile

Figure 6-19 shows a comparison of current profile predicted by LHEAF and the experimental current profile obtained by equilibrium reconstruction which has been constrained by T_e and n_e measured by Thomson scattering, T_i by the impurity, uniform Z_{eff} of 3, and MSE pitch angle measurements in addition to external magnetic diagnostics. A diffusion coefficient $D_{\text{rr}} = 0.02\ m^2/s$ was used in the 3D Fokker-Planck calculation. The error bars on the experimental profile include statistical errors of the pitch angle measurements ($\sim 0.1°$ in the core region and $\sim 0.2°$ in the edge region) and pressure measurements ($\sim 10\%$), and systematic errors associated with the pitch angle calibration technique [115]. Excellent agreement of current profile between the code and the reconstruction is obtained. The total calculated current was 750 kA, as compared with 800 kA in the experiment. For comparison, we calculated the current profile using the GENRAY/CQL3D ray-tracing/Fokker-Planck code [86, 165]. Although it also shows good agreement in terms of the total current (870 kA), quite significantly the profile does not agree as well as the fullwave simulation. In particular, the ray-tracing predicts more localized LHCD inside $r/a \sim 0.7$. To illustrate the difference between these profiles, Fig. 6-19 (right) shows the current profiles normalized to match the total experimental current, further emphasizing that the full wave calculation predicts the experimental current profile better than the ray-tracing one.

Hard X-Ray spectrum and profiles

Figures 6-20 compare the simulated and measured energy spectrum and profiles for each chord. Despite being spatially wide, the simulated profiles are still narrower compared to the measured

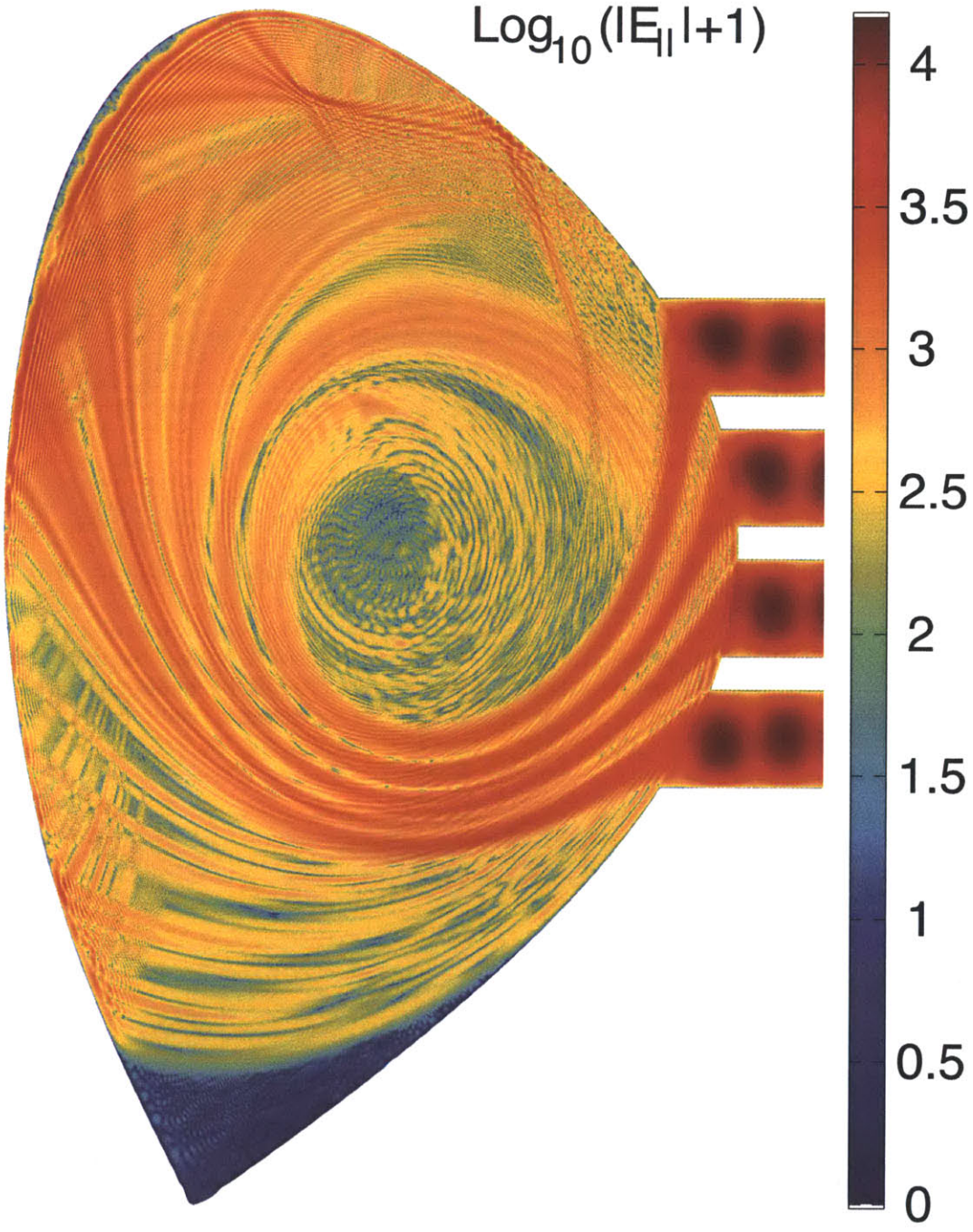

Figure 6-15: The waves are launched by four waveguides on the low field side of tokamak and propagate through the core plasma, where they are self-consistently absorbed via electron Landau damping. Most of the waves undergo multiple reflections at the LH wave cutoff layer or the plasma separatrix, before being absorbed by the plasma.

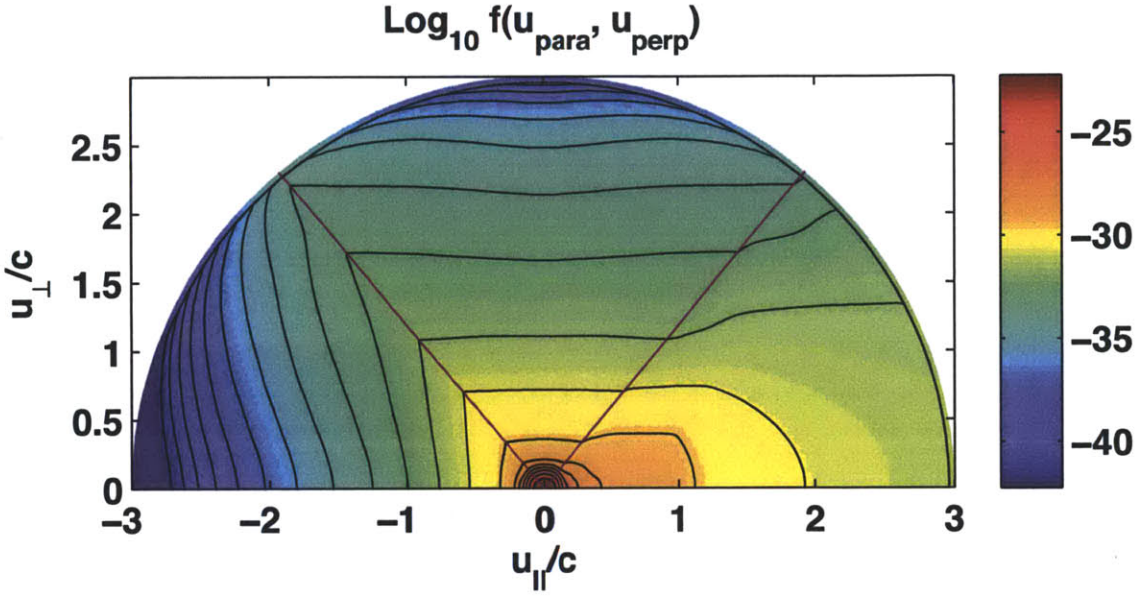

Figure 6-16: Logarithmic plot of the VERD steady state midplane electrons velocity distribution function for the Alcator C-Mod high density discharge presented in Chap. 7 at $\rho = r/a = 0.8$. Plots are as a function of $u \equiv \gamma v$. Clearly identifiable are the thermal region (circular contours at low velocity), the RF induced plateau (distorted contours at high velocity) and the trapped region (symmetric region within the magenta lines). Pitch angle scattering populates the distribution function of fast electrons even where the quasilinear diffusion coefficient is small.

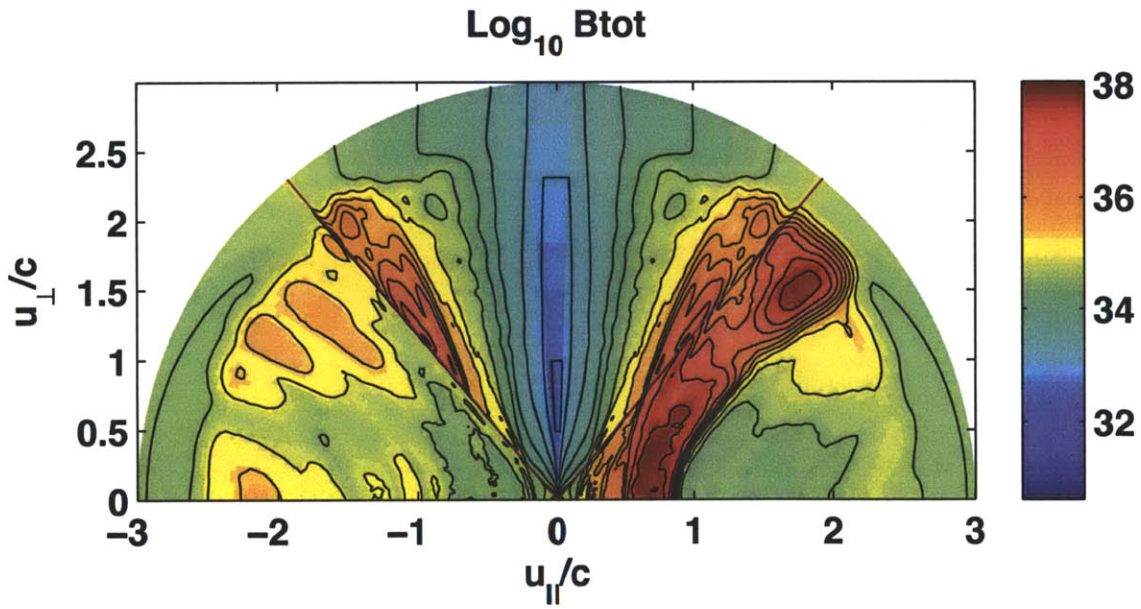

Figure 6-17: Logarithmic plot of the VERD bounce averaged relativistic electrons momentum diffusion coefficient corresponding to Fig. 6-16.

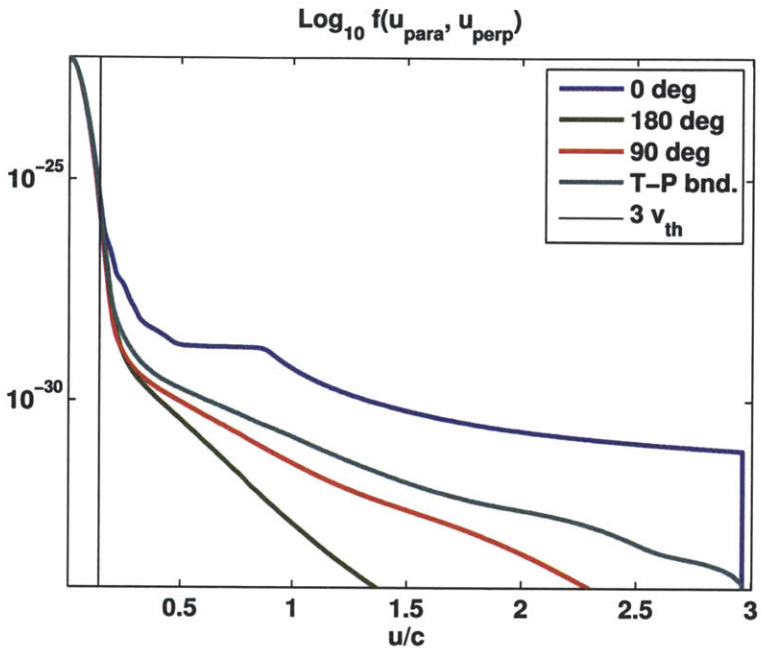

Figure 6-18: Cutout of the distribution function shown in Fig. 6-16. The distribution function deviates from being thermal around $v \approx 3\,v_{th}$.

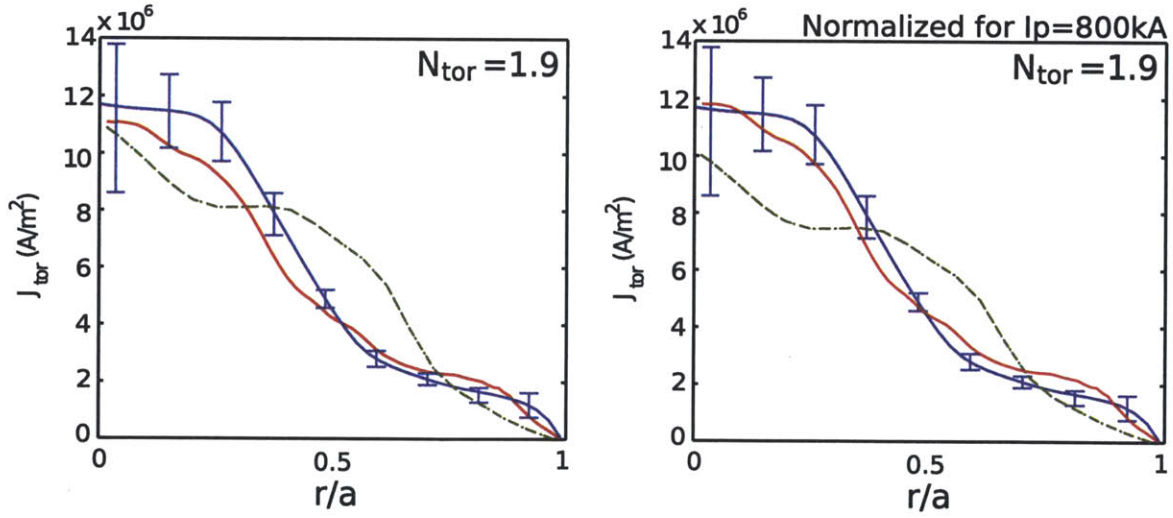

Figure 6-19: (Left) The toroidal current profile evaluated by full wave code LHEAF analysis (red) and kinetic-MSE constrained EFIT (blue) on the low field side mid-plane. The green line is the current profile calculated by the GENRAY/CQL3D ray-tracing/Fokker-Planck code. The error bars of experimental profile include statistical errors of the pitch angle measurements ($\sim 0.1°$ (in the core region) and $\sim 0.2°$ (in the edge region)) and pressure measurements ($\sim 10\%$), and systematical errors associated with the pitch angle calibration technique [115]. (Right) Same as left, but the current profiles are normalized to have the same total current.

ones, a possible indication that fast electron radial diffusion is higher than what was assumed in the simulation. Nonetheless, LHEAF was able to reproduce the slight change in slope that is observed in the experiment near chords 10 and 20. Other authors have compared the Alcator C-Mod HXR measurements with the prediction by a synthetic diagnostic in the CQL3D Fokker-Planck code but with poor agreement near the plasma edge. In particular, the experimental x-rays profiles from both GENRAY/CQL3D [73] and TORIC-LH/CQL3D [15] simulations were much narrower than the experimental ones, with almost no radiation coming from the plasma edge [3].

The comparison shows that the edge chords of the synthetic diagnostic see fewer photons than what is measured experimentally. In LHEAF, the inability of the current modeling tools to accurately reproduce the experimentally observed HXR counts at the edge comes as no surprise. In fact, the simulated HXR emissivity is forced to be effectively zero at the plasma edge (see Fig. 7-9), where the distribution function in the 3DFP module VERD is set as a boundary condition to be Maxwellian. At the LCFS the particle flux $\Gamma_{rr} = -D\frac{\partial f}{\partial r}$ self-consistently adjusts so to be a perfect sink for radial diffusion.

Comparing fullwave and ray-tracing in velocity space

The discrepancies between the LHEAF and GENRAY/CQL3D results can be explained by the different wave spectra predicted by these codes Ref. [18]. In the left pannel of Fig. 6-21, the radial profile of D_{QL} evaluated along the positive $v_{\parallel}$ axis is shown as calculated by LHEAF. For comparison with GENRAY, on the right of Fig. 6-21 the radial profile of the phase velocity along the ray trajectories is shown. The trajectory of a ray starting from the mid-plane is highlighted by a thick red line and can be used as a guideline on how to interpret the fullwave result. Notice how the region of high D_{QL} coincides well with this rays trajectory. The ray is launched at $n_{\parallel} = 1.9$ and propagates inward until it hits the boundary determined by the accessibility condition. The ray experiences one reflection before being damped when its phase velocity matches $\sim 3v_{Te}$, indicated as a blue line.

An important difference between the wave spectra calculated by LHEAF and ray-tracing is observed in the low velocity region at $r/a > 0.7$ (circled in Fig. 6-21). In this region, the fullwave calculation shows a significant value of D_{QL}, but no rays pass through it. In LHEAF, the broad wave spectrum allows the power absorption profiles and driven current profile smoothly extend toward the plasma edge. By contrast, ray-tracing deposits all the power in a narrower region ($r/a \leqslant 0.6$).

The maximum extent of the wave spectrum can be evaluated for each single toroidal mode number by the wave kinematic analysis [166, 57]. Boundaries determined by such analysis are shown by black dashed lines in Fig. 6-21 and exactly coincide with the extent of the wave spectrum predicted by LHEAF. In general, multipass regime simulations done in LHEAF predict a much broader spectrum than ray-tracing does, independently of the antenna phasing and plasma parameters. By contrast, simulations in a strong single pass absorption regime, achieved by artificially raising the plasma temperature, do not show such a feature.

Including a SOL region in GENRAY had little effect in expanding ray trajectories towards the low-velocity region discussed in Fig. 6-21. The spectral broadening predicted by LHEAF did not change when a SOL region was included in the model, suggesting that the this effect is independent on the details of the density profile near the plasma boundary.

These observations suggest that full wave effects, which is not treated by the WKB approximation, can play a significant role in expanding the waves spectrum and produce observable differences in LHCD driven current profile. Although the toroidicity induced up-shift certainly plays a role in expanding the wave spectrum towards the low velocity regime, it is not enough to explain the experimental results.

[3] However, those simulations did not include the effects of spatial diffusion in the Fokker-Planck calculation.

(a) HXR energy spectrum

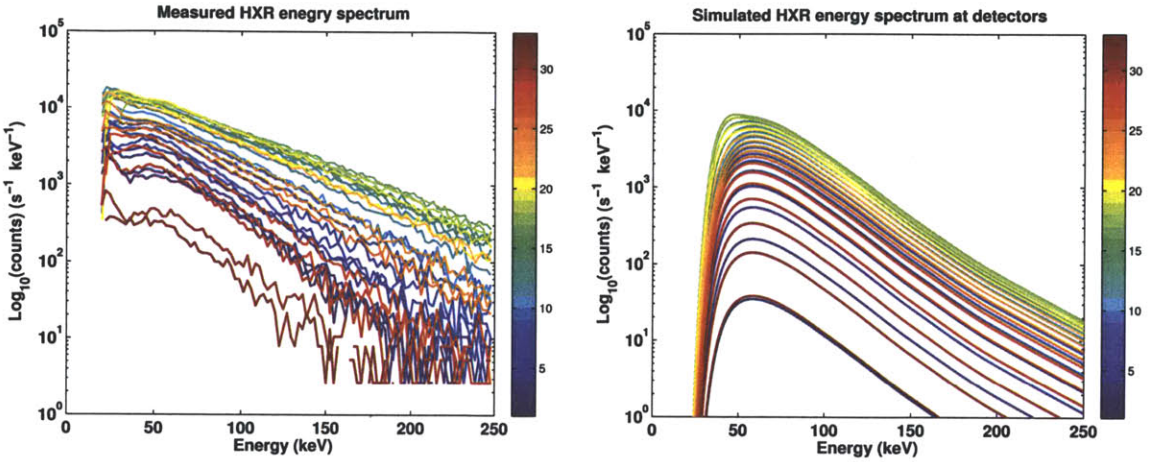

(b) HXR spatial profile

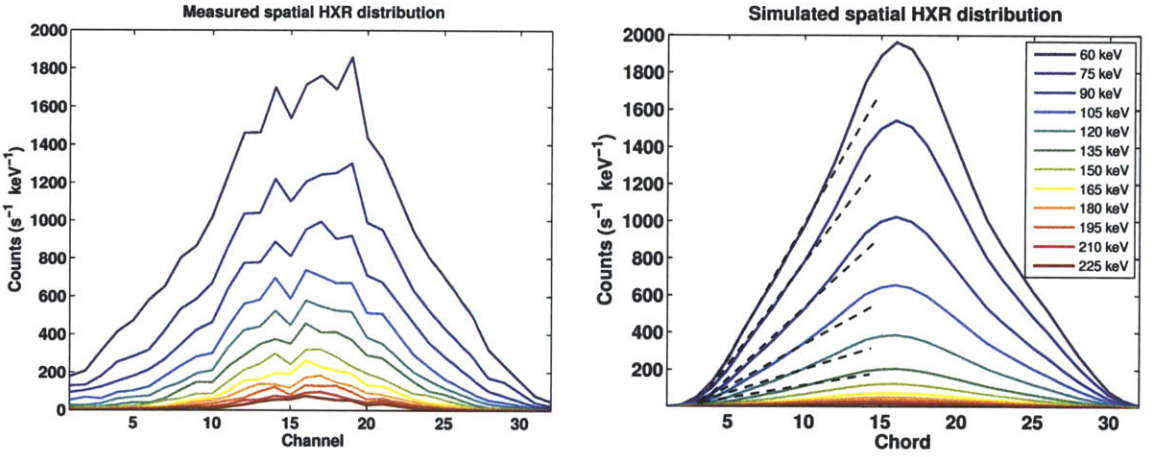

Figure 6-20: Logarithmic plot of the measured and simulated count rates evaluated for 2.3 keV, 150 ms bins centered at 1.0 s. (a) Plot as a function of energy, chords are colored from blue to red according to their number. (b) Plot as a function of chord, the dashed lines highlight the change in slope near chords 10 and 20 for the LHEAF simulation.

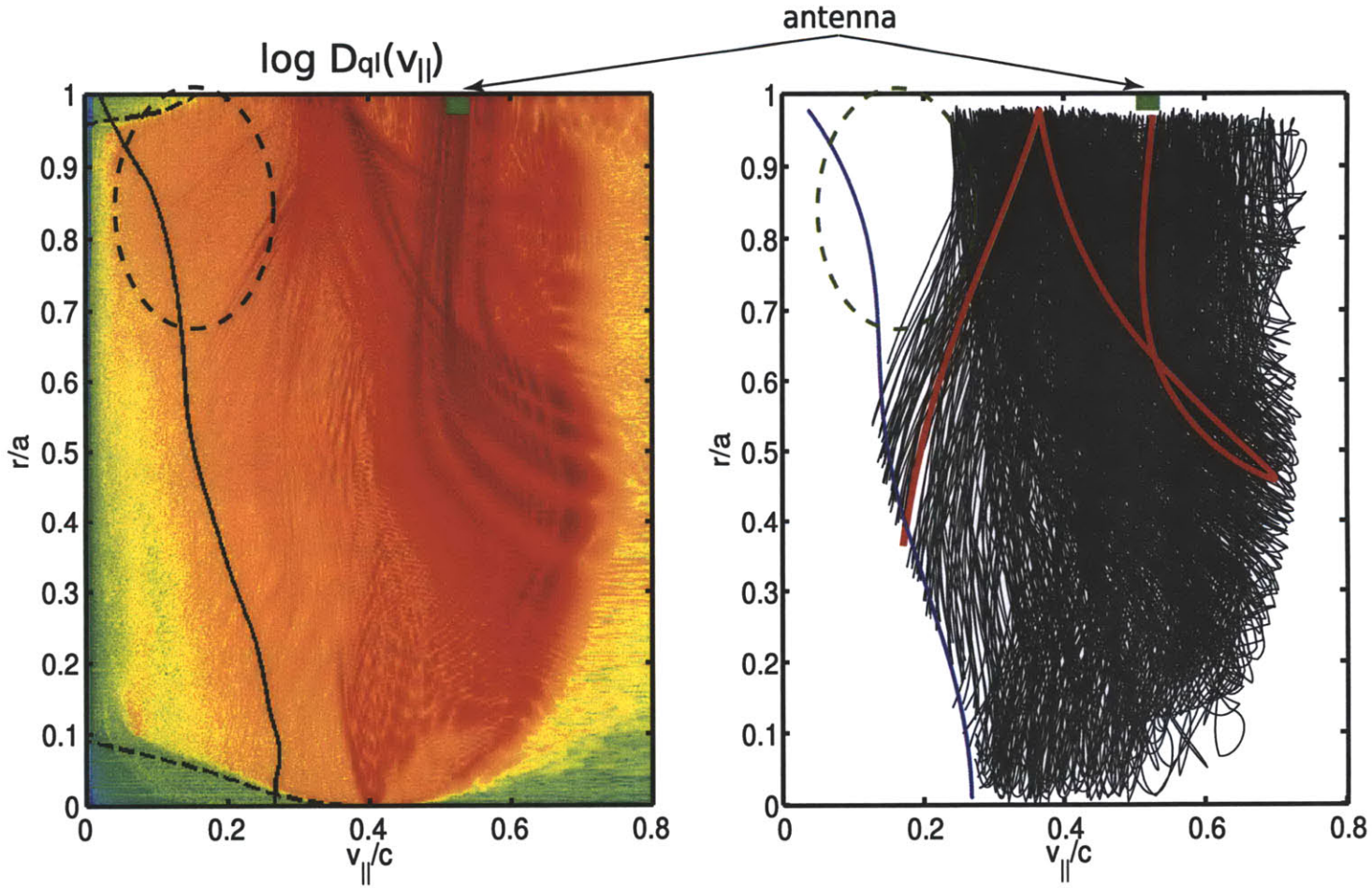

Figure 6-21: (Left) The radial profile of the parallel D_{QL} as a function of $v_{\parallel}/c$ and the normalized minor radius $\rho = r/a$, as calculated by the LHEAF code. (Right) The parallel velocity of resonant electron predicted from $n_{\parallel}$ along the ray trajectories calculated by GENRAY. The green squares indicate the launched antenna spectrum. Results first published in Ref. [18].

Chapter 7

Simulation of high density Alcator C-Mod discharges using LHEAF

In this chapter LHEAF simulations of high density Alcator C-Mod discharges are presented. LHEAF has been applied to the density limit problem (see Sec. 2.2.3) with the expectation that this model will give the most complete answer possible, within the physics of the wave equation. In fact, not only is LHEAF a fullwave solver, but it can treat the SOL, LH launcher, and core LH wave physics in a self-consistent way.

For the purpose of this study a 2D SOL model which includes the effects of flux expansion and parallel heat transport [28] has been developed. Considerable effort has been made to diagnose and model the plasma edge and the divertor regions, so as to create the most realistic simulation environment. This study has also been the main drive for optimization of the code both in terms of accuracy and solution time. In fact, high density simulations are usually associated with lower temperatures, and finer meshes are required to accurately model the wave-particle interaction at the edge.

Results show that SOL collisional absorption is lower than what was previously estimated by raytracing/Fokker-Planck modeling [25, 58]. Nonetheless, the experimental drop of HXR emission is well reproduced by the fullwave simulations and is attributed to an efficient $n_{\parallel}$ upshift induced by reflection and propagation in the SOL and fullwave effects. Wavelet based analysis of the wave fields shows that short wavelength structures (i.e. $n_{\parallel}$ upshift) occur after reflection off the vessel walls. Ultimately LHEAF simulations, suggest that fullwave effects can play a significant role at filling the spectral gap and result in a more off-axis power deposition profile.

The resulting physical picture is rather different from the one developed previously using ray-tracing codes which need to rely on a strongly collisional SOL to reproduce the experimental results. Although this result does not exclude in itself the role of parasitic SOL power loss, it is important that the experimental trends can be reproduced to a large degree without invoking such mechanisms.

7.1 Description of the SOL

Lower hybrid wave simulations are often restricted to within the plasma separatrix, most of the times due to inherent limitations within the codes. However, LH waves are not confined by the presence of the separatrix, rather by the presence of the ω_p cutoff layer and the vessel walls. To be precise, one would expect the LH waves field to exponentially decay beyond the ω_p cutoff layer [1] and consequently the simulation domain should extend even beyond this boundary to account for the correct wave propagation. Where and how the waves are reflected can significantly affect the

[1] An in-depth study of the LH wave behaviour in the vicinity of the ω_p cutoff layer can be found in Ref. [18].

evolution of the $n_{\|}$ spectrum (see Sec. 2.3.1 and Fig. 7-21). Furthermore, including a realistic SOL model is of capital important when investigating the origin of the LHCD density limit, since experimental evidence points to the edge region as where current drive is lost for increasing plasma densities.

The LHEAF formulation is well-suited for specifying plasma parameters at any location in space. The inclusion of a SOL model comes at the expense of a bigger simulation volume, which (in most cases) extends up to the first wall. However the efficacy of using an FEM based code for modeling the SOL should not be understated here. First as was shown in Secs. 6.2.3 and 6.2.4, the size of the problem only increases by R^2 rather than by R^3 or R^6 if one was using a semi-spectral or spectral method. Second, the FEM method makes it straightforward to accommodate the complicated structures which are native to the SOL.

In theory, simulation results from 2D fluid/kinetic SOL codes could be used to generate self-consistent 2D maps of the plasma density, temperature and neutrals. However, at the time of writing this thesis, the EIRENE [167, 168] code has just recently been installed at the Alcator C-Mod experiment and is undergoing validation [2] Waiting for a self-consistent 2D SOL model to become available for Alcator C-Mod, a two-points SOL model with flux expansion and parallel heat transport has been developed in LHEAF. To the author's knowledge this is one of the most (if not the most) sophisticated SOL model that has been used to date in a tokamak plasma wave simulation.

7.1.1 The SOIL module: Two-points SOL model with flux expansion and parallel heat transport

On Alcator C-Mod, measurements by the outer and inner wall scanning probes (described in Sec. 3.2.2) have shown that although the electron pressure in the SOL is a constant function of the flux surface, both temperature and density change along the field lines [118, 119]. The simplest model that accounts for temperature gradients along a field line assumes that thermal energy is primarily lost from the low-field side boundary of the plasma and that classical Spitzer parallel heat conduction is the dominant heat transport mechanism along field lines. This model has been implemented in LHEAF, as the Scrape-Off In LHEAF (SOIL) module.

According to this model, large changes in heat flux $q_{\|}$ can be accommodated by small changes of T (in view of the dependence of the heat conduction coefficient $K_{\|} = \kappa_0 T^{5/2}$) and can be expressed along the flux tube coordinate $s_{\|}$ as:

$$q_{\|} = P_{\mathrm{SOL}}/A_{q_{\|}} = -K_{\|}\frac{dT}{ds_{\|}} = -\kappa_0 T^{5/2}\frac{dT}{ds_{\|}}\ Wm^{-2} \tag{7.1}$$

where, $A_{q_{\|}}$ is the total cross-sectional area of the SOL for power flow P_{SOL} and for a pure hydrogenic plasma $\kappa_0 \sim 2000$ for electrons. See Ref. [169] for an extensive treatment of the SOL physics.

Equation 7.1 is readily integrated to give the temperature along the field line:

$$T_{s_{\|}} = \left[T_{\mathrm{MIDP}} - \frac{7}{2}\frac{(P_{\mathrm{SOL}}/A_{q_{\|}})s_{\|}}{\kappa_0}\right]^{2/7} \tag{7.2}$$

If the upstream midplane (MIDP) and downstream wall (WALL) temperatures are known, then the temperature profile along a flux tube can be calculated as

$$T(s_{\|}) = \left[T_s^{7/2} - \left(T_{\mathrm{MIDP}}^{7/2} - T_{\mathrm{WALL}}^{7/2}\right)\Delta s_{\|}\right]^{2/7} \tag{7.3}$$

[2] The availability of the 2D poloidal neutral distribution would be the starting point to evaluate the amount of wave power which is lost in ionization. This mechanism could be significant in Alcator C-Mod, because the high-density conditions enhance the plasma-neutral and neutral-neutral interactions.

where $\Delta s_{\|}$ is the normalized distance between the midplane and the wall (e.g. divertor).

The local pitch angle of the field lines plays a crucial role on the temperature gradient along a field line, since the field line length becomes very long in the vicinity of the X-points and consequently that is where most of the temperature drop occurs. Plots of the normalized poloidal distance $\Delta s_{\text{poloidal}}$ and the normalized flux tube distance $\Delta s_{\|}$ are shown in Fig. 7-1.

On Alcator C-Mod, the plasma electron density and temperature in the core plasma are evaluated by using the Thomson scattering diagnostic [3]. As discussed in Sec. 3.2.2, the SOL measurements are instead provided by reciprocating Langmuir probes and the SOL reflectometer [4]. Finally, the measurements at the wall are provided by the outer, inner and upper divertor Langmuir probes. Since the density and collision frequency at the wall are not constrained by this model, the measurement by the divertor Langmuir probes can be used as a benchmark for the accuracy of the 2D SOL model.

Measurements have also shown that the density and temperature rapidly decays away from flux surfaces which are not mapped to the outer midplane [118, 119]. In the model, it is therefore a good approximation to set the temperature and density on these flux surfaces to be low (e.g. 0.1 eV, 10^{14} m^{-3}). The exact choice of the temperature and density for the flux surfaces which do not map to the midplane is quite arbitrary. Although different combinations of density and temperature can lead to different collision frequency, the waves are cutoff in these regions and decay with short e-folding length. The solution to the wave problem has been verified to be robust with respect to the temperature and density choice in these regions.

7.2 Modeling Alcator C-Mod LHCD density limit

Three Alcator C-Mod discharges have been selected to study the dependency of the HXR emission as a function of density. These are deuterium plasma discharges which share similar magnetic plasma topology (upper single null, 5.4 T, 800 kA) but have different plasma density (and temperature). Discharges #1080429007 at 0.84 s, #1080429007 at 1.14 s and #1080513024 at 1.14 s have been chosen to sample the HXR density limit plot of Fig. 2-4 at the line averaged densities of $\bar{n}_e = 0.7 \times 10^{20}$ m^{-3}, 1.0×10^{20} m^{-3} and 1.3×10^{20} m^{-3}, respectively. In the simulations Z_{eff} was taken to be constant across the plasma and equal to 2.0, 1.5 and 1.15 for the low, moderate and high density cases. Similarly, the loop voltage is also assumed to be constant and equal to 0.2 V, 1.0 V and 1.0 V.

These discharges have been specifically chosen because of the availability of the reciprocating Langmuir probe data, which allowed a reliable reconstruction of the density and temperature profiles shown in Fig. 7-2. Figure 7-3 compares the density and temperature profiles for the three discharges. The plasma equilibrium was calculated using EFIT (only magnetics) on a 129×192 grid. Figure 7-4 shows final 2D plasma topology, temperature, density (and consequently collision frequency) which were input to the LHEAF simulations.

For the sake of collisional damping Z_{eff} is set to be 1 (i.e. Z_{eff} used in the FP codes is inconsistent with $Z_{eff} = 1$ used in the EM solver). This decision was dictated by the absence of Z_{eff} measurements in the SOL of Alcator C-Mod and the availability of only an average Z_{eff} measurement for the plasma core (also affected by large uncertainty). This choice purposely underestimates the role of collisions in the SOL and underlines the contrast between the LHEAF results and the ray-tracing results.

[3] The ECE diagnostic is usually not used for measuring the temperature, since the profiles are affected by fast electron radiation in LHCD discharges.

[4] When the experimental profiles in the SOL are not available, a simple exponential decay is assumed to connect core profiles to the density and temperature measured by the Langmuir probes which are installed with the LH Launcher.

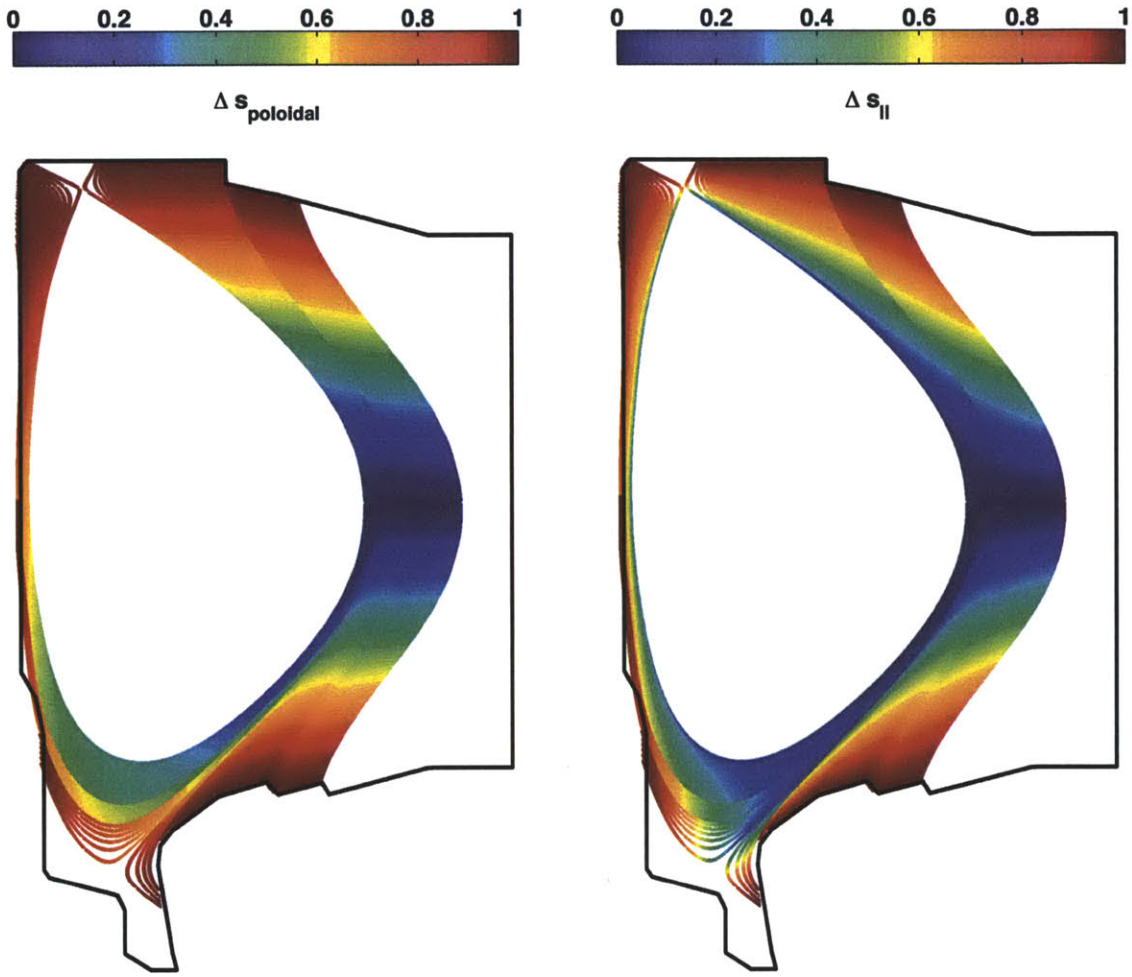

Figure 7-1: Plot of the normalized poloidal distance $\Delta s_{\text{poloidal}}$ and flux tube distance $\Delta s_{\|}$ from the midplane to the vacuum vessel wall, for a typical LHCD discharge on Alcator C-Mod. The normalization is such that both $\Delta s_{\text{poloidal}}$ and $\Delta s_{\|}$ equal one at the walls. The local pitch angle of the field lines plays a crucial role at localizing the temperature gradients in the vicinity of regions with larger flux expansion.

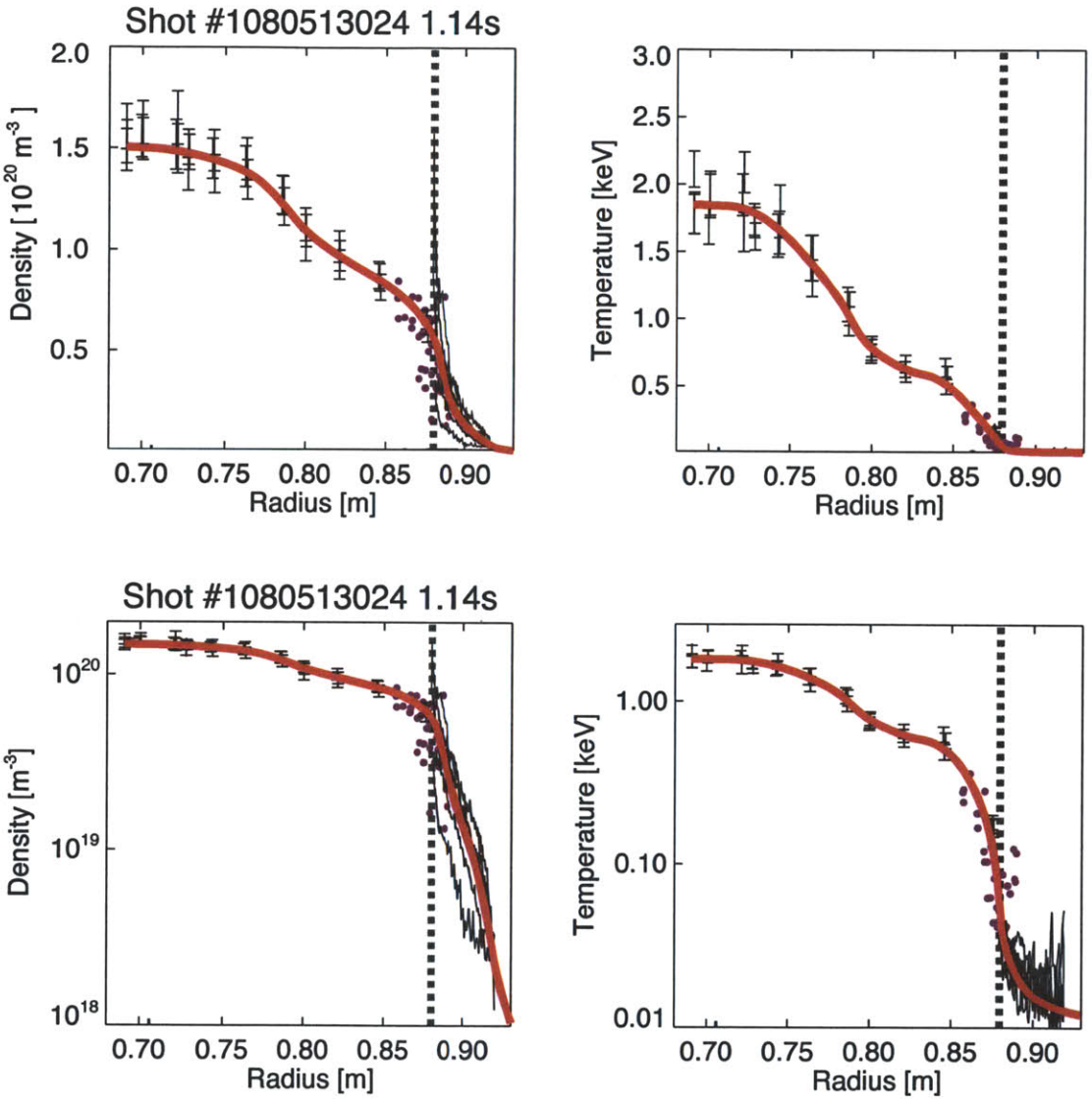

Figure 7-2: Linear and logarithmic plot of the density and temperature profiles used in LHEAF (red curve) for the high density discharge. The profiles have been reconstructed based on the measurements of the core/edge Thomson scattering (three time slices), the A-port scanning probe and LH launcher Langmuir probes diagnostics.

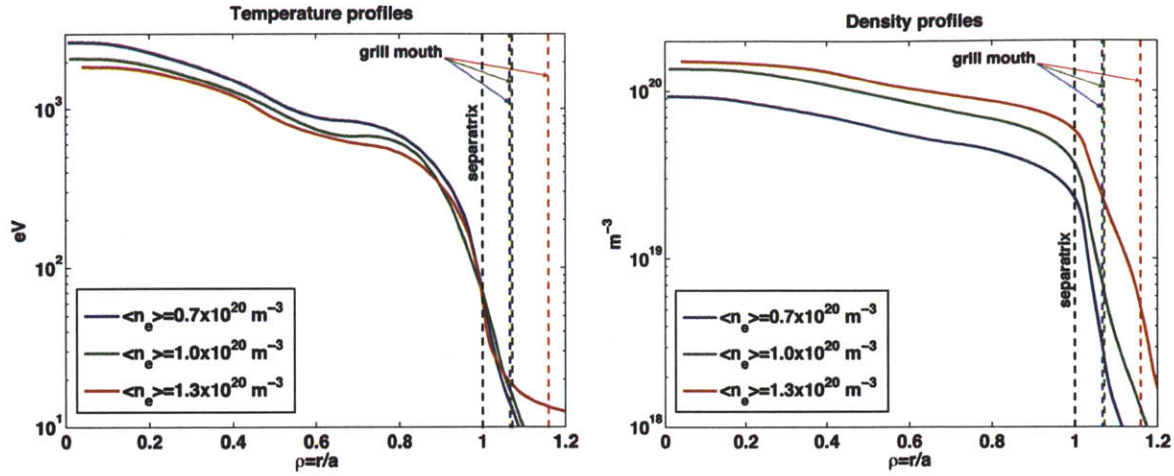

Figure 7-3: Density and temperature profiles used in high density LHEAF simulations plotted as a function of $\rho = r/a$. In the experiment, the plasma outer gap was larger for the higher density case so to ensure good wave coupling. The density (and temperature) at the grill mouth are similar in all three cases.

7.2.1 Wave fields, core/SOL absorption and driven current

The LHEAF wave fields and the power deposition cross-section are shown in Fig. 7-5 for the three density cases.

Wave propagation

Four waveguide rows inject $\sim 600\ kW$ of net power with a single $n_{\parallel} = 1.9$ into the plasma from the low field side of Alcator C-Mod. Such power corresponds to the amount contained in the main lobe of the launched power spectrum, that is $\sim 80\%$ of the forward power measured in the experiment. From the antenna, the waves propagate through the SOL, into the plasma where they undergo some reflections before being absorbed by electron Landau damping and collisional damping.

As the density is increased the wave fields are not able to penetrate to the core of the plasma. This effect is due to the fact that the group velocity of the slow-wave is almost perpendicular to the wave-vector $\vec{k}$ and makes smaller angles with the magnetic field for increasing plasma density $v_{g\parallel}/v_{g\perp} = k_{\perp}/k_{\parallel} \approx \omega_{pe}/\omega$ (resonance cone propagation explained in Sec. 2.1.2). This implies that at higher densities the waves are unable to go across and must follow the magnetic field lines.

A fast fanning-out of the waves resonance cones is observed to occur in the vicinity of the locus of closest approach to the plasma core. As we shall see in Sec. 7.2.4, this is an indication that the waves propagation is close to the mode conversion to the (electromagnetic) fast-wave, and can be explained in terms of the wave's group velocity, which near the confluence point picks up a perpendicular component to $\vec{B}$. The rapid fanning out of the waves indicates that diffraction is likely to occur, which may affect the results of ray tracing in this region.

Though week in amplitude, one can observe spiral-like structures close to the center of the plasma which are associated with the formation of caustics (e.g. $k_r = 0$, see Sec. 2.3.1). Both the accessibility of the waves and the formation of the caustic structures will be analyzed in detail in Sec. 7.2.5.

Finally, after propagating through the plasma, the waves undergo reflection either at the $\omega_p = \omega$

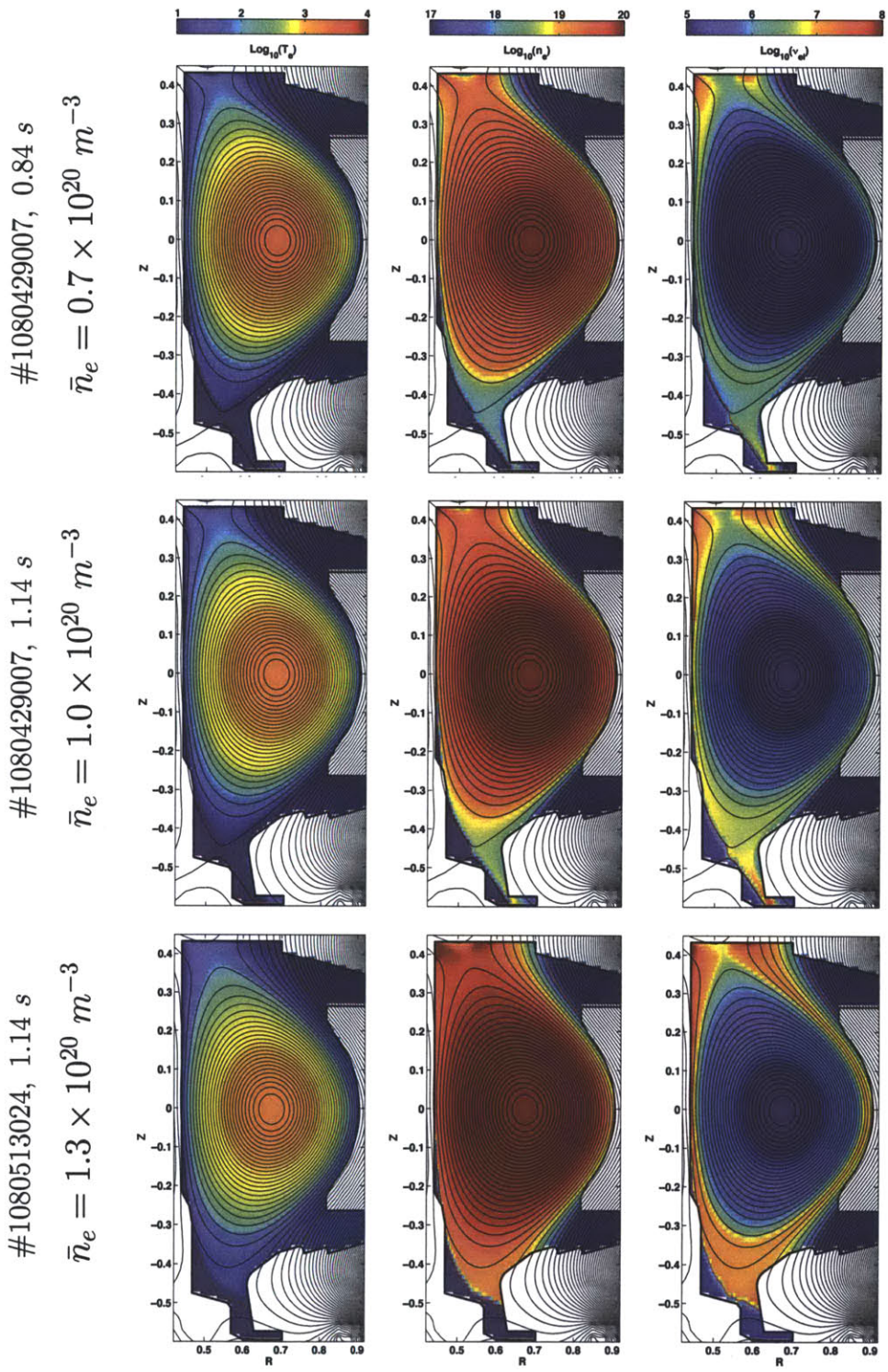

Figure 7-4: Temperature, density and collision frequency from LHEAF 2D SOL model of the three discharges considered in this study. Clearly visible are the poloidal asymmetries in the SOL collision frequency which arise from the non-constancy of density and temperature on open field lines.

slow-wave cutoff or the $S^2 - D^2 = 0$ fast-wave cutoff [5]. For high enough density, the waves can reach the vacuum vessel walls and be reflected there.

Power deposition and current profiles

LHEAF simulations predict that the power deposition is consistently more off-axis at higher densities. Inspection of the absorption cross sections of Fig. 7-5, shows that the power is mostly damped by ELD after the waves reflect off the inner wall or the upper divertor region.

Figure 7-5, shows that according to LEHAF with a realistic 2D SOL model collisional absorption is lower that what was previously found in earlier ray-tracing modeling [26, 27]. In particular, the LHEAF simulation predicts collisional absorption fractions of $\sim 1\%$ at $\bar{n}_e = 0.7 \times 10^{20}\ m^{-3}$, $\sim 2\%$ at $\bar{n}_e = 1.0 \times 10^{20}\ m^{-3}$ and $\sim 7\%$ at $\bar{n}_e = 1.3 \times 10^{20}\ m^{-3}$, compared to ray-tracing calculations with collisional SOL of similar discharges which predicted that as much as $\sim 35\%$, $\sim 75\%$ and $\sim 80\%$ is lost at the same respective densities [26]. In LHEAF, most of the collisional absorption in the SOL occurs in the upper divertor, in view of its cooler temperature and higher density. This is consistent with the experimental observations of an increased ionization rate in this region. By comparison, the power absorbed in the vicinity of the grill is modest compared to the one in the divertor (at least at this $n_\parallel$).

The VERD 3DFP module was used to post-processed the fullwave fields with and without diffusion. Two values of the radial diffusion coefficient D_{rr} defined in Eq. 6.14 were used: $0.02\ m^2/s$ and $0.10\ m^2/s$. As shown in Fig. 7-6, radial diffusion affects mostly the LH driven current and the HXR profiles, while the power deposition profile was found to be almost independent of this parameter. As the amount of diffusion is increased, the fast electrons comprising the high energy tail of the distribution function are spread from regions of higher density to regions of lower density, resulting in smoother current profiles. In addition, fast electrons close to the plasma edge escape out of the separatrix where they are assumed to be lost, resulting in an overall reduction of the current drive efficiency. Finally, the core current density can in some cases increase as the result of diffusion, since the plasma volume at the core is smaller than at the edge.

7.2.2 HXR emission

Figure 7-7 shows the comparison of the HXR emissivity integrated from 40 to 200 keV for the core viewing chords (numbers 9 to 24) of the HXR diagnostic camera. Only the core chords (9 to 24) are used for this comparison. The energy integration and chord number summation ranges have been chosen to be compatible with existing publications [25]. Remarkably LHEAF simulations were found to reproduce qualitatively well the experimentally observed steep drop in HXR emissivity even though most of the power is absorbed in the core region by ELD. The results were found to be robust with respect to the amount of radial diffusion used in the model.

The same comparison for the edge chords (chords 1 to 8 and 25 to 32) is shown in Fig. 7-8. At the edge the simulated HXR emissivity is affected by radial diffusion, and a significant amount ($D_{rr} = 0.10\ m^2/s$) is necessary for the simulations to agree with the experiments. Nonetheless, the HXR emissivity drops by orders of magnitude throughout the whole plasma, independently of the amount of radial diffusion used in the simulations. In this sense, radial diffusion is not necessary to explain the density limit. However some transport mechanism is required for redistributing the HXR population across the plasma and the synthetic HXR camera to agree with the experimental measurements.

Figure 7-9 compares the synthetic HXR emission profiles with the experimental ones for different amounts of radial diffusion. As the amount of diffusion is increased, the emission from the edge chords of the diagnostic show a significant drop, indicating that the fast electrons at plasma periphery are

[5] More precisely the left-hand fast-wave cutoff $S - D = 0$ at lower density and the right-hand fast-wave cutoff $S + D = 0$ at higher density

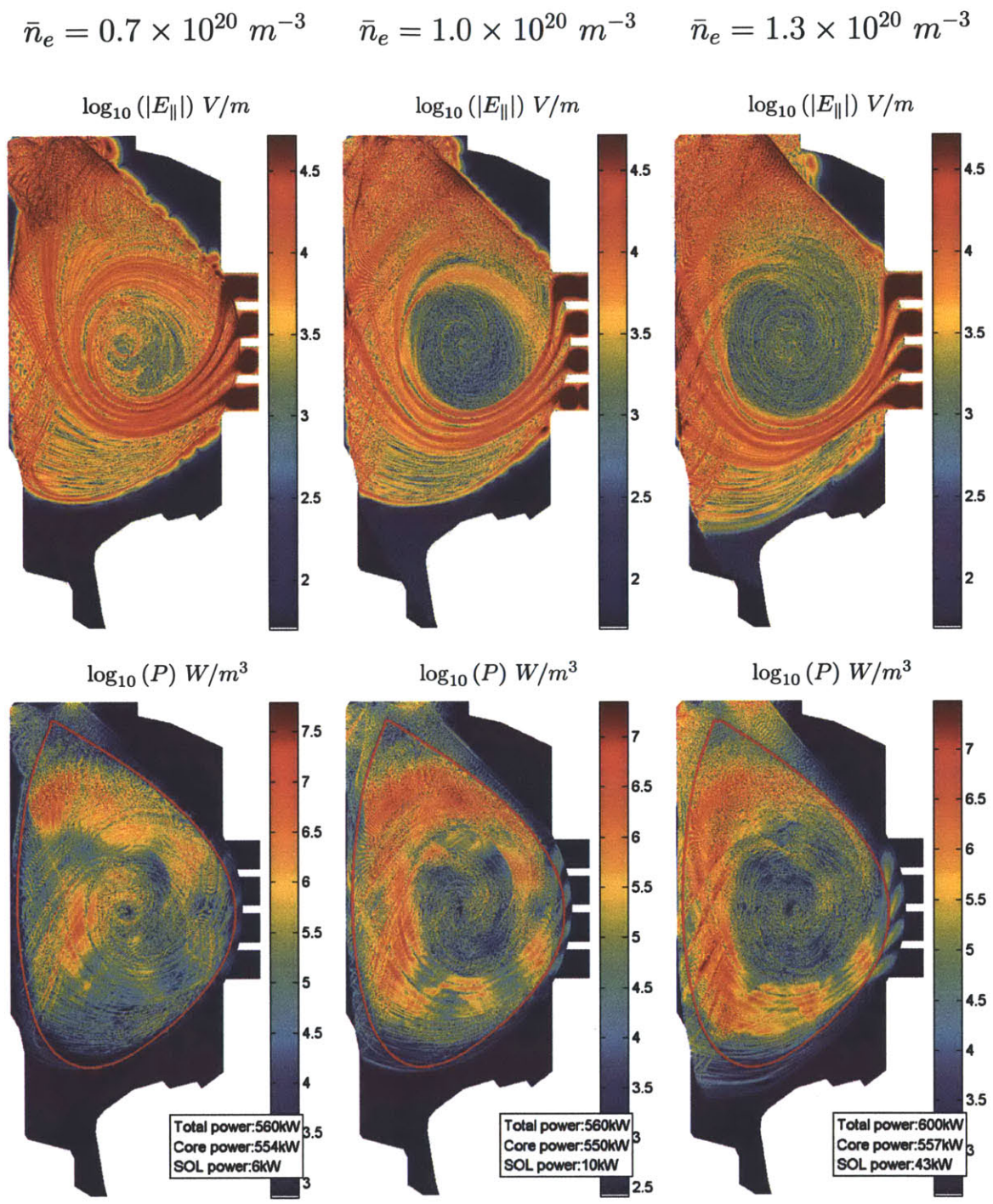

Figure 7-5: Top three figures show the logarithmic plot of the parallel electric field magnitude as simulated by LHEAF. On the bottom, the corresponding power deposition profiles are plotted, showing that the power absorbed in the SOL amounts only for a small fraction of the total power for all three density cases.

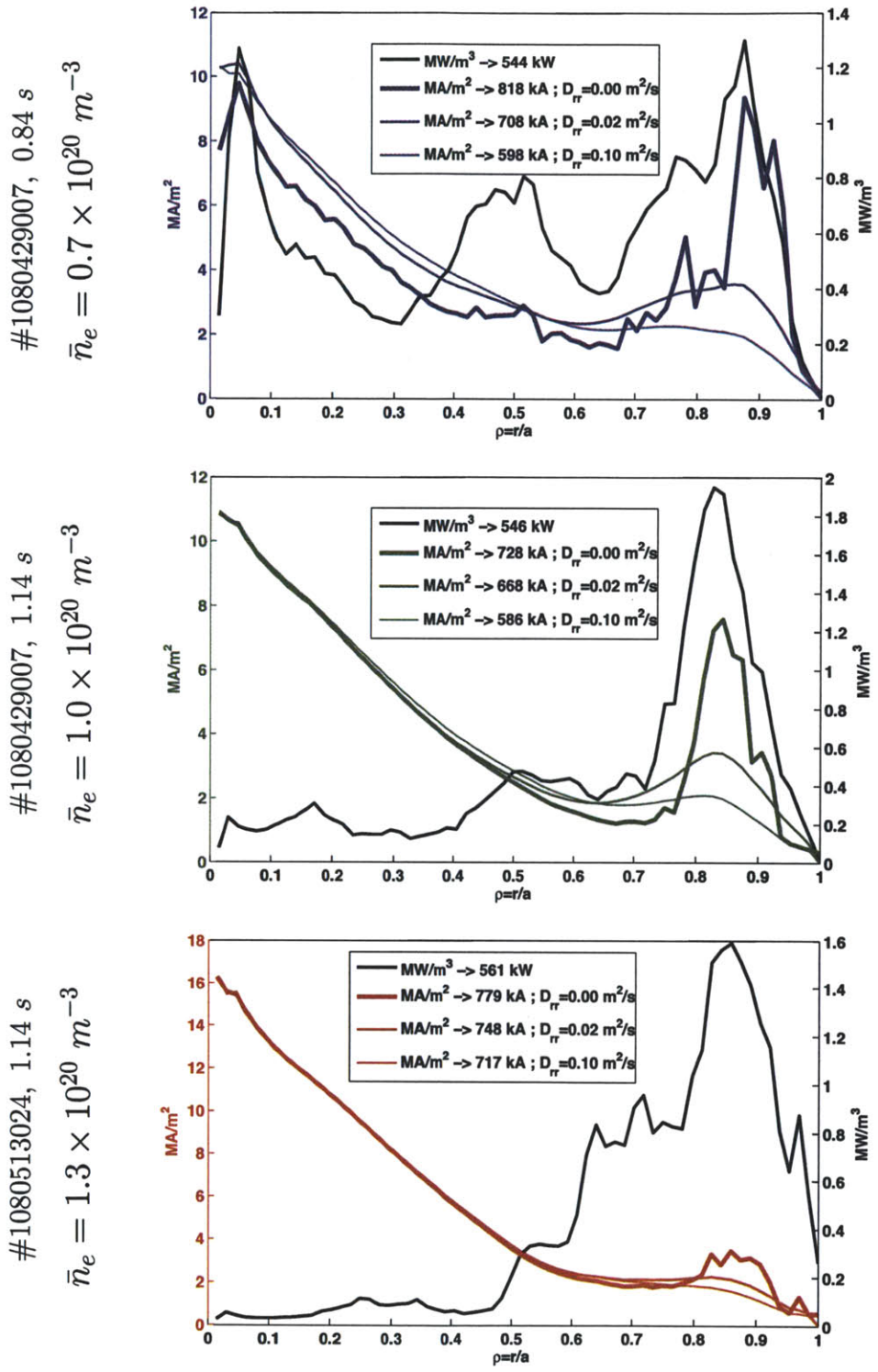

Figure 7-6: LH power absorption and current profiles for the three density cases and different amount of radial diffusion. For higher values of D_{rr}, the current drive efficiency gets reduced, while the power absorption is instead almost independent.

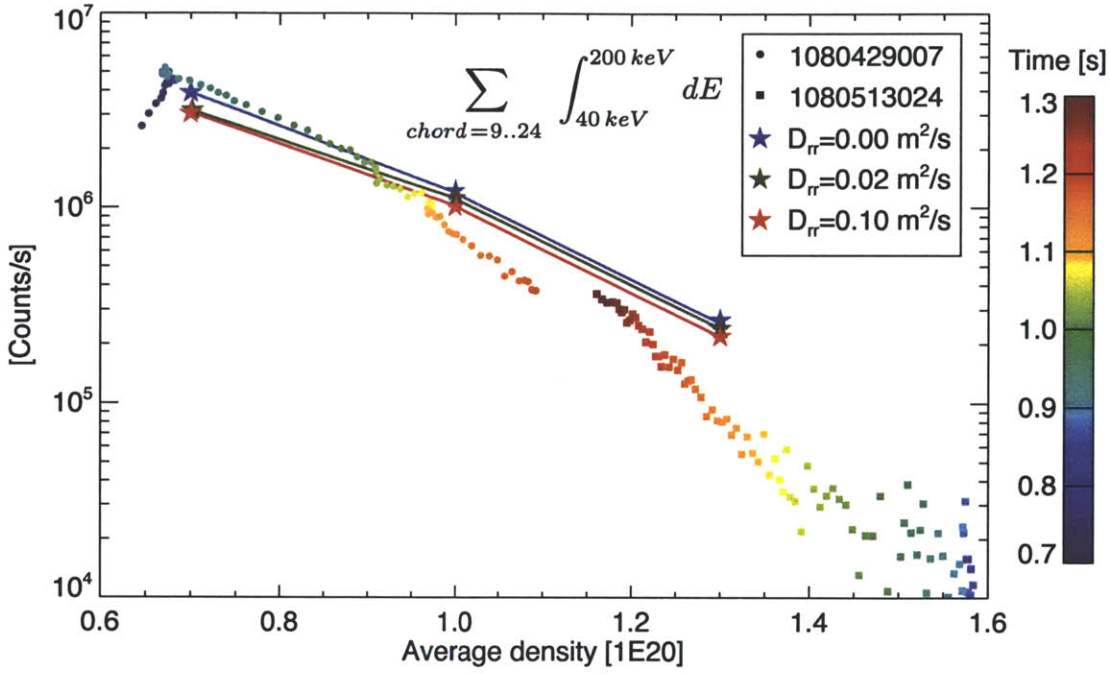

Figure 7-7: Comparison of simulated and measured HXR core emissivity (chords 9 to 24) as a function of density. LHEAF simulations were found to reproduce qualitatively well the experimentally observed steep drop in HXR emissivity even though most of the power is absorbed in the core region by ELD.

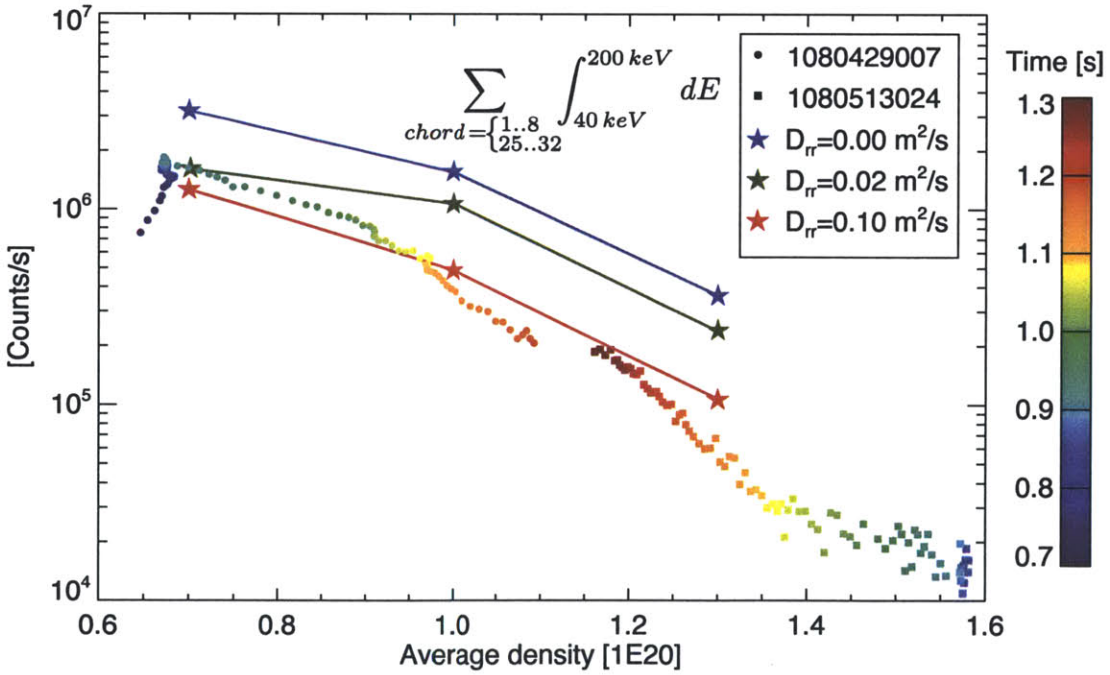

Figure 7-8: Comparison of simulated and measured HXR edge emissivity (chords 1 to 8 and 25 to 32) as a function of density. Radial diffusion of fast electrons can significantly reduce the emissivity from the edge chords.

transported outside of the LCFS where they are promptly lost. At the same time, fast electrons populate the core of the plasma, where they were originally absent in the higher density cases. This can be seen in Figs. 7-10, 7-11 and 7-12, which show the HXR plasma emissivity at 60, 130 and 200 keV as seen by the HXR camera geometry, for different amount of radial diffusion. In these plots, up-down and low-high field side asymmetries can also be appreciated. The former results from the headlight effect of the bremsstrahlung cross section and the geometric orientation of the magnetic field lines with respect to the HXR camera viewing chords. The latter results from the changes of the trapped particle region along a flux surface.

7.2.3 Radial diffusion of fast electrons

The slowing down rate for electrons above the thermal energy is proportional to $1/(\gamma v)^3$. For increasing velocity v, eventually an energy is reached where the transport time becomes less than the slowing down time. Above that energy, radial transport becomes important and fast electrons can diffuse across flux surfaces.

LHEAF simulations show that radial diffusion can change the localization of fast electrons and affect the performance of the current drive. In LHEAF simulations, some amount of radial diffusion is needed to obtain reasonable agreement with the HXR profiles, however this can not be too high, otherwise the total amount of current does not agree with the experiments, especially at low current. Qualitatively, a value of D_{rr} between 0.02 and 0.10 m^2/s seams to be a good compromise between the two effects. Similar results have been obtained also with ray-tracing codes and diffusion coefficients $> D_{rr} = 0.05\ m^2/s$ [117]. However radial diffusion was not considered as a possible mechanism for the LHCD density limit and ray-tracing simulations including radial diffusion of fast electrons have yet to be run in this regime.

On Alcator C-Mod, recent measurements by Schmidt have set an upper bound of fast electron diffusion of $D \leq 0.02\ m^2/s$ over a 60 to 100 keV range of energies, indicating that fast electrons do not stray far from the flux surface where they are born before slowing down [117]. As reported in Fig. 7-13, the amount of radial diffusion used in LHEAF to match the experimental profiles is higher than $D \leq 0.02\ m^2/s$, but still comparable to what used in previous ray-tracing simulations by the same author [117]. These numbers must also be compared with initial studies of fast electron diffusion in LHCD tokamak plasmas[170, 171] which had determined an upper bound on fast electron diffusion in the range of $0.2 - 2\ m^2/s$. Similar values are used in LHCD simulations on other devices [172]. Understanding the origin of the discrepancy between the amount of diffusion required in the simulations to match the experimental HXR profiles and the Alcator C-Mod diffusion measurements is important and needs to be further investigated.

A first possible explanation could be that the diffusion coefficient used in the simulations is a proxy for other transport mechanisms that are taking place in the experiment. However, terms such as convection and particle pinch have also been measured by Schmidt to be small $|v| \leq 0.75\ m/s$ [117]. Another possible cause should be sought in the fact that the emissivity model used in Ref. [117] does not account for the low-high field side asymmetry, which can be significant especially at the outermost plasma radii where the measurements were taken (as shown in Fig. 7-11). Neglecting such an asymmetry skews the measurements towards the high field side of the tokamak, where the plasma is more quiescent and smaller values of D are to be expected.

The presence of fast electron transport taking place near the plasma edge is supported by the significant HXR emission that is routinely observed well outside of the LCFS of limited discharges, or from the X-point regions in diverted discharges. These observations contrast with the idea that fast electrons would be promptly lost on open field lines. The physics behind these observations is still unclear, however effects such as interaction of neutrons or high energy γ with the walls or the HXR camera vacuum window have all been excluded. A possible explanation may lie in the different orbits of passing and trapped particles. While passing fast passing particles are immediately lost in the SOL, trapped particles can be confined with a time constant proportional to their collisional

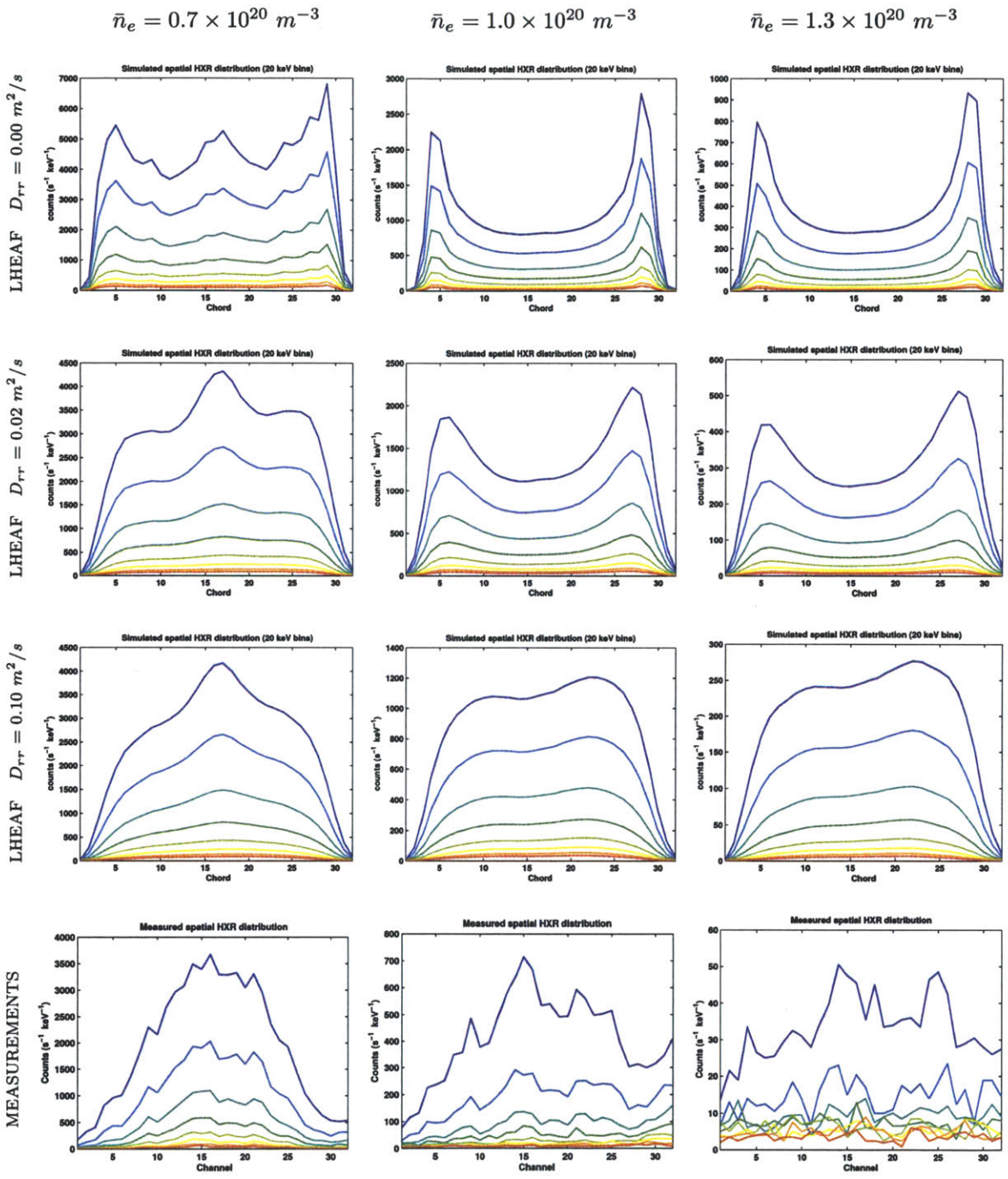

Figure 7-9: Comparison between the simulated and the measured line integrated XHR emissivity for the three line average density cases under study. As explained in Sec. 7.2.3, fast electrons at the plasma edge can be quickly lost by radial particle transport. This effect is reflected in the HXR profiles, which are a sensitive function of the amount of radial diffusion used in the simulations.

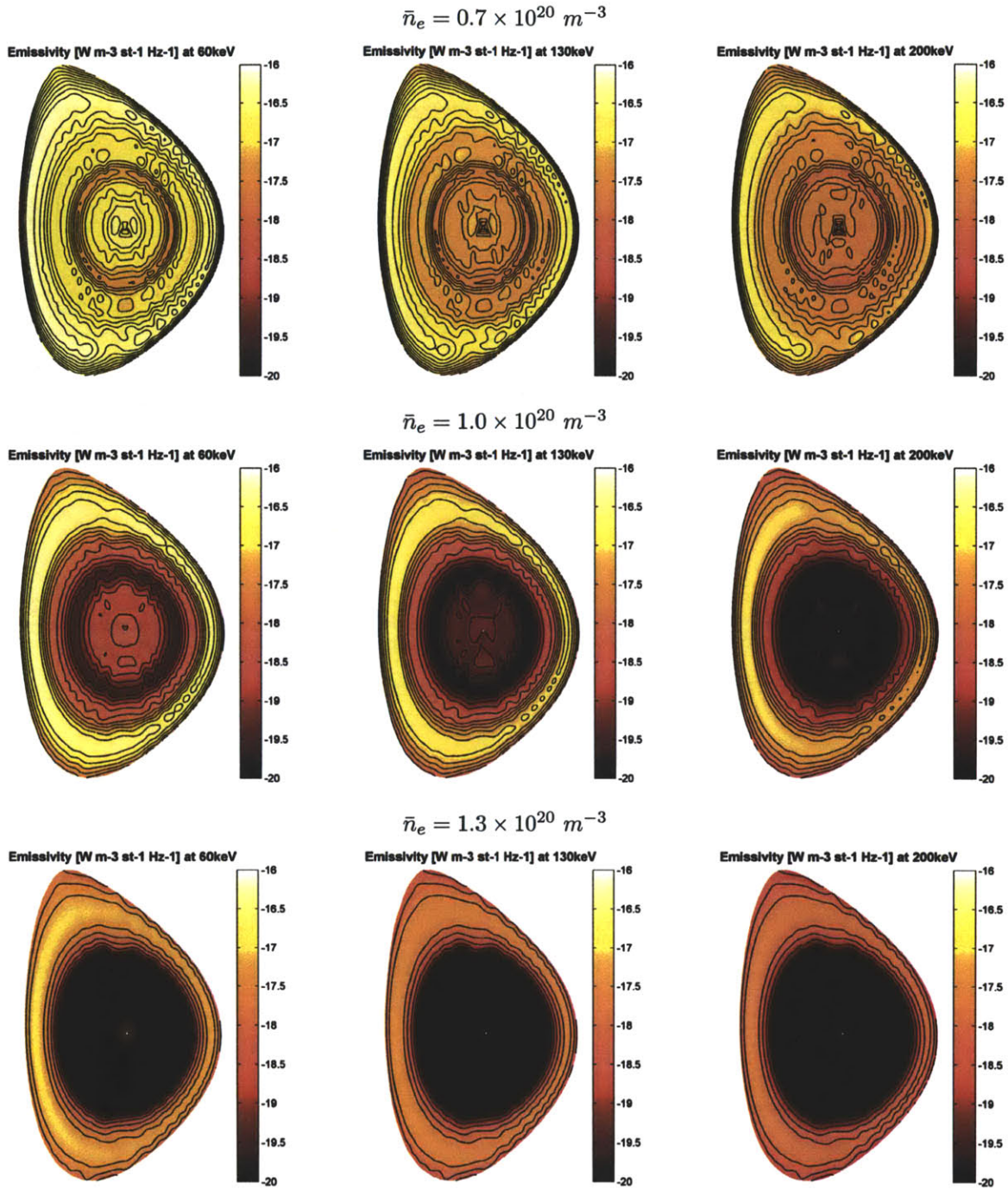

Figure 7-10: Plot of the HXR plasma emissivity at three photon energies as seen by the HXR camera geometry, for the simulations without fast electron radial diffusion. At higher densities the HXR counts rates drops by orders of magnitude throughout the whole plasma, independently of the amount of radial diffusion used in the simulations. In this sense, radial diffusion is not necessary to explain the density limit. However some transport mechanism is required for redistributing the HXR population across the plasma and the synthetic HXR camera to agree with the experimental measurements.

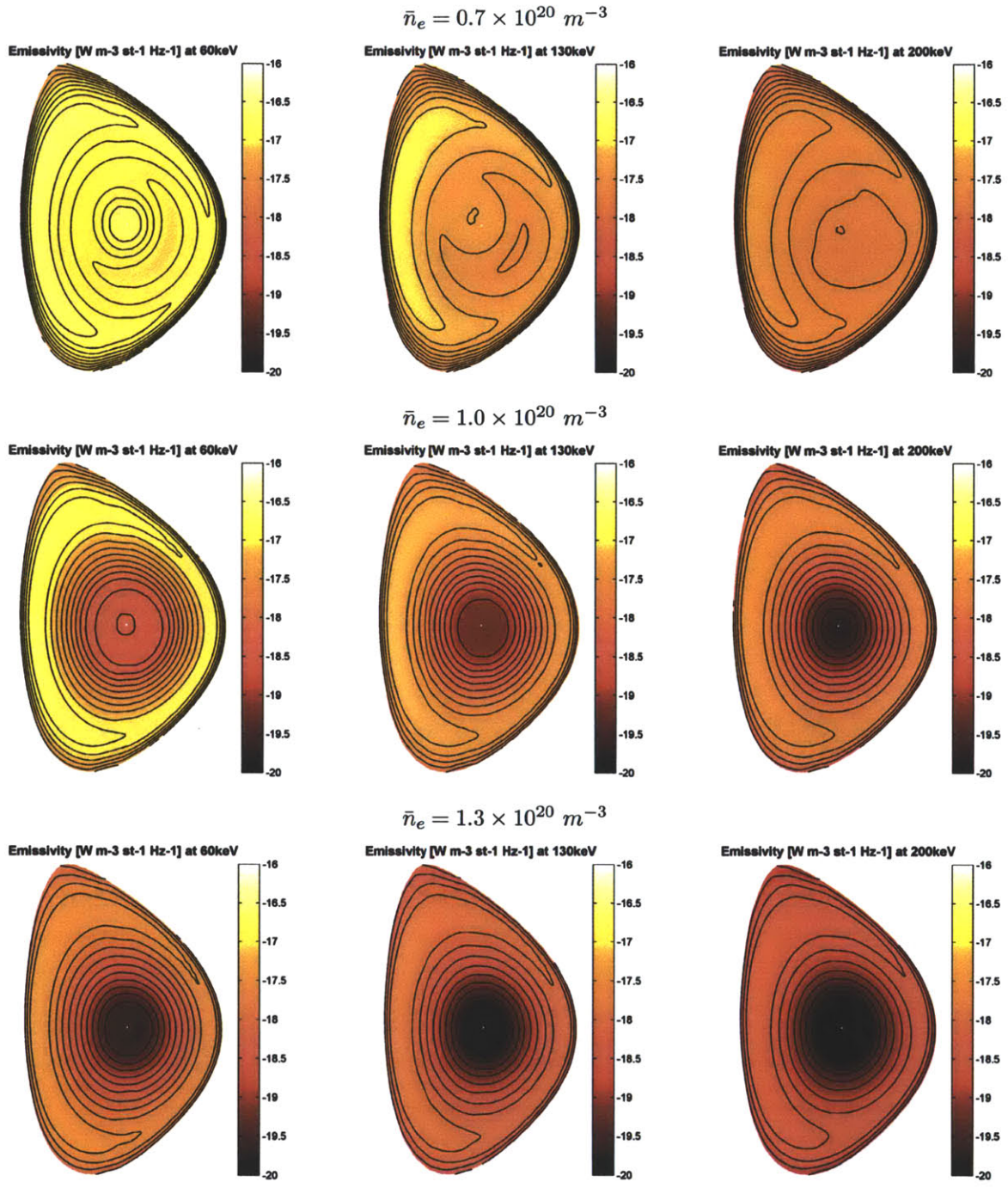

Figure 7-11: Same plot shown in Fig. 7-10 but for simulations with a radial diffusion coefficient of $D_{rr} = 0.02\ m^2/s$. These plots show how in addition of being up-down asymmetric, the emissivity profile is also low-high field side asymmetric. The former is due to the headlight effect of the bremsstrahlung cross section and the geometric orientation of the magnetic field lines with respect to the HXR camera viewing chords. The latter results from the modification of the trapped particle region along a flux surface.

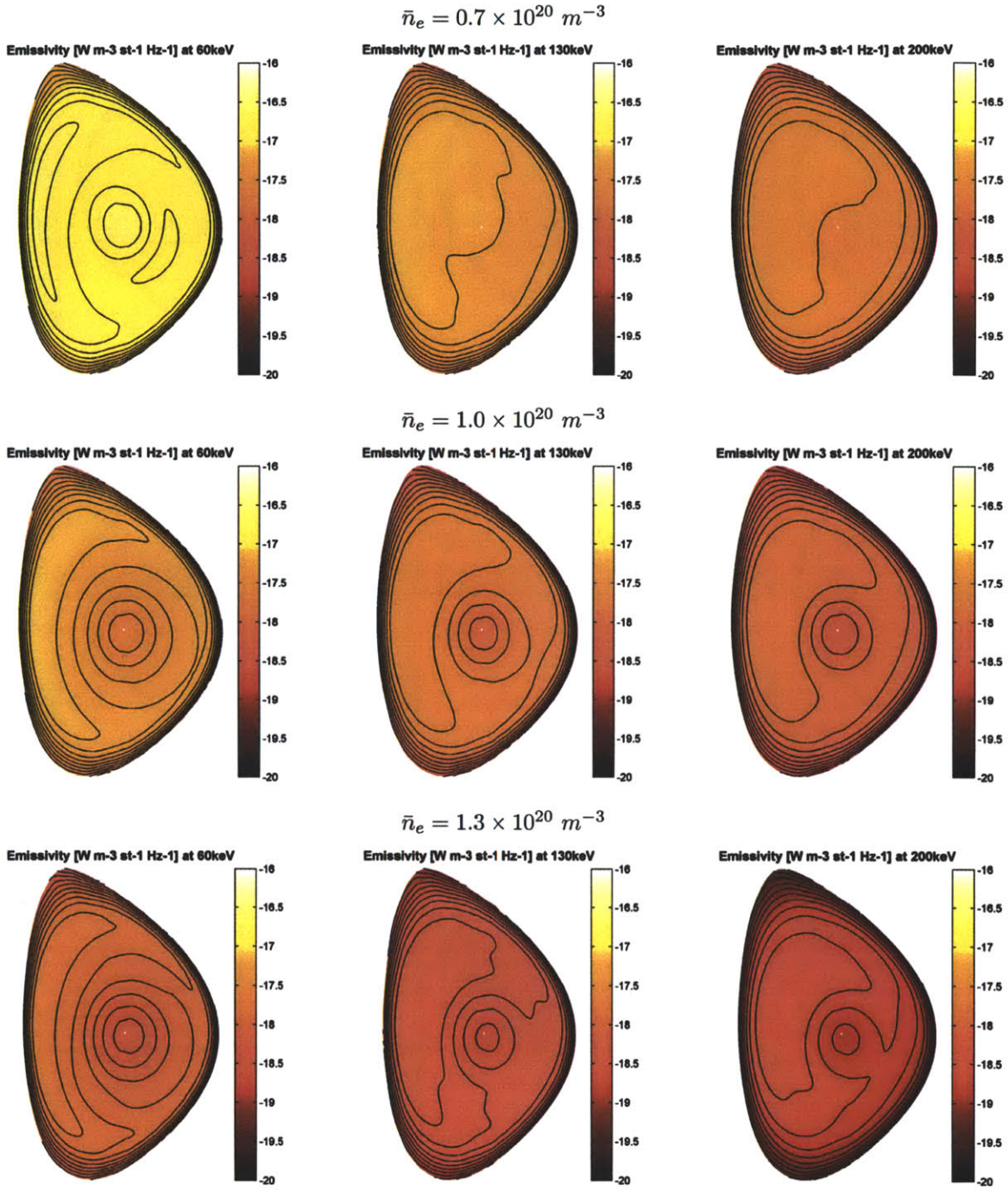

Figure 7-12: Same plot shown in Fig. 7-10 but for simulations with a radial diffusion coefficient of $D_{rr} = 0.10\ m^2/s$. Diffusion has the effect of both loosing fast electrons through the separatrix and populating the core of the plasma, where they were originally absent in the higher density cases.

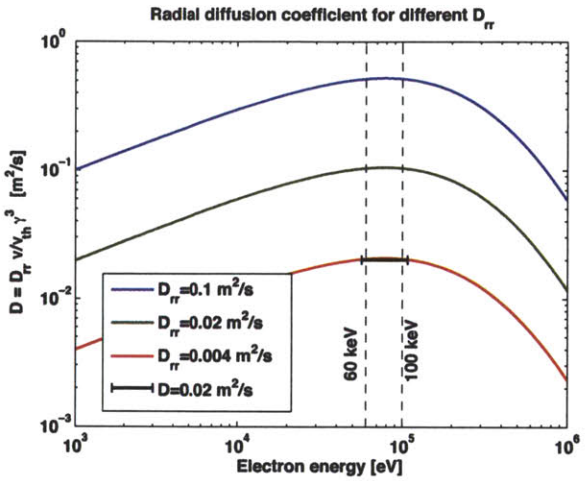

Figure 7-13: Plot of the diffusion coefficient D as a function of the electron kinetic energy, parametrized for D_{rr}. For these plots, a thermal electron temperature of 1 keV was assumed. Ref. [117] sets a constant upper bound of $D \leq 0.02\ m^2/s$ over the region between 60 to 100 keV, where the measurements were made. According to the fast electron diffusion model used, this would correspond to a $D_{rr} \approx 0.004\ m^2/s$. Measurement of the radial diffusion coefficient over a broader energy range would be important to validate the model of Eq. 6.14 used in the simulations.

time τ_c. If such time is much smaller than their diffusion time $\tau_c \ll \tau_D = \frac{(\Delta r)^2}{D} = -\frac{(\Delta r)^2}{\Gamma_{rr}} \left(\frac{\partial f}{\partial r}\right)^{-1}$, which is reasonable for high energy particles at the edge, then trapped fast particles could effectively diffuse in the SOL region. If this speculation is correct, a low-high field side asymmetry in the SOL HXR emission should be measured in view of the reduced number of trapped particles on the high field side. Such behaviour could also be included in the VERD 3DFP module, by allowing control of the particle flux outside fo the LCFS $\Gamma_{rr}(v_\parallel, v_\perp, a)$ and using different values for the trapped and the passing particles. Limited discharges with small elongation have many HXR camera chords mapping well outside of the LCFS and could provide a good experimental basis for this work.

7.2.4 Velocity space analysis

The panels of Fig. 7-14,7-15 and 7-16 show, for the three density cases, the surface plots of the RF quasilinear diffusion coefficient D_{QL}, the LH power absorption, the parallel distribution function and the total current as a function of $\beta_\parallel = v_\parallel/c$ and of the normalized minor radius $\rho = r/a$. The quantities which result from the 2D/3D Fokker-Planck analysis have been integrated in the $u_\perp$ direction so to have only a $u_\parallel$ dependence.

Quasilinear diffusion coefficient $D_{\mathrm{QL}}(v_\parallel, \rho)$

Plot of the RF quasilinear diffusion coefficient D_{QL} (first panel) gives insight about the evolution of the wave $n_\parallel$ spectrum (since to first order $D_{\mathrm{QL}}(v_\parallel) \propto E_\parallel^2(v_\parallel)$). For this purpose it is useful to analyse Fig. 7-14 with respect to the electric field and power deposition plots shown in Fig. 7-5. Indeed following the regions of high D_{QL} starting from $\rho = 1$ and $v_\parallel/c \approx 0.5$ (launching position), one sees that first the waves' $n_\parallel$ downshifts as they propagate towards plasma core up to $\rho \approx 0.5$ and subsequently the waves' $n_\parallel$ upshifts as they propagate back towards the plasma edge.

One can also notice how the wave fields are confined in the region of parallel velocity space lying between $3\,v_{Te}$ (highlighted by a dashed red-black line) and the accessibility condition for a

slow-wave $v_{\text{maxacc}} = 1/n_{\text{maxacc}}$ (highlighted by a dashed white-black line and calculated for the maximum B field on a flux surface, hence the $_{\text{max}}$ subscript). After crossing the $3\,v_{Te}$ boundary, the wave spectrum diminishes due to ELD.

At the v_{maxacc} boundary the two roots of the dispersion relation coalesce [6]. Whether mode conversion to the fast-wave does takes place, depends upon the competition between the toroidal ($k_\phi B_\phi/B$), poloidal ($k_\theta B_\theta/B$) and radial ($k_r B_r/B$) components of the $n_\parallel$ spectrum, which for typical Alcator C-Mod LCHD plasma parameters are all comparable in magnitude. Although the $n_\parallel$ evolution near the mode-conversion boundary is very dynamic, the behaviour in this region is very consistent and, as the wave fields approach the v_{maxacc} boundary, most of the wave spectrum remains a slow-wave (low velocity side of v_{maxacc}). Understanding of this behaviour has been obtained using ray-tracing simulations and is presented in Appx. A.

Absorbed LH power $P(v_\parallel, \rho)$

The LH wave power deposition (second panel) starts in the vicinity of $v_\parallel = 3\,v_{Te}$ and as the density is raised it mostly localizes towards the plasma edge. This means that after being launched, the waves are slowed down inside of the plasma by an order of magnitude and are able to damp also in the cool edge region of the plasma. The mechanism by which the spectral gap is bridged so effectively must be sought in the local transformation of the $n_\parallel$ spectrum which is taking place throughout the plasma and after waves reflect and propagate through the SOL. This is the subject of Sec. 7.2.5. The power absorption goes to zero in the vicinity of the magenta line, which indicates the electrons Dreicer velocity [173, 174].

Distribution function $f(v_\parallel, \rho)$ and toroidal current $J(v_\parallel, \rho)$

Once the waves start damping, the distribution function deviates from a Maxwellian (third panel) and, through its $v_\parallel$ asymmetry, current is generated (fourth panel). The large low-velocity contribution to the current is the DC electric field (non-zero loop-voltage). The high-velocity contribution is instead the result of the LH waves.

The most prominent effect of increasing radial diffusion is that the fast electron tail which was generated by LH waves at plasma periphery is lost. Such loss is directly appreciable in the HXR profiles of Fig. 7-9 and can be understood by comparing the distribution function and current profile of Fig. 7-14 (no radial diffusion) with the one of Figs. 7-15 ($D_{rr} = 0.02\ m^2/s$) and 7-16 ($D_{rr} = 0.10\ m^2/s$). As radial diffusion is increased, the high energy fast electrons are transported from $r/a \approx 0.9$ towards the edge of the plasma where they are lost. Transport of fast electrons to the plasma core can lead to interesting non-monotonically decreasing distribution function in $v_\parallel$. The power deposition profile is almost independent on the amount of radial diffusion, since it is dominated by the dynamics at low energy ($v \approx 3\,v_{Te}$).

Meshing

Knowledge of the spectral content as a function of the radial location allows one to verify the adequacy of the mesh used in LHEAF simulations, especially at high densities where this could be a major concern. In order for FEM simulations to be accurate, the mesh must satisfy the Nyquist-Shannon sampling theorem, meaning that the mesh must be at least half of the shortest wavelength in the problem. Figure 7-14 shows that short wavelength modes with $n_\parallel \geq 10$ appear only at the edge of the plasma, because in the core they are well damped by ELD.

For electrostatic waves $n_\perp \approx \sqrt{-P/S}n_\parallel$, which at the separatrix $n_\perp \approx 13 n_\parallel$ for a high density discharge. Since in these LHEAF simulations each hexahedral (cubic) mesh element has sides of length $\Delta L = 0.25\ mm$, the maximum $n_\parallel$ that can be correctly represented is $n_{\parallel\text{Nyquist}} =$

[6] Since the magnetic field strength B varies along a flux surface, the accessibility condition may also be violated for lower phase velocities, though this cannot be seen in $(v_\parallel, \rho)$ space.

$\frac{c}{f}\sqrt{-\frac{S}{P}}\frac{1}{2\Delta L} \approx 10$. On the basis of the electron Landau damping resonant condition $v_{\parallel} = 3v_{th}$, one can associate a temperature of 250 eV as the minimum temperature below which $n_{\parallel}$ values lower than 10 would be damped. In the high density simulations, such temperature occurs at $r/a = 0.93$. The situation improves for the moderate and low density discharges, since the term $\sqrt{-P/S}$ decreases with the square root of the density, while at the same time the plasma edge tends to become hotter (though the temperature at the separatrix is always pinned down to ~ 80 eV).

The best solution for the mesh problem would be to use a finer mesh. Unfortunately, reducing by half the mesh elements size (to correctly represent $n_{\parallel \max} \approx 10$) means quadrupling the number of unknowns (i.e. going from 30 million to 120 million DoFs), which is very computationally expensive. The effects of finite mesh resolution and how SOL collisional damping can mild this issue are further discussed in Sec. 7.3.

7.2.5 Wavelet analysis to investigate importance of fullwave effects

In fullwave methods the information about the local $n_{\parallel}$ wave spectrum is not readily available as in ray-tracing codes and must be recovered by the fullwave fields. Fourier Transform (FT) of the parallel wave fields along the field lines can provide insight into what spectral components exist on flux surfaces at different radial locations (see first panel of Fig. 7-14 and Ref. [88, 15]). However, FT does not provide any information about the poloidal distribution of different spectral components.

Based on the experience built upon ray-tracing codes, one may expect certain spectral components to be spatially localized, at least for the cases when stochastic effects are unimportant [175, 176]. In mathematical terms that is to say the wave fields are non-stationary along a flux surface. The general problem of finding the different spectral components along a field line requires using a localized set of basis functions ("windowed transforms"), and using an optimal window size for each k. The Continuous Wavelet Transform (CWT) is a tool designed for the analysis of non-stationary signals and is well-suited to this problem.

In this section, the CWT is used to postprocess the complicated fullwave field pattern generated by the LHEAF code. In particular, the electric field parallel to the static magnetic field lines is decomposed into its $n_{\parallel}$ spectral components [7]. The following analysis is based on the techniques first described in Ref. [177, 178] for the local mode analysis of ICRF fullwave solution and has been guided by the work of Pereverzev [30, 179]. The mathematical formulation about CWT and further technical details about the analysis presented here are given in Appx. D.

Launched $n_{\parallel}$ spectrum

Inspection of the wavelet spectrum evaluated at the LCFS shown in Fig. 7-17, reveals that the launched $n_{\parallel}$ spectrum in the vicinity of the launcher is not monochromatic. Since LHEAF simulations model a single toroidal mode number ($n_{\phi} = 1.9$ at the grill mouth), the physical reason for such a broad launched $n_{\parallel}$ spectrum must be sought in the non-zero poloidal spectrum launched by the antenna ($n_r \neq 0$, $n_{\theta} \neq 0$):

$$n_{\parallel} = \frac{\vec{n} \cdot \vec{B}}{|\vec{B}|} = \frac{n_r B_r + n_{\theta} B_{\theta} + n_{\phi} B_{\Phi}}{|\vec{B}|} \tag{7.4}$$

In fact, high order modes are excited at the waveguide-plasma interface. In other words since LH grill antennas have the poloidal dimension of the waveguides which is about one half of the guided wavelength, Fresnel diffraction can affect the wave phenomena.

[7] In theory, the perpendicular component $n_{\perp}$ could be easily calculated if one knew on which brach of the dispersion relation (slow or fast) the waves were propagating. For the case of LHCD, it would be reasonable to assume that all of the waves are on the slow brach. However, at different locations in the plasma, different $n_{\parallel}$ component would contribute to the same $n_{\perp}$. In practice this would make the interpretation of the reconstructed $n_{\perp}$ somewhat difficult in the that wavelet power spectra at different $n_{\parallel}$ have different phase and real space resolution.

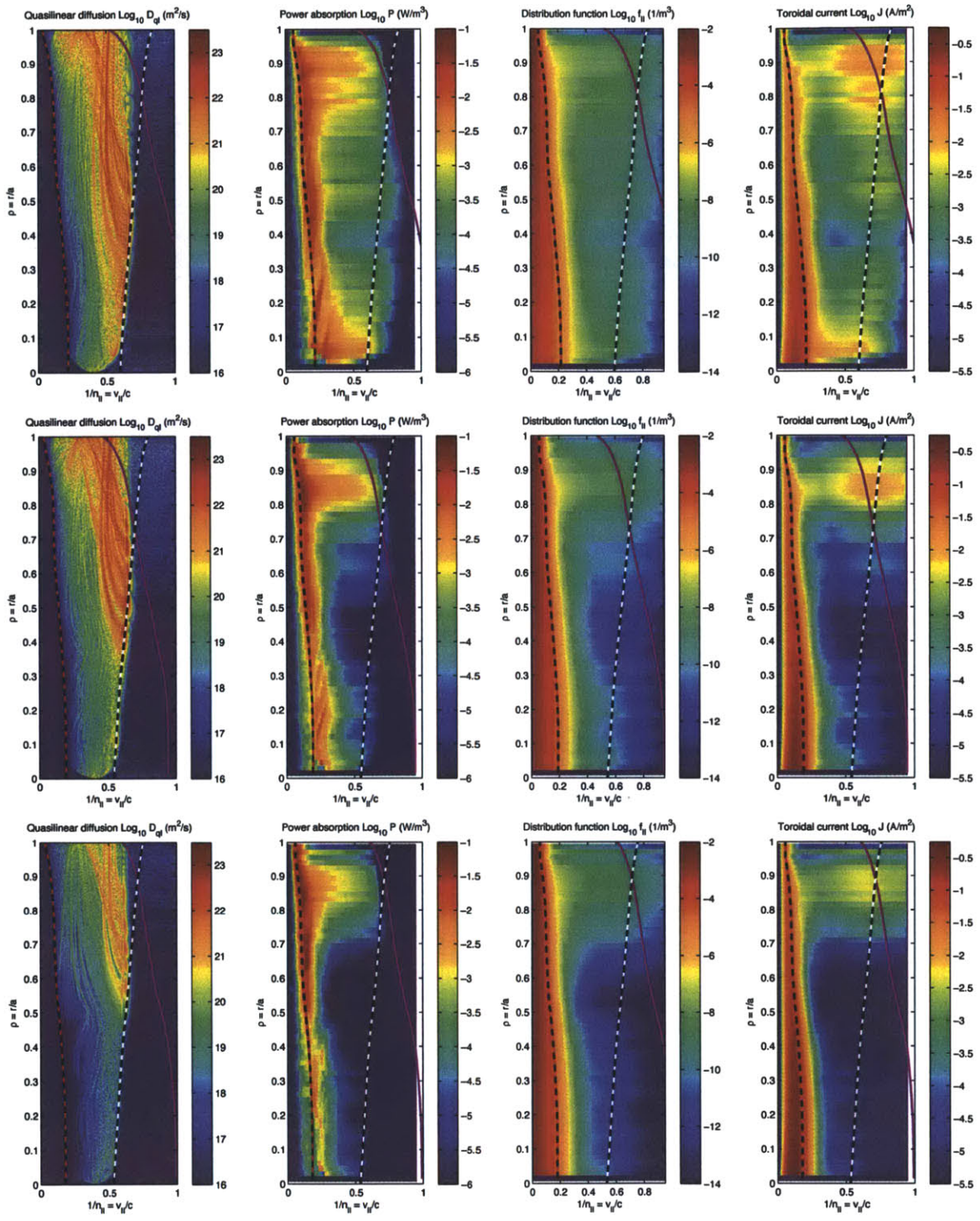

Figure 7-14: Velocity space analysis with no radial diffusion. The surface plots show the RF quasi-linear diffusion coefficient D_{QL}, the LH power absorption, the parallel distribution function and the total current as a function of $\beta_{\parallel} = v_{\parallel}/c = 1/n_{\parallel}$ and of the normalized minor radius $\rho = r/a$. Power absorption and current have been integrated in the $u_{\perp}$ direction so to have only a $u_{\parallel}$ dependence. The dashed red-black, dashed white-black and magenta lines represent the $3\,v_{Te}$, accessibility and Dreicer field velocities, respectively.

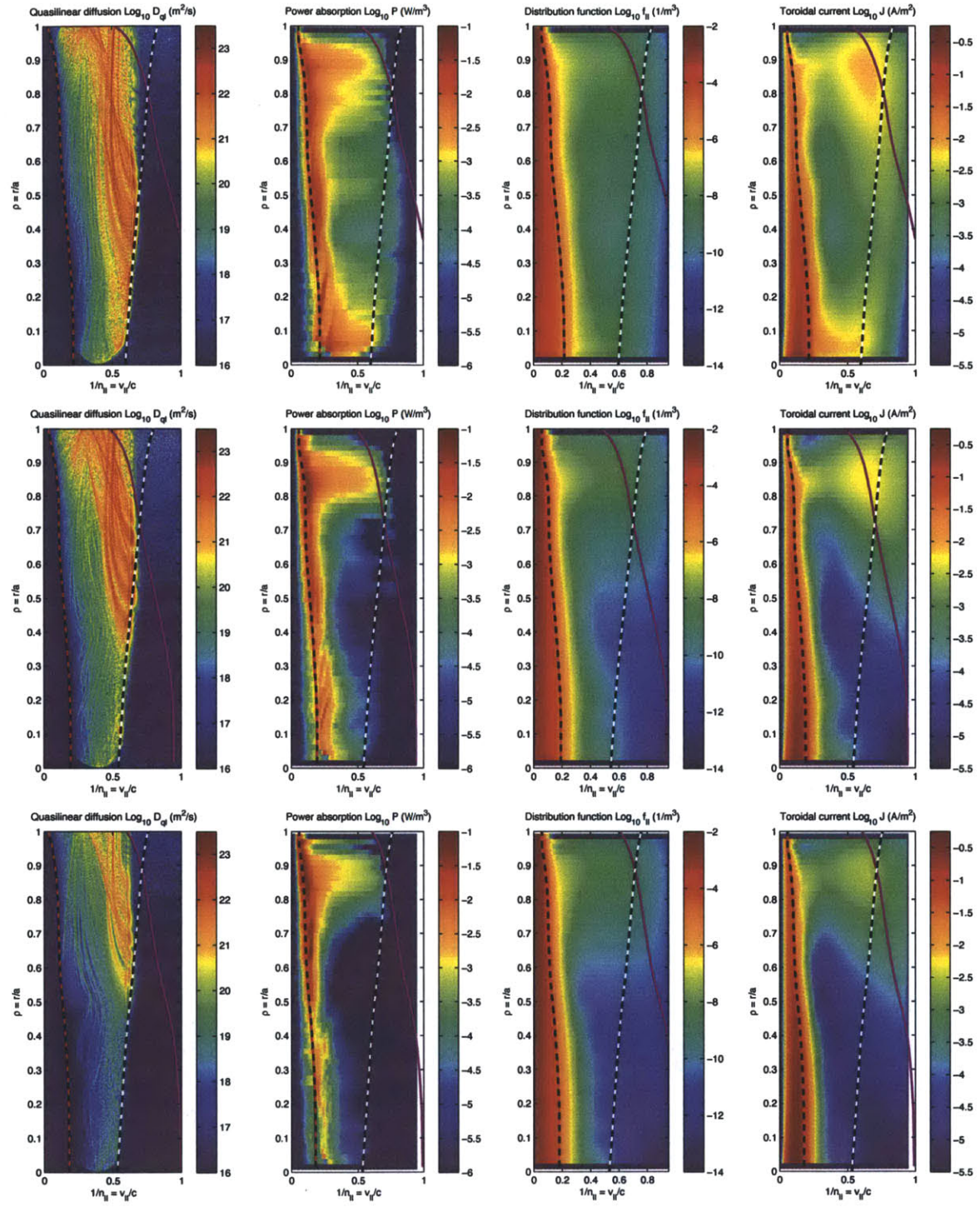

Figure 7-15: Velocity space analysis with radial diffusion coefficient $D_{rr} = 0.02\ m^2/s$. The power absorption is nearly independent of the amount of diffusion, while the LHCD driven current driven at the edge is significantly reduced.

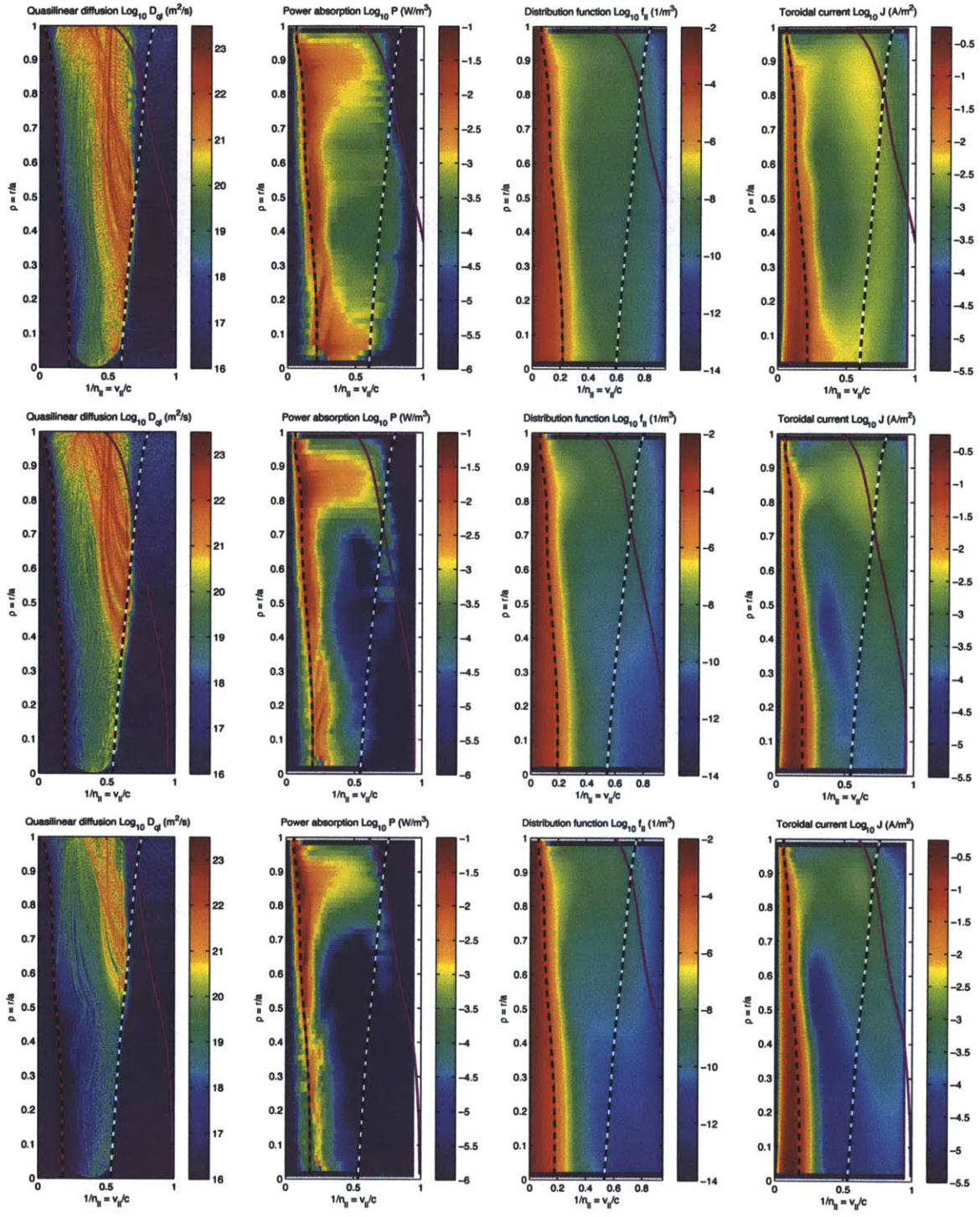

Figure 7-16: Velocity space analysis of high density discharge $\bar{n}_e = 1.3 \times 10^{20}\ m^{-3}$ with radial diffusion coefficient $D_{rr} = 0.10\ m^2/s$. The power absorption is nearly independent of the amount of diffusion, while the LHCD driven current driven at the edge is significantly reduced.

In Fig. 7-17, at the poloidal angles of $\theta = -41, -23, -5$ and 13 *deg* one finds four peaks centered around $n_\parallel = 1.9$ which have a with a Full-Width Half-Maximum (FWHM) of $\Delta n_\parallel \approx 0.26$. Accounting for the finite spectral resolution of the wavelet analysis at $n_\parallel \approx 1.9$ of $\Delta n_H = 0.157$ results in a "true" $\Delta n_\parallel \approx 0.1$, assuming that the original spectrum is gaussian in shape.

Coupling codes such as TOPICA and ALOHA, which account for the 3D structure of the grill allow to calculate both the toroidal and the poloidal launched power spectrum [94]. For the case of Alcator C-Mod, the FWHM of the toroidal and poloidal spectrum are $\Delta n_{\phi,antenna} \approx 0.42$ and $\Delta n_{\theta,antenna} \approx 0.96$ respectively. The spectral $n_\parallel$ widths of the peaks measured by LHEAF wavelet analysis is consistent with the projection of the launched poloidal spectrum from these coupling codes, projected in the parallel direction, which is $\Delta n_\parallel = \Delta n_{\theta,antenna} \hat{\theta} \cdot \vec{B} \approx 0.1$, assuming a pitch angle of ≈ 10 *deg*.

In LHEAF the matching of the fields between the launcher waveguides and the plasma are taken into account in an exact way. The presence of the Fresnel fringes due to the finite width of the waveguides and the interference pattern from multiple poloidally radiating apertures is as multiple secondary peaks which are visible both in physical space (Fig. 7-5) and phase space (Fig. 7-14). Different poloidal spectrum can have a significant effect on the Fokker Planck calculations and may be an importance source of difference among fullwave codes. For example, in codes TORIC-LH or AORSA the wave excitation occurs at the separatrix with a toroidally aligned electric field which does not account for higher waveguide modes.

In ray-tracing calculations it is customary to launch rays either from the same location (e.g. the center of a waveguide) but with a $n_\parallel, n_\perp$ spectrum [26], or distribute the rays in real space but assume that the $n_\parallel, n_\perp$ spectrum is a delta function [77]. The initial condition of each ray is chosen in such a way that the wave vector is perpendicular to the flux surface, while satisfying the LH wave dispersion relation. In practice however, different $n_\parallel$ and $n_\perp$ spectral components are generated at different locations of the launcher. In theory, it could be possible to use wavelet analysis of the wave fields from coupling codes to generate a 4D map telling the distribution of power in $n_\parallel, n_\perp$ at every poloidal/radial location in front of the launcher. In this sense, Fig. 7-17 is an example of such a map but in 2D ($n_\parallel$, poloidal location). Using this map one could think of launching many rays [8], each with different $1.5 < n_\parallel < 2.5$ and at -50 *deg* $< \theta < 25$ *deg* and a power distribution set according wavelet power spectrum.

Spectral evolution

The result of the wavelet analysis applied to the entire plasma cross-section is shown in Figs. 7-18, 7-18 and 7-20 for the low, moderate and high density discharge. Since the $n_\parallel$ spectrum changes continuously along the wave propagation, up or down shifting of the spectrum can be studied by tracking the evolution of the wavelet power spectrum peaks across different $n_\parallel$ frames. The spectral broadness instead can be estimated by counting for how may $n_\parallel$ frames does a feature persist at the same physical location in the plasma.

Indeed the waves launched from the antenna region with $n_\parallel = 1.9$, first downshift ($n_\parallel < 1.9$) and subsequently upshift ($n_\parallel > 1.9$), confirming the result of the analysis carried out in the first panel of Fig. 7-14. Broad spectral features associated with strong $n_\parallel$ upshift are observed after the waves reflect off the inner wall and the upper divertor region. By contrast, reflection off the ω_p cutoff layer in the vicinity of the lower-outer divertor results in $n_\parallel$ downshift. This is in agreement with the

[8] The use of a large number of rays is considered as the standard prescription in conventional ray-tracing in order for the rays to describe the launched spectrum. In the work by Peysson and Decker a single ray is launched from each poloidal location and the parameter $\Delta n_\parallel$ takes the physical meaning of the width of a gaussian beam, as in beam tracing calculations. If the antenna was large enough, then it might be a reasonable approximation to consider just a single ray [180]. When the antenna is small, several beams might be launched to try to cover the spectrum. However, then a problem arises since although the fields are additive the mean square widths of the beams are not. In other words, the sum of narrow Gaussian beams, each shifted relative to the other, is not the same as one wide gaussian beam.

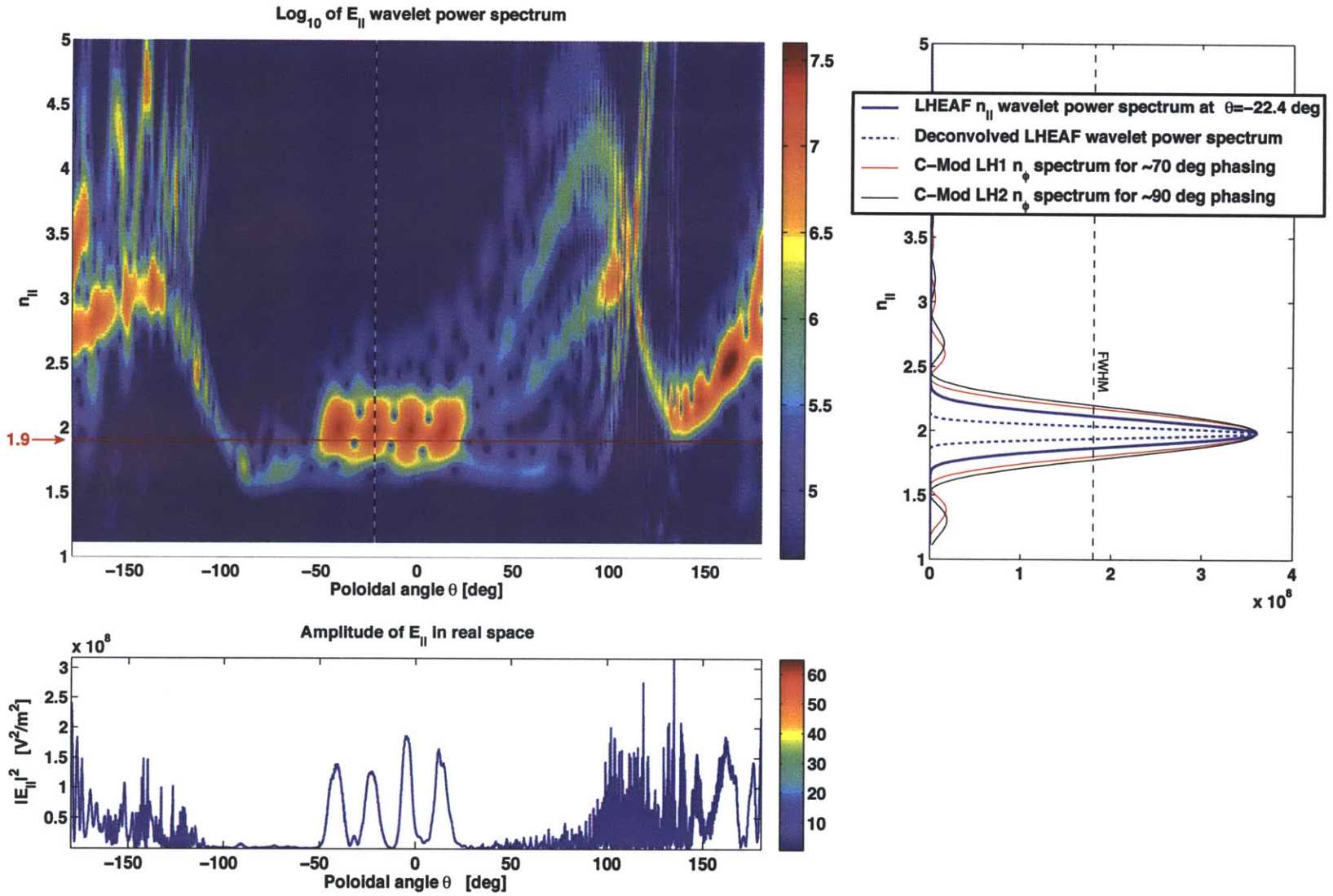

Figure 7-17: Logarithmic wavelet power spectrum of the parallel electric field at the LCFS for the high density discharge. Four peaks are clearly visible, each corresponding to the waves launched from a poloidal row of waveguides composing the grill antenna. For reference, at the bottom is plotted the square magnitude of the parallel electric field $E_{\|}$. The peaks are centered at $n_{\|} \approx 2$ because at first the waves $n_{\|}$ tends to increase slightly due to the $1/R$ dependence of n_{ϕ} in Eq. 2.36, before decreasing due to the combined effects of toroidicity (M variation) and magnetic shear (B_{Θ} variations) in Eq. 2.36. On the right, a cutout of the wavelet power spectrum at $\theta = 22.4$ *deg* is shown and compared with the toroidal launched spectrum.

dependency of the $n_\parallel$ spectrum evolution on the launching location described in Sec. 2.3.1. Strong changes of the $n_\parallel$ spectrum in the SOL region are expected, since the reflecting surfaces are not aligned with the static magnetic field, as explained in Fig. 7-21.

This analysis highlights the presence of spiral-like structures near the center of the plasma which are associated with the formation of caustics. At a caustic, the slow-wave becomes tangent to a magnetic surface and undergoes radial reflection. In these conditions, the transverse dimension of the LH resonance cone is comparable to the perpendicular wavelength, wave diffraction becomes significant and the waves are blurred both in real and spectral space (compared to a ray-tracing solution). Such phenomena was first studied by Pereverzev [30] in the context of beam-tracing simulations, in Ref. [16] for fullwave solution in a pseudo-toroidal geometry and is also observed in the LHEAF fullwave solution. Quite spectacular is the low density case of case of Fig. 7-18, where the waves clearly spiral around or just outside of the magnetic axis depending on their $n_\parallel$. That the reflected wave is the same slow wave as the incident wave can be deduced by the absence of any fanning structure which is typically accompanied with fast-wave propagation. Careful inspection of the region in which radial reflection takes place shows that the field is excluded from a region around the centre. This is the "whispering gallery effect" which is also observed in ray-tracing [77] and beam-tracing [30] simulations.

The slow- fast- wave confluence point (highlighted by a white-black line) shows which region of the plasma is accessible for waves with a given $n_\parallel$. The waves which are circumscribed by the line are inaccessible. At first one may be surprised to see wave fields an $n_\parallel \approx 1.3$ in this region, however this observation can be explained by the fact that beyond the confluence point, the roots of the dispersion relation are complex conjugate, hence the two waves are evanescent. A different point of view of the same phenomenon is given in the velocity analysis Figs. 7-14, 7-15 and 7-16, where the wave fields exponentially decay for $v_\parallel > v_{\mathrm{maxacc}}$. Worth pointing out that near such layers the Eikonal approximation is also bound to break down.

Finally, the features at high $n_\parallel$ occur as the natural evolution of the waves spectrum (and not random artifacts), a strong proof that indeed in LHEAF the wave spectrum is well resolved.

7.3 A new physics picture

Based on the previous analysis, LHEAF simulations provide a new interpretation of the density limit based on the combined effect of an efficient upshift of the $n_\parallel$ spectrum. Phase space analysis shows that that short wavelength structures occur close to the separatrix and result in power absorption in the periphery of the plasma. According to wavelet analysis, most of the $n_\parallel$ upshift occurs after the waves reflect and propagate in the SOL of the divertor region. Although the presence of a SOL is important to determine the phase space trajectory of the waves, it is important to remember that strong upshifts were also observed in simulations in which the SOL model was absent, as pointed out in Fig. 6-21 and Ref. [18]. These observations point to also fullwave effects as being an important factor at determining the broadening of the wave $n_\parallel$ parallel spectrum.

Figure 7-22 shows a plot of the power absorption as a function of the $n_\parallel$ of the waves (obtained by integrating in ρ the second panel of Fig. 7-14). Recalling that the power absorption is proportional to df/dv, the peaks (① and ③) and valley (②) in the power absorption profile can be recognized to correspond to specific features in the electrons distribution function: ① deviation from Maxwellian ② plateau ③ decay due to wave accessibility.

Clearly as the density is increased the $n_\parallel$ spectrum becomes broader, skewed to higher values and the peak corresponding to the wave accessibility (③) drops. All of these observations suggest that at higher densities the quasilinear plateau ② is not fully developped in the region $3\,v_{Te} < v_\parallel < v_{\mathrm{acc}}$. Going back to the current drive efficiency calculation of Sec. 2.2.2, we recall that the $1/n_\parallel^2$ term in

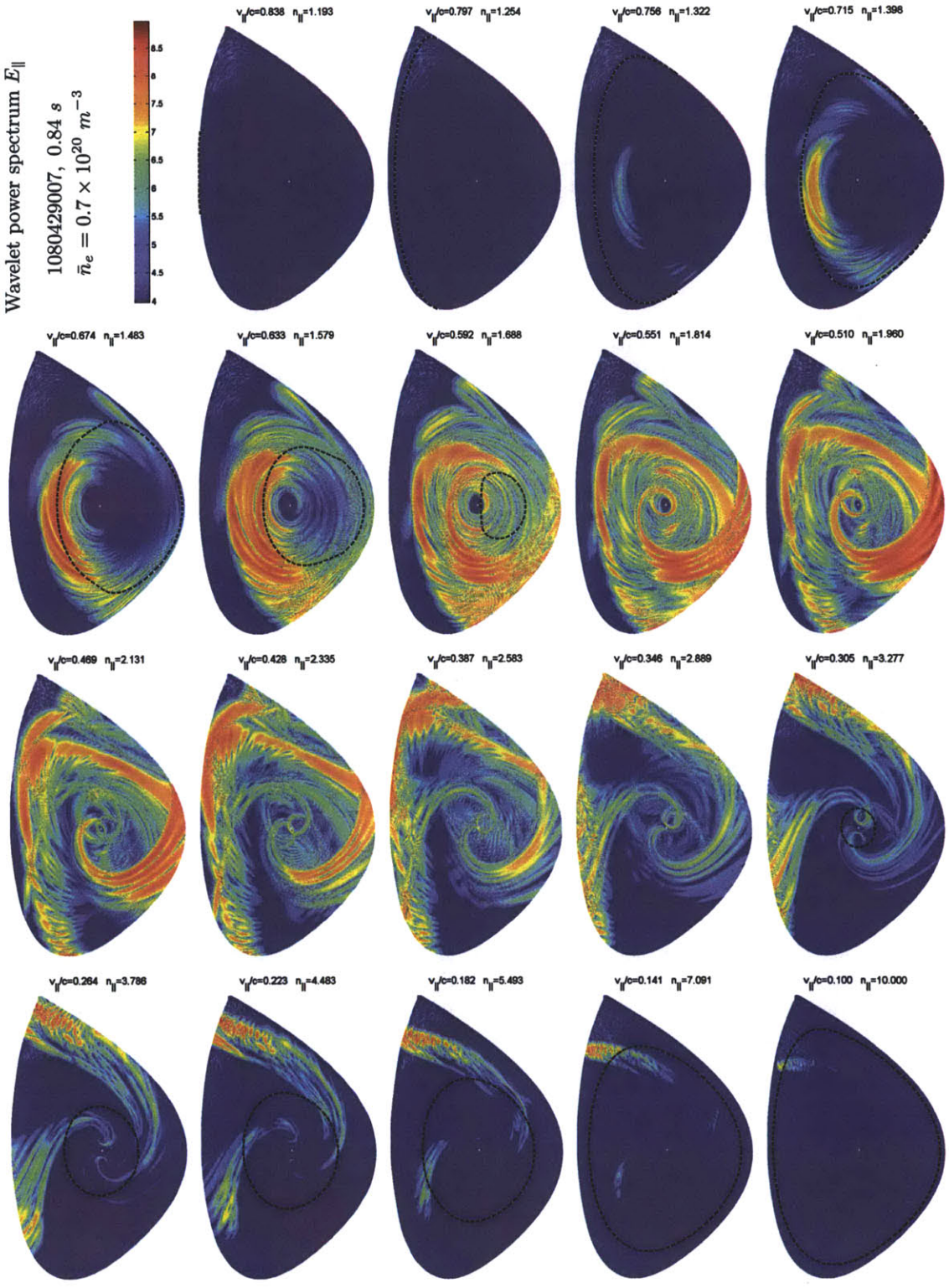

Figure 7-18: Logarithmic plots of a set of $E_\parallel$ wavelet power spectra for the low density discharge. Plots are equispaced in $v_\parallel/c = 1/n_\parallel$ and normalized to the same absolute magnitude. White-black and red-black dashed lines represents the accessibility condition and the $3\,v_{Te}$ boundaries, respectively.

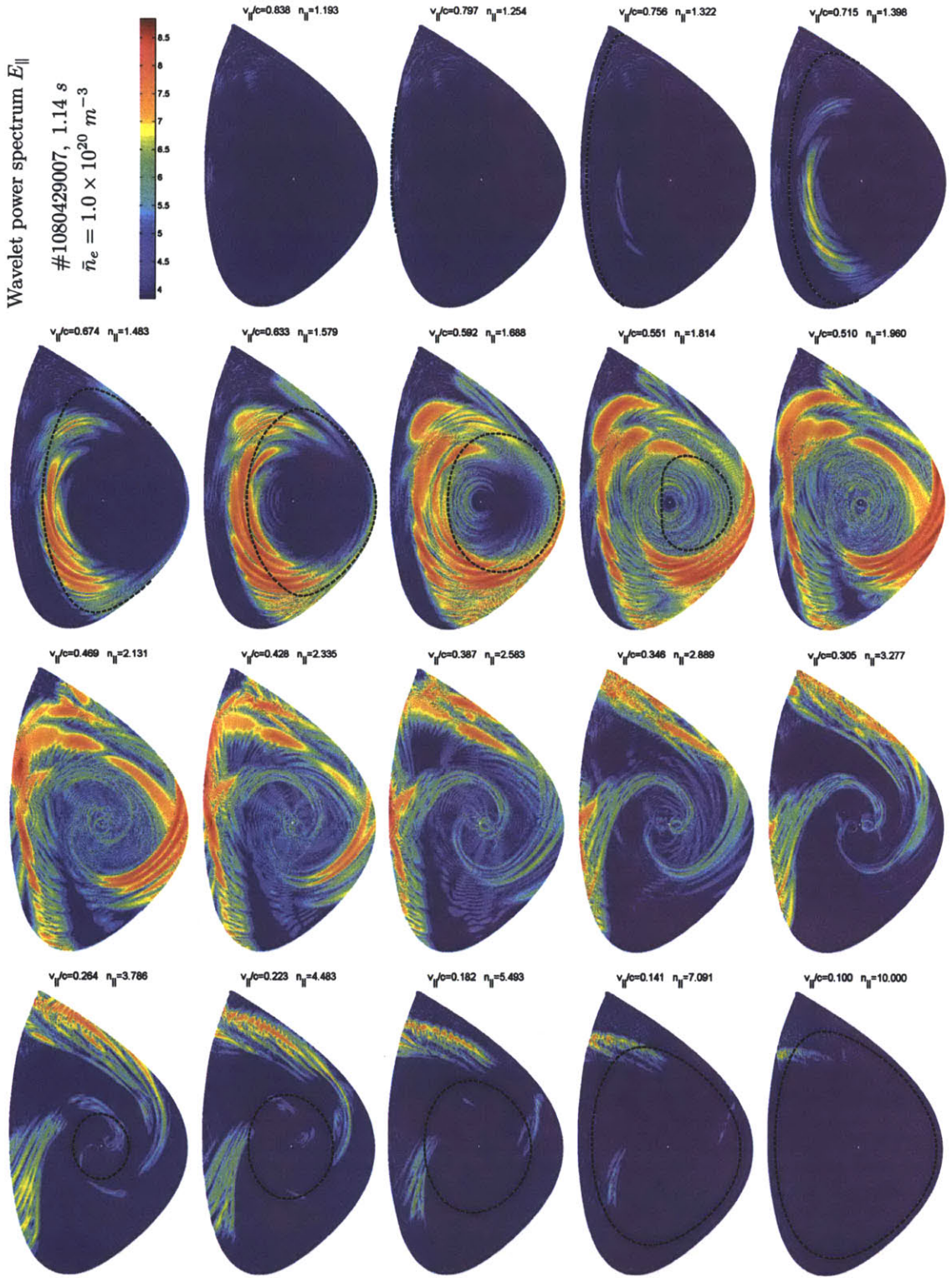

Figure 7-19: Same plot of Fig. 7-18 but for the moderate density discharge.

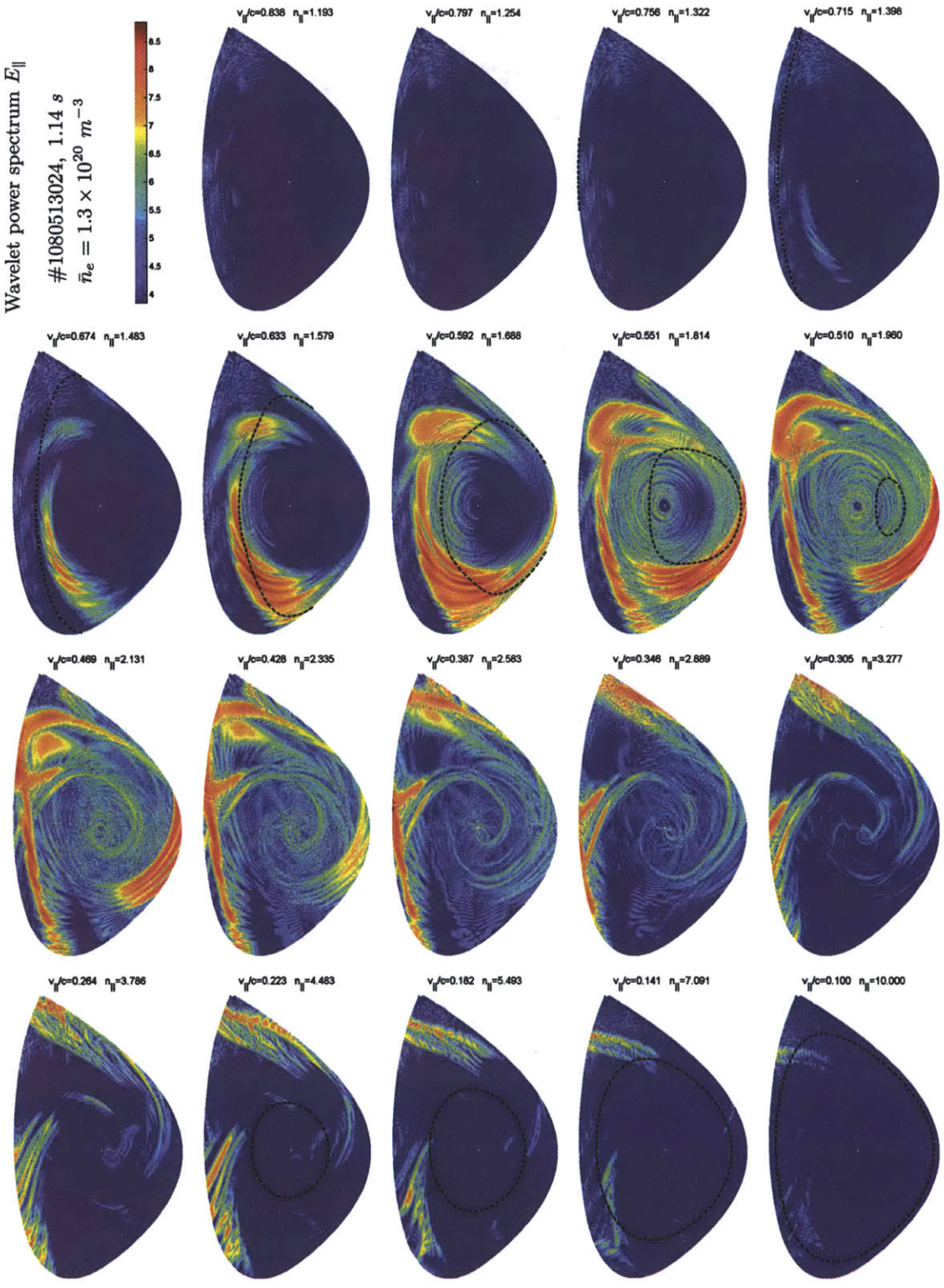

Figure 7-20: Same plot of Fig. 7-18 but for the high density discharge.

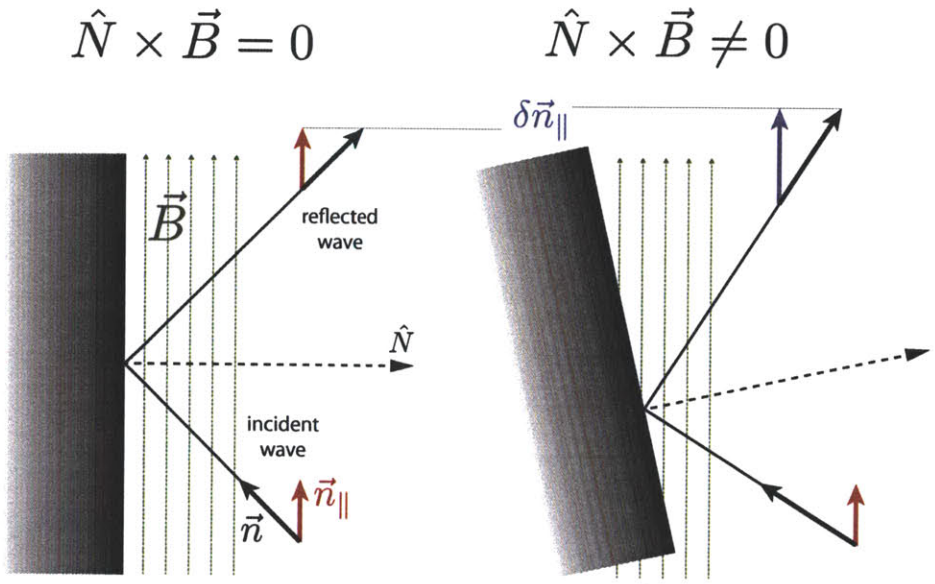

Figure 7-21: If the static magnetic field is not tangential to the wall surface, then $n_{\|}$ can suddenly change after the wave reflect off the walls. A similar effect can occur if the density is not constant along a magnetic field line, as in the SOIL model which accounts for parallel heat transport. In the low density SOL the wave propagation is determined by the density profile and $n_{\|}$ is free to evolve depending on the alignement of the flux surfaces to the surfaces of constant density.

the LHCD efficiency

$$\frac{j}{P} \propto \frac{1}{n_e n_{\|}^2} \tag{7.5}$$

arises because of the dependency of the plasma collision frequency on the particles velocity $\nu \propto n_e v^{-3}$. As the waves interact at the plasma edge, where the temperature is low and the collision frequency is high, a lot of power is invested in making the distribution function deviate from being Maxwellian ①. Hence, as the peak corresponding to the wave accessibility (③) drops, one can not assume $n_{\|} = \text{const} = n_{\|,\text{launched}}$ or $= n_{\|,\text{acc}}$ when calculating the LHCD efficiency. To exacerbate this effect is the fact that at larger radii the waves power density is inherently lower. Furthermore, at the plasma edge a considerable fraction of fast electrons is trapped and thus does not contribute to current drive.

A word of caution should be said about the resolution used in these LHEAF simulations, for which short wavelength modes with $n_{\|} > n_{\|\text{nyquist}}$ are the result of a spline interpolation. Following the procedure explained in Sec. 7.2.4, the $n_{\|\text{nyquist}}$ can be calculated to be $\approx 13.6, 11.4, 10.0$ for the low, moderate and high density simulations. Although a smaller mesh size is ultimately needed to confirm the LHEAF results, it should be noted that the peak of the absorption occurs for $n_{\|} < n_{\|\text{nyquist}}$ and a strong upshift observed also for the low and moderate density cases, where the mesh resolution problem is not as important. This gives confidence in the robustness of the LHEAF simulations.

7.3.1 Possible solutions around the LHCD density limit

Figure 7-22 suggests that there are two possible solutions to the LHCD density limit observed on Alcator C-Mod. First, is to increase the amount of injected power, since in this case one would expect the power absorbed at low velocities to eventually saturate and a quasilinear plateau to

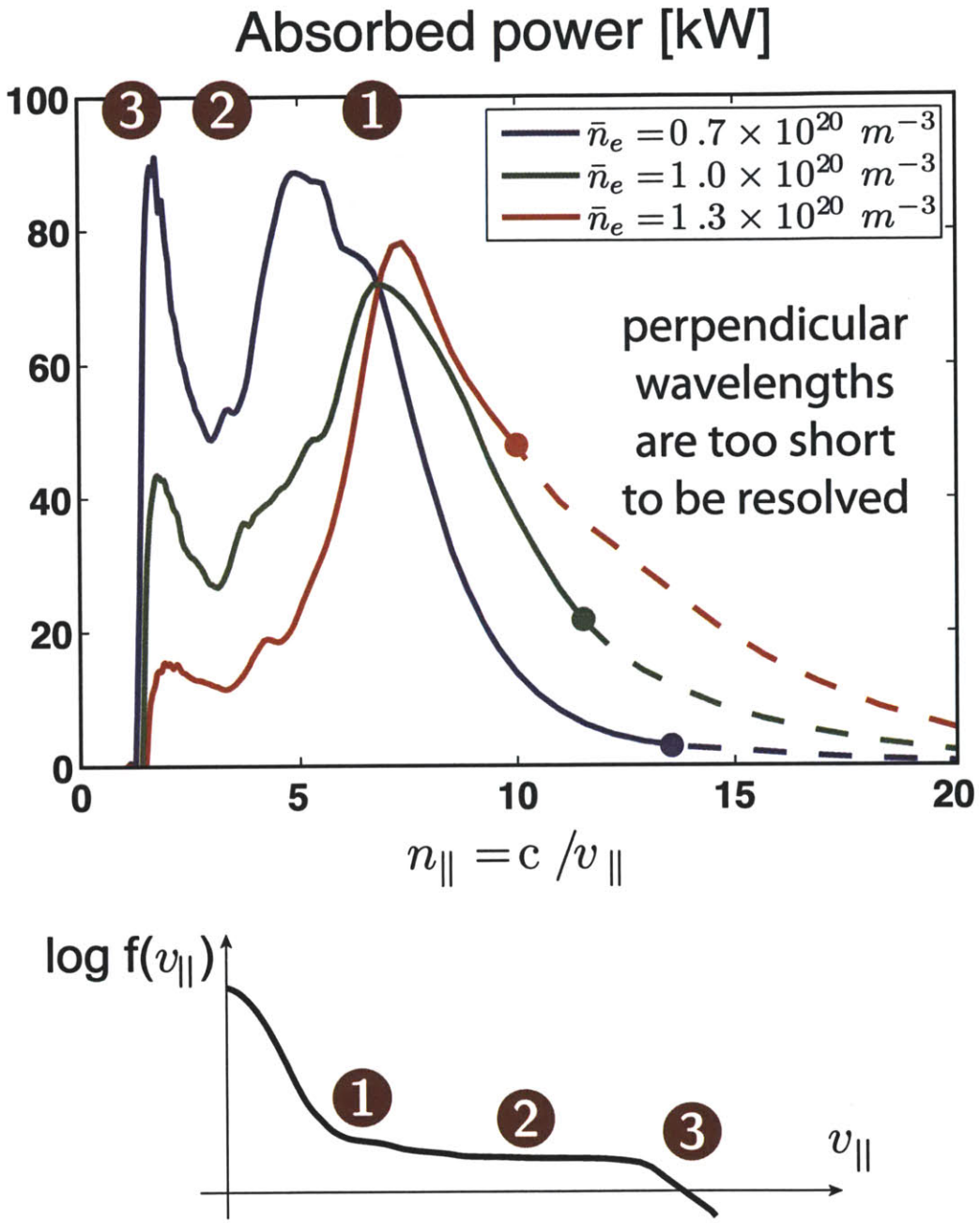

Figure 7-22: In LHEAF, as the density is increased the $n_{||}$ range over which absorption occurs becomes broader and skewed towards higher $n_{||}$ values. The peaks (① and ③) and valley (②) in the power absorption profile can be recognized to correspond to specific features in the electrons distribution function, here represented schematically: ① deviation from Maxwellian ② plateau ③ decay due to wave accessibility.

become flat in the region $3\,v_{Te} < v_{\parallel} < v_{\rm acc}$. Second, is to move the power absorption more towards the plasma core. Work by Shiraiwa [181, 182] has identified two methods by which this can be achieved: increasing the plasma temperature or by modifying the waves trajectory in phase space.

Indeed, on Alcator C-Mod, high density $\bar{n}_e \sim 1.4 \times 10^{20}\ m^{-3}$, hot 4 keV plasma discharges plasmas have been successful at recovering LHCD efficiency [181, 183]. However, these were ICRF heated He plasmas with high field 8 T, high current 1.2 MA; that is a completely different parameter space than what usually used for LHCD on Alcator C-Mod. Pinpointing the reason for the success of these experiments is therefore difficult.

Another approach, proposed by Shiraiwa [181, 182] is to move the launcher position away from the midplane, as previously done on the PLT and JT60 tokamaks [184, 185]. A design of off-midplane launcher (LH3) is currently under consideration exploit a phase space synergy [186] with the existing launcher (LH2) and fill the spectral gap which lies between the phase velocity of the faster wave and the thermal velocity of the electrons around $r/a \approx 0.5$.

Fortunately, the effect uncovered by this work occurs only in the so-called multi-pass regime, where multiple passes typically involving several reflections in the SOL plasma occur before the LH waves are absorbed. Furthermore, as LH waves launched in ITER would be heavily damped before reaching the separatrix, this is not expected to be a problem.

7.3.2 Effect of non-resonant collisional damping

The resulting physical picture is rather different from the one developed previously using ray-tracing codes which need to rely on a strongly collisional SOL to reproduce the experimental results. Although this result does not exclude in itself the role of other parasitic loss mechanisms in the SOL, it is important that the experimental trends can be reproduced to a large degree without invoking such effects.

It is important to recall that in the LHEAF simulations presented in this chapter, collisional damping has been purposely underestimated by setting Z_{eff} is set to be 1 when evaluating collisional damping. Such mechanism is very effective at damping short wavelengths modes (in an exponential way). If the collision frequency was to be increased (either by changes in the SOL profiles or Z_{eff} profiles), amount of power in the high frequency part of the spectrum may be significantly reduced. As a side effect, increasing collisional damping, would also be beneficial from a mesh resolution point of view, making the demand for a finer mesh unnecessary.

As the collision frequency is increased, the effects on the LCHD efficiency can be expected to be non-linear. First of all, a significant fraction of the launched power could be lost in such non-resonant process, similarly to what has been observed in GENRAY/CQL3D simulations. Second, the efficient damping of the high spectral components could prevent the spectral gap to be bridged at the edge, thus leading to a further reduction of CD. This effect would probably be very effective at reducing the emissivity from the edge channel HXR chords which is observed at the moment in LHEAF simulations and may lower the amount of radial diffusion required for the simulated HXR profiles to agree with the experiments.

7.3.3 Consistency with experimental observations in the SOL

As explained in Sec. 2.2.3, the LHCD density limit is associated with increased SOL ionization, density, presence of thermoelectric currents. According to the LHEAF modeling it is possible to speculate that these experimental observations are the result of LH power being damped at the plasma edge by ELD and then being quickly transported in the SOL. Since the SOL plasma temperature is pinned down by parallel heat transport, the SOL primarily reacts by increasing its density (hence the higher ionization, density and thermoelectric currents). In this sense, these observations should be retained as an effect of an edge localized damping and not as the direct cause of loss of current drive.

Another interesting aspect is that experimentally the LHCD density limit was found to be insensitive to the launched $n_{\parallel,\text{launched}}$ (see Fig. 2-4). This result is in agreement with the new physics picture drawn by LHEAF, since most of the damping occurs at high $n_{\parallel}$ and the wave dynamics is determined by the locations of the $3\,v_{Te}$ and v_{acc} boundaries. Such result does not change at lower densities, where data indicates a much weaker dependence than the $1/n^2_{\parallel,\text{launched}}$ [73].

7.3.4 In perspective of ray-tracing simulations

When the power absorption is weak, conventional ray-tracing requires a large number of passes for the spectral gap can be bridged. In this strong multi-pass absorption regime the ray propagation becomes an highly stochastic process [175, 176]. However, this is not observed in LHEAF simulations, since most waves undergo only few (two or three) reflections while still filling the propagation domain up to the absorption boundary (see Fig. 7-14). The non-stochasticity of the wave fields has also been confirmed by wavelet analysis, which has shown that these are non-stationary along a flux surface, Fig. 7-20 [9].

In this sense, LHEAF results are more consistent with the physical picture proposed by Peysson and Decker [187, 180, 172], who artificially broadened the spectrum along the ray path (linearly increasing $\Delta n_{\parallel}$) and found that the spectral gap can be efficiently bridged without the rays propagation being stochastic. Interestingly, in the simulations the LH driven current was found to become rapidly independent of the amount of broadening used and agree with the correct non-inductive current level measured on Tore-Supra. The authors conclude that the CD efficiency results from a competition between two different mechanisms: stochastic toroidal upshift or broadening of the LH power spectrum. When the absorption of the LH wave is weak, spectral broadening predominates over toroidal upshift for bridging the spectral gap. When such broadening occurs, the author found that the LHCD efficiency becomes poor, since the fast electron tail cannot be pulled up to high energies.

It is worth pointing out that ray-tracing calculations with a strong edge loss mechanism also challenge the physic picture of stochastic filling of the spectral gap. In fact, this prescription limits the length of the ray trajectories and therefore how much the spectral gap can be stochasticity filled. Nonetheless, on Alcator C-Mod this has been shown to partly solve the discrepancy for the high density regime (see Fig. 2-4) and the same has been hypothesized for discharges with low $n_{\parallel}$, where the single pass absorption is weak [117].

Ultimately, the new understanding of the density limit based on the results of LHEAF simulations gives justification to use ray-tracing codes with strong absorption close to separatrix. In fact, the effect of loosing a significant fraction of power in collisions is phenomenologically similar to having power absorbed at the plasma edge by ELD but with little current drive efficiency [183].

[9] For artificially low damping (collisional and collisionless), the vacuum vessel can be made to act as a cavity resonator where the waves fill almost uniformly the computational domain. In such case the wave fields become stochastic and their amplitude is set by the Q of the cavity. However this is not the case for realistic Alcator C-Mod LHCD discharges.

Conclusions and future work

This thesis focuses on several different aspects of the LH wave physics, the common theme being the development of fullwave simulation codes (based on the commercial software COMSOL) which have been used in support of experimental work. The tools developed throughout this thesis have been used to tackle long lasting problems in the LHCD community and open the ground for new exciting research. In the following, possible leads for future work are pointed out.

To start, the RF design of an innovative LH launcher has been optimized with the aid of the commercial software CST Microwave Studio in combination with the TOPLHA code. The predictions done at the design stage were subsequently experimentally verified with a dedicated microwave probe diagnostic. This antenna has been successful in its mission of reliably delivering power to the plasma with low transmission losses and a similar design is now under consideration for an additional LH antenna to be installed in the near future on Alcator C-Mod.

High reflection coefficients have been a long standing issue for all Alcator C-Mod LH systems. This issue has been studied in a dedicated set of experiments which suggested the existence of an evanescent layer between the plasma and the launcher. A model of the density in front of the antenna, using a smaller vacuum gap for increasing plasma densities, was empirically found based on the agreement of the linear coupling code GRILL with the measurements. The subsequent availability of SOL density profiles from a reflectometer diagnostic drove the development of POND, a fullwave coupling code which takes into account the interaction of high power LH waves and the plasma edge based on the non-linear ponderomotive force theory. According to simulations, the effect of ponderomotive forces is compatible with the density depletion which is observed in front of the grill in presence of high power LH waves.

As a future work, the POND code may be extended to investigate the vortex structures which are routinely observed on the visible camera diagnostic on Alcator C-Mod and other devices during high power operation. Since their structure is inherently 3D, the FEM approach and the iteration scheme used by POND might be easily adapted to include the additional physics that has been proposed to explain this phenomena [79]. Finally, following the same procedure used in the LHEAF code, the POND code could be modified to include collisionless damping of the high $n_{\parallel}$ spectral components on thermal electrons. Such code would then be the perfect candidate to study of high energetic electron production in the SOL region by high power near field effects, as done in Ref. [188].

This study has driven the design for a new set of private limiters for the upcoming campaign that will be movable with the launcher instead of being fixed to the vessel wall, thus allowing a greater flexibility in the positioning in the launcher with respect to the plasma. Coupling studies in the new configuration should be pursued. In particular, by this design the LH launcher can be placed in front or behind the main limiters and other structures (e.g. ICRF antennas), allowing strong changes in the density scale lengths in front of the launcher. This aspect has been reported to be important for non-linear coupling effects on ToreSupra [138, 137]. Access to higher temperature regions in the SOL plasma is also expected to play a positive role at reducing the effect of ponderomotive forces.

Finally, the problem of wave propagation, absorption and current drive in the core plasma was studied with the fullwave code LHEAF. Its formulation is based on an innovative iterative scheme

which allows the inclusion of hot plasma effects in a conventional 3D FEM code. The code has been verified with ray-tracing and spectral fullwave codes for a Maxwellian plasma. Inclusion of a 1D Fokker-Planck module in the iteration loop accounts for the deformation of the distribution function on the wave damping, while a 3D bounce-averaged zero-banana-width relativistic Fokker-Planck module is used to postprocess the wave fields of the last iteration and generate a 2D distribution function that is used to accurately evaluate the driven current. A synthetic HXR diagnostic has also been developed to allow direct comparison with the experiment.

Additional synthetic diagnostics should be developed in LHEAF to allow for a stronger validation with the experiments and narrow down the uncertainties in the input parameters of the simulations. In particular, an ECE synthetic diagnostic would of particular interest because measurements from this diagnostic are independent of the ionization state of the ions Z_{eff}.

Differences between raytracing and fullwave results have been identified in the low $v_{\|}$ region near the plasma edge. This region of phase space, which is consistently found to be void of rays where instead significant wave power is observed. Absence of rays with a sufficiently slow phase velocity prevents the spectral gap to be bridged, causing ray-tracing simulations to deposit power more in the plasma core. This problem can only be camouflaged by enhancing the role of edge parasitic absorption. This is a remarkable result, (especially considering that in ray-tracing a broad $n_{\|}$ spectrum is launched) which points to fullwave effects as being the cause of this difference.

A systematic study to understand the importance of fullwave effects should be pursued. These include diffraction, tunneling, focusing and interference (the latter two may be important for the calculation of D_{QL}). Also mode coupling can occur when curvature is introduced eider by toroidicity or by non-circularity of the plasma cross section can contribute to the low $n_{\|}$ part of the wave spectrum. For this study use of ad-hoc models is likely to be required, in order to enhance the importance of fullwave effects. Comparisons with ray-tracing and beam tracing simulations should be used to identify the occurrence of fullwave effects and understand the validity regime of these approximations. Of particular interest would also be to use LHEAF to simulate LHCD discharges in high aspect-ratio circular experiments such as Tore Supra, TRIAM-1M or TFTR, which have little toroidally induced upshift and fullwave induced spectral broadening could play an important role.

Finally, the LHCD high density limit has been investigated. To start, an advanced Pulse Height Analysis (PHA) analysis was developed to correct for pileup and baseline drift effects on the Alcator C-Mod HXR camera diagnostic. This analysis fundamentally redefined the nature of the LHCD density limit as a process than degrades the LHCD efficiency continuously across all densities and does not occur suddenly at $\bar{n}_e = 10^{20}\ m^{-3}$.

From an experimental point of view, improvements could be made to the HXR camera diagnostic on Alcator C-Mod. In particular, measures should be taken to minimize the spurious counts that occur in presence of DD fusion and which significantly degrades the signal to noise ratio in high density DD discharges with ICRF. Also, still unclear is the physics behind the significant HXR emission that is routinely observed well outside of the LCFS of limited discharges, or from the X-point regions in diverted discharges. A possible explanation worth of testing is given in Sec. 7.2.3. A vertical HXR detector array would be beneficial to further characterize this phenomenon and would allow more reliable tomographic inversion. If anything, even the addition of a single detector at this location would suffice to confirm the improved HXR count rates which is observed in limited discharges [58].

As a second step, the full wave FEM code LHEAF was then applied to high density discharges, to investigate the role of fullwave effects and of the SOL in the loss of current drive efficiency. For this purpose, a physics-based 2D SOL model that takes into account the effect of flux expansion and parallel heat transfer was included in LHEAF. A systematic study using three similar discharges at different densities has shown that the decrease in LHCD efficiency can be reproduced without invoking any additional loss processes other than electron Landau damping. This result differs from previous ray-tracing Fokker-Planck studies, which require a significant fraction of the power to be lost in the SOL by collisional damping (more than 60% at high density) to obtain good agreement

with the experiments. The implications of this result are profound and suggest that the key to improve the LHCD performance at high density is to operate at higher plasma temperatures and to push the power deposition profile inward to avoid prompt loss of fast electrons.

To confirm the consistency of the LHEAF results, more Alcator C-Mod discharges should be analyzed. In particular, good candidates are the limited discharges and the high temperature, high current, high field He plasmas have shown to give good current drive performance (the latter ones both in HXR and loop voltage measurements). Calculation of the LHCD efficiency in the numerical simulations should also be carried out and compared to the experimental values following the method described in Ref. [72, 73]. In the simulations Z_{eff} is a large source of uncertainty and measures should be taken to provide a reliable measurement of its profile at least in the core of the plasma.

To conclude, there are several additional improvements that could be made to the LHEAF code. A possible roadmap is as follows:

- Extension of wavelet analysis outside of the last closed flux surface. Electron Landau damping in the SOL could also be implemented, as long as the plasma is assumed to be Maxwellian.
- The 3DFP solver VERD should be included in the LHEAF iteration loop to verify convergence to similar absorption profile and wave fields as for iteration using $\text{LHEAF}_{\text{1DFP}}$ module.
- Strong wave fields can suddenly accelerate electrons. In such cases one can not assume that the change of particle velocities during the wave-particle interaction is small and evaluation of quasilinear diffusion coefficient D_{QL} should be done by direct orbit integration (notice that technically speaking in this regime quasilinear theory breaks down). For the purpose of LH waves, FLR effects can be neglected and bounce orbit can be calculated assuming conservation of magnetic moment.
- At the LCFS the particle flux $\Gamma_{rr} = D\frac{\partial f}{\partial r}$ self-consistently adjusts so to be a perfect sink for radial diffusion. As a fist step to overcome this limitation, one could modify the boundary conditions in the $\text{LHEAF}_{\text{3DFP}}$ module so to allow variable flux of particles outside of the last-closed-flux-surface. The parameter Γ_{rr} could be then used as a free parameter to match the experimentally observed HXR emission at the plasma edge and possibly empirically estimate the value of $D(v_{\|})$.
- Extension of the LHEAF formulation to other regimes besides ELD should be considered. Conceivably this could be achieved by calculating an effective local damping to be used in the FEM simulation, using direct orbit integration of test particles with different $(v_{\|}, v_{\perp})$. By the same orbit integration both the wave damping and D_{QL} used in the Fokker-Planck code would be calculated. The damping of each test particle would be weighted by the number of particles with the same $(v_{\|}, v_{\perp})$ in the distribution function to find an effective local damping of the waves.
- Development of an open source FEM solver for the solution of the EM problem would be important to avoid license restrictions which using a commercial software such as COMSOL and MATLAB impose.
- Solution of problems with more than 30 million of DoFs would be improtant to increase the resolution of existing simulations and allow studies in larger devices.

Appendix A

Evolution of $n_{||}$ in a strongly shaped plasma

In a toroidal geometry, the evolution of the $n_{||}$ spectrum is a competition among different effects which strongly depend upon the density profiles and magnetic field topology. Although some intuitive understanding can be obtained by analytic solutions in simplified cases, a numerical study is ultimately necessary to understand the wave behaviour in a realistic geometry. For this purpose, the ray-tracing code GENRAY has been used.

Although GENRAY operates in R, Z, ϕ coordinate system[1], more physical insight can be obtained by converting the GENRAY solution into a r, θ, ϕ toroidal coordinate system. Here $r = R - R_0$ and $\theta = \arctan(z/r)$, where $z = Z - Z_0$ and R_0, Z_0 are the coordinates of the magnetic axis. Then the ray $n_{||}$ can be then split into toroidal, poloidal and radial contributions, defined as:

$$n_{||} = \frac{\vec{n} \cdot \vec{B}}{B} = \frac{n_\phi B_\phi + n_\theta B_\theta + n_r B_r}{B} = n_{||\phi} + n_{||\theta} + n_{||r} \tag{A.1}$$

where

$$\begin{aligned} n_\theta &= -n_R \sin(\theta) + n_Z \cos(\theta) \\ n_r &= n_R \cos(\theta) + n_Z \sin(\theta) \end{aligned} \tag{A.2}$$

and similarly

$$\begin{aligned} B_\theta &= -B_R \sin(\theta) + B_Z \cos(\theta) \\ B_r &= B_R \cos(\theta) + B_Z \sin(\theta) \end{aligned} \tag{A.3}$$

Figures A-1, A-2, A-3 and A-4 shows the evolution along a ray of $n_{||}$ and of its $n_{||\phi}$, $n_{||\theta}$, $n_{||r}$ components as a function of the poloidal angle θ and the ray lenght for a $\bar{n}_e = 1.55 \times 10^{20}\ m^{-3}$ discharge (shot #1080513024 at 1.0 s).

Substituting the toroidal mode number N, which is conserved in a toroidal geometry, in the expression of $n_{||\phi}$

$$n_{||\phi} = \frac{N}{R} \frac{B_\phi}{B} \frac{c}{\omega} \tag{A.4}$$

one sees that $n_{||\phi}$ has a $1/R$ dependency which is clearly visible in the green curve of Figs. A-1, A-2, A-3 and A-4.

[1]The R, Z, ϕ coordinate systems is common in ray-tracing codes, since it facilitates the input of experimental quantities such as the EFIT magnetic equilibrium which is in R and Z coordinates

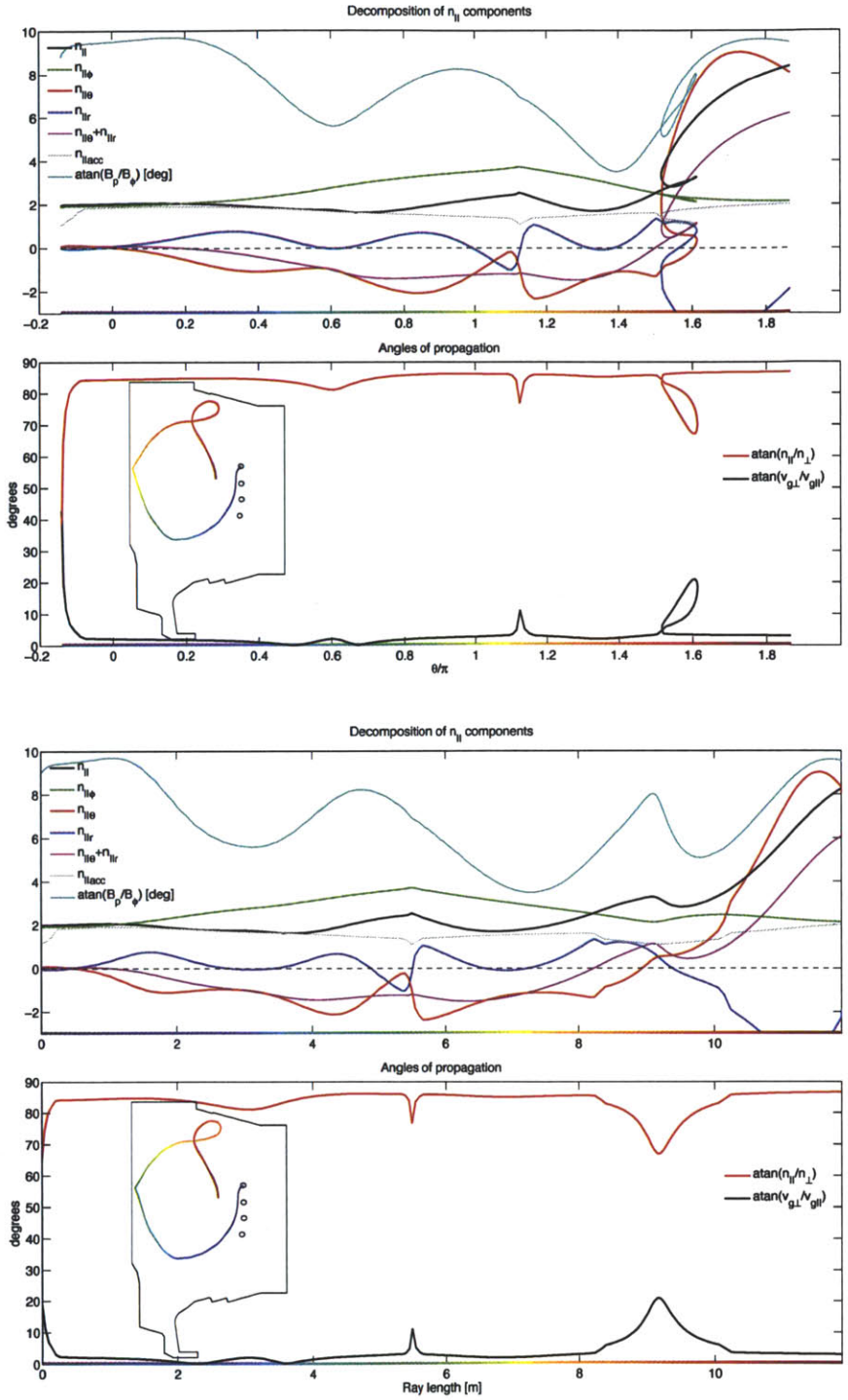

Figure A-1: Evolution along a ray of $n_{\parallel}$ and of its $n_{\parallel\phi}$, $n_{\parallel\theta}$, $n_{\parallel r}$ components as a function of the poloidal angle θ and the ray length. The ray is launched from the A row with an initial $n_{\parallel}$ of 1.9. Also plotted are the angle that the phase and group velocity make with the static magnetic field, which can be used as an indication of how much the wave have an electrostatic or electromagnetic behaviour.

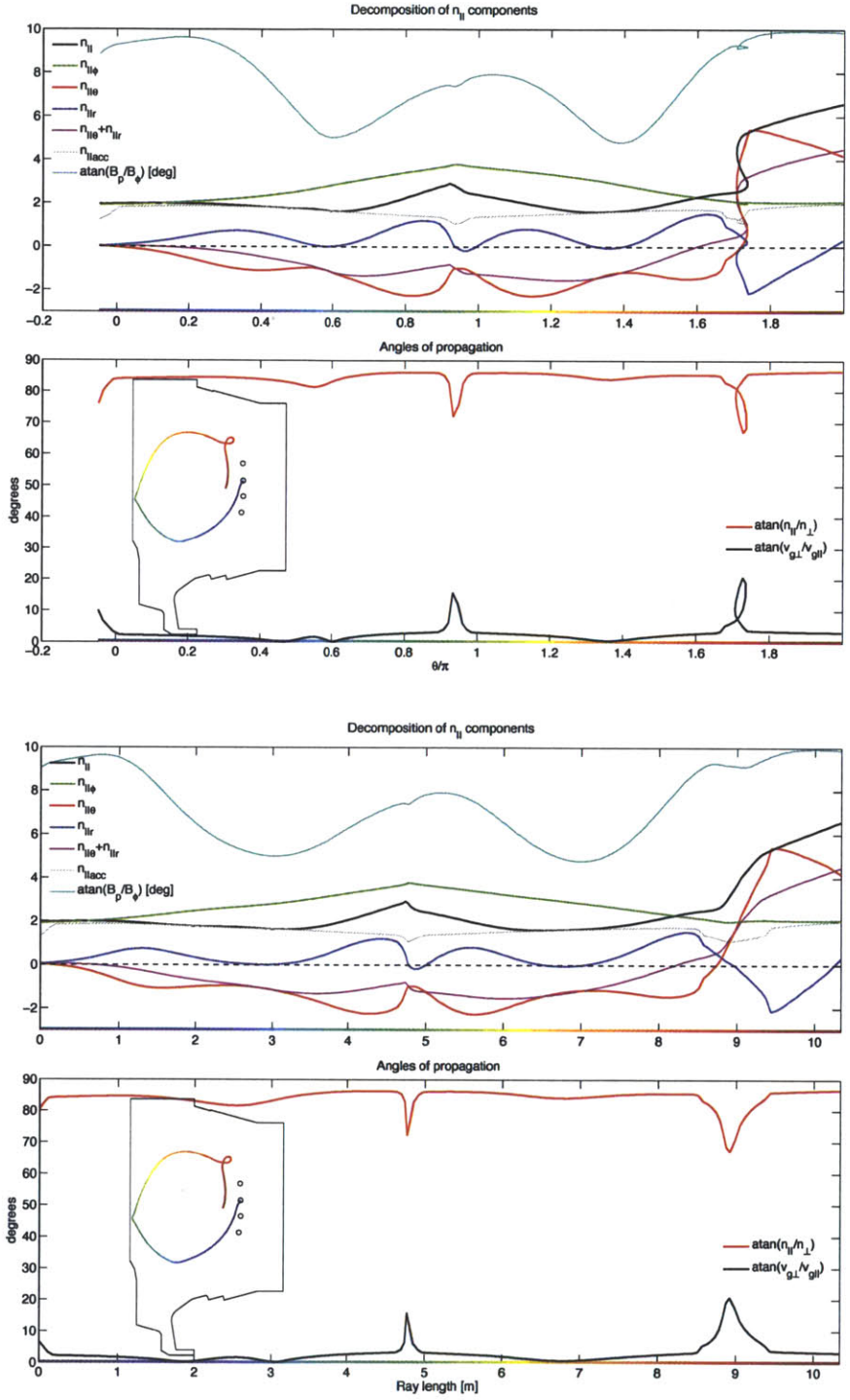

Figure A-2: Same as Fig. A-1 but from the B row launching position.

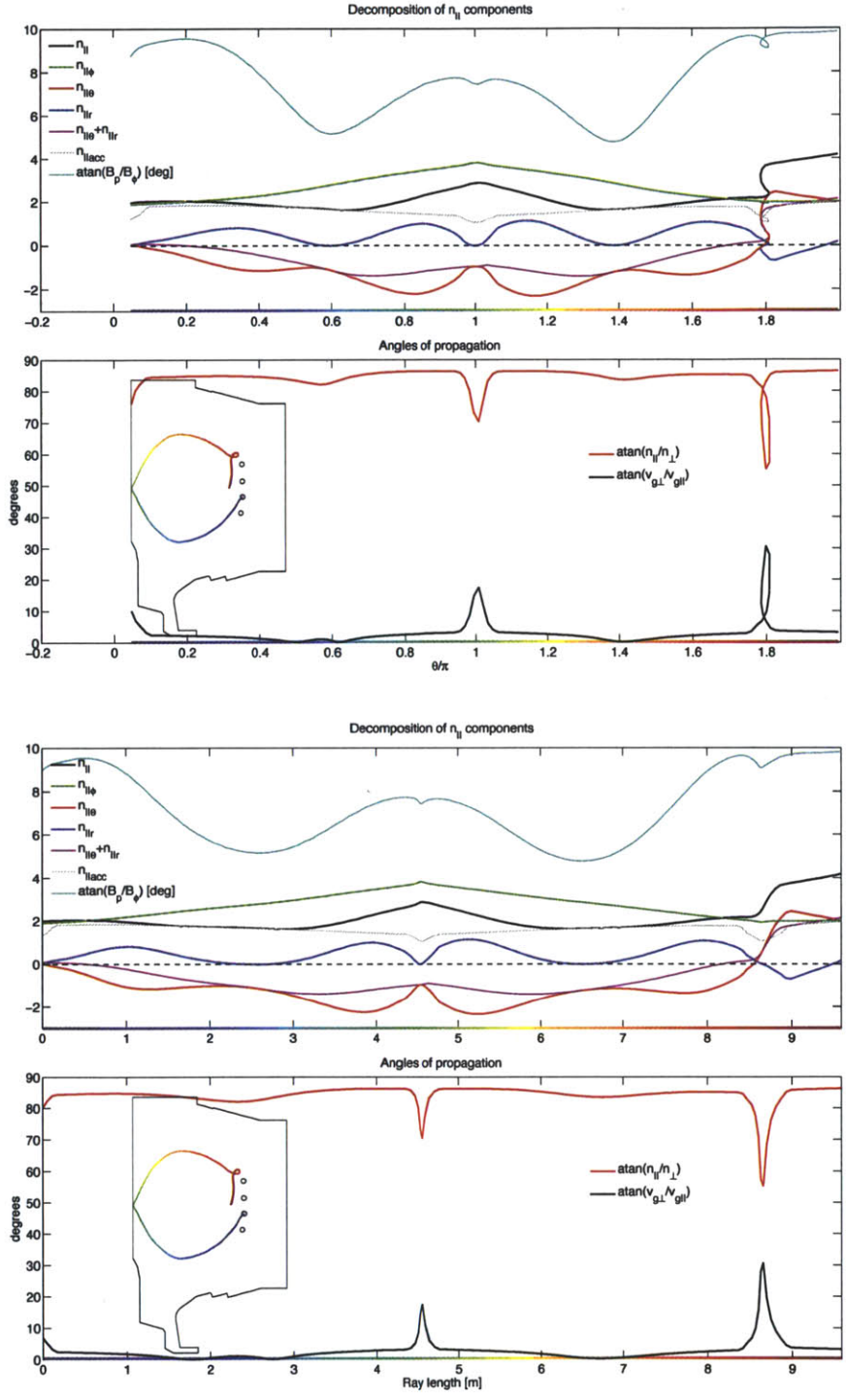

Figure A-3: Same as Fig. A-1 but from the C row launching position.

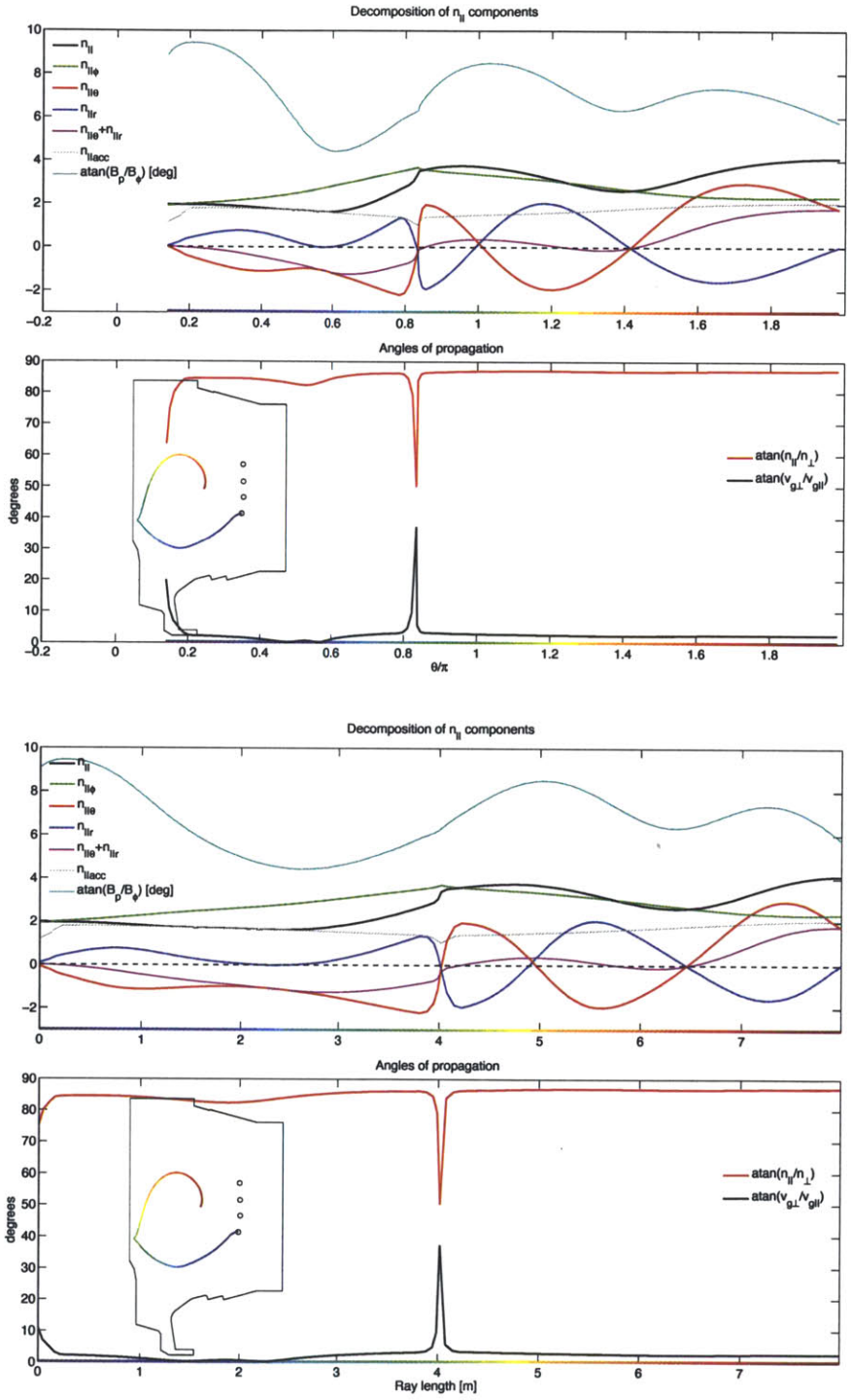

Figure A-4: Same as Fig. A-1 but from the D row launching position.

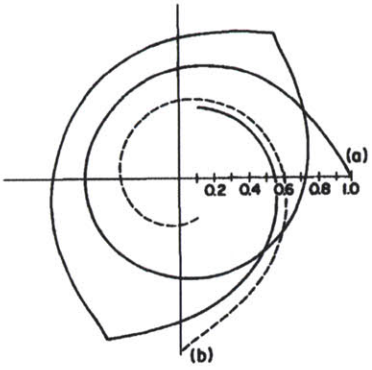

FIG. 6. Ray trajectories in the (r-θ) plane for Alcator C parameters and $n_{\parallel} = 3.0$ initially. (a) Ray launched from $\theta = 0$ (shown as a solid line) and (b) ray launched from $\theta = 3\pi/2$ (shown as a dashed line).

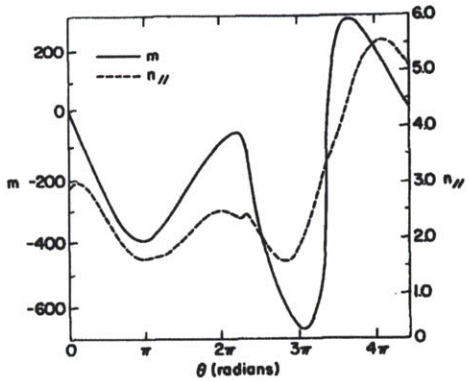

FIG. 7. Variations in m and $n_{\parallel}$ along the ray trajectory shown in Fig. 6 (launched from $\theta = 0$), and plotted vs θ.

Figure A-5: Extracts from Ref. [76], showing that in a toroidal plasma with circular cross-section, the rays poloidal mode number m and $n_{\parallel}$ follows very closely the $\sin(\theta)$ behaviour which is predicted by Eq. A.6.

Substituting the poloidal mode number M, which is not conserved in a toroidal geometry, in the expression of $n_{\parallel\theta}$, one gets:

$$n_{\parallel\theta} = \frac{M}{r}\frac{B_\theta}{B}\frac{c}{\omega} \tag{A.5}$$

The analysis of toroidal variations in the poloidal mode number M has been carried out in Ref. [76] and for a purely electrostatic approximation, the following relation holds

$$\frac{dM}{d\theta} = -\frac{\partial D/\partial\theta}{\partial D/\partial M} \approx -k_{\parallel} q(r) \left(1 + \frac{\omega_{pe}^2}{\Omega_e^2 S}\right) \frac{r\sin(\theta)}{R} \tag{A.6}$$

One property that can be seen immediately is that the sign of $dm/d\theta$ is a function of $\sin(\theta)$ and hence $n_{\parallel\theta}$ should decrease for $0 < \theta < \pi$ and increase for $\pi < \theta < 2\pi$. Previous ray-tracing simulations in toroidal geometries with circular cross sections [76] reproduce well the trends predicted by Eq. A.6, as reported in Fig. A-5. However, an examination of the red curves Figs. A-1, A-2, A-3 and A-4 shows that for the case of Alcator C-Mod, such trend is not followed as closely by the $n_{\parallel\theta}$ component and the poloidal mode number M (not shown). Instead the $n_{\parallel}$ and the local magnetic pitch angle $\arctan(B_p/B_\phi)$ correlate well with each other.

Until the rays start to excurse in the low-field-side SOL, the contribution of $n_{\parallel\theta} + n_{\parallel r}$ is systematically negative, thus effectively lowering the effect of the $n_{\parallel\phi}$ upshift. When the rays reach the low-field-side SOL, they spend a lot of time (length) there, which makes the $n_{\parallel\theta} + n_{\parallel r}$ components to become positive (and thus contribute to the $n_{\parallel}$ upshift). In this region strong variations in $n_{\parallel\theta}$ ought to be expected because of the dependency of Eq. A.6 on the safety factor $q(r)$ (or actually on the magnetic field line pitch angle $q \rightarrow \frac{B_p}{B_\phi}$), which at the edge of a tokamak plasma can be large. This term can explain the large variations in $n_{\parallel\theta}$ which lead to strong upshifts as the waves re-enter the core plasma after propagating in the SOL. Most importantly however, Eq. A.6 depends on $k_{\parallel}$ itself, which can make $n_{\parallel\theta}$ to grow exponentially when this term is the dominant contribution to $n_{\parallel}$. For comparison, on the high-field-side the $n_{\parallel\theta} \approx 0$ so that such positive feedback on $n_{\parallel\theta}$ is absent.

The importance of $n_{\parallel r}$ strongly depends on the plasma topology. In a cylindrical plasma $n_{\parallel r} = 0$.

In a toroidal circular plasma $n_{\parallel r} \neq 0$ because of the Shafranov shift [2] of the plasma equilibrium, though this is generally small. Historically, it is based on this type of equilibria that functional studies of the evolution of $n_{\parallel}$ were done and a common approximation was to neglect this term [76, 55]. However, in the case of strongly shaped plasma the contribution of $n_{\parallel r}$ can be often comparable to that of the $n_{\parallel \theta}$ component. In fact, Figs. A-1, A-2, A-3 and A-4 shows that for the case of Alcator C-Mod, the poloidal (red curve) and radial (blue curve) components tend to cancel each-other, though the net contribution (magenta curve) usually follows the trend of the poloidal component. The opposite cancellation between $n_{\parallel \theta}$ and $n_{\parallel r}$ is an important finding which can explain the reduced upshifts which are in general observed in ray-tracing simulations of LH waves in shaped plasma topologies compared to ones with circular cross-sections.

Shown in Figs. A-1, A-2, A-3 and A-4 is also the angle that the waves group and phase velocity make with the static magnetic field

$$\theta_{\vec{v}g \cdot \vec{B}} = \arctan \frac{v_{g\perp}}{v_{g\parallel}} \tag{A.7}$$

$$\theta_{\vec{v} \cdot \vec{B}} = \arctan \frac{n_{\parallel}}{n_{\perp}} = \arctan \frac{v_{\perp}}{v_{\parallel}} \tag{A.8}$$

As soon as the waves are launched, they have a phase velocity which is directed only in the parallel direction $\vec{v} = v_{\parallel}$ and a group velocity which is only radial $\vec{v}_g = v_{g\perp}$. The waves then become quickly electrostatic and the group velocity of the slow-wave (which is almost perpendicular to the phase velocity) makes a small angles with the magnetic field for increasing plasma density $v_{g\parallel}/v_{g\perp} = k_{\perp}/k_{\parallel} \approx \omega_{pe}/\omega$, as explained in 2.1.2. This implies that electrostatic waves are unable to go across and must follow the magnetic field lines. However, the waves become more electromagnetic in the vicinity of the slow/fast-wave mode conversion layer and close to cutoff, and in this case the waves tend to go more across of the magnetic field lines. In fact, the break in curvature of the ray in the vicinity of the slow/fast-wave mode conversion layer and the cusping and curling behaviour that the rays exhibit in the SOL are the effect such changes in the angle of propagation $\theta_{\vec{v}g \cdot \vec{B}}$.

[2] The outward radial displacement $\Delta(r)$ of the centre of flux surfaces with minor radius r, induced by plasma pressure.

Appendix B

2D/3D Fokker-Planck and implementation of VERD

A 3D Fokker-Planck (FP) code for LHEAF has been written by Dr. S. Shiraiwa. This code, referred to as the VERD (**VE**locity and **R**adial **D**iffusion), calculates the radial distribution of a 2D (in momentum-space) bounce-averaged, electron distribution function in toroidal geometry, consistent with deposition of LH wave and a diffusive radial transport model. This calculation is carried out with an array of bounce-averaged Fokker-Planck solvers running on noncircular magnetic flux surfaces, giving the steady-state, toroidally-averaged distribution resulting from a balance between collisions, DC electric field, RF quasilinear diffusion and radial diffusion.

The 3DFP code VERD is implemented as an Object-Oriented MATLAB code and based on the computational methods of Ref. [189]. In this section we describe the code, providing expressions and methodology for calculation of the FP coefficients from each of the constituent processes. The derivations in the following sections follow from Sec. 6.5.2 and are a personal re-adaptation of the work published in the Ref. [189], the CQL3D manual [91], the review paper [161] and notes from Dr. Shiraiwa himself.

B.1 The Fokker-Planck equation

The Fokker-Planck equation is the Boltzmann equation with Fokker-Planck collision terms:

$$\frac{df_s}{dt} = \frac{\partial f_s}{\partial t} + \vec{v} \cdot \frac{\partial f_s}{\partial \vec{r}} + \frac{\vec{F}}{m_s} \cdot \frac{\partial f_s}{\partial \vec{v}} = \left(\frac{\partial f_a}{\partial \vec{t}}\right)_c + S_s \tag{B.1}$$

where, f_s is the distribution function in 6D (3D-$\vec{r}$, 3D-$\vec{v}$) for particles of species s. The collision term is $\left(\partial f_a/\partial \vec{t}\right)_c$, S_s and L_s are the source and loss terms respectively.

The Fokker-Planck collision term for an inverse square law (Coulomb collision in 3D) was derived as a function of the so-called "Rosenbluth potentials" [190, 191]. Since this collision term contains velocity derivatives of f_s multiplied by velocity moments over f_s, Eq. B.1 is a non-linear, partial, integro-differential equation [1] in seven independent variables (3D-$\vec{r}$, 3D-$\vec{v}$, 1D-t).

[1] What gives rise to integro-differential equations are collisions within the same plasma species, while collisions between different species simplifies to purely differential equations.

B.1.1 In 2D-velocity cylindrical coordinate systems

In practice, for a tokamak plasma, two important simplifications can be made, based on the fact that the distribution function of electrons and ions are to a very good degree independent of:

1. the azimutal velocity angle about the ambient magnetic field
2. the spatial toroidal angle in the symmetry direction of the tokamak

in accord with the usual situation $\Omega^{-1} \ll \tau_c$, where Ω is the gyro-frequency of the particles, and the time for achieving toroidal equilibrium on a flux surface is short compared to τ_c or the transport time. This allows Eq. B.1 to be recast [191] from spherical polar coordinates (v, θ, ϕ) to 2D velocity space (v, θ) (cylindrical) and 2D spatial $(\vec{r})$ coordinates. Here, θ is the particle velocity pitch angle measured from the magnetic field direction.

In this regime the particle distribution (more precisely, phase-space distribution of guiding centers) can be taken to be a function of $f(\vec{r}, \epsilon, \mu, t)$, where $\epsilon = (\gamma - 1)mc^2$ is the particle kinetic energy and $\mu = \frac{m u_\perp^2}{2B}$ is the particle magnetic moment. Here, $\gamma = \sqrt{1 + u^2/c^2}$ is the relativistic factor and $\vec{u} = \vec{p}/m$ is the particle momentum per rest mass. The Fokker-Planck equation can at each point $\vec{r}$ in the plasma can be written in terms of a divergence of a flux in momentum space as:

$$\frac{df}{dt} = -\nabla_{\vec{u}} \cdot \vec{\Gamma} + R(f) + S(f) \tag{B.2}$$

where $R(f)$ represents the effect of radial diffusion, and

$$\frac{df}{dt} = \frac{\partial f}{\partial t} + \vec{v}_g \cdot \frac{\partial f}{\partial \vec{r}} + \frac{\partial \mu}{\partial t}\frac{\partial f}{\partial \mu} + \frac{\partial \epsilon}{\partial t}\frac{\partial f}{\partial \epsilon} \tag{B.3}$$

is the total derivative following the particle guiding center

$$\vec{v}_g = v_\parallel \hat{b} + \vec{v}_D \tag{B.4}$$

and $\vec{v}_D$ is the guiding center drift perpendicular to $\hat{b} = \vec{B}/B$.

The $\nabla_{\vec{u}} \cdot \vec{\Gamma}$ term in Eq. B.2 is expressed in conservation form, that is different processes (collisions, DC field, RF heating and current drive, synchrotron radiation term) can be expressed in terms of a momentum space flux vector $\vec{\Gamma} = \Gamma_u \hat{u} + \Gamma_\theta \hat{\theta}$. The resulting equation is divergence free (no sink or source of particles). Possible diffusion from adjacent flux surfaces can also be expressed as the divergence of a flux. This is a desirable form from a computational point of view, since the conservation of the number of particles is embedded in the formulation and does not need to be enforced explicitly. The particle sources/sinks is taken into account separately in Eq. B.2 by the $S(f)$ term.

In it's most generic form the local Fokker-Planck operator $\nabla_{\vec{u}} \cdot \vec{\Gamma}$ can be written as:

$$-\nabla_{\vec{u}} \cdot \vec{\Gamma} = \frac{1}{u^2}\frac{\partial G}{\partial u} + \frac{1}{u^2 \sin\theta}\frac{\partial H}{\partial \theta} \tag{B.5}$$

$$G = u^2 \Gamma_u = \left(A + B\frac{\partial}{\partial u} + C\frac{\partial}{\partial \theta}\right) f \tag{B.6}$$

$$H = u \sin\theta \Gamma_\theta = \left(D + E\frac{\partial}{\partial u} + F\frac{\partial}{\partial \theta}\right) f \tag{B.7}$$

where A, B, C, D, E, F are expressed as a function of integrals over the distribution function.

Since the distribution function is a function of time, one needs to solve for every point in space $\vec{r}$ a time dependent partial integro-differential equation in the 2D velocity space. At each step of the evolution of the distribution function, the Rosenbluth potentials, and consequently A, B, C, D, E, F

must be re-evaluated. A possible approximation is to assume that the background is a Maxwellian plasma. In this case the Fokker-Plank equation simplifies to [189]:

$$\left(\frac{\partial f}{\partial t}\right)_c = \frac{\Gamma}{v^2}\frac{\partial}{\partial v}\left(Af + B\frac{\partial f}{\partial v}\right) + \frac{\Gamma}{v^2 sin(\theta)}\frac{\partial}{\partial \theta}\left(F\frac{\partial f}{\partial \theta}\right) \tag{B.8}$$

with coefficients A, B, F that are not time evolving. Here $\Gamma = \frac{Z^4 q^4}{\epsilon_0 m^2}$.

B.1.2 Zero banana width and bounce averaging

In a torus particles drift off the flux surface because of the toroidally induced ∇B and curvature drifts. The guiding center excursion due to these drifts can be much larger that a gyro radius. Depending on the ratio of the parallel to perpendicular velocities particles can either circulate along the toroidal magnetic field lines (passing) or be spatially confined in a magnetic well (trapped). Using the energy conservation and magnetic moment, it follows that the condition for particles to be trapped can be written as:

$$\frac{v_\parallel^2}{v_\perp^2} < 1 - \frac{B}{B_{\max}} \tag{B.9}$$

and the critical angle θ_c defining the passing/trapped boundary is defined as $\cos\theta_c = v_\parallel / v$.

Because of the shape of the guiding center trajectories, the trapped particle orbits are referred to as "banana" orbits. Similarly to the passing particles, the trapped particles drift monotonically away from the surface for half of the bounce period and then return to the surface during the second half. The distance that a particle drifts off the flux surface is proportional to the time it takes for its guiding center to complete one full mirror trapping period. The banana width is equal to the particle gyro-radius evaluated using the poloidal magnetic field $\rho_{\mathrm{Lpol}} = mv_\perp / qB_{\mathrm{pol}}$. A "Zero Banana Width" approximation, meaning that the collisionless guiding center orbits of the particles move on along a single flux surface, is commonly used in Fokker-Planck codes. This approximation greatly simplifies the numerical problem in that each flux surface can be treated independently and is well justified when dealing with electrons, in view of their small gyro-radius.

A further reduction in dimensionality occurs in cases where the "bounce" time of the particles, τ_b, is short compared to the collision time $\tau_b \ll \tau_c$. The present generation of larger tokamak experiments often operate with most of the plasma in this low-collisionality "banana" regime. In such cases, a "bounce-average" over the bounce or toroidal transit motion of the particle is appropriate, reducing the Fokker-Plack equation to be essentially 1D in the spatial coordinate, since the particle distribution as a function of the poloidal angle becomes a constant when expressed as a function of the collisionless constants of motion. The resulting independent variables are therefore (u, θ_0, ρ, t), where u is the magnitude of the momentum per rest mass, θ_0 is the particle velocity pitch angle measured from the magnetic field direction evaluated at the minimum magnetic field postion on a flux surface and ρ is the normalized radial coordinate from the plasma magnetic axis. If there is one local maximum and one local minimum of the magnetic field on the field line, the distribution function $f(u, \theta, \rho, \theta_{\mathrm{pol}})$ can be obtained by mapping $f_0(u_0, \theta_0, \rho)$, the distribution function evaluated at the outer equatorial plane, at the poloidal angle location θ_{pol} using the relation (based on conservation of angular momentum):

$$\sin^2\theta = \Psi \sin^2\theta_0 \tag{B.10}$$

$$\Psi = \frac{|B(\theta_{\mathrm{pol}})|}{|B_0|} \tag{B.11}$$

The "zero banana width, bounce-averaged" equation is obtained by time-integrating over the

periodic particle motion

$$\langle\langle(.)\rangle\rangle = \frac{1}{2\tau_B}\oint d\tau(.) \tag{B.12}$$

and the partial bounce time τ_B is defined as $\tau_B = \oint d\tau$, $d\tau = dl_B/|v_\parallel|$ and the integral $\oint$ is taken along the particle orbit ($v_\parallel$ varies according to the constants of motion) between the particle turning points for trapped particles and along one turn along the flux surface for passing particles.

The resulting equation is very similar to Eq. B.2

$$\frac{d\lambda f_0}{dt} = \nabla_{\vec{u}_0}\cdot\vec{\Gamma}_0 + \langle\langle R(f_0)\rangle\rangle \ + \langle\langle S(f_0)\rangle\rangle \tag{B.13}$$

where λ is defined as $\lambda = |v_{\parallel 0}|\tau_B$. The momentum-space divergence is analogous to Eq. B.7:

$$\nabla_{\vec{u}_0}\cdot\vec{\Gamma}_0 = \frac{1}{u_0^2}\frac{\partial G}{\partial u_0} + \frac{1}{u_0^2\sin\theta_0}\frac{\partial H}{\partial\theta_0} \tag{B.14}$$

$$G = u_0^2\Gamma_{u0} = \left(A_0 + B_0\frac{\partial}{\partial u_0} + C_0\frac{\partial}{\partial\theta_0}\right)f \tag{B.15}$$

$$H = u_0\sin\theta_0\Gamma_{\theta_0} = \left(D_0 + E_0\frac{\partial}{\partial u_0} + F_0\frac{\partial}{\partial\theta_0}\right)f \tag{B.16}$$

and the bounced averaged coefficients $A_0, B_0, C_0, D_0, E_0, F_0$ are expressed as a function the local coefficients A, B, C, D, E, F as reported in Ref. [189].

B.2 Quasilinear diffusion

Major use of Fokker-Planck codes is the modeling of RF heating and current drive which results from the quasilinear distortion of the particle distribution function in the presence of high power RF. The bounce-averaged coefficients corresponding to this process B_0, C_0, E_0, F_0 can be derived based on expressions for the RF quasilinear (velocity) diffusion operator [14]. The key is therefore to evaluate the quasilinear diffusion coefficient. For ELD the quasilinear diffusion coefficient is modeled as:

$$\frac{\partial f}{\partial t} = -\frac{\partial}{\partial u_\parallel}\left(-D_\parallel\frac{\partial f}{\partial u_\parallel}\right) \tag{B.17}$$

In LHEAF this is done by means of a "velocity space random walk" model. The idea behind this model is to show how a particle velocity changes from its initial velocity as a result of a series of random acceleration / deceleration "events". This diffusion process is characterized by a diffusion coefficient D which depends on the mean time and the average change in velocity between wave-particle interactions. Let's define the velocity variation $\Delta v_j = v_{j+1} - v_j$ as the difference between the velocity before and after the particle has interacted with the wave fields on an infinitesimal time τ, such that the final particle velocity is given by

$$\Delta\vec{v} = \Delta\vec{v}_1 + \Delta\vec{v}_2 + \Delta\vec{v}_3 + ... + \Delta\vec{v}_N = \sum_j \Delta\vec{v}_j \tag{B.18}$$

If the velocity variations are random, one expects that the average of the RF induced velocity variation is zero.

$$<\Delta\vec{v}>= 0 \tag{B.19}$$

However, the mean square variation from the starting velocity is not zero. This follows by noting

that the mean square velocity variation is defined as

$$(\Delta v)^2 = \sum_{i,j} \Delta\vec{v} \cdot \Delta\vec{v} \tag{B.20}$$

The terms with $i \neq j$ average to zero because of the random nature of the interaction. However, the contribution for $i = j$ do not cancel and the ensemble average reduces to:

$$< (\Delta v)^2 >= \sum_j (\Delta v_j)^2 \tag{B.21}$$

One can then define $(\Delta V)^2 =< (\Delta v)^2 > /N$ as the magnitude of the average velocity variation between interactions and $\Delta t = N\tau$ as the total time for N interactions to take place. Substituting for N one obtains:

$$< (\Delta v)^2 >= D\Delta t \tag{B.22}$$

where

$$D = (\Delta \mathrm{V})^2/\tau \tag{B.23}$$

is defined as the diffusion coefficient. As previously mentioned, in the banana regime $\tau_b \ll \tau_c$ and is therefore reasonable to take $\tau = \tau_b$ as the "infinitesimal" step size.

Using such argument, in LHEAF the quasilinear diffusion coefficient at (v_0, θ_0) is calculated starting from the RF induced velocity variation Δv over the bounce or toroidal transit motion of a test particle having initial velocity v_0 and pitch angle θ_0. The average velocity variation between interactions ΔV is calculated by averaging Δv over different RF field phases. The validity of this approach goes in hand with the assumptions which are at the very basis of quasilinear theory, namely that the wave-particle interaction is stochastic and is averaged over a time scale that is very long compared to a wave period. To further simplify the numerical procedure, the change in the particle velocity during the wave-particle interaction is assumed to be negligibly small (also in accordance with quasilinear theory).

In a tokamak equilibrium, the electron Landau resonance condition changes as a function of the poloidal angle. When the perpendicular velocity $v_\perp$ is taken into account, particles which in the 1D analysis were too fast to resonate with the wave fields are now able to meet the resonant condition. This can be readily seen by considering an electron which has a total velocity $v_0 = \sqrt{v_{\parallel 0}^2 + v_{\perp 0}^2}$ at the low field side (minimum of the static magnetic field). As an electron moves along the field line it reaches regions of higher field and conservation of the magnetic moment $\mu = \frac{mv_\perp^2}{2B}$ requires that its parallel velocity decreases as $v_\parallel = \sqrt{v_0^2 - v_\perp^2} = \sqrt{v_0^2 - v_{\perp 0}^2 B/B_{\min}}$. Hence, particles with higher $v_\perp$ can interact with waves having a higher $v_\parallel$ than what is predicted by a simple 1D analysis, as sketched in Fig. B-1. The resonance condition at different poloidal locations is averaged out by the particles as they travel along a magnetic field line (bounce-averaged).

B.3 Radial diffusion

In LHEAF, fast particles transport is modeled as a diffusion process:

$$\frac{\partial f}{\partial t} = -\frac{1}{C(r)} \frac{\partial}{\partial r} \left(-C(r) D \frac{\partial f}{\partial r} \right) \tag{B.24}$$

where $C(r)$ takes into account the shape of the flux surface and $C(r) \to r$ for circular flux surfaces.

A range of radial diffusion coefficient can be specified, however this is most commonly set to have

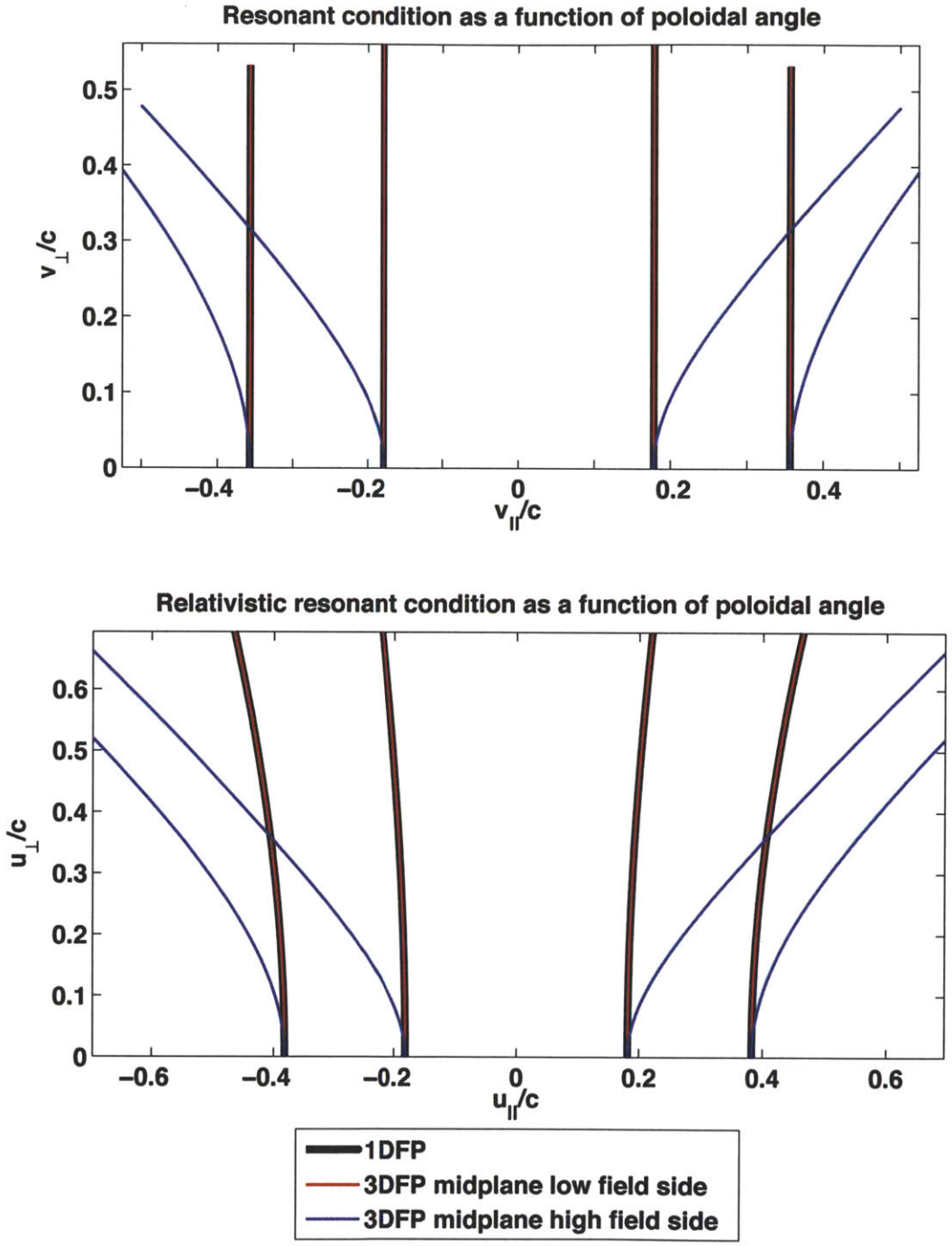

Figure B-1: Plots of the resonant condition in the distribution function velocity space. Differently from a 1DFP, in a 2D/3DFP the distribution function depends on the poloidal angle. For the illustration purposes of this figure, the boundaries of the ELD resonant condition were picked to be $0.18 < v_{\|}/c < 0.36$ and an Alcator C-Mod like geometry was assumed.

the functional form

$$D = D_{rr}\frac{v_{\|}}{v_{te}\gamma^3}\ m^2/s \tag{B.25}$$

as it would be expected for stochastic magnetic field induced transport [162]. Other radial diffusion models have been proposed depending on the underlying physics of the transport phenomena. As an example non resonant $\vec{E}\times\vec{B}$ diffusion would lead to a diffusion which is uniform in velocity space and with mild tail-electron transport effects.

B.4 Boundary condition

The boundary conditions are imposed by specifying the values of $f(u,\theta,r)$ (Dirichlet boundary condition) or its derivative (Neumann boundary condition). Since the Fokker-Planck problem is formulated in three dimensions, two boundary conditions must be set for each dimension, one for each extreme of the computational boundary.

- Physical radial dimension r

$r = a$ The distribution function is set to be Maxwellian, so that $f(u,\theta,a) = f_M$

$r = 0$ $\frac{\partial f(u,\theta,0)}{\partial r} = 0$

- Momentum space u

$u = u_{\max}$ $f(u_{\max},\theta,r) = 0$

$u = 0$ This boundary is degenerate and $f(0,\theta,r) = \text{const}$

- Pitch angle space θ

$\theta = 0$ $\frac{\partial f(u,0,r)}{\partial \theta} = 0$

$\theta = \pi$ $\frac{\partial f(u,\pi,r)}{\partial \theta} = 0$

$\theta = \theta_{PT}$ $\Gamma_{\theta,3} = -\Gamma_{\theta,4} = (\Gamma_{\theta,1} - \Gamma_{\theta,2})/2$

where $u_{\max}$ is the maximum velocity of the simulation domain and θ_{PT} is the pitch angle defining the passing/trapped particles boundary, as depicted in Fig. B-2. Here Γ_θ is the particle flux in the θ direction. In the presence of radial diffusion, a passing particle on one flux surface can become trapped on the adjacent flux surface and viceversa. In such case the particle fluxes are averaged in the same way as the trapped-passing boundary fluxes [192].

B.5 Validity of using 1DFP in the iteration loop and 3DFP for postprocessing

Although accounting for pitch angle scattering and changes of the electron Landau resonance condition as a function of the poloidal angle is key for calculating the right amount of LH driven current (2DFP codes predict more driven current by about 40% [67]), these effects become less important when calculating the LH power absorption. This is because the ELD resonant condition is determined by the low $v_{\|}$ part of the distribution function, and most of the damping occurs where $v_{\|} \approx 3\,v_{th}$. Since the minium particle velocity which interacts with the LH waves is set by particles with $v_\perp = 0$, using a 1DFP solver is a good first approximation for estimating the LH wave power absorption. Also, for the sake of evaluating the power deposition relativistic effects are negligible.

A visual inspection of the 2D distribution function in Fig. 6-16 shows that indeed most of the low $v_{\|}$ fast particles in the LH induced plateau have small $v_\perp$ and that the fraction of pitch angle

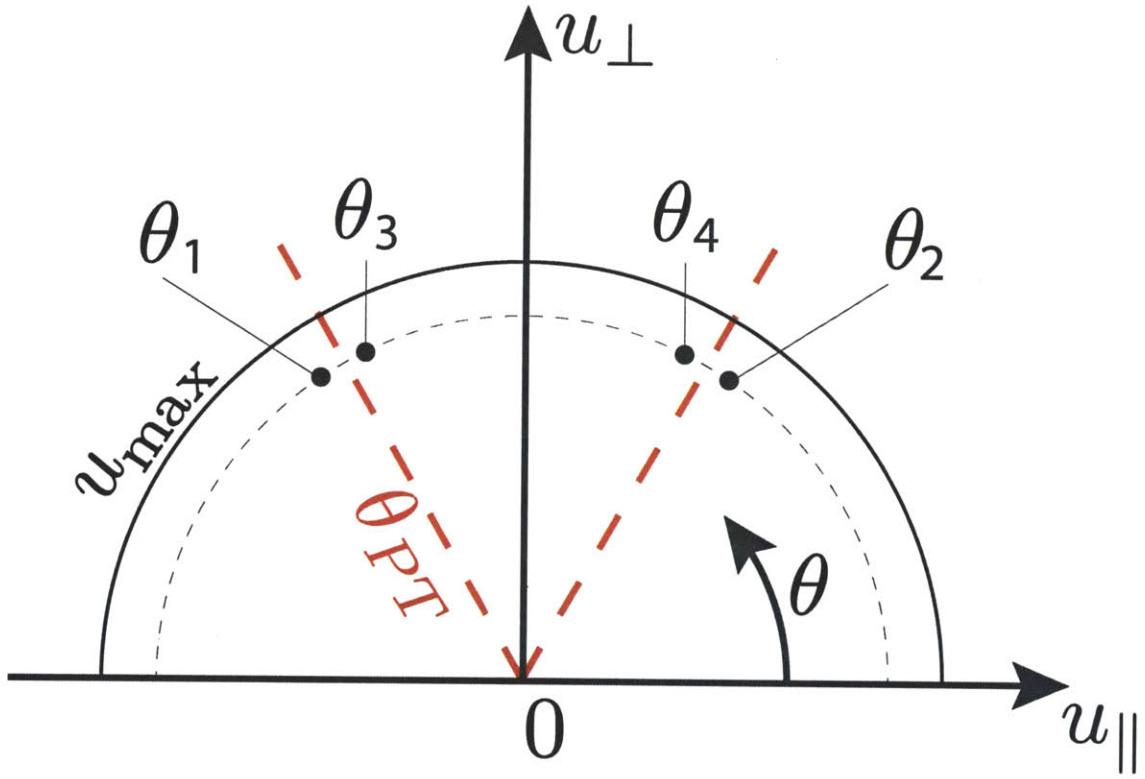

Figure B-2: Phase-space coordinate system and relevant boundaries used in VERD

scattered fast electrons becomes more significant only at higher $v_{\parallel}$. This result can be quantified by comparing the power deposition profiles resulting from a 1DFP and a 3DFP calculation, as in Fig. B-3. Finally, in the LHEAF iteration loop the quantity $\bar{\bar{\epsilon}}^{(N+1)}_{\mathrm{ELDeff}}$ is the input to the EM solver COMSOL and ultimately the most relevant quantity to compare between the 1D and the 3D calculations. Figure B-4 shows good agreement between the $\bar{\bar{\epsilon}}^{(N+1)}_{\mathrm{ELDeff}}$ calculated using the distribution functions from the $LHEAF_{\mathrm{1DFP}}$ and the $LHEAF_{\mathrm{3DFP}}$ modules. For these comparisons the last iteration step ($N = 10$) of the Alcator C-Mod high density discharge presented in Chap. 7 has been used.

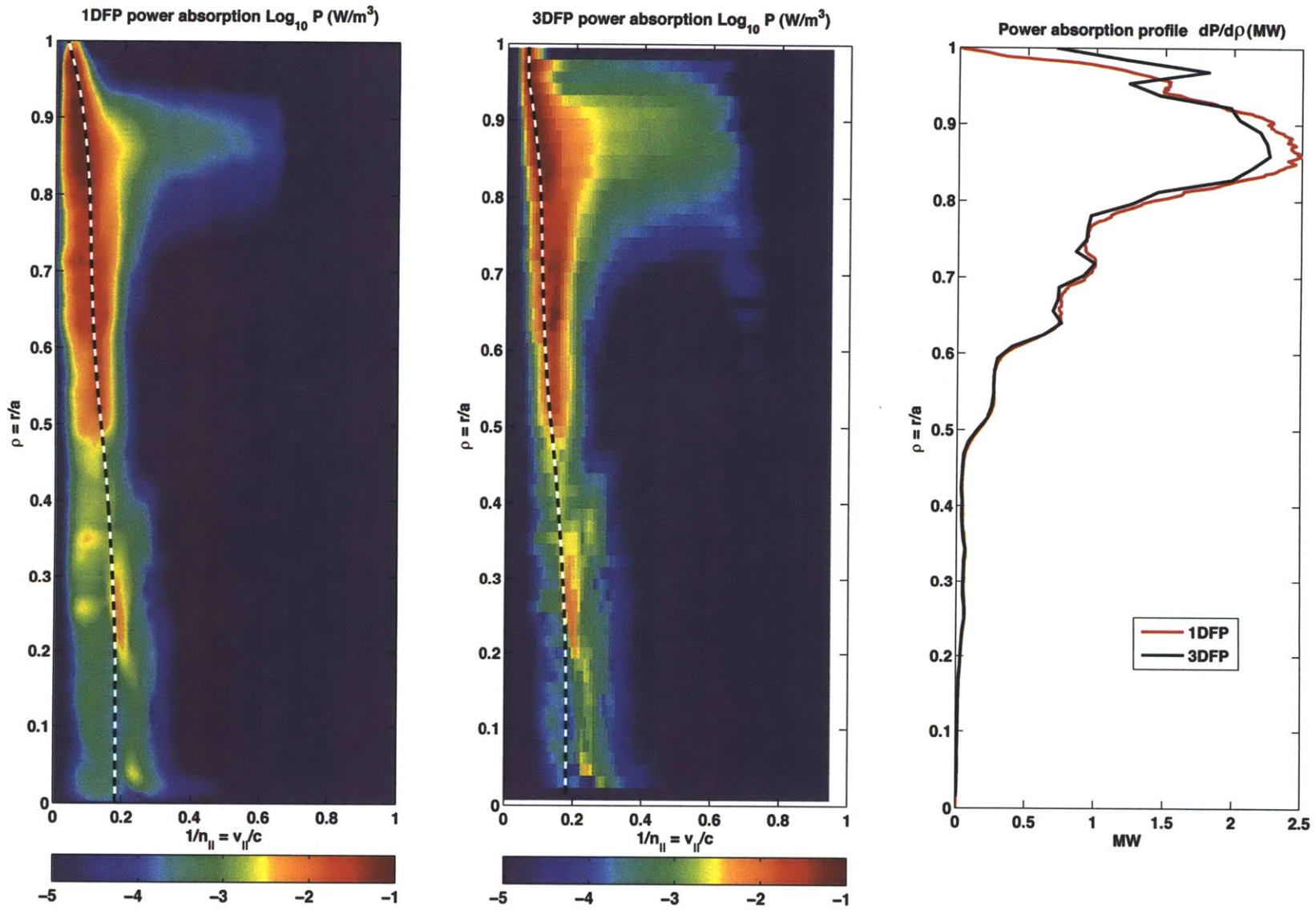

Figure B-3: Comparison of the RF power deposition profile as a function of $\beta_{\|} = v_{\|}/c$ and of the normalized minor radius $\rho = r/a$. The power absorption is dominated by the low-velocity contribution around $v_{\|} \approx 3\, v_{th}$ (black/white dashed line).

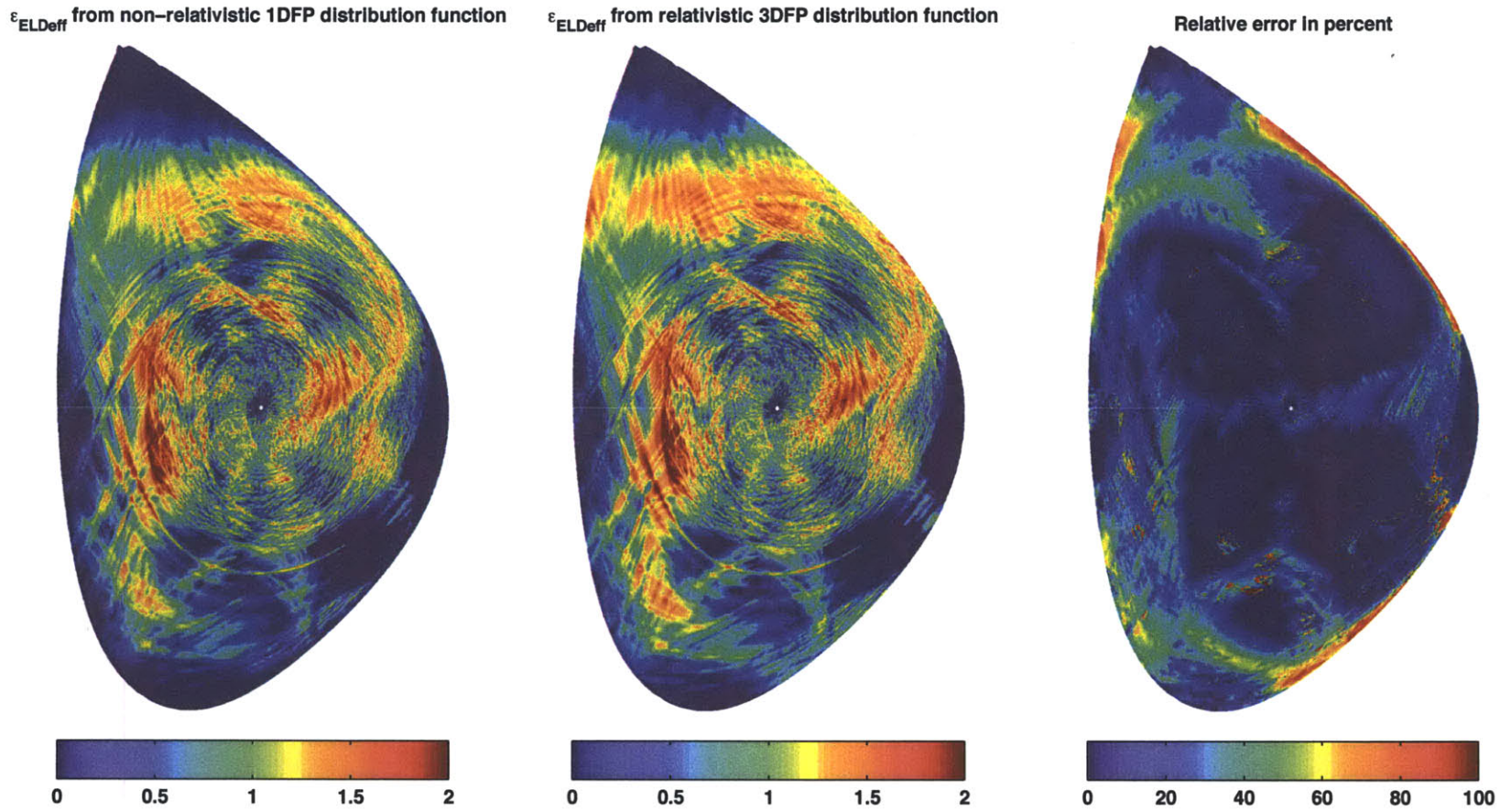

Figure B-4: The $\bar{\bar{\epsilon}}^{(N+1)}_{\mathrm{ELDeff}}$ quantities calculated using the distribution functions from the $LHEAF_{\mathrm{1DFP}}$ and the $LHEAF_{\mathrm{3DFP}}$ modules are in good agreement. The larger difference observed at the larger radii is due to an artificially high temperature in the $LHEAF_{\mathrm{3DFP}}$ module (clipped to 200 eV) to ensure that the low temperature Maxwellian distribution function which used as a boundary condition at the LCFS can be represented on the relatively coarse velocity mesh (180 points in velocity, 220 points in pitch angle).

Appendix C

HXR measurements on Alcator C-Mod with improved pulse height analysis

If the photon flux at the detectors of the HXR camera (see Sec. 3.2.1) is too great, the output of the shaping circuit will be a train of gaussian pulses that will tend to overlap one another, a process called pileup. In addition, since the output of the signal generator is capacitively decoupled, the baseline tends to drift when the incoming photon flux is high. The previous standard analysis of Alcator C-Mod HXR data did not account for these issues, leading to artificially lower count rates and skewed photon energy statistics for highly non-inductive LHCD discharges.

Since the raw pulses are digitized on a fast timescale, it is possible to fit the pulses in question and recover the original peak amplitude information. A new algorithm has been developed to improve the existing HXR analysis and correct for these known issues. In the following we demonstrate the use of the new algorithm when applied to chord 16 (looking at the core plasma) of a highly non-inductive discharge. The algorithm has been implemented in MATLAB and can be summarized in the following steps:

1. Find the time dependent baseline of the raw signal
2. Evaluate the noise level to set a peak finding threshold
3. Evaluate the width of isolated gaussian pulses
4. Iteratively find the location of pulse maxima
5. Least square fit gaussian peaks of width σ_p centered at maxima locations to best reproduce the raw signal

This algorithm is extremely efficient and allows us to fit a large number of peaks in little time ($\approx 10^6$ peaks in ≈ 1 minute) on the same desktop computer. The validity of applying baseline subtraction to the HXR signal has been verified on the test-bench.

C.1 Baseline subtraction

For isolated detection events, the energy of the incoming photon is linearly related to the pulse amplitude measured from a baseline value. The baseline value at the beginning of each shot b_0 is stationary and is easy to determine since the raw signal is free of pulses. However the baseline will

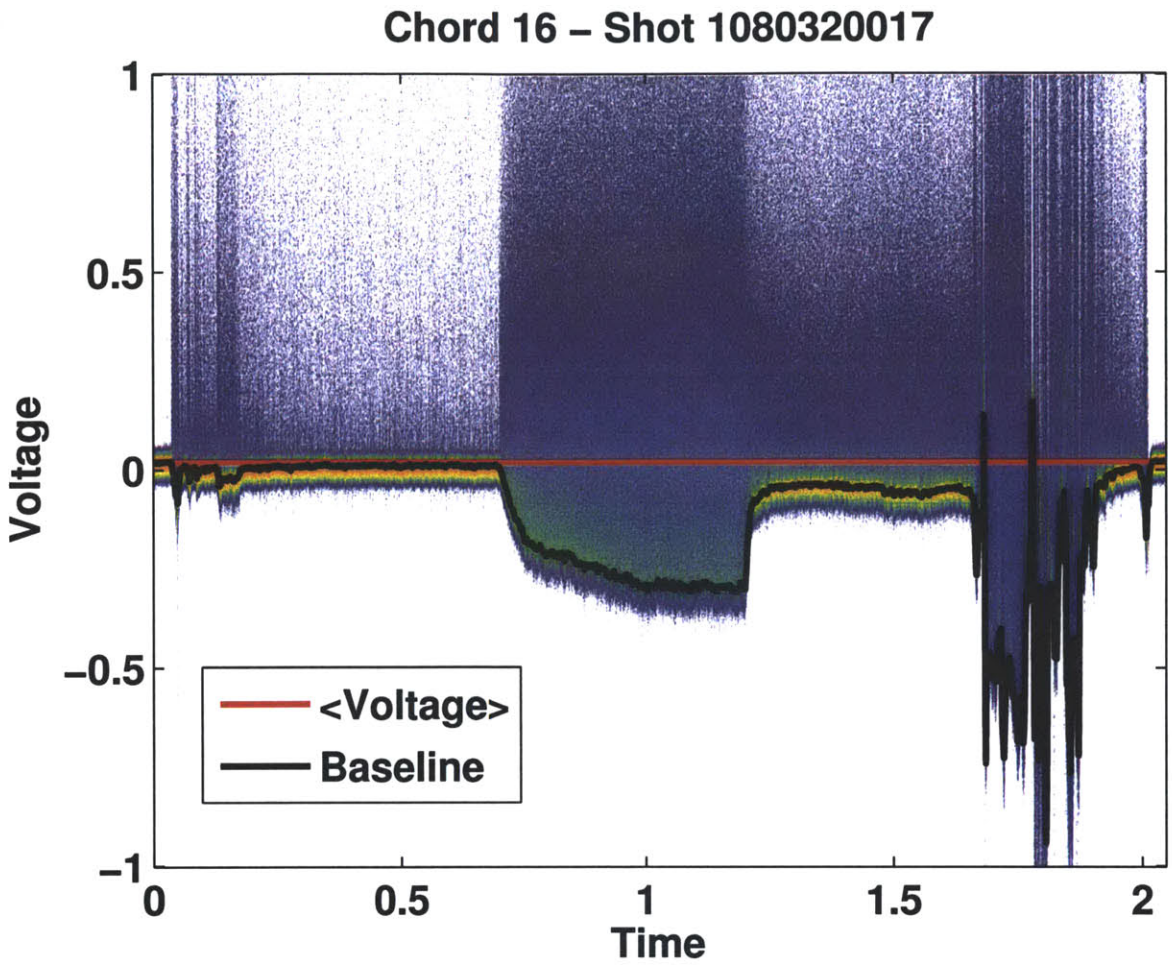

Figure C-1: Logarithmic color plot of binned raw signal (10 ms, 4 mV bins). Over plotted are the estimated baseline value (black line) and average voltage (red line) which is used as baseline value in the existing analysis.

tend to drift as soon as pulses are generated. This effect is always present, but it is particularly severe for the centermost chords when LH is on.

The problem of the baseline drift can be easily solved by estimating the time dependent baseline value and subtracting it from the raw signal. Our algorithm bins the raw signal every 10 ms and defines the baseline value $b(t)$ as the minimum value of each bin offset by a constant such as to match the initial value $b(0) = b_0$. Assuming that the noise level is constant throughout a shot, this approach gives a robust estimate of the baseline value even for small time bins, ultimately compensating for fast baseline variation. Figure C-1 shows the result of this procedure (black line) and compares it with the previous analysis approach of taking the mean value of the signal (red line) as the baseline value.

Once the baseline value is subtracted, an appropriate peak detection threshold can be chosen. A threshold of $5\sigma_N$ is usually used, where σ_N is the variance of the normally distributed noise evaluated in absence of pulses during the first 20 ms of the discharge.

C.2 Fast deconvolution of pileup events

Consider two photons that arrive at the detector at times t_0 and $t_1 = t_0 + \Delta t$ respectively. If the time delay Δt is small enough, the resulting gaussian pulses will overlap each other and the height of the peaks in raw signal will not accurately represent the energy of the incoming photons.

Since a detailed digital sampling is available for each output pulse, it is possible to distinguish those pulses that originate from a single event from those in which more than one event have contributed. Moreover, since the shaping process produces pulses of a predictable shape, the possibility then arises of deconvolving the piled-up pulses into their separate components. The standard approach for pile-up deconvolution is to fit gaussian signals when the time difference between two peaks is below a given threshold. This approach is available as an option with the existing analysis technique, however the required processing times are extremely long ($\approx$ 100 peaks in $\approx$ 1 minute on a desktop computer) and in practice the default policy has been to discard the piled-up pulses which can be a significant fraction of the whole number of pulses for high photon flux discharges.

These limitations have led to the development of a new deconvolution algorithm. The key point of the proposed algorithm is to realize that the width of the gaussian pulses σ_p is set by the shaping electronics and therefore is constant for each chord. The value of σ_p is found by fitting gaussian functions to isolated peaks.

First, the maxima of the raw signals are found by examining the curvature of the signal through numerical derivatives. At this point one can subtract from the raw signal a train of gaussian peaks having width σ_p and height equal to the value of the found maxima. The resulting signal is then searched for new maxima with the same technique. This procedure is iterated until the number of maxima found in the resulting signal is small with respect to the total number of maxima.

Next, a proper peak height deconvolution is done by minimizing the least square error of a synthetic signal composed of the gaussian peaks with respect to the raw signal. Numerically, this results in solving the overdetermined linear system of the form $Qb = c$, where Q is a $p \times q$ matrix of full rank (with $q < p$), c is the $q \times 1$ vector of the raw data (subtracted of its time dependent baseline value) and b is the vector of the unknown peak heights. The kernel Q is a sparse non-square linear system with weights ω_{ij} defined as

$$\omega_{ij} = exp\left[-\left(\frac{t_i - t_j}{\sqrt{2}\sigma_p}\right)^2\right], 1 \leq i \leq p, 1 \leq j \leq q$$

where t_j are the times of the maxima found at the previous step and t_i is the time sample of the data. The solution vector b is constrained to be always positive and is found iteratively following a Majorize-Minimize approach [193]. Choosing the maxima of the raw signal as an initial guess for the unknown vector b ensures a fast convergence. Once the optimal fit is found, then the individual amplitudes of each event are obtained and the mutual interference of the two events is eliminated. Figure C-2 shows the result of this technique when applied to piled-up pulses in chord 16 at about 1.0 s of a discharge with severe pileup.

The comparison between the new puse heigh analysis routine and the existing one is depicted in Fig. C-3 as a logarithmic color plot of the counts as a function of time and energy. The higher count rates of the new analysis result in higher statistics and better resolution of the details in the HXR data.

C.3 Off-site calibration using fast particle signature

At the highest energies of the HXR camera spectrum anomalous count rates are often observed. This feature has been identified to be associated with high energy γ generated for example at breakdown, ramp-down or disruptions.

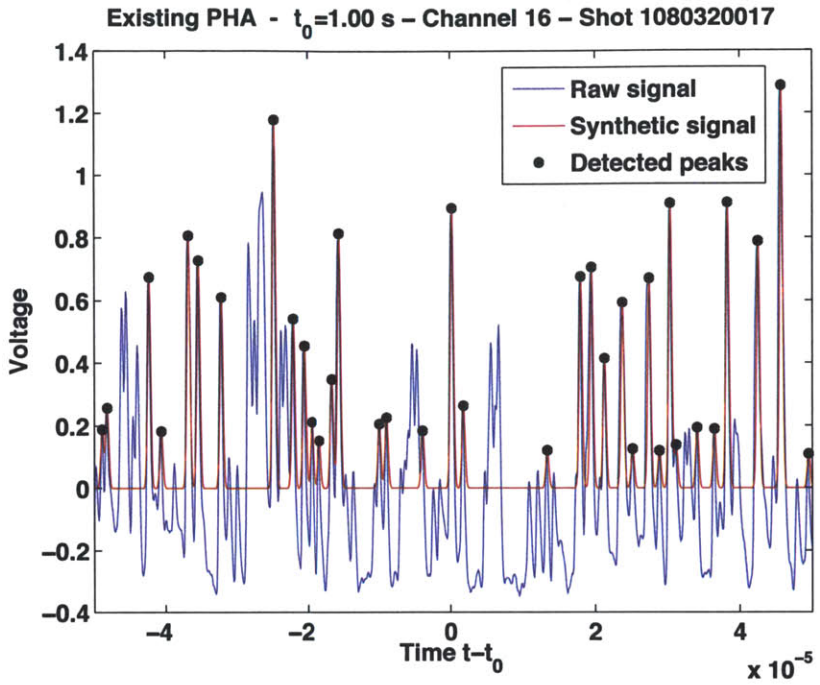

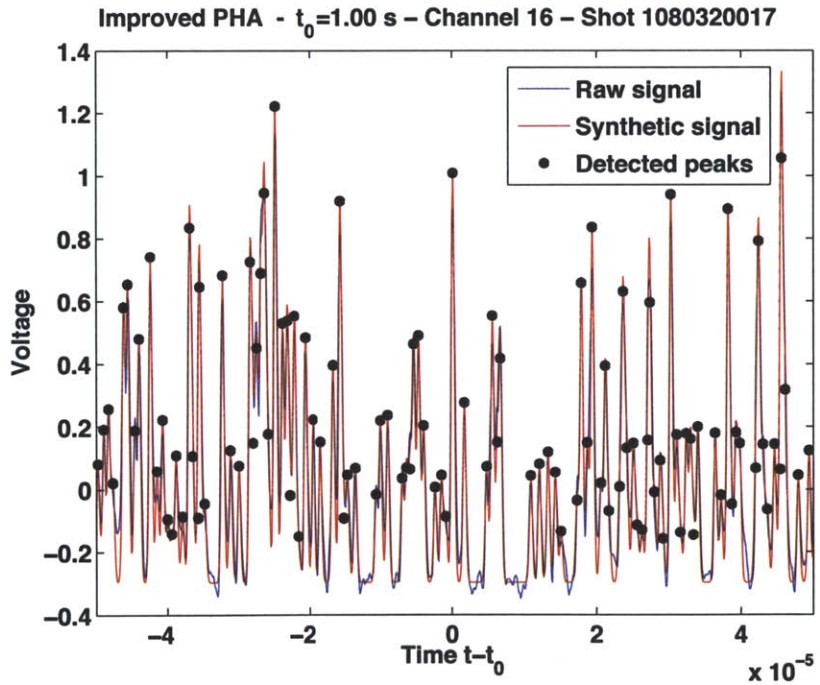

Figure C-2: Comparison of the existing and the improved pulse height analysis procedure. The raw data is shown in blue. The red curve is a synthetic signal which is generated by convolving a gaussian pulse of height 1 and width σ_p with the train of pulses detected by the PHA analysis, shown as black dots.

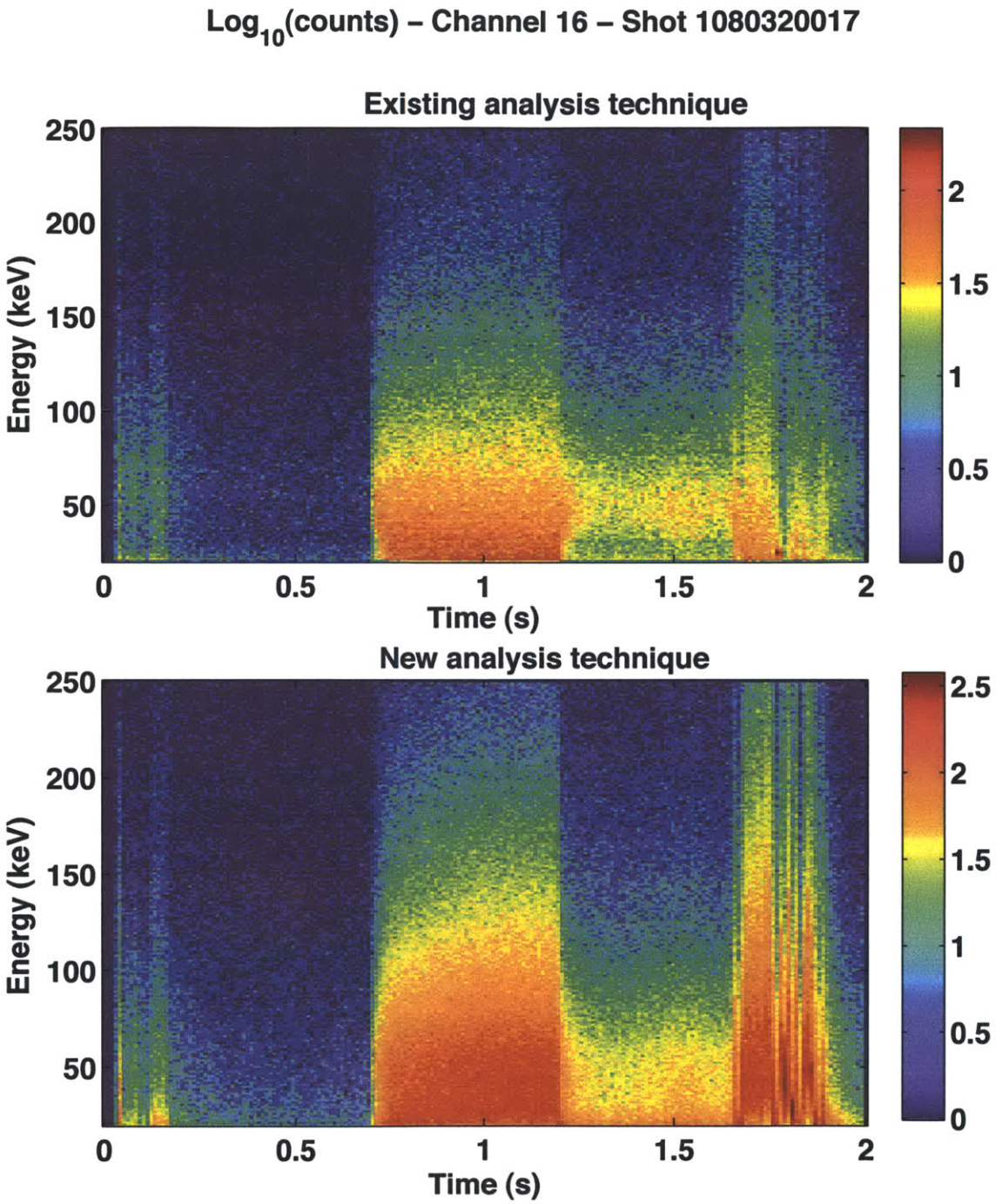

Figure C-3: Logarithmic plot of the counts for existing PHA analysis and comparison with the new one (1 keV, 10 ms bin size). From 0.7 to 1.2 seconds 800 kW of LH power is injected in the plasma with $n_{\|} = 1.55$, generating a large quantity of high energy X-rays. A consistent level of HXR persists after LH turns off, an interesting effect we are currently investigating. HXR are also generated starting at break down and at 1.7 seconds, during the ramp-down phase of the plasma.

Similar spurious counts are also observed at higher densities and especially in presence of ICRH. In this case the HXR baseline is observed to be sawtoothing. Also, no signature is observed in He or H plasmas (see Fig. C-4). These observations point to DD fusion events being a further source of signal, though by which process fast particles generated by the DD fusion reaction (Eq. C.1) are detected at the HXR camera is yet not well understood.

$$\begin{aligned} \mathrm{D} + \mathrm{D} &= \mathrm{T}\ (1.01\ \mathrm{MeV}) + \mathrm{P}\ (3.02\ \mathrm{MeV}) \\ \mathrm{D} + \mathrm{D} &= 3\mathrm{He}\ (.82\ \mathrm{MeV}) + \mathrm{N}\ (2.45\ \mathrm{MeV}) \end{aligned} \tag{C.1}$$

Further analysis by Faust [70], confirmed a linear relationship between the number of HXR counts composing such feature and the measured global neutron count rate [113], with a conversion factor in the order of one HXR event per 3×10^8 neutron events. This phenomenon was identified to be due to non-linearities of the HXR camera electronics (shaping circuitry) rather than by a physical process which emits energy at well defined energies. This is also supported by the fact that the signature associated with high energy particles does not follow the baseline drift.

Assuming that all shaper boards are affected in the same way by such non-linear behaviour, this feature can be used to obtain a relative calibration among channels. To confirm the accuracy of such assumption, further calibrations are needed. However, using this assumption to calibrate the HXR camera system from the digitizers up to the shaping boards, the spatial profiles are found to be qualitatively smoother, that is an encouraging result.

C.4 HXR emissivity drop at high density

As introduced in Sec. 2.2.3, an anomalous loss of Bremsstrahlung emission, which is used as a sensitive proxy for fast electrons generated by LHCD, is observed for increasing plasma densities. The plots of the total HXR counts as a function of the plasma average density using the existing and the new PHA routine are plotted in Fig. C-5 and Fig. C-6, respectively. At the lower densities the two analyses techniques differ significantly, since it is where the count rates are highest and the pileup and baseline drift effects are more significant. In this region, GENRAY/CQL3D raytracing simulations were found to reproduce the total Hard X-Ray (HXR) counts significantly better than previously thought.

Thanks to this improved analysis, it was realized that such feature was an artifact induced by the existing PHA routine and that instead the HXR emission drops steadily across all densities, thus fundamentally redefining the nature of the LHCD density limit. Whatever are the processes involved, these should not occur suddenly at $\bar{n}_e = 1.0 \times 10^{20}\ m^{-3}$, but must instead degrade the LHCD efficiency continuously across the whole density range which was probed in the experiments.

Interestingly, some difference is also found at the highest densities, where pileup events should be rare. These are associated to the DD fusion events discussed in the previous section, which become more significant at higher densities. A possible way to distinguish between "true" and "spurious" counts is from a statistical point of view.

C.5 Statistic of a PHA routine

The discrete probability distribution that expresses the probability of a number of events occurring in a fixed period of time if these events occur with a known average rate and independently of the time since the last event is the Poisson distribution.If the expected number of occurrences in this interval is λ, then the probability that there are exactly $k = 0, 1, 2, \ldots$ occurrences is equal to:

$$P(k, \lambda) = \frac{\lambda^k e^{-\lambda}}{k!} \tag{C.2}$$

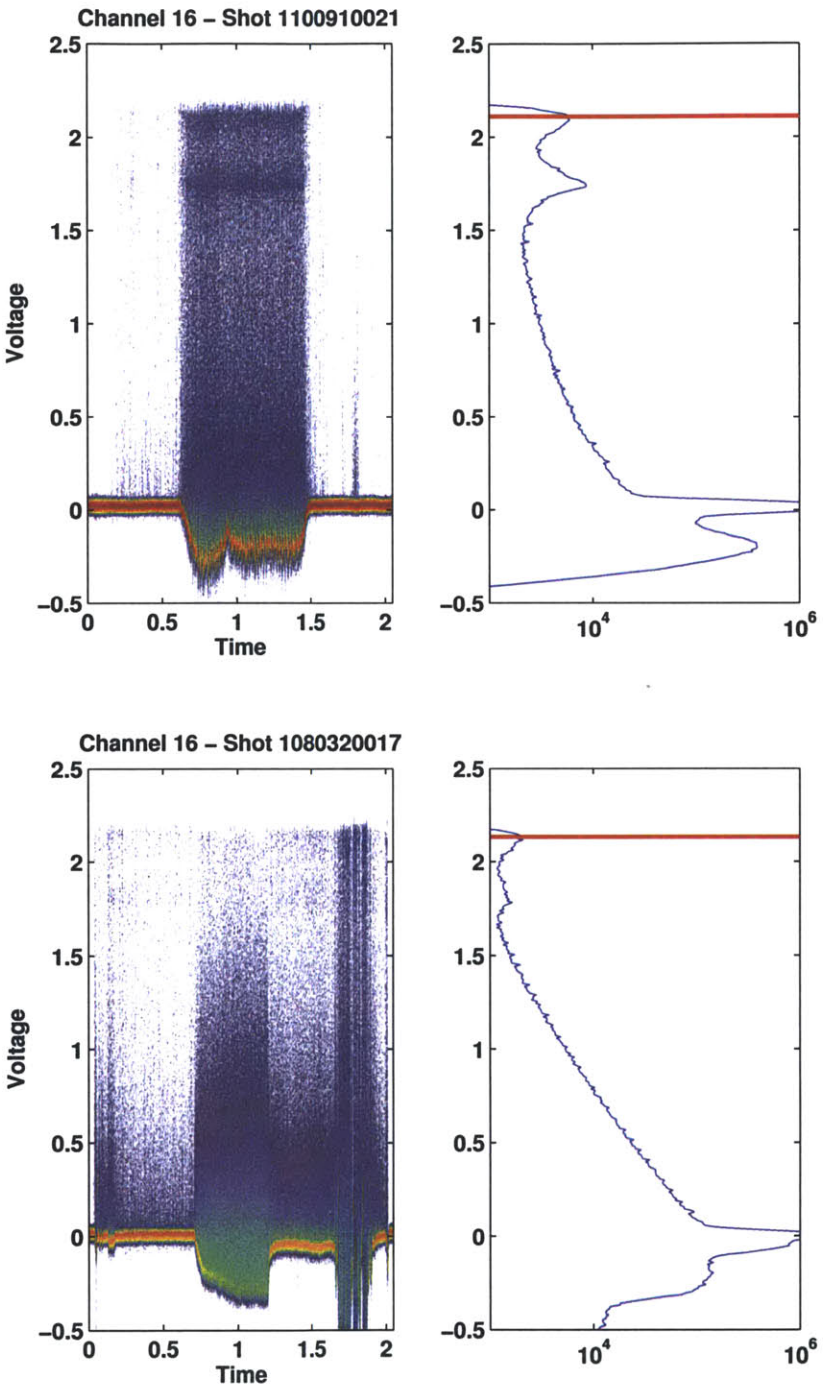

Figure C-4: On the left, the 2D histogram of the HXR camera central channel raw data during I-mode (shot #1100910021) and a good LHCD shot (shot #1080320017). In the former case the signature is clearly visible around 2 V, especially during ICRH (0.7 s to 1.5 s). On the right, the logarithmic histogram of the voltage highlights the presence of the non-linear signature in both discharges. The red line indicates the voltage used for the cross channel calibration.

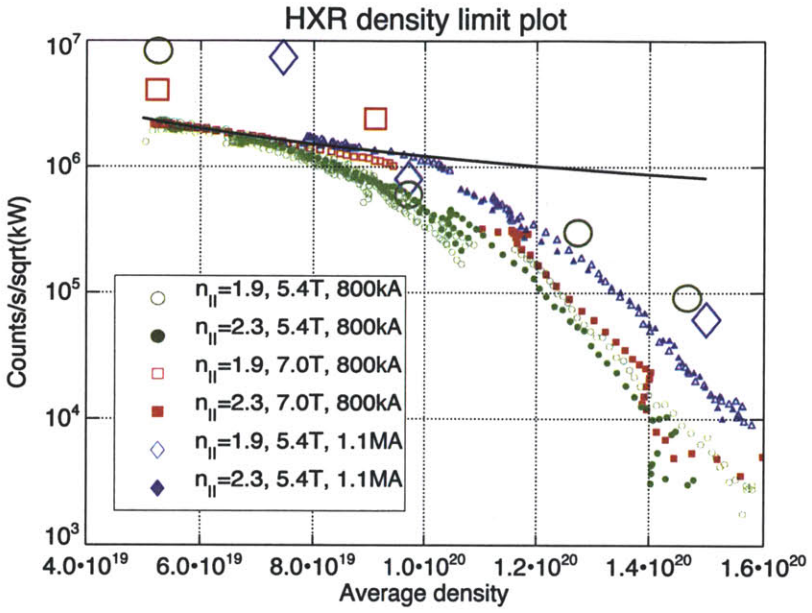

Figure C-5: Measured HXR emission (small symbols) and GENRAY/CQL3D simulations (large symbols) as a function of line averaged density. The experimental data has been generated with the *existing PHA routine* and plotted on a semi-logarithmic scale for X-Rays between 40 and 200 keV. The black curve represents a $1/n_e$ falloff. The count rates in this figure are normalized to the square root of net LH power.

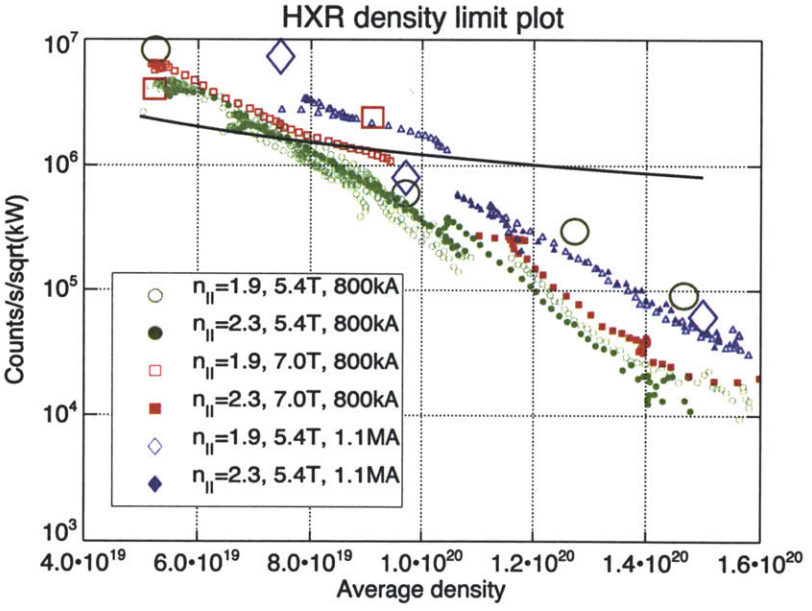

Figure C-6: Same plot of Fig. C-5 but the experimental data has been generated with the *improved PHA routine*. The difference between the two analyses appears at the lowest densities, where the count rates are highest and the pileup and baseline drift effects are more significant. Fortuitously, as a result of the new PHA analysis GENRAY/CQL3D raytracing simulations were able to better reproduce HXR counts at low density.

If we assume that the HXR is Poisson-like then, given the count frequency f (in the units of $\#/s/ch$), the fraction of multiple counts in an interval Δt can be calculated as

$$P(>2,\lambda) = 1 - P(0,\lambda) - P(1,\lambda) \tag{C.3}$$

A lower bound to the number of multiple gaussians which would appear as a single peak in the existing PHA routine can be estimated by setting $\Delta t_o = 2\sigma_{gaussian} \approx 4 \times 10^{-7}\ s$. In the following, events which happen within a time interval $\Delta t < \Delta t_o$ will be labeled as"overlapping".

Figure C-7 summarizes the HXR signal statistic of the $n_{\|} = 1.9, 5.4\ T$, 800 kA data points from Figs. C-5 and C-6. From this detailed analysis several interesting remarks can be extracted:

- The counts for the improved PHA (**green symbols**), the existing PHA (**red symbols**) and their difference (**blue symbols**) are shown. The existing PHA does not consider peaks which happen within a time interval $\Delta t < 2.2 \times 10^{-6}\ s$)
- The number of multiple counts expected by Poisson statistics is calculated according to Eq. C.3 (**black symbols**).
- The number of counts that the improved PHA routine finds after after multiple passes (**yellow symbols**).
- The **purple line** is the result of subtracting half of the number of multiple counts expected by Poisson statistics (black symbols) from the improved PHA routine (green symbols). This is a measure of how much the existing PHA routine should measure if there were at most two gaussians per overlapping event. The purple line is always above and very close to the existing PHA counts (red symbols), and starts to deviate at lower densities, where the count rates are higher and it is more likely that more than two gaussians overlap.
- As soon as the black symbols cross the yellow ones, these become flat. This strongly suggests that (statistically speaking) the overlapping events found by the improved PHA are predominantly actual counts for $\bar{n}_e < 1.1 \times 10^{20}\ m^{-3}$ and artificial counts for $\bar{n}_e > 1.1 \times 10^{20}\ m^{-3}$
- It is likely that most of the spurious overlapping events are due to non-linearities driven by DD fusion events. The **gray symbols** are obtained by multiplying the neutron data to match the yellow points at high density and subtract it from the improved PHA counts. By subtracting these counts from the counts for the improved PHA (**green symbols**) one obtains the **dark green circles**.
- The existing PHA always underestimates the real number of counts, also at high density. (i.e. blue curve always higher than yellow curve, even at high density)

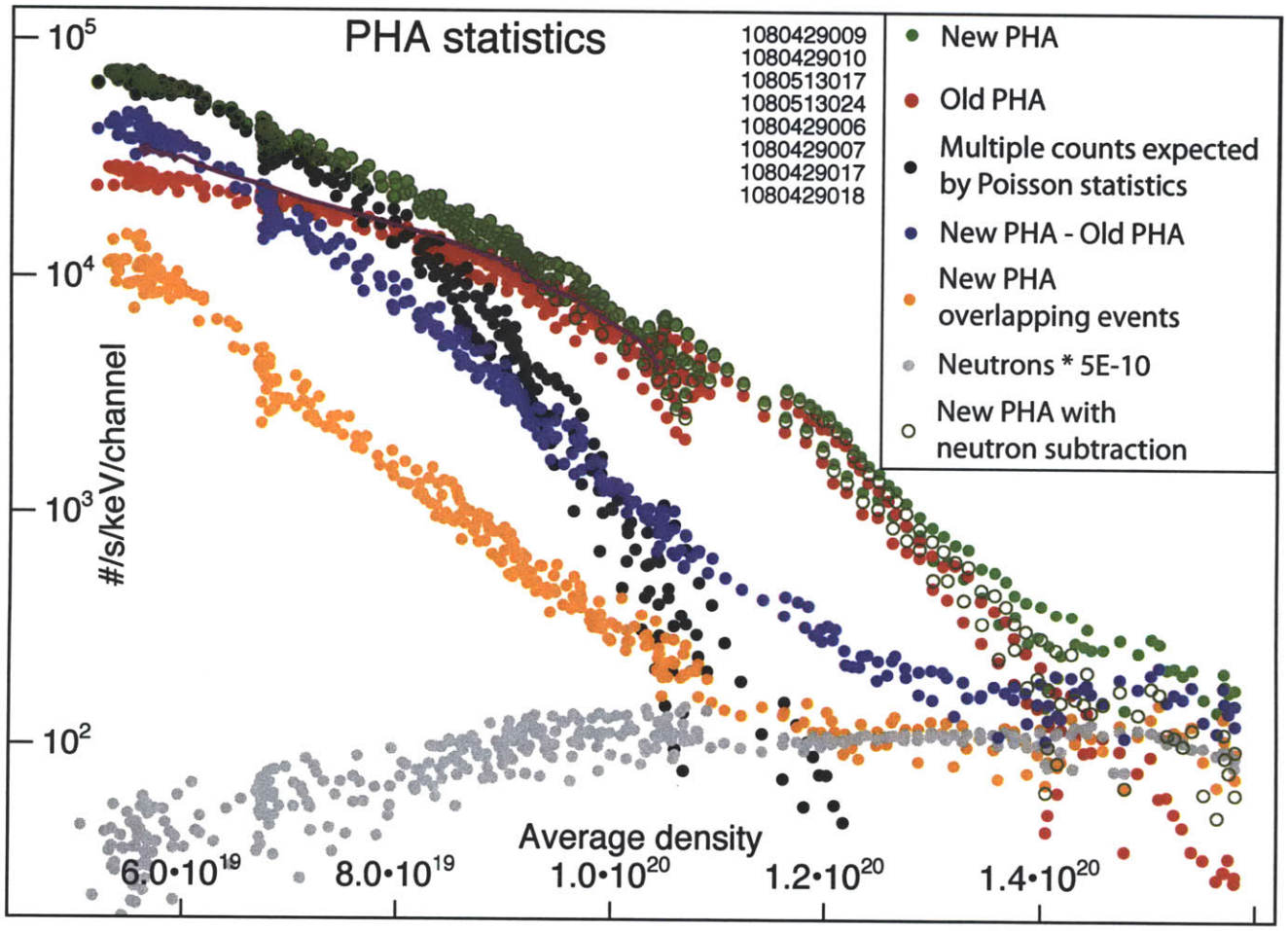

Figure C-7: Statistic analysis of the improved PHA routine and comparison with the existing one. From the count rate $\#/s/keV/ch$ the fraction of multiple counts in an interval Δt can be calculated, assuming that the HXR distribution is Poissonian.

Appendix D

Windowed Fourier transform and wavelet transform

The use of *Windowed Fourier Transform* (WFT) and *Wavelet Transform* (WT) for the visualization of dispersion, amplitude and wave polarization information of fullwave fields was first described in Ref. [177, 178] in the context of full-wave ICRF mode-conversion simulations in 1D. In the following, the formalism of WFT and WT are introduced based on such references.

D.1 Windowed Fourier transform

In WFT, the signal is divided into segments, each small enough for the portions of the signal to be assumed stationary. For this purpose, a window function $w(x)$ of support x_w is convolved with the original signal and at each step of the convolution the Fourier transform of the convolved signal is taken. The width of this window must be equal to the segment of the signal where its stationarity is valid. In practice however, WFT has limitations in terms of spatial/spectral resolution, since the narrower the support window, the better the real-space resolution, and better the assumption of stationarity, but poorer the frequency resolution. This problem is mathematically formulated in terms of two conflicting types of errors: the *Heisenberg error*

$$\Delta k_H = \frac{c}{x_w} \tag{D.1}$$

(where c is a constant that depends on the details of the window function used) and the *gradients error*

$$\Delta k_\nabla = \frac{\partial k}{\partial x} x_w \tag{D.2}$$

Each of these errors vanish for opposite limits of the window dimesion $\lim_{x_w \to \infty} \Delta k_H = 0$ and $\lim_{x_w \to 0} \Delta k_\nabla = 0$. So the optimal window size is obtained by setting $\Delta k_H = \Delta k_\nabla$, from which:

$$x_{w,opt} = \sqrt{\frac{c}{(\partial k/\partial x)^{-1}}} \tag{D.3}$$

Notice that the optimal window size is a function of the spectral component k.

D.2 Wavelet transform

The WT was developed as an alternative approach to the WFT to overcome, to a certain extent, the resolution problem. In WT the signal is multiplied with a function $\Psi(x)$, the *wavelet*, similar to the support window function in the WFT, and the transform is computed separately for different segments of the real-domain signal. However, in WT the width of the wavelet function is set to be $x_w \propto 1/k$. Hence, unlike the WFT, which has a constant resolution at all points and frequencies, the WT has a good spatial and poor spectral resolution for high frequency components, and viceversa for low frequency components. In other words, the WT anaylyzes each frequency component with a resolution matched to its scale.

By this choice the *Heisenberg error relative to each spectral component* $\Delta k_H/k$ is kept constant and the *gradients error relative to each spectral component* equals $\Delta k_\nabla/k = \frac{\partial k/\partial x}{k^2}$, which one may recognize as the adiabatic-change criteria of the WKB theory (Eq. 1.69) discussed in Sec. 1.4.1. Imposing the relative errors to be constant $\Delta k_\nabla/k = \Delta k_H/k$ results in $c = \frac{\partial k/\partial x}{k^2}$ which in practice sets a condition on the window function used depending on how well the adiabatic-change criteria is satisfied in the system under consideration.

Mathematically the WT can be interpreted either as a covolution operation in real space of the wavelet function $\Psi(x)$ with the signal $f(x)$

$$C(x,\alpha) = \int_{-\infty}^{\infty} f(x') \frac{1}{\sqrt{\alpha}} \Psi^\star \left(\frac{x'-x}{\alpha} \right) dx' \tag{D.4}$$

or as a filtering operation in spectral space

$$C(x,\alpha) = \frac{1}{\sqrt{2\pi}} \int_{-\infty}^{\infty} \hat{f}(k) \sqrt{\alpha} \hat{\Psi}^\star(\alpha\, k) \exp^{ikx} dk \tag{D.5}$$

where $\hat{\Psi}(k)$ is the fourier transform of the wavelet function $\Psi(x)$ (i.e. the filter transfer function) and $\hat{f}(k)$ is the spectrum of the signal $f(x)$. Here the parameter α is used to dilate the wavelet function and thus anaylyze each spectral component with a resolution matched to its scale. Numerically, the latter approach is preferred in view of the higher numerical efficiency of the Fast Fourier Transform (FFT) algorithm $O(N \log N)$ compared to a numerical convolution $O(N^2)$.

The relationship between the scale parameter α and the spectral component k can be given only in a broad sense and it's better to speak about the pseudo-frequency corresponding to a scale. A way to do so is to associate a frequency F_c to a wavelet function. This can be identified for example by frequency at which the peak/mean/median of the wavelet function power spectrum occurs. Then, when the wavelet is dilated by a factor α its pseudo-frequency becomes F_c/α.

D.2.1 Morlet wavelet

The Morlet wavelet and its complex analogue [1] are defined as sinusoidal signals multiplied by a Gaussian envelop:

$$\begin{aligned} \Psi(x) &= \exp(-x^2)\cos(c_0\, x)\ , \text{ Morlet wavelet} \\ \Psi(x) &= \exp(-x^2)\exp(i\, c_0\, x)\ , \text{ complex Morlet wavelet} \end{aligned} \tag{D.6}$$

In fact, the Morlet WT can be shown to be matematically equivalent to a WFT with a Gaussian window of width $x_w = c_0/k$. Plots of the Morlet wavelet in real and spectral space are shown in Fig. D-1.

[1] To get complex phase information one needs a complex wavelet whose spectrum is non-zero only for either positive or negative k.

Since the fourier transform of the gaussian envelope is equal to

$$G(k) = \frac{1}{\sqrt{2\pi}} \int_{-\infty}^{\infty} e^{-x^2} e^{i2\pi kx} dk = e^{-k^2} \tag{D.7}$$

the Full-Width Half Maximum FWHM of the Morlet wavelet power spectrum is $\Delta k_H = 2\sqrt{\log(2)}$. As the spectrum is centered at $k = c_0$, the spectral accuracy at every wavelet scale is $\Delta k_H / k \approx 1.66/c_0$.

The parameter c_0 can therefore be used to control the ratio between the Heisenberg and the gradient error. The condition that the WKB approximation is satisfied (i.e. small gradients error) and that the eikonal wavenumber is well resolved (i.e. small Heisenberg error) can be written as: $kL \gg kx_w = c_0 \gg 1$, where L is the spatial resolution. For the analysis carried out in Sec. 7.2.5 the parameter c_0 was empirically set to 20 (equivalent to a spectral resolution of $\Delta k/k \approx 0.083$) as it was visually judged to give the best tradeoff in spectral-spatial resolution. This translates in a parallel spatial resolution of the order of 20 $cm/n_{\|}$ on Alcator C-Mod.

D.2.2 ELD as a wavelet

Worth pointing out is that the Morlet wavelet of Fig. D-1, resembles very closely to the imaginary susceptibility arising from Electron Landau Damping (ELD) for a Maxwellian plasma $\chi_{\mathrm{ELD}}(z)$, shown in Fig. 6-3(b). This suggests that is possible to interpret $\chi_{\mathrm{ELD}}(z)$ as a wavelet whose support scales depending on the plasma temperature, thus selecting specific spectral $k_{\|}$ components with which the waves can interact. According to this picture the $\bar{\bar{\epsilon}}_{\mathrm{ELDeff}}$ construct which used in the LHEAF iterative procedure is nothing but the result of such special wavelet analysis.

$$\Psi(x) = \exp^{-x^2/2} \cos(c_0 x)$$

$$Psi(k) = \frac{1}{\sqrt{2\pi}} \int_{-\infty}^{\infty} \Psi(x) e^{-i2\pi kz} dk$$

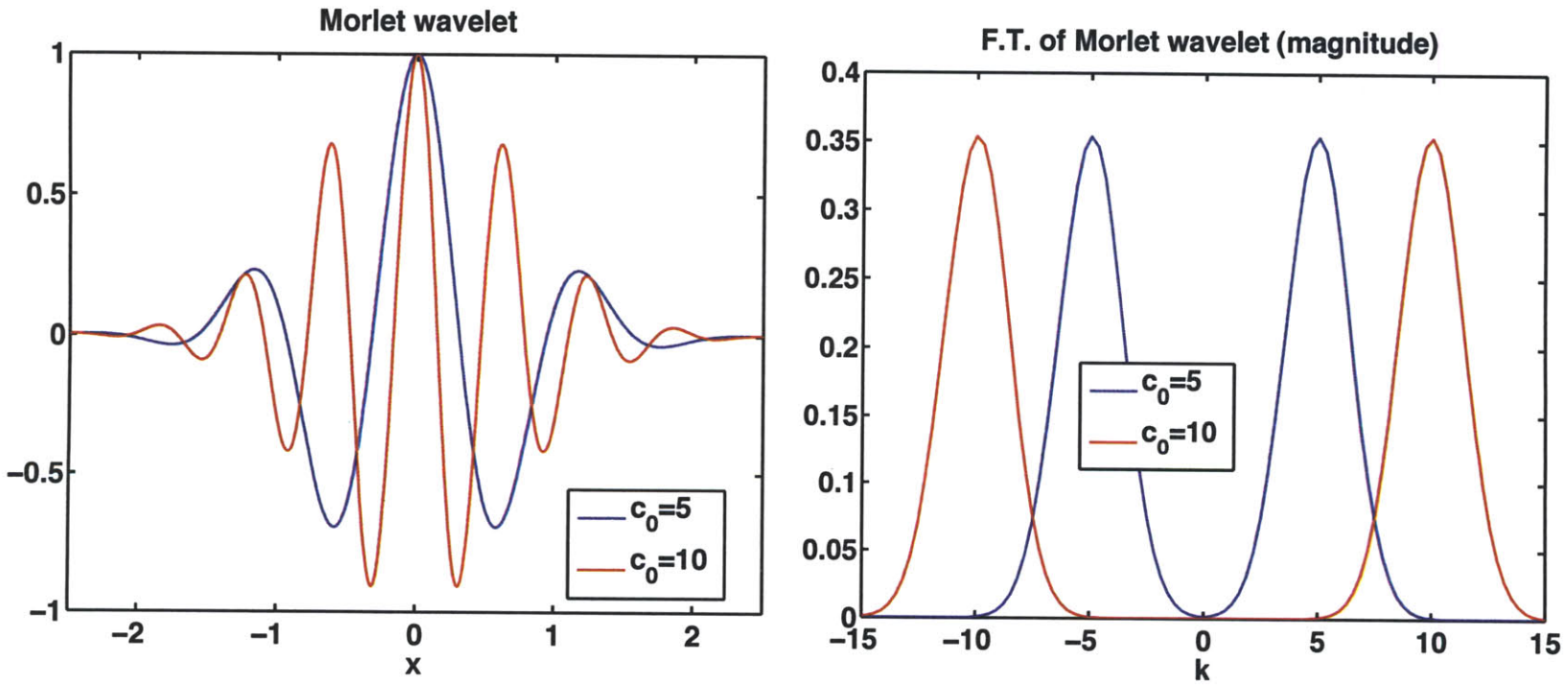

Figure D-1: Morlet wavelet and its Fourier transform (magnitude) plotted for two different values of the parameter c_0. The parameter c_0 can be used to agjust the ratio between the errors Δk_H and Δk_∇.

Bibliography

[1] P. Koert, P. Macgibbon, R. Vieira, D. Terry, R. Leccacorvi, J. Doody, and W. Beck. Waveguide splitter for lower hybrid current drive. In *American Nuclear Society (ANS) Topical Meeting on the Technology of Fusion Energy*, volume 56, pages 109–113. American Nuclear Society, 2009.

[2] O. Meneghini, J. Hillairet, M. Goniche, R. Bilato, D. Voyer, and R. Parker. TOPLHA and ALOHA: comparison between Lower Hybrid wave coupling codes. In *American Physical Society, 50th Annual Meeting of the Division of Plasma Physics, November 17-21, 2008, abstract PP6.078*, 2008.

[3] V. Lancellotti, D. Milanesio, R. Maggiora, G. Vecchi, and V. Kyrytsya. TOPICA: an accurate and efficient numerical tool for analysis and design of ICRF antennas. *Nuclear fusion*, 46:S476, 2006.

[4] X. Litaudon, G. Berger-By, P. Bibet, JP Bizarro, JJ Capitain, J. Carrasco, M. Goniche, GT Hoang, K. Kupfer, R. Magne, et al. Lower hybrid wave coupling in Tore Supra through multijunction launchers. *Nuclear Fusion*, 32:1883–1898, 1992.

[5] M. Brambilla. Waveguide launching of lower hybrid waves. *Nuclear Fusion*, 19:1343–1357, 1979.

[6] P. Jacquet, Y. Demers, GA Chaudron, V. Glaude, A. Cote, A. Dube, R. Mireault, A. Robert, and L. Vachon. Microwave probe diagnostic for the lower hybrid multijunction antenna on TdeV. *Review of Scientific Instruments*, 68:1176, 1997.

[7] G.R. Hanson, J.B. Wilgen, C. Lau, Y. Lin, G.M. Wallace, and S.J. Wukitch. Scrape-off layer reflectometer for Alcator C-Mod. *Review of Scientific Instruments*, 79:10F114, 2008.

[8] C. Lau, G Hanson, J. Wilgen, Y. Lin, and S. Wukitch. Scrape-off layer reflectometer for Alcator C-Mod. *Review of Scientific Instruments*, 81:10D918, 2010.

[9] V.S. Chan and S.C. Chiu. Wave-plasma coupling at the lower hybrid frequency. *Physics of Fluids*, 22:1724, 1979.

[10] A. Fukuyama, T. Morishita, and Y. Furutani. Nonlinear coupling of the slow wave structure with the lower-hybrid waves near the plasma surface. *Plasma Physics*, 22:565–578, 1980.

[11] V. A. Petrzilka, R. Klima, and P. Pavlo. On the ponderomotive effects at the lower hybrid waves excitation. *Czechoslovak Journal of Physics*, 33:1002–1010, 1983. 10.1007/BF01832346.

[12] O. Meneghini, S. Shiraiwa, and R. Parker. Full wave simulation of lower hybrid waves in Maxwellian plasma based on the finite element method. *Physics of Plasmas*, 16:090701, 2009.

[13] S. Shiraiwa, O. Meneghini, R. Parker, P. Bonoli, M. Garrett, M.C. Kaufman, J.C. Wright, and S. Wukitch. Plasma wave simulation based on a versatile finite element method solver. *Physics of Plasmas*, 17:056119, 2010.

[14] S. Shiraiwa, O. Meneghini, R. Parker, G. Wallace, and J. Wilson. Plasma wave simulation based on versatile FEM solver on Alcator C-mod. *AIP Conference Proceedings*, 1187(1):363–366, 2009.

[15] J.C. Wright, J. Lee, E. Valeo, P. Bonoli, C.K. Phillips, E.F. Jaeger, and R.W. Harvey. Challenges in Self-Consistent Full-Wave Simulations of Lower Hybrid Waves. *Plasma Science, IEEE Transactions on*, 38(9):2136–2143, 2010.

[16] O. Meneghini and S. Shiraiwa. Full wave simulation of Lower Hybrid waves in ITER plasmas based on the finite element method. *Plasma and Fusion Research*, 5:S2081, 2010.

[17] O. Meneghini, S. Shiraiwa, and R. Parker. Integration of Fokker Planck calculation in full wave FEM simulation of LH waves. In *American Physical Society, 51th Annual Meeting of the Division of Plasma Physics, November 2-6, 2009, abstract PP8.003*, 2009.

[18] S. Shiraiwa, J. Ko, O. Meneghini, R. Parker, AE Schmidt, S. Scott, M. Greenwald, AE Hubbard, J. Hughes, Y. Ma, et al. Full wave effects on the lower hybrid wave spectrum and driven current profile in tokamak plasmas. *Physics of Plasmas*, 18:080705, 2011.

[19] Y. Peysson and J. Decker. Fast electron bremsstrahlung in axisymmetric magnetic configuration. *Physics of Plasmas*, 15:092509, 2008.

[20] O. Meneghini, S. Shiraiwa, I. Faust, R. Parker, A. Schmidt, and G. Wallace. Fullwave simulations of Lower hybrid waves coupled to 3D Fokker Planck solver: comparison with Alcator C-Mod experiments. In *1st International Youth Conference on Fusion Energy, in conjunction with 23rd IAEA FEC, Daejeon, Republic of Korea*, 2010.

[21] J. Liptac, R. Parker, V. Tang, Y. Peysson, and J. Decker. Hard x-ray diagnostic for lower hybrid experiments on Alcator C-Mod. *Review of Scientific Instruments*, 77:103504, 2006.

[22] Y. Peysson. Effect of plasma fluctuations on lower hybrid current drive. *AIP Conference Proceedings of 19th Topical Conference on Radio Frequency Power in Plasmas*, 2011. To be published.

[23] R. Cesario, A. Cardinali, C. Castaldo, F. Paoletti, W. Fundamenski, S. Hacquin, and the JET-EFDA workprogramme contributors. Spectral broadening of lower hybrid waves produced by parametric instability in current drive experiments of tokamak plasmas. *Nuclear Fusion*, 46(4):462, 2006.

[24] R Cesario, L Amicucci, C Castaldo, M Kempenaars, S Jachmich, J Mailloux, O Tudisco, A Galli, A Krivska, and JET-EFDA contributors. Plasma edge density and lower hybrid current drive in JET (Joint European Torus). *Plasma Physics and Controlled Fusion*, 53(8):085011, 2011.

[25] G. M. Wallace, R. R. Parker, P. T. Bonoli, A. E. Hubbard, J. W. Hughes, B. L. LaBombard, O. Meneghini, A. E. Schmidt, S. Shiraiwa, D. G. Whyte, J. C. Wright, S. J. Wukitch, R. W. Harvey, A. P. Smirnov, and J. R. Wilson. Absorption of lower hybrid waves in the scrape off layer of a diverted tokamak. *Physics of Plasmas*, 17(8):082508, 2010.

[26] G. Wallace. *Behavior of Lower Hybrid Waves in the Scrape Off Layer of a Diverted Tokamak.* PhD thesis, MIT, 2010.

[27] GM Wallace, PT Bonoli, AE Hubbard, BL LaBombard, O. Meneghini, RR Parker, AE Schmidt, S. Shiraiwa, DG Whyte, JC Wright, et al. Absorption of lower hybrid waves in the scrape off layer and possible implications for ITER. *Bulletin of the American Physical Society*, 55, 2010.

[28] O. Meneghini. SOL Effects on LH Wave Coupling and Current Drive Performance on Alcator C-Mod. *AIP Conference Proceedings of 19th Topical Conference on Radio Frequency Power in Plasmas*, 2011.

[29] O. Meneghini, S. Shiraiwa, I. Faust, R. Parker, and G. Wallace. Validation of the LHEAF code against Alcator C-Mod LHCD discharges. In *38th EPS Conference on Plasma Physics*, 2011.

[30] G.V. Pereverzev. Use of the multidimensional WKB method to describe propagation of lower hybrid waves in tokamak plasma. *Nuclear Fusion*, 32(7):1091, 1992.

[31] JC Wright, PT Bonoli, M. Brambilla, F. Meo, E. D'Azevedo, DB Batchelor, EF Jaeger, LA Berry, CK Phillips, and A. Pletzer. Full wave simulations of fast wave mode conversion and lower hybrid wave propagation in tokamaks. *Physics of Plasmas*, 11:2473, 2004.

[32] Thomas Howard Stix. *Waves in Plasmas.* American Institute of Physics Publishing, 1992.

[33] M. Brambilla. *Kinetic theory of plasma waves: homogeneous plasmas.* Oxford University Press, USA, 1998.

[34] D.G. Swanson. *Plasma Waves, Second Edition.* IOP Publishing, 2003.

[35] R. Fitzpatrick, R.D. Hazeltine, and F.L. Waelbroeck. *The Physics of Plasmas.* The University of Texas at Austin, 2008.

[36] Ian Hutchinson. *Principles of Plasma Diagnostics (second edition).* Cambridge University press, 2001.

[37] F.F. Chen and MA Lieberman. *Introduction to plasma physics and controlled fusion.* : Plenum Press, New York, 1984.

[38] L.D. Landau and E.M. Lifšic. Course of theoretical physics: The classical theory of fields. 2, 2009.

[39] P.T. Bonoli and R.C. Englade. Simulation model for lower hybrid current drive. *Physics of Fluids*, 29(9):2937, 1986.

[40] M. Porkolab, PT Bonoli, and SC Chiu. Collisional damping of the fast magnetosonic wave in the tokamak edge plasma. In *Eleventh Topical Conference on Radio Frequency Power in Plasmas: Palm Springs, CA, May 1995*, number 355, page 231. AIP Press, 1996.

[41] J.P. Freidberg. *Plasma physics and fusion energy.* Cambridge University Press, 2007.

[42] N.J. Fisch. Confining a tokamak plasma with rf-driven currents. *Physical Review Letters*, 41(13):873–876, 1978.

[43] CF Kennel and F. Engelmann. Velocity space diffusion from weak plasma turbulence in a magnetic field. *Physics of Fluids*, 9(12):2377, 1966.

[44] I. Lerche. Quasilinear Theory of Resonant Diffusion in a Magneto-Active, Relativistic Plasma. *Physics of Fluids*, 11:1720, 1968.

[45] S. Weinberg. Eikonal method in magnetohydrodynamics. *Physical Review*, 126(6):1899, 1962.

[46] A. Cardinali, L. Morini, C. Castaldo, R. Cesario, and F. Zonca. Analysis of the validity of the asymptotic techniques in the lower hybrid wave equation solution for reactor applications. *Physics of Plasmas*, 14:112506, 2007.

[47] P. Rodrigues and J.P.S. Bizarro. Images of electrostatic lower-hybrid-wave beam propagation in tokamak plasmas using a paraxial WKB approach. *Plasma Science, IEEE Transactions on*, 30(1):68 –69, feb 2002.

[48] AS Richardson, PT Bonoli, and JC Wright. The lower hybrid wave cutoff: A case study in eikonal methods. *Physics of Plasmas*, 17:052107, 2010.

[49] PM Bellan and M. Porkolab. Propagation and mode conversion of lower-hybrid waves generated by a finite source. *Physics of Fluids*, 17:1592, 1974.

[50] C.F.F. Karney. Stochastic Ion Heating by a Lower Hybrid Wave: II. *Phys. Fluids*, 22(11):2188–2209, 1979.

[51] S. Bernabei, C. Daughney, P. Efthimion, W. Hooke, J. Hosea, F. Jobes, A. Martin, E. Mazzucato, E. Meservey, R. Motley, et al. Lower-hybrid current drive in the PLT tokamak. *Physical Review Letters*, 49(17):1255–1258, 1982.

[52] N.J. Fisch. Theory of current drive in plasmas. *Reviews of modern physics*, 59(1):175, 1987.

[53] D. van Houtte, G. Martin, A. Bcoulet, J. Bucalossi, G. Giruzzi, G.T. Hoang, Th. Loarer, B. Saoutic, and the Tore Supra Team. Recent fully non-inductive operation results in Tore Supra with 6 min, 1 GJ plasma discharges. *Nuclear Fusion*, 44(5):L11, 2004.

[54] M. Porkolab. Survey of lower hybrid experiments. *IEEE Transactions on Plasma Science*, 12(2):107–117, 1984.

[55] F. Santini. Developments in Lower Hybrid theory. Technical Report International School of Plasma Physics, Course and Workshop on Applications of RF waves to Tokamak Plasmas, (Varenna, Italy), 1985. p 251.

[56] C. Gormezano. Review of lower hybrid wave heating and current drive. *Plasma Physics and Controlled Fusion*, 28:1365, 1986.

[57] E. Barbato. Recent progress in lower hybrid current drive theory and experiments. *Plasma Physics and Controlled Fusion*, 40(8A):A63, 1998.

[58] G. Wallace. Lower hybrid current drive in a high density diverted tokamak. *AIP Conference Proceedings of 19th Topical Conference on Radio Frequency Power in Plasmas*, 2011. To be published.

[59] M Goniche, L Amicucci, Y Baranov, V Basiuk, G Calabro, A Cardinali, C Castaldo, R Cesario, J Decker, D Dodt, A Ekedahl, L Figini, J Garcia, G Giruzzi, J Hillairet, G T Hoang, A Hubbard, E Joffrin, K Kirov, X Litaudon, J Mailloux, T Oosako, R Parker, V Pericoli-Ridolfini, Y Peysson, P Platania, F Rimini, P K Sharma, C Sozzi, and G Wallace. Lower hybrid current drive for the steady-state scenario. *Plasma Physics and Controlled Fusion*, 52(12):124031, 2010.

[60] R. Cesario. Lower hybrid current drive at plasma densities required for thermonuclear reactors. *AIP Conference Proceedings of 19th Topical Conference on Radio Frequency Power in Plasmas*, 2011. To be published.

[61] F. Troyon and FW Perkins. Lower-hybrid heating in large Tokamak. In *RF Plasma Heating*, volume 1, 1975.

[62] R. L. Stenzel and W. Gekelman. Electrostatic waves near the lower hybrid frequency. *Phys. Rev. A*, 11(6):2057–2060, Jun 1975.

[63] P.M. Bellan and M. Porkolab. Experimental studies of lower hybrid wave propagation. *Physics of Fluids*, 19:995, 1976.

[64] L Landau. On the vibration of the electronic plasma. *J. Phys. USSR*, (10):25, 1946.

[65] A. Lenard and Ira B. Bernstein. Plasma Oscillations with Diffusion in Velocity Space. *Phys. Rev.*, 112(5):1456–1459, Dec 1958.

[66] C.F.F. Karney, N.J. Fisch, United States. Dept. of Energy, and Princeton University. Plasma Physics Laboratory. Numerical studies of current generation by radio-frequency traveling waves. *Physics of Fluids*, 22(9):1817, 1979.

[67] N. J. Fisch and A. H. Boozer. Creating an Asymmetric Plasma Resistivity with Waves. *Phys. Rev. Lett.*, 45(9):720–722, Sep 1980.

[68] V. Fuchs, RA Cairns, MM Shoucri, K. Hizanidis, and A. Bers. A one-dimensional model for lower-hybrid current drive including perpendicular dynamics. *Physics of Fluids*, 28:3619, 1985.

[69] M. Porkolab. Parametric instabilities due to lower-hybrid radio frequency heating of tokamak plasmas. *Physics of Fluids*, 20:2058, 1977.

[70] I. Faust. Lower Hybrid Wave Induced SOL Emissivity Variation at High Density on the Alcator C-Mod Tokamak. *AIP Conference Proceedings of 19th Topical Conference on Radio Frequency Power in Plasmas*, 2011. To be published.

[71] G.M. Wallace, A.E. Hubbard, P.T. Bonoli, I.C. Faust, R.W. Harvey, J.W. Hughes, B.L. LaBombard, O. Meneghini, R.R. Parker, A.E. Schmidt, S. Shiraiwa, A.P. Smirnov, D.G. Whyte, J.R. Wilson, J.C. Wright, S.J. Wukitch, and the Alcator C-Mod Team. Lower hybrid current drive at high density in Alcator C-Mod. *Nuclear Fusion*, 51(8):083032, 2011.

[72] G. Giruzzi, E. Barbato, S. Bernabei, and A. Cardinali. Measurement of the hot electrical conductivity in the PBX-M tokamak. *Nuclear Fusion*, 37(5):673, 1997.

[73] PT Bonoli, J. Ko, R. Parker, AE Schmidt, G. Wallace, JC Wright, CL Fiore, AE Hubbard, J. Irby, E. Marmar, et al. Lower hybrid current drive experiments on Alcator C-Mod: Comparison with theory and simulations. *Physics of plasmas*, 15:056117, 2008.

[74] Yu.F. Baranov and V.I. Fedorov. Lower-hybrid wave propagation in tokamaks. *Nuclear Fusion*, 20(9):1111, 1980.

[75] DW Ignat. Toroidal effects on propagation, damping, and linear mode conversion of lower hybrid waves. *Physics of Fluids*, 24:1110, 1981.

[76] P.T. Bonoli and E. Ott. Toroidal and scattering effects on lower-hybrid wave propagation. *Physics of Fluids*, 25:359, 1982.

[77] M Brambilla and A Cardinali. Eikonal description of HF waves in toroidal plasmas. *Plasma Physics*, 24(10):1187, 1982.

[78] M. Abramowitz and I.A. Stegun. *Handbook of mathematical functions with formulas, graphs, and mathematical tables*, volume 55. Dover publications, 1964.

[79] RW Motley. Vortex formation during radio frequency heating of plasma. *Physics of Fluids*, 23:2050, 1980.

[80] H. Motz and C.J.H. Watson. RF confinement and acceleration of plasmas. *Advances in electronics and electron physics*, 23:153, 1967.

[81] John R. Cary and Allan N. Kaufman. Ponderomotive Force and Linear Susceptibility in Vlasov Plasma. *Phys. Rev. Lett.*, 39(7):402–404, Aug 1977.

[82] A.C. England, O.C. Eldridge, S.F. Knowlton, M. Porkolab, and J.R. Wilson. Power transmission and coupling for radiofrequency heating of plasmas. *Nuclear Fusion*, 29(9):1527, 1989.

[83] RW Motley and WM Hooke. Active-passive waveguide array for wave excitation in plasmas. Technical report, Princeton Univ., NJ (USA). Plasma Physics Lab., 1979.

[84] P. Bibet, X. Litaudon, and D. Moreau. Conceptual study of a reflector waveguide array for launching lower hybrid waves in reactor grade plasmas. *Nuclear Fusion*, 35(10):1213, 1995.

[85] Jorge H. Belo, Philippe Bibet, Joo P.S. Bizarro, Bernard Bertrand, Roberto Cesario, Mauro Corona, Paul Finburg, Alan S. Kaye, Frederic Leguern, Alain Lioure, Joelle Mailloux, Francesco Mirizzi, Jef Ongena, Christophe Portafaix, Pietro Testoni, Angelo A. Tuccillo, Jean-Claude Vallet, Bob Walton, Robert J. Warren, and David J. Wilson. An ITER-relevant passive active multijunction launcher for lower hybrid current drive in JET-grade plasmas. *Nuclear Fusion*, 51(8):083017, 2011.

[86] AP Smimov and RW Harvey. Calculations of the Current Drive in DIII-D with the GENRAY Ray Tracing Code. *Bull. APS*, 40, 1995.

[87] JC Wright, PT Bonoli, CK Phillips, E. Valeo, and RW Harvey. Full wave simulations of lower hybrid wave propagation in tokamaks. *MIT-PSFC report*, 1187:351–358, 2009.

[88] J.C. Wright, PT Bonoli, AE Schmidt, CK Phillips, EJ Valeo, RW Harvey, and MA Brambilla. An assessment of full wave effects on the propagation and absorption of lower hybrid waves. *Physics of Plasmas*, 16:072502, 2009.

[89] EF Jaeger, LA Berry, E. D'Azevedo, DB Batchelor, and MD Carter. All-orders spectral calculation of radio-frequency heating in two-dimensional toroidal plasmas. *Physics of Plasmas*, 8:1573, 2001.

[90] D.L. Green, E.F. Jaeger, L.A. Berry, and P.M. Ryan. Predicting HHFW Heating Efficiency on NSTX via Whole-Device Full-Wave Simulation. *AIP Conference Proceedings of 19th Topical Conference on Radio Frequency Power in Plasmas*, 2011. To be published.

[91] RW Harvey and MG McCoy. The cql3d fokker-planck code. *Advances in Simulation and Modeling of Thermonuclear Plasmas*, page 498, 2005.

[92] G.R. Simpson. A generalized n-port cascade connection. In *Microwave Symposium Digest, 1981 IEEE MTT-S International*, pages 507–509. IEEE, 1981.

[93] R. Bilato and M. Brambilla. FELHS code for Lower–Hybrid launcher coupling and near fields. page P5, 2008.

[94] J. Hillairet, D. Voyer, A. Ekedahl, M. Goniche, M. Kazda, O. Meneghini, D. Milanesio, and M. Preynas. ALOHA: an Advanced LOwer Hybrid Antenna coupling code. *Nuclear Fusion*, 50(12):125010, 2010.

[95] MA Irzak and ON Shcherbinin. Theory of waveguide antennas for plasma heating and current drive. *Nuclear fusion*, 35:1341, 1995.

[96] D. Milanesio, V. Lancellotti, O. Meneghini, R. Maggiora, G. Vecchi, and R. Bilato. TOPLHA: an accurate and efficient numerical tool for analysis and design of LH antennas. *AIP Conference Proceedings*, 933(1):301–304, 2007.

[97] R. Mittra and S.W. Lee. *Analytical techniques in the theory of guided waves.* Macmillan, 1971.

[98] J. Hillairet, O. Meneghini, D. Milanesio, D. Voyer, and M. Goniche. Comparisons between the TOPLHA and the ALOHA codes on Lower Hybrid antenna coupling. *AIP Conference Proceedings*, 1187(1):379–382, 2009.

[99] COMSOL Multiphysics, www.comsol.com/.

[100] M. Kaufman. *Lower Hybrid Experiments Using an Interdigital Line Antenna on the Reversed Field Pinch.* PhD thesis, University of Wisconsin-Madison, 2009.

[101] Y. Takase, A. Ejiri, H. Kakuda, Y. Nagashima, T. Wakatsuki, O. Watanabe, P. Bonoli, O. Meneghini, S. Shiraiwa, J. Wright, C. Moeller, H. Kasahara, R. Kumazawa, T. Mutoh, K. Saito, and TST-2 Group. Development of a plasma current ramp-up technique for spherical tokamaks by the lower hybrid wave. *Nuclear Fusion*, 51(6):063017, 2011.

[102] ML Garrett, SJ Wukitch, S. Shiraiwa, O. Meneghini, Y. Lin, P. Koert, and W. Beck. ICRF Antenna Design Studies for Alcator C-Mod. In *APS Meeting Abstracts*, volume 1, page 8032P, 2009.

[103] ML Garrett, SJ Wukitch, W. Beck, P. Koert, Y. Lin, and R. Parker. ICRF Antenna Optimization for Alcator C-Mod. *Bulletin of the American Physical Society*, 55, 2010.

[104] IH Hutchinson, R. Boivin, F. Bombarda, P. Bonoli, S. Fairfax, C. Fiore, J. Goetz, S. Golovato, R. Granetz, M. Greenwald, et al. First results from Alcator-C-MOD. *Physics of Plasmas*, 1(5):1511, 1994.

[105] D. Bora, P.K. Sharma, S.L. Rao, R.G. Trivedi, M.K. Gupta, K. Ambulkar, K. Mishra, P.R. Parmar, K. Kumar, and A. Thakur. Design criteria and current status of LHCD system on SST1 machine. *Fusion Engineering and Design*, 82(2):141 – 152, 2007.

[106] V. Pericoli-Ridolfini, Ph. Bibet, F. Mirizzi, M.L. Apicella, E. Barbato, P. Buratti, G. Calabr, A. Cardinali, G. Granucci, L. Panaccione, S. Podda, C. Sozzi, and A.A. Tuccillo. LHCD and coupling experiments with an ITER-like PAM launcher on the FTU tokamak. *Nuclear Fusion*, 45(9):1085, 2005.

[107] Computer Simulation Technologies - Microwave Studio, www.cst.com.

[108] O Meneghini. Computational electromagnetics for design-oriented analysis of plasma facing antennas. Master's thesis, Politecnico di Torino, 2004.

[109] D. Milanesio, O. Meneghini, V. Lancellotti, R. Maggiora, and G. Vecchi. A multi-cavity approach for enhanced efficiency in TOPICA RF antenna code. *Nuclear Fusion*, 49:115019, 2009.

[110] D.M. Pozar. *Microwave engineering.* Wiley-India, 2009.

[111] O. Meneghini, S. Shiraiwa, W. Beck, J. Irby, P. Koert, R. R. Parker, R. Viera, J. Wilson, and S. Wukitch. Integrated numerical design of an innovative Lower Hybrid launcher for Alcator C-Mod. *AIP Conference Proceedings*, 1187(1):423–426, 2009.

[112] S. Shiraiwa, O. Meneghini, W. Beck, J. Doody, P. MacGibbon, D. Irby, J. abd Johnson, P. Koert, C. Lau, R.R. Parker, D. Terry, R. Viera, G. Wallace, J. Wilson, S. Wukitch, and Alcator CMod Team. Design and Commissioning of a Novel LHCD Launcher on Alcator C-Mod. In *IAEA conference proceedings*, 2010.

[113] NP Basse, A. Dominguez, EM Edlund, CL Fiore, RS Granetz, AE Hubbard, JW Hughes, IH Hutchinson, JH Irby, B. LaBombard, et al. Diagnostic systems on alcator C-mod. *Fusion science and technology*, 51(3):476–507, 2007.

[114] L.L. Lao, H. St. John, R.D. Stambaugh, A.G. Kellman, and W. Pfeiffer. Reconstruction of current profile parameters and plasma shapes in tokamaks. *Nuclear Fusion*, 25(11):1611, 1985.

[115] Jinseok Ko, Steve Scott, Syun'ichi Shiraiwa, Martin Greenwald, Ronald Parker, and Gregory Wallace. Intrashot motional Stark effect calibration technique for lower hybrid current drive experiments. *Review of Scientific Instruments*, 81(3):033505, 2010.

[116] J. Liptac. *Lower Hybrid modeling and experiments on Alcator C-Mod.* PhD thesis, MIT, 2006.

[117] A Schmidt. *Measurements and Modeling of Lower Hybrid Driven Fast Electrons on Alcator C-Mod.* PhD thesis, Massachusetts Institute of Technology, 2011.

[118] B. LaBombard, JE Rice, AE Hubbard, JW Hughes, M. Greenwald, J. Irby, Y. Lin, B. Lipschultz, ES Marmar, CS Pitcher, et al. Transport-driven Scrape-Off-Layer flows and the boundary conditions imposed at the magnetic separatrix in a tokamak plasma. *Nuclear fusion*, 44:1047, 2004.

[119] Noah Smick. *Plasma Flows in the Alcator C-Mod Scrape-Off Layer.* PhD thesis, MIT, 2009.

[120] F. Leuterer, F. Soldner, M. Brambilla, M. Munich, F. Monaco, M. Zouhar, R. Bartiromo, A. Tuccillo, S. Bernabei, and C. Forest. Coupling of the 2X24 waveguide grill for lower hybrid waves in ASDEX. *Plasma Physics and Controlled Fusion*, 33:169–180, 1991.

[121] J. Stevens, M. Ono, R. Horton, and J. R. Wilson. Edge density profile effects for lower hybrid waveguide coupling. *Nuclear Fusion*, 21:1259–1264, 1981.

[122] JH Belo and P. Bibet. Coupling properties of Tore Supra's ITER-like LH PAM launcher. *Proceedings of the 31st EPS on Contr. Fusion and Plasma Physics*, 2004.

[123] P. Jacquet, Y. Demers, V. Glaude, C. Boucher, A. Cote, C. Cote, and M. St-Onge. LHCD antenna coupling experiments on the TdeV tokamak. *AIP Conference Proceedings*, 355(1):122–125, 1996.

[124] RE Bell, S. Bernabei, N. Greenough, L. Lagin, B. Leblanc, M. Okabayashi, H. Takahashi, L. Schmitz, L. Blush, RP Doerner, et al. Lower hybrid wave coupling in PBX-M. *Nuclear Fusion*, 34:271, 1994.

[125] M. Goniche, D. Guilhem, P. Bibet, P. Froissard, X. Litaudon, G. Rey, J. Mailloux, Y. Demers, V. Fuchs, P. Jacquet, et al. Enhanced heat flux in the scrape-off layer due to electrons accelerated in the near field of lower hybrid grills. *Nuclear Fusion*, 38:919–937, 1998.

[126] C Gormezano and D Moreau. Lower hybrid wave coupling in the Wega Tokamak. *Plasma Physics and Controlled Fusion*, 26(3):553, 1984.

[127] V Pericoli-Ridolfini, A Ekedahl, S K Erents, J Mailloux, S Podda, Y Sarazin, A A Tuccillo, and EFDA-JET Workprogramme contributors. Study and optimization of lower hybrid wave coupling in advanced scenario plasmas in JET. *Plasma Physics and Controlled Fusion*, 46(2):349, 2004.

[128] V. Petrzilka, G. Corrigan, P. Belo, V. Fuchs, A. Ekedahl, M. Goniche, J. Hillairet, P. Jacquet, J. Mailloux, M.-L. Mayoral, J. Ongena, V. Parail, and JET EFDA contributors. Edge2d modeling of ponderomotive density depletion in front of the JET LH grill. In *Proc. 37th EPS Conf. on Control. Fusion and Plasma Physics*, 2010.

[129] AA Tuccillo, E. Barbato, L Gabellieri, G. Granucci, S. Ide, et al. 8 GHz experiment on FTU. In *Strong Microwaves in Plasmas (Proceedings of the Int. Workshop on Strong Microwaves in Plasmas, Nizhny Novgorod, Russia, August 15-22 1993)*, volume 1, page 47, 1994.

[130] F. Mirizzi, C. Gourlan, A. Marra, M. Roccon, A Tucillo, P. Bibet, P. Froissard, M Goniche, F. Kazarian, J. Mailloux, et al. Toward an active passive waveguide array for lower hybrid application on ITER. In *SOFT: Symposium on fusion technology*, 1998.

[131] F. Mirizzi, ML Apicella, P. Bibet, G. Calabrŋ, L. Panaccione, V. Pericoli-Ridolfini, S. Podda, and AA Tuccillo. The test of a PAM launcher on FTU: The first step toward the LHCD launcher for ITER. *Fusion Engineering and Design*, 74(1-4):237–242, 2005.

[132] Y. Ikeda, O. Naito, M. Seki, T. Kondoh, S. Ide, K. Anno, H. Fukuda, Y. Ikeda, T. Kitai, K. Kiyono, M. Sawahata, S. Shinozaki, K. Suganuma, N. Suzuki, and K. Ushigusa. Simple multijunction launcher with oversized waveguides for lower hybrid current drive on JT-60U. *Fusion Engineering and Design*, 24(3):287 – 298, 1994.

[133] VA Petrzilka, F. Leuterer, F.X. Soldner, L. Giannone, and R. Schubert. Non-linear coupling of the lower hybrid grill in ASDEX. *Nuclear fusion*, 31:1758, 1991.

[134] F Clairet, C Bottereau, J M Chareau, M Paume, and R Sabot. Edge density profile measurements by X-mode reflectometry on Tore Supra. *Plasma Physics and Controlled Fusion*, 43(4):429, 2001.

[135] KM Rantamaki, TJH Pa ttikangas, SJ Karttunen, KM Alm-Lytz, JP Verboncoeur, and P. Mardahl. Electromagnetic particle-in-cell simulations of a lower hybrid grill. *Plasma physics and controlled fusion*, 44:1349, 2002.

[136] GJ Morales. Coupling of lower-hybrid radiation at the plasma edge. *Physics of Fluids*, 20:1164, 1977.

[137] A. Ekedahl, B. Frincu, M. Goniche, J. Hillairet, and V. Petrzilka. Non-Linear Effects on the LH Wave Coupling in Tore Supra and Impact on the LH Current Drive Efficiency. *AIP Conference Proceedings*, 1187:407, 2009.

[138] B. Frincu. Report on non linear effects on Tore Supra. Master's thesis, Grenoble Institute of Technology, 2009.

[139] A. E. Schmidt, P. T. Bonoli, R. Parker, M. Porkolab, G. Wallace, J. C. Wright, J. R. Wilson, R. W. Harvey, and A.P. Smirnov. Evidence of spectrum control over lower hybrid power deposition on Alcator C-Mod. In *Bull. Am. Phys. Soc.*, volume 53, page 121, Nov. 2008.

[140] M. Brambilla. A full wave code for ion cyclotron waves in toroidal plasmas. Technical Report IPP 5/66, Max-Planck-Institute fur plasmaphysik, 1996.

[141] A. Fukuyama, E. Yokota, and T. Akutsu. Global Analysis of ICRF Waves and Alfven Eighenmodes in Toroidal Helical Plasmas. In *18th IAEA conference on fusion energy*, pages IAEA–CN–77/THP2/26, Sorrento, Italy, 2000.

[142] D. Moreau, Y. Peysson, J.M. Rax, A. Samain, and J.C. Dumas. Variational description of lower hybrid wave propagation and absorption in fusion plasmas. *Nuclear Fusion*, 30(1):97, 1990.

[143] Y. Peysson, E. Sbelin, X. Litaudon, D. Moreau, J.-C. Miellou, M.M. Shoucri, and I.P. Shkarofsky. Full wave modelling of lower hybrid current drive in tokamaks. *Nuclear Fusion*, 38(6):939, 1998.

[144] M Brambilla. Numerical simulation of ion cyclotron waves in tokamak plasmas. *Plasma Physics and Controlled Fusion*, 41(1):1, 1999.

[145] MATLAB, www.matlab.com/.

[146] D. Sjoberg, C. Engstrom, G. Kristensson, D.J.N. Wall, and N. Wellander. A Floquet-Bloch decomposition of Maxwell's equations applied to homogenization. *Multiscale Modeling and Simulation*, 4(1):149–171, 2006.

[147] T.A. Davis. Algorithm 832: UMFPACK V4. 3—an unsymmetric-pattern multifrontal method. *ACM Transactions on Mathematical Software (TOMS)*, 30(2):199, 2004.

[148] O. Schenk and K. G
"artner. Solving unsymmetric sparse systems of linear equations with PARDISO. *Future Generation Computer Systems*, 20(3):475–487, 2004.

[149] P.R. Amestoy, I.S. Duff, J.Y. L'Excellent, and J. Koster. A fully asynchronous multifrontal solver using distributed dynamic scheduling. *SIAM Journal on Matrix Analysis and Applications*, 23(1):15–41, 2002.

[150] P.R. Amestoy et al. Algorithm 837: AMD, an approximate minimum degree ordering algorithm. *ACM Transactions on Mathematical Software (TOMS)*, 30(3):388, 2004.

[151] M. Porkolab, JJ Schuss, B. Lloyd, Y. Takase, S. Texter, P. Bonoli, C. Fiore, R. Gandy, D. Gwinn, B. Lipschultz, et al. Observation of lower-hybrid current drive at high densities in the Alcator C tokamak. *Physical Review Letters*, 53(5):450–453, 1984.

[152] M. Porkolab, B. Lloyd, Y. Takase, P. Bonoli, C. Fiore, R. Gandy, R. Granetz, D. Griffin, D. Gwinn, B. Lipschultz, E. Marmar, S. McCool, A. Pachtman, D. Pappas, R. Parker, P. Pribyl, J. Rice, J. Terry, S. Texter, R. Watterson, and S. Wolfe. High-Power Electron Landau-Heating Experiments in the Lower Hybrid Frequency Range in a Tokamak Plasma. *Phys. Rev. Lett.*, 53:1229, 1984.

[153] F. Kazarian, B. Beaumont, E. Bertrand, L. Delpech, S. Dutheil, C. Goletto, M. Prou, A. Beunas, F. Peauger, and Ph. Thouvenin. Developing the next LHCD source for Tore Supra. *Fusion Engineering and Design*, 74(1-4):425 – 429, 2005. Proceedings of the 23rd Symposium of Fusion Technology - SOFT 23.

[154] M. Goniche, JA Dobbing, A. Ekedahl, P. Schild, and FX S
"oldner. *Long distance coupling of lower hybrid waves in JET using gas feed.* 1997.

[155] A. Ekedahl, G. Granucci, J. Mailloux, Y. Baranov, S.K. Erents, E. Joffrin, X. Litaudon, A. Loarte, P.J. Lomas, D.C. McDonald, V. Petrzilka, K. Rantamki, F.G. Rimini, C. Silva, M. Stamp, A.A. Tuccillo, and JET EFDA Contributors. Long distance coupling of lower hybrid waves in JET plasmas with edge and core transport barriers. *Nuclear Fusion*, 45(5):351, 2005.

[156] A. Ekedahl, K. Rantamaki, M. Goniche, J. Mailloux, V. Petrzilka, B. Alper, Y. Baranov, V. Basiuk, P. Beaumont, G. Corrigan, et al. Effect of gas injection during LH wave coupling at ITER-relevant plasma wall distances in JET. *Plasma Physics and Controlled Fusion*, 51:044001, 2009.

[157] G.T. Hoang, A. Bécoulet, J. Jacquinot, J.F. Artaud, Y.S. Bae, B. Beaumont, JH Belo, G. Berger-By, J.P.S. Bizarro, P. Bonoli, et al. A lower hybrid current drive system for ITER. *Nuclear Fusion*, 49:075001, 2009.

[158] ITER technical basis document (IAEA,vienna,2001) doc.no. GAO FDR 1 00-07-13 r1.0 Section 4.3.3. pp. ITER technical basis document, doc.no. GAO FDR 1 00-07-13 r1.0 Section 4.3.3, IAEA, Vienna, 2001.

[159] DW Ignat, EJ Valeo, and SC Jardin. Dynamic modelling of lower hybrid current drive. *Nuclear fusion*, 34:837, 1994.

[160] I.P. Shkarofsky and M.M. Shoucri. Modelling of lower hybrid current drive in the presence of spatial radial diffusion. *Nuclear Fusion*, 37:539, 1997.

[161] C.F.F. Karney. Fokker-Planck and quasilinear codes. *Computer Physics Reports*, 4(3-4):183–244, 1986.

[162] H.E. Mynick and J.D. Strachan. Transport of runaway and thermal electrons due to magnetic microturbulence. *Physics of Fluids*, 24:695, 1981.

[163] H.W. Koch and J.W. Motz. Bremsstrahlung cross-section formulas and related data. *Reviews of Modern Physics*, 31(4):920–955, 1959.

[164] O. Meneghini, S. Shiraiwa, I. Faust, R. Parker, A. Schmidt, and G. Wallace. Fullwave simulations of Lower hybrid waves coupled to 3D Fokker Planck solver: comparison with Alcator C-Mod experiments. *Fusion Science and Technology*, 60(1T):40–47, July 2011.

[165] R. W. Harvey and M. McCoy. In *the IAEA Technical Committee Meeting on Simulation and Modeling of Thermonuclear Plasmas*, 1992. USDOC NTIS Document No. DE93002962.

[166] F. Paoletti, D.W. Ignat, J. Kesner, S. Bernabei, R. Kaita, B. Leblanc, F.M. Levinton, and S.C. Luckhardt. Lower hybrid current drive accessibility study with reconstructed magnetic equilibria in PBX-M. *Nuclear Fusion*, 34(6):771, 1994.

[167] A.S.K.V. Kotov, D. Reitera, and A.S. Kukushkinb. Numerical study of the iter divertor plasma with the b2-eirene code package. *Bericht des Forschungszentrums Julich-4257*, 47:875–879, 2007.

[168] V. Kotov, D. Reiter, RA Pitts, S. Jachmich, A. Huber, and DP Coster. Numerical modelling of high density JET divertor plasma with the SOLPS4. 2 (B2-EIRENE) code. *Plasma Physics and Controlled Fusion*, 50:105012, 2008.

[169] Stangeby. *The Plasma Boundary of Magnetic Fusion Devices.* IOP Publishing Ltd., 2000.

[170] S. Jones, S. Goeler, S. Bernabei, D. Ignat, J. Kesner, R. Kaita, S. Luckhardt, F. Paoletti, and F. Rimini. Calculation of an upper limit for an effective fast electron diffusion constant using the hard X-ray camera on PBX-M. *Plasma physics and controlled fusion*, 35:1003, 1993.

[171] S. Knowlton, M. Porkolab, and Y. Takase. Experimental studies of the radial diffusion of energetic electrons in lower-hybrid wave heated plasmas in the Alcator-C tokamak. *Physics of plasmas*, 1:891, 1994.

[172] Y. Peysson, J. Decker, and V. Basiuk. Simulations of Tore Supra Lower Hybrid Current Drive Experiments. In *34th EPS Conference on Plasma Physics, Warsaw*, pages 2–6, 2007.

[173] H. Dreicer. Electron and ion runaway in a fully ionized gas. I. *Physical Review*, 115(2):238, 1959.

[174] H. Dreicer. Electron and ion runaway in a fully ionized gas. II. *Physical Review*, 117(2):329, 1960.

[175] K. Kupfer, D. Moreau, and X. Litaudon. Statistical theory of wave propagation and multipass absorption for current drive in tokamaks. *Physics of Fluids B: Plasma Physics*, 5:4391, 1993.

[176] JP Bizarro. On the dynamics of the launched power spectrum during lower hybrid current drive in tokamaks. *Nuclear fusion*, 33:831, 1993.

[177] DA D'Ippolito, JR Myra, EF Jaeger, LA Berry, and DB Batchelor. Local Mode Analysis of 2D ICRF Wave Solutions. *AIP Conference Proceedings*, 694:463–466, 2003.

[178] D. A. D'Ippolito and J. R. Myra. Local Mode Analysis using Windowed Fourier Transform and Wavelet Techniques. Technical report, Lodestar Research Corporation, 2004.

[179] GV Pereverzev. Effect of diffraction on absorption of lower hybrid waves in a tokamak. *Soviet Journal of Experimental and Theoretical Physics Letters*, 44:549, 1986.

[180] Y. Peysson and J. Decker. Advanced Lower Hybrid Current Drive Modeling. *AIP Conference Proceedings*, 933(1):293–296, 2007.

[181] S. Shiraiwa, PT Bonoli, I. Faust, O. Meneghini, A Hubbard, R. Parker, G Wallace, and D. J. Wilson. Progress in modeling and experiment to approach AT regime on Alcator C-Mod. In *APS Meeting Abstracts*, volume 1, page 8005P, 2011.

[182] S. Shiraiwa. Progress in modeling and experiment to approach AT regime on Alcator C-Mod. In *19th International Toki Conference, Toki, Japan*, 2011.

[183] G Wallace. Absorption of lower hybrid waves in the scrape off layer of a diverted tokamak. In *APS Meeting Abstracts*, 2011.

[184] S. Bernabei, R. Bell, TK Chu, A. Cavallo, S. Guharay, W. Hooke, J. Hosea, F. Jobes, D. McNeill, E. Meservey, et al. Top-versus-side launch of lower hybrid waves in PLT. *Nuclear fusion*, 26:111, 1986.

[185] S. Ide, O. Naito, T. Kondoh, Y. Ikeda, and K. Ushigusa. Response of lower hybrid wave driven current profile on wave launching position. *Nuclear fusion*, 36:1057, 1996.

[186] S. Ide, O. Naito, T. Kondoh, Y. Ikeda, and K. Ushigusa. Enhancement of Absorption of Lower Hybrid Wave by Filling the Spectral Gap. *Phys. Rev. Lett.*, 73(17):2312–2315, Oct 1994.

[187] J. Decker and Y. Peysson. On Self-consistent Simulation of the Lower Hybrid Current Drive. In *33rd EPS Conference on Plasma Physics, Roma, Italy*, pages 19–23, 2006.

[188] V. Petrzilka, V Fuchs, J. Gunn, N. Fedorczak, A. Ekedahl, M. Goniche, J. Hillairet, and P. Pavlo. Theory of fast particle generation in front of LH grills. *Plasma Physics and Controlled Fusion*, 53(5):054016, 2011.

[189] J. Killeen, G.D. Kerbel, M.G. McCoy, and A.A. Mirin. *Computational methods for kinetic models of magnetically confined plasmas*. Springer-Verlag, 1986.

[190] C. L. Longmire and M. N. Rosenbluth. Diffusion of Charged Particles across a Magnetic Field. *Phys. Rev.*, 103:507–510, Aug 1956.

[191] M.N. Rosenbluth and CL Longmire. Stability of plasmas confined by magnetic fields* 1. *Annals of Physics*, 1(2):120–140, 1957.

[192] J. Decker. *Electron Bernstein wave current drive modeling in toroidal plasma confinement.* PhD thesis, Massachusetts Institute of Technology. Dept. of Electrical Engineering and Computer Science., 2005.

[193] H.A.L. Kiers. Setting up alternating least squares and iterative majorization algorithms for solving various matrix optimization problems. *Computational statistics & data analysis*, 41(1):157–170, 2002.

At LHD in Toki, Japan

With Ted Golfinopoulos and Syunichi Shiraiwa

US-JAPAN RF workshop in San Diego

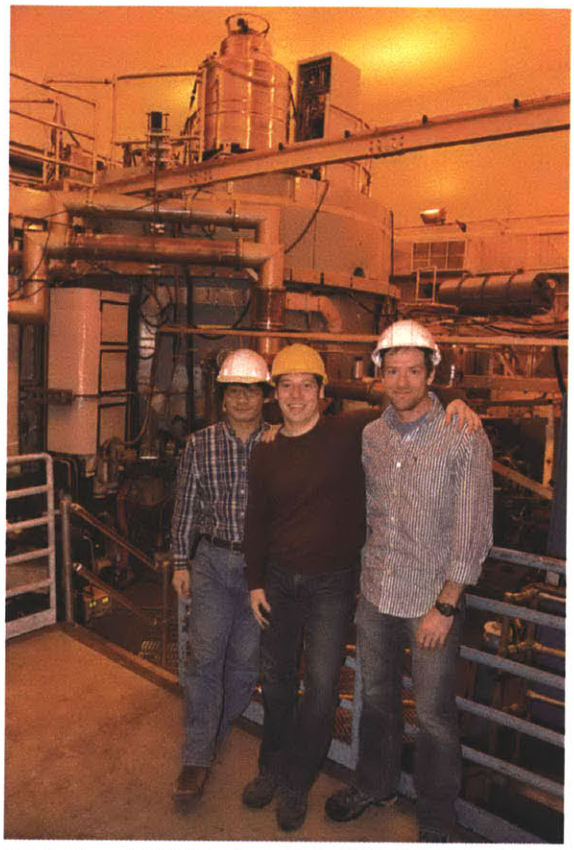

With Syunichi Shiraiwa and Mike Garrett,
Alcator C-Mod in the background

Inside of the Alcator C-Mod vessel,
the LH2 antenna is in the background

AUGUST 2011 VOLUME 18 NUMBER 8

PHYSICS OF PLASMAS

Full wave effects on the lower hybrid wave spectrum and driven current profile in tokamak plasmas by S. Shiraiwa, J. Ko, O. Meneghini *et al.*

AIP